

December 2020

Structural and Functional Characterization of L-Enduracididine Biosynthetic Enzymes

Nemanja Vuksanovic
University of Wisconsin-Milwaukee

Follow this and additional works at: <https://dc.uwm.edu/etd>



Part of the [Biochemistry Commons](#)

Recommended Citation

Vuksanovic, Nemanja, "Structural and Functional Characterization of L-Enduracididine Biosynthetic Enzymes" (2020). *Theses and Dissertations*. 2615.
<https://dc.uwm.edu/etd/2615>

This Dissertation is brought to you for free and open access by UWM Digital Commons. It has been accepted for inclusion in Theses and Dissertations by an authorized administrator of UWM Digital Commons. For more information, please contact open-access@uwm.edu.

STRUCTURAL AND FUNCTIONAL CHARACTERIZATION OF L-ENDURACIDIDINE
BIOSYNTHETIC ENZYMES

by

Nemanja Vuksanovic

A Dissertation Submitted in
Partial Fulfillment of the
Requirements for the Degree of

Doctor of Philosophy
in Chemistry

at

The University of Wisconsin-Milwaukee

December 2020

ABSTRACT

STRUCTURAL AND FUNCTIONAL CHARACTERIZATION OF L-ENDURACIDIDINE BIOSYNTHETIC ENZYMES

by

Nemanja Vuksanovic

The University of Wisconsin-Milwaukee, 2020
Under the Supervision of Professor Nicholas R. Silvaggi

The mannopeptimycins produced by *Streptomyces hygroscopicus* are non-ribosomal peptide antibiotics with activity against a number of Gram-positive pathogens, including drug-resistant strains like methicillin-resistant *Staphylococcus aureus* (MRSA) and vancomycin-resistant enterococci (VRE). Attempts to synthesize more potent mannopeptimycin analogues have so far not been successful. One reason this has proven difficult is that the mannopeptimycins contain the unusual non-proteinogenic amino acid L-enduracididine, or its hydroxylated derivative β -hydroxy enduracididine (β hEnd,). This amino acid is not commercially available and, while synthetic routes have been developed, they are multi-step processes starting from an advanced intermediate. Understanding enzymatic synthesis of L-End is an important goal, because it may lead to a more efficient enzymatic or chemoenzymatic route to this interesting building block.

The first enzyme in the L-End pathway is MppP, an unprecedented PLP-dependent L-Arg oxidase that catalyzes a 4-electron oxidation to give 4-hydroxy-2-ketoarginine (4HKA). Our previously proposed mechanism involved several speculative steps lacking the support of experimental data characterizing the species involved, such as the formation of 4,5-unsaturated intermediate and superoxide anion. Through the use of pre-steady state kinetics studies, EPR spectroscopy, and NMR spectroscopy, this work has provided answers to several outstanding questions regarding the mechanism of MppP.

In addition to MppP, the L-End pathway contains another unusual enzyme whose apparent function is completely different from that predicted by sequence analysis. MppR was predicted to be an acetoacetate decarboxylase (ADC), but structural studies suggested that MppR was likely responsible for the conversion of 4HKA to 2-ketoenduracididine (2KE). However, this activity had not been demonstrated kinetically owing to the lack of an assay. This study has confirmed and quantified turnover of 4HKA to 2KE by MppR through a development of a quenched-flow LC-MS/MS assay. Preliminary kinetic studies and substrate screening of MppQ have also been carried out, confirming its role as a *bona fide* aminotransferase responsible for catalyzing the final step in the synthesis of L-End. Through characterization of all enzymes involved, this work represents a significant advance towards the complete understanding of L-End biosynthesis.

© Copyright by Nemanja Vuksanovic, 2020
All Rights Reserved

TABLE OF CONTENTS

ABSTRACT.....	ii
LIST OF FIGURES.....	viii
LIST OF TABLES.....	xv
LIST OF SCHEMES.....	xvi
ABBREVIATIONS.....	xviii
ACKNOWLEDGMENTS.....	xxii
Chapter 1.....	1
1.1 Naturally occurring antimicrobial peptides.....	2
1.2 Arginine-Rich, Cell-Penetrating Peptides.....	8
1.3 Polymer-Based Peptidomimetics.....	10
1.4 Vancomycin: A New Trick for an Old Antibiotic.....	16
1.5 Peptide-Based Natural Products.....	18
1.5.1 Teixobactin.....	18
1.5.2 Enduracylinones.....	22
1.5.3 Ramoplanin and Enduracidin.....	23
1.5.4 Mannopectimycins.....	26
1.5.5 The tuberactinomycins.....	32
1.5.6 Pentaminomycins.....	33
1.5.7 Streptothricin F.....	35
1.6 References.....	37
Chapter 2.....	42
2.1 Introduction.....	42
2.2 Materials and Methods.....	46
2.3 Results and discussion.....	55
2.4 References.....	69
Chapter 3.....	71
3.1 Introduction.....	71
3.2 Materials and Methods.....	74
3.3 Results and Discussion.....	79
3.4. References.....	93

Chapter 4.....	96
4.1 Introduction	96
4.1.1 Quench-Flow Methods in Enzymology	97
4.1.2 Hydrophilic Interaction Liquid Chromatography	101
4.1.3 Mass Spectrometry	105
4.2 Materials and Methods.....	110
4.2.1 Cloning, Purification, and Expression of <i>Streptomyces hygroscopicus</i> MppR.....	110
4.2.2 Cloning, Expression and purification of <i>Arthropobacter protoformiae</i> D-Amino Acid Oxidase (D-AAO)	111
4.2.3 Reaction of DAAO with threo-4(R/S)-hydroxy-D,L-arginine mixture	113
4.2.4 Preparation of 4(S)-hydroxy-2-ketoarginine standards	115
4.2.5 Quench Flow and LC-MS/MS analysis of MppR kinetics with 4(S)HKA	120
4.3 Discussion.....	127
4.4 References	130
Chapter 5.....	131
5.1 Introduction	132
5.1.1 Preliminary MppP mechanism	134
5.1.2 Determination of microscopic rate constants	138
5.1.3 Outstanding questions regarding the MppP mechanism	140
5.1.4 Superoxide oxide detection using electron paramagnetic resonance (EPR)	140
5.1.5 Characterizing the carbon-centered radical intermediate	143
5.1.6 Mechanistic studies of MppP using nuclear magnetic resonance (NMR)	145
5.1.7. Single turnover kinetic experiments with MppP	146
5.1.8. Single turnover experiments with 3,4-dehydro L-arginine.....	147
5.1.9 Determining the extinction coefficient of the first quinonoid intermediate (Q1).....	148
5.1.10 Inhibition of MppP by vinylglycine.....	149
5.1.11 Solvent isotope effects on MppP catalysis	149
5.1.11 Factors affecting the ratio of MppP products.....	150
5.1.12 Using quenched-flow LC-MS/MS to accurately determine the product ratio at early times in the oxidation of L-arginine by SwMppP.....	150
5.2 Materials and Methods.....	151
5.2.1 CMH reaction with MppP.....	151
5.2.2	151
NMR of MppP reaction in the presence of CMH	151

5.2.3 Reaction of MppP in the presence of nitric oxide	152
5.2.4 Reaction of MppP and L-Arg in deuterium oxide.....	152
5.2.5 Wild-type MppP single turnover with L-Arg	153
5.2.6 Wild-type MppP single turnover with DHR.....	156
5.2.7 MppP and DHR product analysis.....	156
5.2.8 Determination of Quinonoid 1 extinction coefficient.....	157
5.2.9 Wild-type MppP reaction with L-Arg in the presence of vinyl glycine.....	158
5.2.10 Wild-type MppP single turnover of L-Arg in deuterium oxide.....	158
5.2.11 Wild-MppP reactions with L-Arg at different pH and temperature values	159
5.2.12 Quench-flow LC-MS/MS of wild-type MppP reaction with L-Arg	160
5.3 Results	161
5.3.1 MppP reaction with L-Arg generates superoxide	161
5.3.2. NMR analysis of MppP reaction in the presence of CMH.....	162
5.3.3 Capturing nitric oxide adduct.....	165
5.3.4 MppP mechanism does not involve 4,5 unsaturated intermediate	167
5.3.5 Revised MppP mechanism	170
5.3.6 Single turnover experiments improved Kintek Explorer fit	172
5.3.7. Product analysis of MppP reaction with DHR	175
5.3.8 Determination of Q1 extinction coefficient.....	180
5.3.9 Vinyl glycine inhibits MppP activity	181
5.3.10 Analysis of solvent isotope effects.....	182
5.3.11 Ratio of 4HKA/2KA varies with pH and temperature.....	183
5.3.12 The ratio of 4HKA/2KA determined using quench-flow based method	186
5.4 Conclusions	191
5.5 References	192
APPENDIX: NMR spectra of enzymatically produced 2-ketoarginine.....	193
CURRICULUM VITAE.....	195

LIST OF FIGURES

Figure 1-1. A) Dimer of gramicidin A in complex with cesium ions. (PDB: 1AV2). ¹¹ B) Structure of hybrid peptide of cecropin A and magainin 2 solved using NMR (PDB: 1D9L). ¹² C) Crystallographic dimer of alpha defensin HNP-3 (PDB:1DFN) ^{13, 14} . Disulfide bridges and arginines side chains are displayed. Note that one of the arginine sidechains is truncated due to a lack of electron density.D) Monomer of human beta defensin-1 (PDB:1IJU). ¹⁴ Disulfide bridges and lysines sidechains are displayed. E) Cathelicidin LL-37 (PDB: 5NMN). ¹⁵ Note that R29 and R34 have alternative sidechain conformations displayed. Images were generated using UCSF Chimera. ¹⁶	3
Figure 1-2. The bidentate hydrogen bonding of arginine with phosphate groups of the lipid bilayer results in positive Gaussian curvature of the membrane along with negative curvature component in orthogonal direction, leading to saddle-splay curvature and membrane destabilization. Image adapted from Mishra et al. ²⁴	6
Figure 1-3. The mechanism by which commonly used cell-penetrating peptide, nonaarginine (R9), cross the bacterial cell membrane. A-D Adsorption of R9 leads to a formation of a bifurcated bilayer which extends until it merges with another bilayer resulting in a multilamellar structure (E). F The instability in this multilamellar structure leads to an opening of a pore which allows R9 to enter the cell. Adapted from Allolio et al. ³³	9
Figure 1-4. Polymethacrylate based peptidomimetic random copolymer with hydrophobic and cationic side chains.....	10
Figure 1-5. Peptidomimetics with arginine and lysine mimicking sidechains synthesized by Gabriel et al.	11
Figure 1-6. Polymethacrylate based arginine and lysine mimics synthesized using Reversible Addition-Fragmentation chain Transfer (RAFT).....	13
Figure 1-7. Random copolymer arginine and lysine mimetics synthesized by Exley et al.....	14
Figure 1-8. Short linear peptides incorporating guanidine motif and bulky hydrophobic side chains synthesized by Baldassare et al.	15
Figure 1-9. Structure of lipid II, a peptidoglycan precursor.....	16
Figure 1-10. Structure of vancomycin conjugated with a varying number of arginine residues.	17
Figure 1-11. Structure of teixobactin, a novel antibiotic featuring enduracididine.	19

Figure 1-12. Non-isosteres of enduracididine incorporated in teixobactin which led to the highest antibacterial activity.	21
Figure 1-13. Structures of newly discovered aromatic polyketides containing N-methyl enduracididine.	22
Figure 1-14. Structure of ramoplanin A2. Ornithine residues are highlighted in yellow.....	23
Figure 1-15. Structures of enduracidins A and B.	25
Figure 1-16. Structures of mannopeptimycins.	26
Figure 1-17. Ester and carbonate analogues of mannopeptimycin α	28
Figure 1-18. Ether analogues of mannopeptimycin.	29
Figure 1-19. A) Substituted benzoxazole mannopeptimycin analogues B) Structures of 2-thiosubstituted benzoxazole analogues C) Aglycone analogue of mannopeptimycin.....	30
Figure 1-20. Structures of capreomycin IA, viomycin and tuberactinomycin O.....	32
Figure 1-21. Structures of newly discovered pentaminomycins.	34
Figure 1-22. Structure of Streptothricin F, an aminoglycoside antibiotic containing streptolidine.....	35
Figure 2-1. Chromatogram of enzymatically produced mixture of 4(S)HKA and 2KA in 20 mM ammonium acetate, pH 7.0.....	50
Figure 2-2. Chromatogram of enzymatically produced 2KE along with reaction by-products. The majority of 2KE appears to have been decarboxylated during the drying process, significantly decreasing product yield.....	51
Figure 2-3. ShMppQ homodimer, with one monomer shown as ribbon representation and other shown as surface representation.	56
Figure 2-4. The $2 F_o - F_c $ (magenta mesh) and simulated annealing composite omit (green mesh) electron density maps are shown for the K250-PLP adduct at 1.2σ (map radius 2.5 \AA) in a stereoview of the ShMppQ active site (A). A second stereoview of the active site (B) is shown without electron density and in a different orientation (rotated $\sim 60^\circ$ in the horizontal) to give a clearer picture of the linkage between K250 and the cofactor. A schematic representation of the active site (C) shows the interactions of active site functional groups with the cofactor and each other (associated distances are given in \AA). ...	59
Figure 2-5. The $2 F_o - F_c $ (magenta mesh) and simulated annealing composite omit (green mesh) electron density maps are shown for the PMP at 1.2σ (map radius 2.5 \AA) in a stereoview of the ShMppQ active site (A). A second stereoview of the active site (B) is shown without electron density and in a	

different orientation (rotated ~60 ° in the horizontal) to give a clearer picture of the PMP and catalytic lysine. A schematic representation of the active site (C) shows the interactions of active site functional groups with the cofactor and each other (associated distances are given in Å). 60

Figure 2-6. Michaelis-Menten curve for the reaction of ShMppQ with **7** and L-Ala. 62

Figure 2-7. MS chromatograms of MppQ reaction with **5** and L-Ala at 10 (A) and 50 seconds (B). 64

Figure 2-8. Production of **1** in a reaction of ShMppQ with **6** and L-Ala. The peaks corresponding to all fragments generated from 173 m/z precursor ion were integrated and areas under the curve plotted on the y-axis. 65

Figure 2-9. Production of 2KA (174 m/z) and lack of produced L-Arg (175 m/z) in reactions of MppQ with glyoxylate and glycine, respectively. The coupling partner in each reaction was **7**. 66

Figure 2-10. Reactivity of MppQ and **7** with various amino donor substrates. 67

Figure 3-1. The L-enduracididine biosynthetic pathway begins with L-arginine (**1**), which is oxidized by the unusual PLP-dependent L-Arg oxidase, MppP, to 4(R)-hydroxy-2-ketoarginine (**2**). MppP, at least in vitro, releases the partially oxidized dead-end product 2-ketoarginine (**3**) in about 40% of catalytic cycles. The oxidized arginine derivative **2** is cyclized by MppR to create the iminoimidazolidine ring of the intermediate **4** (i.e. 2-ketoenduracididine). MppQ is thought to catalyze the transamination of **4** with an as-yet-unidentified amino donor substrate to yield the finished amino acid L-enduracididine (**5**). MppQ also catalyzes the transamination of the dead-end product **3** to regenerate L-Arg, though it has not been ascertained if this is a physiologically relevant catalytic activity or an adventitious in vitro phenomenon. 72

Figure 3-2. EcGhrA is active as a dimer of 35 kDa protomers as shown in (A). One protomer is shown in cartoon representation, and the other as a solvent-accessible surface. Each protomer is comprised of two domains: a nucleotide binding domain (blue) and a substrate binding domain (green). In the absence of NADP(H), the substrate binding domain is disordered (B). This figure was generated using the POVSCRIPT+ modification of MOLSCRIPT^{34, 35} 85

Figure 3-3. The view of EcGhrA active site with glyoxylate (A) and 2-ketoarginine (B) bound. The $2|F_o| - |F_c|$ electron density map contoured at 1.0σ is shown as blue mesh, and the $2|F_o| - |F_c|$ composite omit map, also contoured at 1.0σ , is shown as green mesh. The (A) and (B) were prepared using the POVSCRIPT+ modification of MOLSCRIPT. The 3D views were displayed in 2D in (C) and (D) to clearly show distances between ligands and the active site residues. All distances were calculated using tools provided in COOT. 86

Figure 3-4 The view of wild-type EcGhrA active site with α -ketoglutarate bound. The $2|F_o| - |F_c|$ electron density map contoured at 1.0σ is shown as blue mesh, and the $2|F_o| - |F_c|$ composite omit map, also contoured at 1.0σ , is shown as green mesh. The image was generated using the POVSCRIPT+ modification of MOLSCRIPT. 87

Figure 3-5. Michaelis-Menten (with substrate inhibition) curve for reaction of wild-type EcGhrA with glyoxylate.	88
Figure 3-6. The view of EcGhrA ^{W45F} active site. The image was generated using the POVSCRIPT+ modification of MOLSCRIPT.	89
Figure 4-1. Schematic representation of quench-flow instrument adapted from Lymn and Taylor, 1970.	98
Figure 4-2. Schematic representation of a time-delay quench flow apparatus (Adaptation from Barman et al. 2006)	99
Figure 4-3. A) HILIC “click” saccharide stationary phase. B) Mixed mode HILIC stationary phase. C) Structure of the sulfobetaine functional group of the ZIC-HILIC stationary phase. Adapted from Buszewski and Noga, 2011.	103
Figure 4-4. Separation of MppP reactant and products using ZIC-HILIC.	104
Figure 4-5. Graphical representation of ionization mechanism employed by electrospray ionization (ESI) (adapted from Ho et al., 2003)	105
Figure 4-6. Schematic representation of a triple quadrupole mass spectrometer (Shimadzu LCMS-8040). Adapted from LCMS 8040 Brochure, Shimadzu Corporation, 2012.	106
Figure 4-7. Schematic representation of a quadrupole mass-analyzer. Adapted from El-Aneed et al., 2009	108
Figure 4-8. Mass spectrum of threo-4(R/S)-hydroxy-D,L-arginine mixture in the precursor ion scan mode.	113
Figure 4-9. MS precursor ion scan of DAAO after overnight reaction with the threo-4(R/S)-hydroxy-D,L-arginine mixture (A). A similar MS precursor ion scan after the second addition of DAAO (B).	114
Figure 4-10. ¹ H NMR spectrum of enzymatically produced 4(S)HKA doped with L-Trp in deuterium oxide.	116
Figure 4-11. Decarboxylated 4(S)HKA standard curve used to determine the concentration of DAAO-derived 4(S)HKA.	118
Figure 4-12. Schematic representation of a quenched-flow qPOD double-mixing experiment.	120
Figure 4-13. Side view of the qPod device showing the “pushing syringe” (grey) and the collection valve in the DRIVE position (A). Schematic diagram of the qPod collection valve showing the sample path in both the DRIVE and COLLECT positions (B). Diagram adapted from qPOD manual (TgK Scientific, 2007).....	122

Figure 4-14. Only the deprotonated form of p-nitrophenol absorbs UV light at 400 nm.....	123
Figure 4-15. LC-MS chromatograms showing an increase in the production of 2KE over a period of 60 seconds. The CE values represent collisional energies used to generate the product ions.....	125
Figure 4-16. Calibration curve used to determine concentrations of 2KE produced by MppR (A). Time-dependent production of 2KE at various concentrations of 4(S)HKA (B). Michaelis-Menten curve for a reaction of MppR with 4(S)HKA (C). For panels B and C, the weighted ($1/Y^2$) non-linear regression fit with outliers detected and removed was performed in GraphPad Prism. The 95% CI (symmetric) of 2KE concentration or initial rates is represented by error bars.	127
Figure 5-1. Structure of MppP active site with 4(S)HKA bound. (Han et al., 2018).....	134
Figure 5-2. The structure of DMPO, a nitron compound commonly used in spin trapping.....	141
Figure 5-3. Reaction of CMH with superoxide generates the stable nitron radical CM•.....	143
Figure 5-4. Decomposition of DEANO under acidic conditions produces two molecules of nitric oxide and one of diethylamine.....	145
Figure 5-5. Pseudo first-order double-mixing reaction of MppP and L-Arg. Note the multiple phases and broad range of parameters as indicated by gray area around every simulated fit.	146
Figure 5-6. Structure of DHR.....	148
Figure 5-7. First-derivative plots of the time-dependent EPR spectra of the MppP reaction with L-Arg in the presence of CMH (selected time points chosen for clarity).	161
Figure 5-8. ^1H NMR spectra from reaction mixtures containing MppP and L-arginine in the absence of CMH (a) and in the presence of CMH (b).....	164
Figure 5-9. Potential adduct formed by MppP reaction intermediate and nitric oxide.....	165
Figure 5-10. First quadrupole scan of the L-Arg, DEANO, Cat(Fe^{3+})NO control sample in positive ESI mode (a). First quadrupole scan of the test sample containing L-Arg, DEANO, Cat(Fe^{3+})NO, and MppP.	166
Figure 5-11. ^1H NMR spectra of MppP reaction with L-arginine carried out in deuterium oxide (bottom) and water (top) (A). Zoomed in ^1H NMR spectra of MppP and L-Arg reactions in deuterium oxide and water, showing only the diastereotopic protons on alpha carbon. (B) Measured J-constants for anti and gauche protons. (C) "Simplified" peaks due to smaller J-constants of deuterium exchanged protons...	168
Figure 5-12. (A,B,D) Single-turnover experiments of MppP and L-Arg. The double-mixing experiment monitoring absorbance at 560 nm shows just one peak, unlike when carried out under pseudo first-order	

conditions. (C) Pseudo first-order experiment monitoring fluorescence produced by excitation at 415 nm. 173

Figure 5-13. Two-dimensional FitSpace plots showing the range of values for each rate constant in the kinetic model that are consistent with the data. Single, sharp peaks indicate well constrained estimates. A sharp rise followed by a plateau signifies that the lower limit is well defined, while the opposite pattern, a plateau followed by a sharp drop, defines an upper limit on the rate constant. Flat lines (e.g. $k+8$) show that the rate constant is completely unconstrained by the data. No plots are calculated for rate constants that were fixed in the model (e.g. the irreversible steps for the reactions with dioxygen). 175

Figure 5-14. (A) upon mixing with enzyme, DHR solution briefly turns purple, confirming formation of a highly conjugated quinonoid 2. (B) The tonomer used for anaerobic reaction of MppP and DHR. The side arm on the right has a septum in order to allow for injection of methanol to quench the reaction, while maintaining anaerobic environment. 176

Figure 5-15. MS scan of reaction of MppP and DHR. The most intense peak corresponds to decarboxylated 2-ketoarginine 177

Figure 5-16. (A) The single-turnover single-mixing reaction of MppP and DHR monitored via absorbance at 560 nm. Under anaerobic condition, the quinonoid 2 accumulates followed by rapid decay phase. (B) Single-turnover double-mixing reaction of MppP and DHR with a range of added dioxygen concentrations. 178

Figure 5-17. UV-VIS scans of MppP reaction with L-Arg under anaerobic conditions leading to accumulation of quinonoid 1 intermediate. The subsequent scans show that the absorbance at 510 nm is stable meaning that all arginine is bound, and no oxygen is present to allow decay of quinonoid 1. 180

Figure 5-18. Inhibition curves for MppP reaction in the presence of vinylglycine. The green curve represents the reaction of MppP and L-Arg without vinylglycine. The blue curve represents the reaction of MppP and L-Arg in the presence of vinylglycine without first incubating enzyme and vinylglycine. Red curve was obtained for the experiment incubating enzyme and vinylglycine for 15 minutes prior to adding L-Arg 181

Figure 5-19. (A) Single-mixing 415 nm excitation fluorescence experiment of MppP and L-Arg in the presence of deuterium oxide. (B) Double-mixing experiments at 510 and 560 nm of MppP and L-Arg in the presence of deuterium oxide. (C) Single-mixing experiment at 510 nm of MppP and L-Arg in the presence of deuterium oxide. 183

Figure 5-20. (A) ^1H NMR spectrum of MppP reaction with L-Arg carried out in phosphate pH 8.4. (B) ^1H NMR spectrum of MppP reaction with L-Arg carried out in water. (C) ^1H NMR spectrum of MppP reaction with L-Arg carried out in ADA pH 6.2 185

Figure 5-21. (A) ^1H NMR spectrum of MppP reaction with L-Arg in 10 mM phosphate pH 8.4 at 37 °C. (B) ^1H NMR spectrum of MppP reaction with L-Arg in 10 mM phosphate pH 8.4 at 4 °C. 186

Figure 5-22. ¹H NMR spectrum of reaction of MppP and L-Arg. The relative ratio between 4HKA and 2KA was used to quantify standards used in LC-MS/MS experiments. 187

Figure 5-23. Separation of decarboxylated 4HKA and 2KA using ZIC HILIC on Shimadzu LCMS 8060 for a reaction of 20 μM MppP and 480 μM L-Arg quenched after 15 seconds 188

Figure 5-24. (A) Standard curve for 4HKA. (B) Standard curve for 2KA..... 189

Figure 5-25. (A) The production of 4HKA and 2KA by MppP in a reaction with 480 μM L-Arg. (B) The ratio between 4HKA and 2KA over time..... 190

LIST OF TABLES

Table 2-1. Crystallographic data collection and refinement statistics of MppQ·PLP and MppQ·PMP	68
Table 3-1. Crystallographic tables for GR and ligand complexes	90
Table 3-2. Steady state parameters of EcGhrA and EcGhrA ^{W45F} with GLX, 2KA, OA, and α KG.....	92

LIST OF SCHEMES

Scheme 1-1. The reaction of L-arginine with peptidylarginine deaminase (PAD) yields L-citrulline and ammonium ion.....	7
Scheme 1-2. Biosynthetic pathway of 2S,3R-capreomycinidone.	32
Scheme 1-3. Streptolidine biosynthetic pathway.	36
Scheme 2-1. Compounds discussed in this chapter. 1 , L-enduracididine (L-End); 2 , β -hydroxyenduracididine (β hEnd); 3 , L-arginine (L-Arg); 4 , L-capreomycinidone (L-Cap); 5 , 2-oxo-4-hydroxy-5-guanidinovaleric acid (<i>i.e.</i> 4-hydroxy-ketoarginine, 4HKA); 6 , 2-ketoenduracididine (2KE); 7 , 2-oxo-5-guanidinovaleric acid (<i>i.e.</i> 2-ketoarginine, 2KA).	43
Scheme 2-2. The proposed roles of MppP/R/Q in the biosynthetic pathway of L-End.	45
Scheme 2-3. An assay of MppQ reaction with 7 and L-Ala, coupled with LDH reaction with pyruvate produced by MppQ.....	62
Scheme 3-1. EcGhrA substrates investigated in this work.	73
Scheme 4-1. Reaction of <i>Artropobacter protoformiae</i> D-amino acid oxidase with the diastereomeric mixture of threo-4(R/S)-hydroxy-D,L-arginine.....	111
Scheme 4-2. Both 1 and 2 lactonize under acidic conditions.....	126
Scheme 4-3. Graphical representation of the quench-flow method coupled with LC-MS/MS described in this chapter.	129
Scheme 5-1. MppP produces 4HKA and a partially oxidized abortive product 2KA.	132
Scheme 5-2. Spectroscopically active intermediates in the MppP reaction with L-arginine. A) Internal aldimine. B) External aldimine. C) First quinonoid intermediate. D) Second quinonoid intermediate	135
Scheme 5-3. The initially proposed mechanism of L-arginine oxidation catalyzed by MppP.	137
Scheme 5-4. The Kintek Explorer model with rate constants for the first proposed MppP mechanism.....	139
Scheme 5-5. Revised MppP mechanism without 4,5-unsaturated intermediate.	148

Scheme 5-6. The revised kinetic model for MppP fit using KinTek Explorer. The peroxy intermediates (PI1 and PI2) were included based on the NMR experiments that eliminated any 4-5 unsaturated species from the mechanism as described earlier. The green rate constants are relatively well constrained based on the FitSpace results (see Figure 5-11). Orange constants have broader parameter ranges, while red ones are poorly constrained. The black constants have been fixed during global fitting as they were assumed to involve rapid equilibrium. 171

Scheme 5-7. Reaction of MppP with 3,4-dehydroarginine leads to the formation of external aldimine and then proceeds directly to quinonoid 2 (Q2) intermediate. 174

LIST OF ABBREVIATIONS

2-HAD	D-2-hydroxyacid dehydrogenase
2KA	2-ketoarginine
2KE	2-ketoenduracididine
4HKA	4-hydroxy-ketoarginine
α KG	α -ketoglutarate
AATase	Aspartate aminotransferase
AMP	Antimicrobial peptide
APMA	aminopropyl methacrylamide
Arg	Arginine
BTP	Bis-tris propane
Cat	Catalase
CMH	1-Hydroxy-3-methoxycarbonyl- 2,2,5,5-tetramethylpyrrolidine
CPP	Cell penetrating peptide
DAAO	D-amino acid oxidase
DEANO	2-(N,N-diethylamino)-diazeneolate- 2-oxide
DMPO	5,5-Dimethyl-1-Pyrroline-N-Oxide
DHR	3,4-dehydroarginine
DTT	Dithiothreitol
EcAAT	<i>E. coli</i> aspartate aminotransferase

EPR	Electron paramagnetic resonance
ESI-MS	Electrospray ionization mass spectroscopy
GLX	Glyoxylate
GPMA	Guanadinopropyl methacrylamide
GR	Glyoxylate reductase
HEPES	(4-(2-hydroxyethyl)-1- piperazineethanesulfonic acid)
HILIC	Hydrophilic interaction liquid chromatography
IPTG	isopropyl β -D-1- thiogalactopyranoside
LAAO	L-amino acid oxidase
L-Chp	δ -chloro- ϵ -hydroxy-L- phenylglycine
L-End	L-enduracididine
L- β hEnd	L- β -hydroxyenduracididine
EcLDH	<i>E. coli</i> lactate dehydrogenase
MIC	Minimum inhibitory concentration
MES	2-(N-morpholino)ethanesulfonic acid
MRM	Multiple reaction monitoring

MRSA	Methicillin-resistant <i>Staphylococcus aureus</i>
NADH	Nicotinamide adenine dinucleotide
NMR	Nuclear magnetic resonance
NmEnd	N-methyl enduracididine
OA	Oxaloacetate
PAD	Peptidyl arginine deiminase
PCR	Polymerase chain reaction
PDB	Protein Data Bank
PEG	Polyethylene glycol
PGON	Polyguanidine oxanorbornene
PLP	Pyridoxal 5'-phosphate
PMP	Pyridoxamine phosphate
PNP	p-nitrophenol
PI	Peroxo intermediate
Q1	Quinonoid 1
Q2	Quinonoid 2
QF	Quench-flow
RAFT	Reversible addition-fragmentation chain transfer
SAR	Structure-activity relationship
SAXS	Small angle X-ray scattering

SDS-PAGE	Sodium dodecyl sulfate–polyacrylamide gel electrophoresis
SRM	Single reaction monitoring
SSM	Secondary structure matching
TLS	Translation-libration-screw
TRIS	Tris(hydroxymethyl)aminomethane
TRMS	Time-resolved mass spectrometry
VRE	Vancomycin-resistant enterococci

ACKNOWLEDGMENTS

First and foremost, I must thank my advisor, Professor Nicholas R. Silvaggi, for his support and guidance during the past five years. He allowed me to join his lab even though I had no previous experience in biochemical research, and had given me a high level of independence in designing my experiments and taking projects in new directions. He also showed tremendous patience during times when the progress was slow, and the obstacles seemed daunting, and inspired me to become a better scientist. He was nothing but a source of enthusiasm and encouragement during any discussion we had during my time in the Silvaggi Lab.

I would also like to thank my committee members, Professor Alexander Arnold, Professor Mark L. Dietz, Professor Graham R. Moran, Professor Arsenio A. Pacheco, and Professor Alan W. Schwabacher for their scientific advice and helpful discussions. I would have likely not even enrolled in the graduate program, had it not been for Professor Arnold. He took interest in my application and was the first professor I had correspondence with at University of Wisconsin-Milwaukee. Since then he has helped me many times with both research and career related questions. It was a great experience collaborating with Arnold Lab and Johnston Lab on the project involving development of novel pepsin inhibitors for the treatment of laryngopharyngeal reflux. I would like to thank Professor Dietz for his advice regarding development of analytical methods. I've learned so much about enzyme kinetics, ranging from stopped flow experiments to fluorescence titrations from Professor Moran. He and his students, Joseph Roman and Matthew Hoag, allowed me to use their instruments whenever I needed to collect data, as well as helped me with insightful comments, and I am grateful for their help. I'd like to thank Dr. Pacheco for

teaching me about air-free techniques and use of nitric oxide in enzymatic studies. Much of this work would not have been possible without organic compounds synthesized by Schwabacher Lab. I must thank Professor Schwabacher for helping me learn so much about organic chemistry, and his students Trevor Hagemann and Tyler Fenske for synthesizing the molecules I used in my experiments. I'd be remiss not to thank Professor David Frick, for being a great collaborator and providing me with an opportunity to get involved in exciting projects, as well as Anna Benko, who taught me about the principles of quantitative mass spectroscopy.

I also must thank the staff scientists of LS-CAT at Advanced Photon Source, Dr. Spencer Anderson, Dr. Joseph Brunzelle, Dr. Elena Kondrashkina, and Dr. Zdzislaw Wawrzak for helping me with experiment troubleshooting and data processing.

I'm grateful to the former and current graduate students from the Silvaggi Lab, Lisa Mydy, Lanlan Han, Lamia Badhon, and Trevor Melkonian, for making my time in graduate school more fun and less stressful. The late night brainstorming sessions with Trevor about future direction of the projects and countless trips to APS for data collection, played an instrumental role in my success in graduate school.

I was fortunate to mentor amazing undergraduate researchers, Dante Serrano, Brandon Patterson, Parker May, and Anamarie Tomaich, whose assistance was very helpful in completing my projects. Dante Serrano assisted in the development of quench-flow based LC-MS/MS methods and kinetic studies of MppQ, which are discussed in Chapters 2 and 5. Brandon Patterson was a part of the interesting journey into the field of protein engineering and designing a more selective glyoxylate reductase mutant, which I discuss in Chapter 3. I spent one summer mentoring Parker May and Anamarie Tomaich on a novel project and their energy and enthusiasm for research were truly inspiring.

Outside of University of Wisconsin-Milwaukee, I'd like to thank Professor Douglas Weibel and Professor Samuel Gellman for their advice and guidance.

I would not have been prepared well for graduate school, without my undergraduate research mentor, Professor Brad Chamberlain. Working in his lab was crucial in my development as a scientist. I also must thank Professor Olga Michels, whose courses helped me develop interest in organic chemistry.

A special thanks goes to my first chemistry instructor in the U.S.A., Mr. Bernard Hermanson. I took his course when I barely knew English and didn't even know what chemical glassware looked like. It's been more than a decade since then and he has remained a friend and a mentor, always happy to hear about my new adventures in the scientific world.

The grad school journey can often be difficult and stressful, but friendships with some great people have helped me persevere in trying to achieve my dreams. I'm grateful for my enduring friendship with Allen Wang, whose discussions with me about science and life, helped shape me both as a person and a scientist. I'd also like to thank my friend Alireza Aghayee, who suggested that I should move to Milwaukee and encouraged me to continue my education.

Finally, I want to thank my mom, Marina Vuksanovic. Her support and encouragement from the time I've first come to the U.S.A. as a high school exchange student until now, have helped me stay motivated and never lose sight of my goals.

Dedicated to my mother, whose love and support are endless.

Chapter 1

The role of arginine and its analogues in the antibacterial activity of peptides

Antibiotics dramatically altered human society in the latter half of the 20th century by preventing millions of deaths from bacterial infections. However, antibiotic resistance was problematic even at the outset, and in the beginning of the 21st century it continues to pose a growing global threat.¹

² Bacteria causing tuberculosis, other respiratory tract illnesses, and sexually transmitted diseases—many diseases that were once thought to be all but eradicated—have again become major public health issues due to antibiotic resistance. Antibiotics like β -lactams and fluoroquinolones, which are typically a part of the first-line treatments, are becoming less effective.³ The major problem with these antibiotics is that bacteria can acquire genes necessary for resistance relatively easy via horizontal gene transfer. The reason for these drugs' original effectiveness is also their Achilles' heel: they target bacterial enzymes involved in cell wall biosynthesis or DNA coil relaxation with high affinity. In many cases a few mutations, or in some cases a single mutation, are sufficient to alter a bacterial enzyme such that a particular antibiotic can no longer bind to it. In the case of β -lactams, in addition to producing β -lactamases, bacteria can alter their penicillin binding proteins, which is the case in methicillin-resistant *Staphylococcus aureus* (MRSA).⁴ Resistance to fluoroquinolones can arise due to mutations in DNA gyrase and topoisomerase IV.⁵ In the case of macrolides, lactone-based bacteriostatics that inhibit protein synthesis, resistance occurs due to methylation of ribosomal RNA.⁶ This review will discuss the

role that arginine and its analogues play as components of peptide-based antibiotics with promising activities against drug-resistant bacteria. Although penicillins and cephalosporins are also peptide-derived, this review will focus on linear peptides, depsipeptides with glycan and lipid moieties, and synthetic antimicrobial peptidomimetics with modes of action that make it more challenging for bacteria to become resistant.

1.1 Naturally occurring antimicrobial peptides

Antimicrobial peptides (AMPs) have been a target of research for several decades, as they constitute a key defense mechanism in eukaryotes. Their role goes beyond antimicrobial activity as they can modulate immune system responses as well as target viruses and cancer cells. The very first AMPs were actually discovered in bacteria and plants in the early 20th century.^{7, 8} Bacterial AMPs, like the gramicidins, are hydrophobic peptides that act as ionophores, forming channels in the membrane that destroy cells by altering ion gradients (Figure 1-1A).^{9, 10}

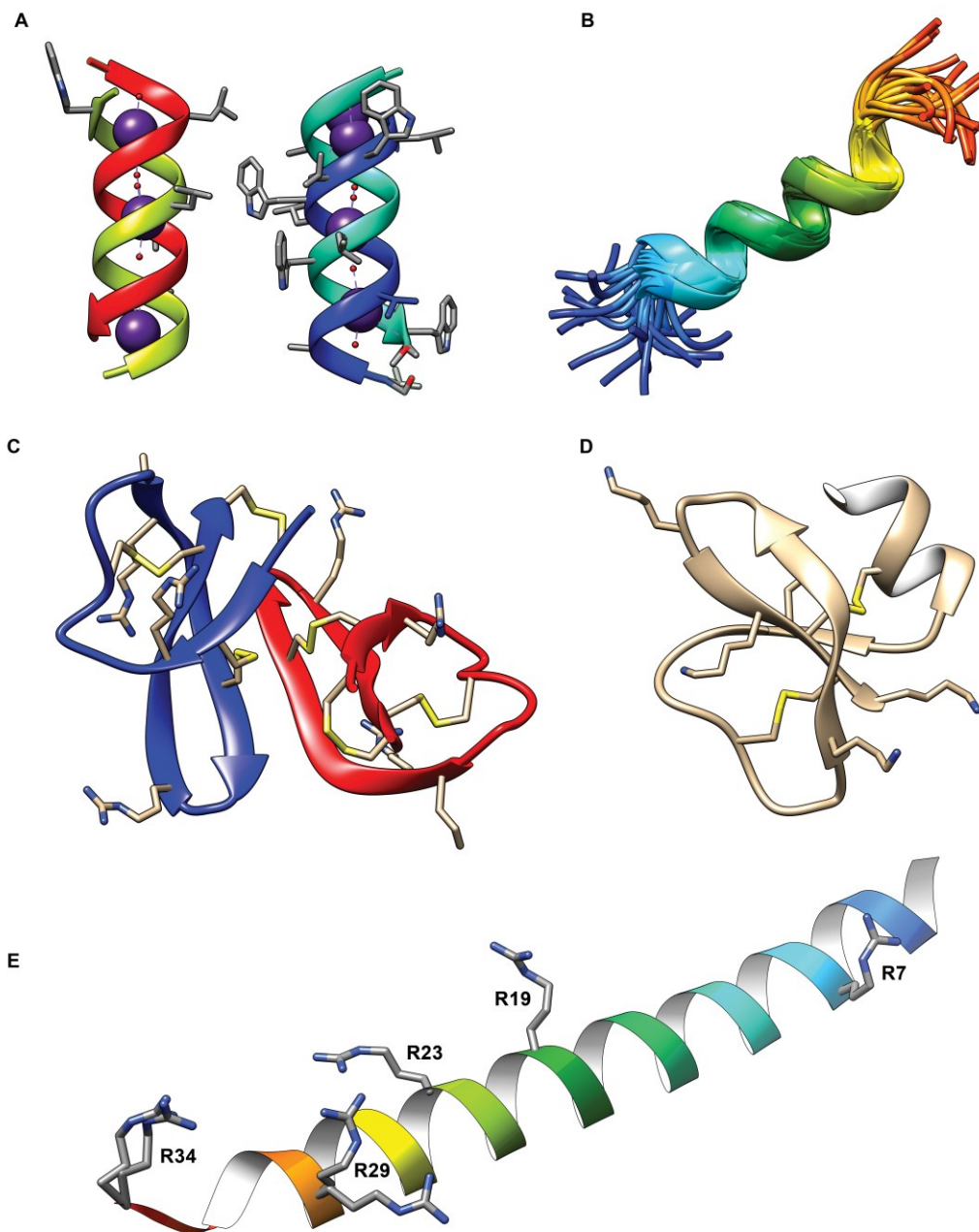


Figure 1-1. A) Dimer of gramicidin A in complex with cesium ions. (PDB: 1AV2).¹¹ B) Structure of hybrid peptide of cecropin A and magainin 2 solved using NMR (PDB: 1D9L).¹² C) Crystallographic dimer of alpha defensin HNP-3 (PDB:1DFN)^{13, 14}. Disulfide bridges and arginines side chains are displayed. Note that one of the arginine sidechains is truncated due to a lack of electron density.D) Monomer of human beta defensin-1 (PDB:1IJU).¹⁴ Disulfide bridges and lysines sidechains are displayed. E) Cathelicidin LL-37 (PDB: 5NMN).¹⁵ Note that R29 and R34 have alternative sidechain conformations displayed. Images were generated using UCSF Chimera.¹⁶

However, not much work was done on antibacterial AMPs, since antibiotics like penicillin became true miracle drugs. The rise of drug resistance led scientists to look into natural sources for novel antibiotics, and the potential of AMPs for therapeutic uses first generated interest in the second half of the 20th century. The discovery of a potent AMP in the Cecropia moth solved the question of how insects deal with bacterial infections. Cecropins are typically less than 40 amino acids long and show activity against both Gram-positive and Gram-negative bacteria. All cecropins contain lysine residues that provide a net positive charge that allows them to bind to the negatively charged phosphate groups in the membrane and disrupt it.¹⁷ Another class of AMPs that has been extensively studied are magainins, first isolated from African clawed frog (*Xenopus laevis*).¹⁸ These peptides are disordered in the solution and order into alpha-helical secondary structure upon binding to the membranes (Figure 1-1B).^{19, 20}

In humans and several other eukaryotes, there are two major families of peptides that can be classified as AMPs: defensins and cathelicidins. In addition to cationic residues, defensins contain six cysteines that form disulfides bridges giving structural stability to the peptide. Defensins are classified as α - or β -defensins based on the positioning of these disulfide bridges. The α -defensins typically have more arginine residues in their sequences, while β -defensins have more lysine residues (Figure 1-1C, Figure1-1D).²¹

This is particularly interesting because arginine occurs relatively infrequently in mammalian proteins, and less frequently than lysine, making a strong case that these residues comprise an important functional element of the α -defensins.²² The potential advantage of arginine over lysine

can be explained through their respective properties. While they are both basic, the guanidine group of arginine has a significantly higher pKa than the primary amine of the lysine sidechain. This means that essentially all of arginine residues will be positively charged even in hydrophobic membrane environment. The nature of the guanidine group leads to delocalization of the positive charge, allowing arginine to interact with other molecules in ways that lysine cannot. Arginine can participate in more hydrogen bonding interactions, and can interact with conjugated π systems in multiple ways.²² Peptides that rely on cationic interactions face an additional challenge. In environments with high salt concentrations, salt ions can compete with charged residues for binding to the membrane, thus potentially lessening the biological activity of the peptide. Arginine is more resistant to high salt concentrations due its multi-modal interactions. However, this does not mean that arginine is always the best option for any type of cationic peptide. As demonstrated herein, the structure and mechanistic details dictating the manner of interaction play a major role in determining the optimum cationic residue, leading to highly variable results across different peptides.

To determine to what extent the identity of the positively charged residues impacts the functions of cationic peptides, Zou et al. carried out a detailed study comparing arginine, lysine and several analogues thereof in the defensins.^{22, 23} The results showed that in α -defensins, the substitution of arginine for lysine leads to less potent antibacterial activity. However, this effect varied significantly across different bacteria; for some strains, the arginine-substituted α -defensins were more potent. This can be explained by the different negatively charged residues that these peptides interact with on the surfaces of Gram-positive or Gram-negative bacteria. For instance, anionic phospholipids are present on the outer membranes of Gram-negative bacteria, while Gram-positive bacteria lack the outer membrane and have teichoic acid and lipoteichoic acid moieties

protruding from the peptidoglycan layer. Using the arginine analogue homoarginine in α -defensins had a detrimental effect. Homoarginine has an additional methylene carbon, placing the positive charge farther from the peptide backbone and potentially allowing better interactions with the membrane. However, it is likely that other neutral residues also play a role in binding, and that a longer carbon chain of homoarginine disrupts these additional interactions with the membrane.

Further studies aimed at understanding why arginine to lysine substitutions affect some α -defensins significantly, while in some the activity remains unchanged, employed small angle X-ray scattering (SAXS) to observe phase changes in lipid-peptide complexes. Two α -defensins with the same net cationic charge, Crp4 and RMAD4, were studied.²³ In order to destabilize the lipid membrane, electrostatic interactions with cationic residues need to generate negative Gaussian curvature (saddle curvature) in the membrane. Arginine is more effective than lysine at inducing

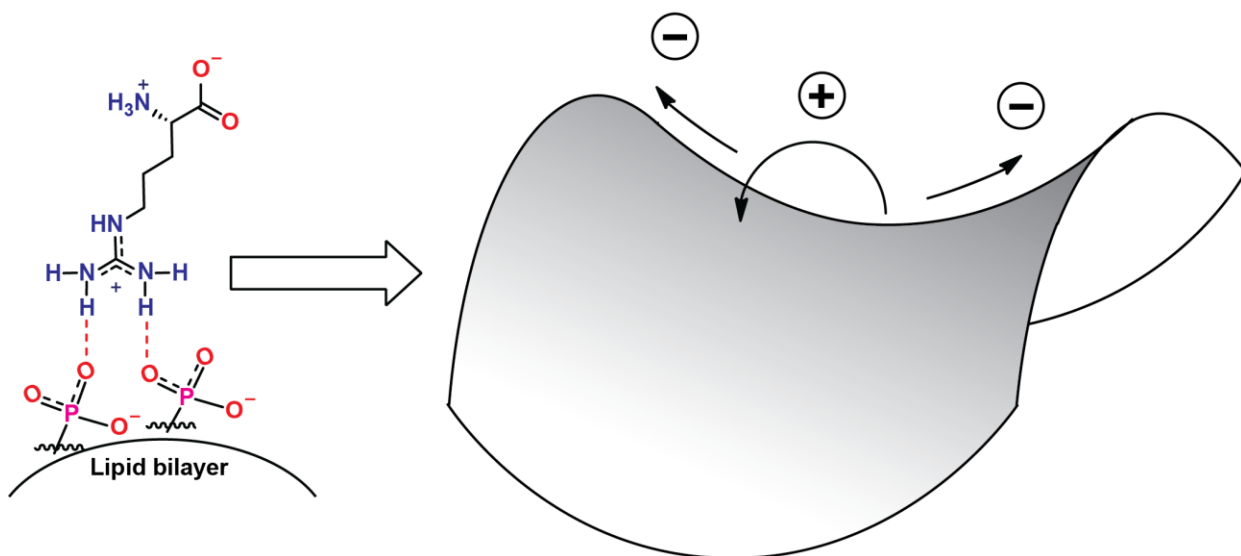


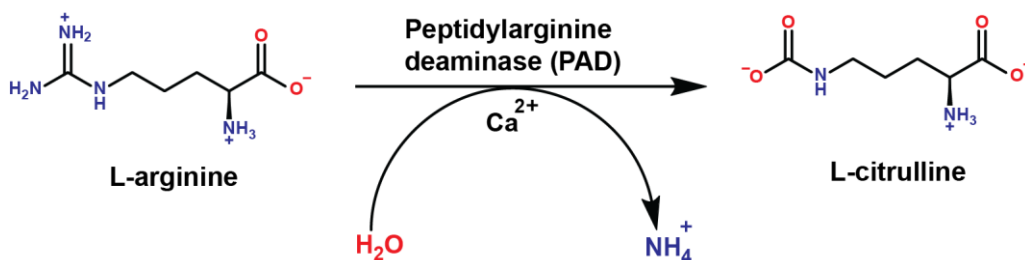
Figure 1-2. The bidentate hydrogen bonding of arginine with phosphate groups of the lipid bilayer results in positive Gaussian curvature of the membrane along with negative curvature component in orthogonal direction, leading to saddle-splay curvature and membrane destabilization. Image adapted from Mishra et al.²⁴

this curvature. The greater hydrogen bonding potential of arginine allows it to generate both negative and positive stress components in the membrane (Figure 1-2).^{24,25}

Lysine on the other hand, with its localized charge, can only generate the negative Gaussian curvature component, decreasing its ability to disrupt bacterial membranes. It should be noted, however, that membrane disruption requires a critical density of guanidinium groups. Below this threshold number of arginine residues, the ability of arginine to induce saddle curvature will be comparable to lysine. Conversely, if there is significant clustering of lysine residues, they will mimic the multi-dentate hydrogen bonding networks of clustered arginine residues.

Cathelicidins such as LL-37 are linear antimicrobial peptides that play an important role in the human immune system response against bacterial and viral infections. It contains several arginine residues that are responsible for its ability to damage bacterial membranes (Figure 1-1E).²⁶ Unlike magainins and cecropins, this peptide has ordered secondary structure in the solution, and tends to form tetramers and higher oligomers.²⁷

This is particularly important for Gram-negative bacteria which possess outer membrane. LL-37 is a target of human peptidyl arginine deiminases (PADs), which convert arginine to citrulline, an



Scheme 1-1. The reaction of L-arginine with peptidylarginine deaminase (PAD) yields L-citrulline and ammonium ion.

analogue of arginine where the guanidinium group is replaced with urea, and consequently is no longer cationic (Scheme 1-1).²⁸

This results in a loss of the antimicrobial activity of the peptide. Humans PADs are thought to play a role in homeostatic regulation of LL-37, since this peptide is involved in inflammatory response and autoimmune diseases.²⁸ Interestingly, PAD expression is upregulated during human rhinovirus (HRV) infections, which is likely one mechanism that the virus uses to evade the immune system.²⁹ Although it appears that the only determinant in the activity of LL-37 is the presence of positive charges, the positions of these charges in the peptide chain have been shown to be important as well. Wang et al. went beyond relying solely on MIC values when comparing different AMPs, as MIC values do not report whether the bacteria are dead or their growth has simply stopped, or how fast the antibiotic kills the bacteria. They did a positional swap of arginine and lysine residues in a derivative of LL-37 and probed membrane permeability over time.³⁰ It was found that the effectiveness of the lysine/arginine-swapped peptide was different than of the native form, and that the greatest effect was exhibited when the interfacial arginine residue, R23, in the amphipathic helix was replaced by lysine. This led to an inferior kinetic profile and increased cytotoxicity. This suggests that these peptides have evolved to feature arginine instead of lysine, as this may have made them a more effective defense against bacteria.

1.2 Arginine-Rich, Cell-Penetrating Peptides

Cell-penetrating peptides (CPPs) are short (typically less than 10 amino acid) peptides typically containing arginine. Unlike AMPs these peptides do not need to maintain amphipathic character; they can solely consist of charged residues and be disordered in the aqueous solution. They are capable of membrane translocation and are therefore very useful for conjugation with

drugs, as they can transport them across membrane.^{31, 32} Unlike AMPs they do not permeabilize and disrupt membrane, and their mechanism of action was debated until 2018, when Allolio et al. used a combination of experimental techniques and molecular dynamics to show that arginine-rich CPPs cross the membrane passively by inducing membrane multilamellarity (Figure 1-3).³³

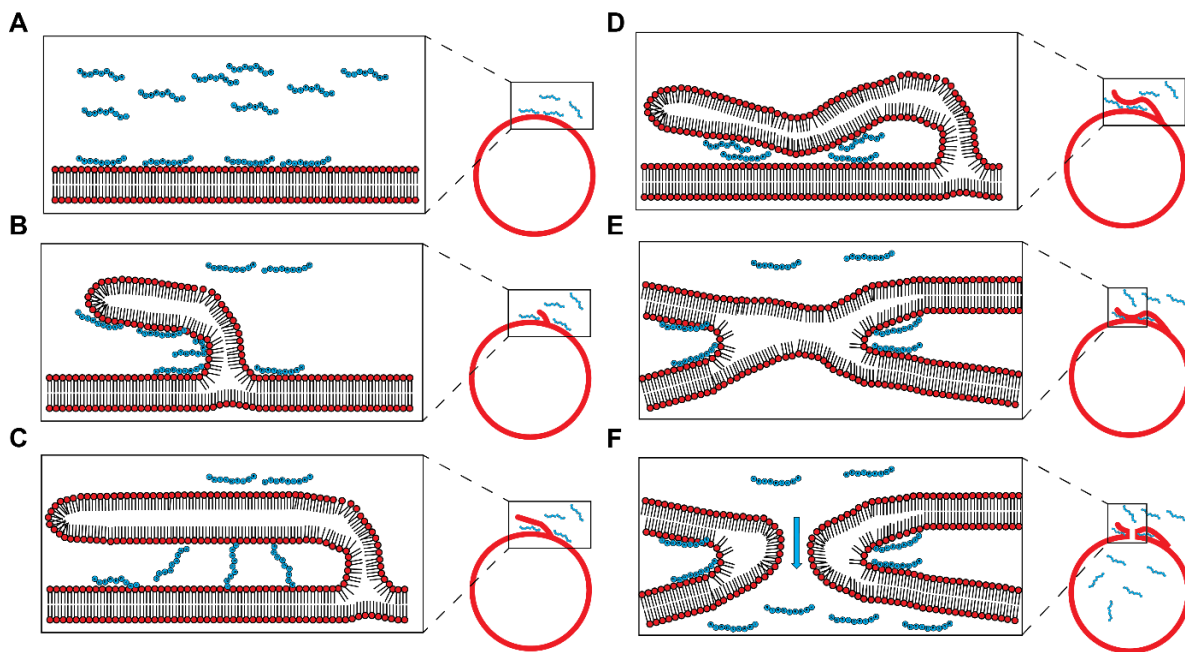


Figure 1-3. The mechanism by which commonly used cell-penetrating peptide, nonaarginine (R9), cross the bacterial cell membrane. A-D Adsorption of R9 leads to a formation of a bifurcated bilayer which extends until it merges with another bilayer resulting in a multilamellar structure (E). F The instability in this multilamellar structure leads to an opening of a pore which allows R9 to enter the cell. Adapted from Allolio et al.³³

Even though arginine-rich CPPs have a different mode of action from AMPs, the two are capable of synergistic action. In 2019, Lee et al. synthesized a conjugate of two different AMPs with a nona-arginine (R9) CPP in the hope of enhancing the antimicrobial activity of AMPs.³⁴ They observed a 4- to 16-fold increase in activity against Gram-negative bacteria. Having the R9 CPP attached allowed the AMPs to cross the membrane and bind intracellular contents in addition to disrupting the membrane. Thanks to the magnitude of the positive charge, the R9-AMP conjugates

could bind to DNA with much higher affinity, thus becoming more efficient at killing bacteria. More importantly, having a multi-modal mechanism of action makes it less likely that bacteria will develop resistance.

1.3 Polymer-Based Peptidomimetics

Large-scale synthesis of antimicrobial peptides, even when confined to proteinogenic amino acids, can be quite expensive and difficult, which prompted the development of polymer-based

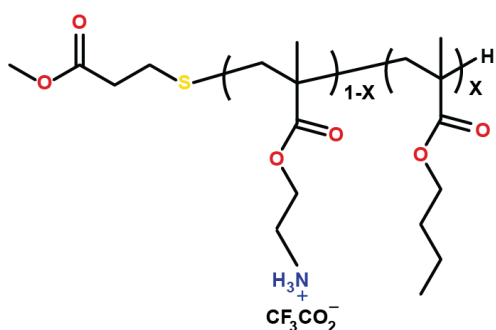


Figure 1-4. Polymethacrylate based peptidomimetic random copolymer with hydrophobic and cationic side chains.

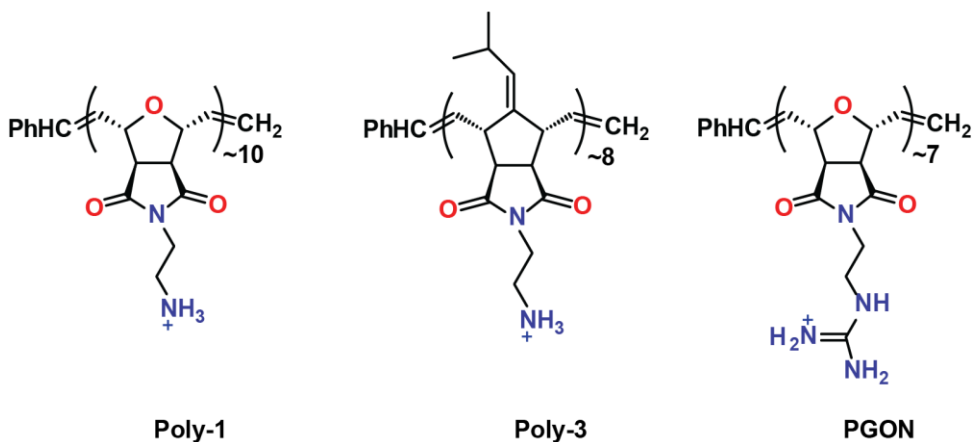


Figure 1-5. Peptidomimetics with arginine and lysine mimicking sidechains synthesized by Gabriel et al.

antimicrobial peptidomimetics. Using polymers is significantly cheaper and also allows for facile structural modifications in a quest to improve antimicrobial activity. Additionally, there is no possibility of degradation by proteases.³⁵⁻³⁷ Making charged amphipathic copolymers that are antibacterial is not difficult; they are essentially like detergents. Such peptidomimetic molecules cover the surfaces of bacterial cells in a “carpet-like” manner and dissolve the membrane. The difficult task was to engineer in selectivity for bacterial membranes to prevent cytotoxicity toward human cells. These polymers need to follow the same set of rules as natural AMPs, meaning that hydrophobic and hydrophilic polymers need to be co-polymerized to achieve amphipathic character and a positive charge at physiological pH is also required. Polymer-based peptidomimetics also need to have relatively low molecular weight. This allows them to be excreted from the body renally, thus obviating the need for biodegradability. In 2005, Kuroda et al. designed polymethacrylate-based random copolymers with hydrophilic and hydrophobic sidechains (Figure 1-4).³⁸ The hydrophilic chain had a charged primary amine and provided significant selectivity over human cells while retaining antibacterial activity. These first efforts of

making polymer-based peptidomimetics used lysine mimics to provide cell penetrating ability. Since naturally occurring

AMPs featuring arginine residues were generally more efficient at membrane penetration, Gabriel et al. decided to design peptidomimetics with arginine-mimicking sidechains (Figure 1-5). These polymers helped provide information about the optimum ratio of hydrophilicity and hydrophobicity. Their first two oxanorbornene homopolymers both had ethyl amines and one of them had an isopropyl substituted oxanorbornene. The first one was too hydrophilic and couldn't bind the membrane at all, while the one with isopropyl groups was too hydrophobic and while active, it exhibited hemolytic properties. The optimal amphiphilic ratio was achieved in polyguanidine oxanorbornene (PGON). What was also unique about this arginine-like homopolymer was that, unlike typical AMPs, it did not damage the cell membrane. It simply translocated across the membrane as cell-penetrating peptides do and killed the bacteria.

In 2013, Locoock et al. conducted a direct comparison of the activity of copolymers containing either amine or guanidine moieties (Figure 1-6).³⁹ The polymethacrylate-based polymers synthesized via reversible addition-fragmentation chain transfer (RAFT)⁴⁰ and containing guanidine groups were significantly more potent against *Staphylococcus epidermidis* and *Candida*

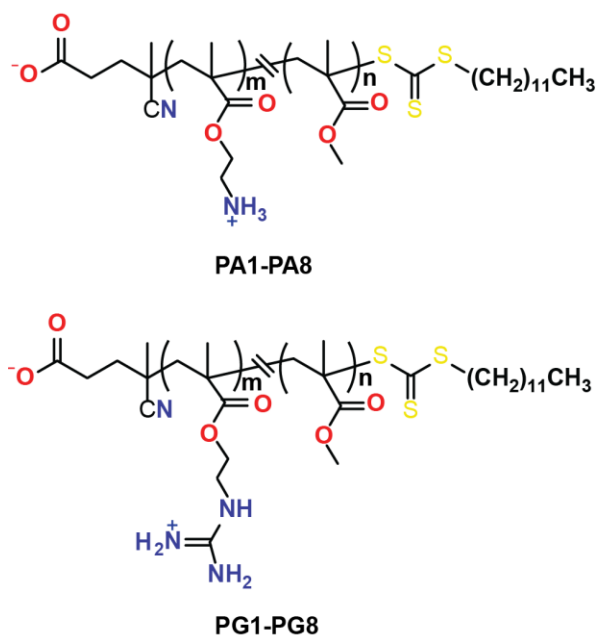


Figure 1-6. Polymethacrylate based arginine and lysine mimics synthesized using Reversible Addition-Fragmentation chain Transfer (RAFT).

albicans.

Exley et al. used RAFT (Reversible Addition-Fragmentation chain Transfer) polymerization to synthesize co-polymer mimetics containing guanidinopropyl methacrylamide (GPMA) to play the same role as the guanidine moiety found in arginine and aminopropyl methacrylamide (APMA) to mimic lysine (Figure 1-7).⁴¹

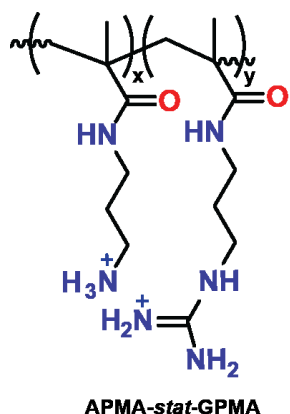


Figure 1-7. Random copolymer arginine and lysine mimetics synthesized by Exley et al.

Surprisingly, the highest antimicrobial activity was observed for a homopolymer of APMA mimicking lysine. Adding GPMA as a copolymer component reduced the activity and increased toxicity towards mammalian cells. Higher salt concentrations also had a more detrimental effect on arginine mimics. Salt inhibition can be a serious problem; for instance, in patients with cystic fibrosis, bronchopulmonary fluid has a high concentration of salt.^{42, 43} In an effort to develop novel antimicrobial agents, Baldassare et al. used arginine mimetics to balance the charge and lipophilicity.⁴⁴ They synthesized peptides containing either 1-(4-(aminomethyl)benzyl) guanidine, 3,5-diguanidino benzoic acid, and aromatic α -guanidino amino acids (Figure 1-8).

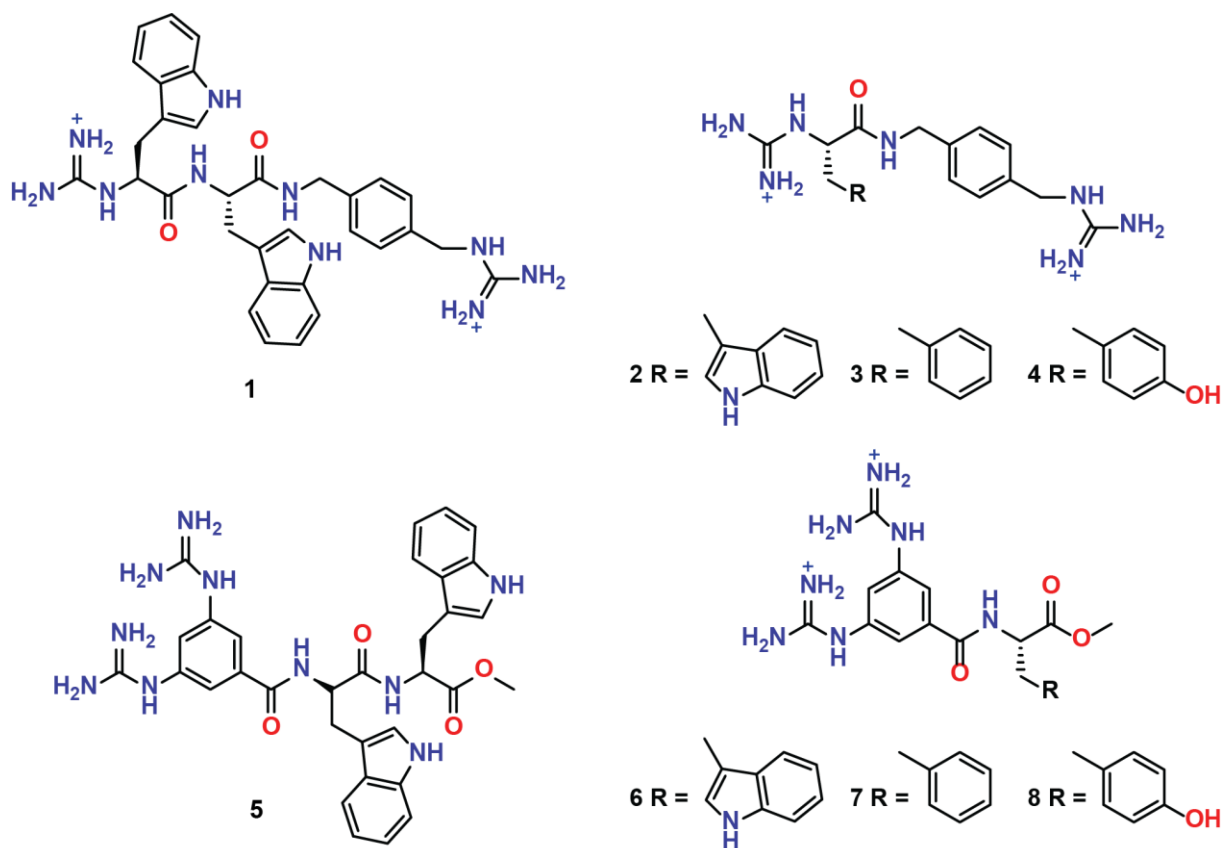


Figure 1-8. Short linear peptides incorporating guanidine motif and bulky hydrophobic side chains synthesized by Baldassare *et al.*

Compounds **1,2** and **5,6** showed high antimicrobial activity against Gram-positive and modest activity against Gram-negative bacteria.

1.4 Vancomycin: A New Trick for an Old Antibiotic

Vancomycin was approved by the Food And Drug Administration (FDA) in 1958, making it the first approved glycopeptide antibiotic.⁴⁵ Due to its severe side effects, it is typically used in patients allergic to β -lactams and as a last line of treatment for drug-resistant bacteria. Vancomycin is a 7-residue, tricyclic glycopeptide (Figure 1-10). Vancomycin shows activity only against Gram-positive bacteria.⁴⁵ Its mechanism of action involves binding to terminal D-Ala-D-Ala of the lipid

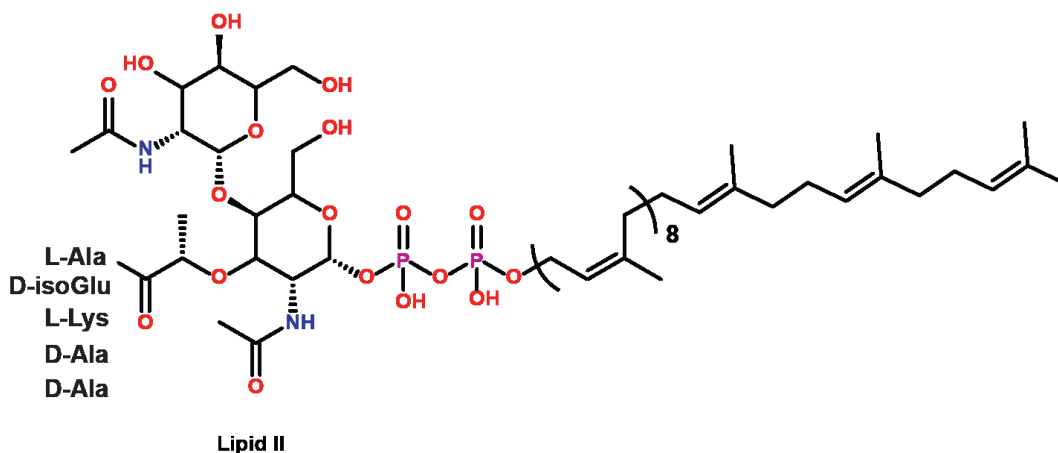


Figure 1-9. Structure of lipid II, a peptidoglycan precursor.

II intermediate of peptidoglycan biosynthesis (Figure 1-9), thus stopping the cell wall synthesis. Its inability to kill Gram-negative bacteria is a result of its inability to penetrate the outer membrane and target D-Ala-D-Ala.

Antonoplis et al. attempted to solve this problem by synthesizing conjugates of vancomycin with arginine in which they varied the number of arginine residues attached (Figure 1-10).⁴⁶

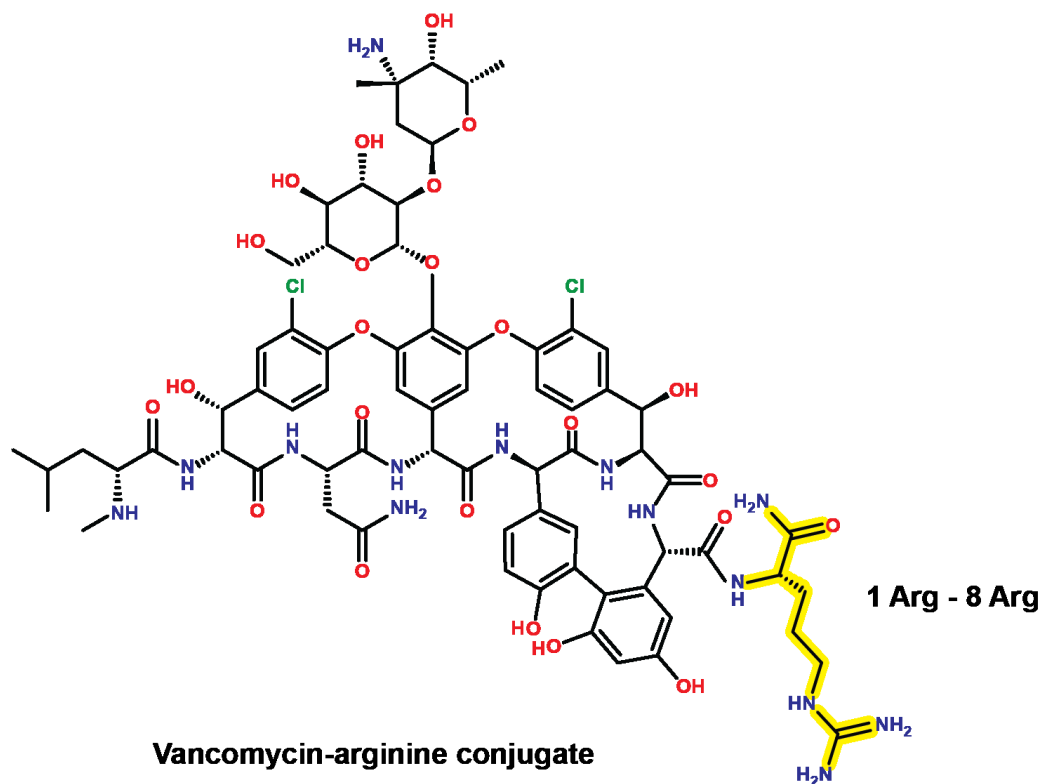


Figure 1-10. Structure of vancomycin conjugated with a varying number of arginine residues.

It was thought that, presence of positive charge on arginine would allow vancomycin to cross the membrane of Gram negative bacteria via self-promoted uptake. This phenomenon has been described before in polymyxin B and several other cationic antibiotics.^{47,48} Polymyxin B's charged amino groups allow it to directly compete with divalent cations for binding to lipopolysaccharide sites (LPS) and displace them. The displacement of cations and subsequent change in the chemical environment destabilizes the membrane allowing the uptake. [b]. It turned out that the highest activity against carbapenem-resistant *E. coli* was achieved with a conjugate having a single arginine residue as opposed to those with 2-8 eight arginine residue chains. This could indicate

that an excess of positive charge could prevent the antibiotic from crossing the outer membrane. It is possible that such highly charged conjugates could still cause membrane leakage and cell death, but not effectively enough to make them viable antibiotics.

1.5 Peptide-Based Natural Products

Many antibacterial depsipeptides contain arginine or one of its derivatives. Depsipeptides are a class of naturally, usually non-ribosomally, produced peptides in which one or more peptide bonds have been replaced with ester bonds resulting in a circular peptide.⁴⁹⁻⁵² This section will examine the roles of arginine (or arginine derivatives) in several therapeutically important natural products. The studies detailed below show that arginine and its derivatives range from being crucial for activity to not even being a part of the pharmacophore. Such variable results mean that, without elaborate SAR studies, it is difficult to predict the role of an arginine or arginine-derived residue in any particular compound.

1.5.1 Teixobactin

In 2015, as a part of their effort to discover novel antibiotics in soil bacteria, Lewis et al. designed a device called isolation chip (iChip).⁵³ The purpose of iChip was to overcome the inability to successfully grow the majority of soil bacteria under laboratory conditions. Using iChip, a sample of soil can be diluted using molten agar and nutrients so that on average only a single cell can be grown in one of the device's compartments. The iChip device is then covered with semi-permeable membranes and placed back in the soil. This method allows nutrients from the soil to enter the device and provide an optimum growth environment which cannot be achieved in the laboratory.

This work led to the discovery and characterization of a novel cyclic depsipeptide antibiotic that they named teixobactin (Figure 1-11).⁵³

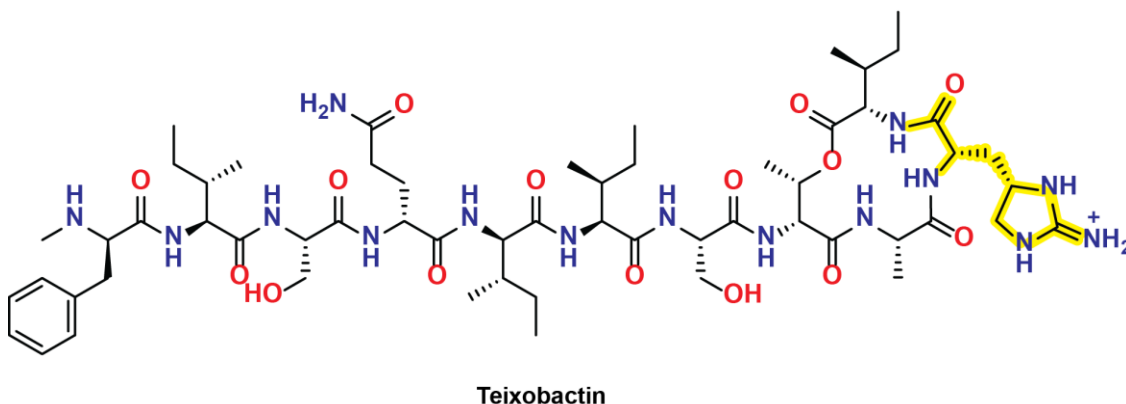


Figure 1-11. Structure of teixobactin, a novel antibiotic featuring enduracididine.

Teixobactin showed potent activity against MRSA and no resistance occurring up to a 27-day administration of sub-lethal doses. While highly active against Gram-positive bacteria, it is mostly inactive against Gram-negative bacteria. This novel antibiotic works by disrupting the synthesis of peptidoglycan, which is not an unusual mechanism of action. Teixobactin, however, does it in a novel fashion by forming a complex with both the lipid II intermediate and the teichoic acid moiety of the Gram-positive cell wall.⁵⁴ The structure of teixobactin contains L-allo-enduracididine (L-allo-End), a rare, non-proteinogenic amino that poses a roadblock on the path towards a facile total synthesis of teixobactin.⁵⁵ L-allo-enduracididine is a cyclic analogue of L-arginine, produced from L-arginine via a series of enzymatic steps.⁵⁶⁻⁵⁸ Given the potential value of this unique antibiotic, many research groups sought to decipher the role of L-allo-End in the antibacterial activity of teixobactin. In 2015, Jad et al. synthesized an analogue of teixobactin in which L-allo-enduracididine was replaced with L-arginine. The authors obtained minimum inhibitory concentration (MIC) values and compared them to teixobactin. The MIC assay values

for Gram-positive bacteria such as *S. aureus* and *B. subtilis* were 8- and 25-times higher for the L-arginine containing analogue, respectively.⁵⁹

Independently, Parmar et al. have also synthesized the same analogue of teixobactin, alongside with an enantiomerically different teixobactin analogue produced by changing select D-amino acids to L-amino acids (Phe, Gln and Ile).⁶⁰ Their MIC assay results agreed with the results published by Jad et al. showing the MIC for Arg10-teixobactin to be 8-times higher for *S.aureus* and 2.5-times higher for *E. coli*. This shows that even though the guanidine moiety remains present, slight differences in the physicochemical properties of the teixobactin analogues yields differences in the MIC values. In 2016, as a part of their work on the total synthesis of teixobactin, Jin et al. synthesized an analogue with L-allo-enduracididine replaced by ornithine.⁶¹ This analogue had reduced activity against MRSA, leading to the conclusion that L-allo-enduracididine plays an essential role in the antibacterial activity. In a highlight published in 2015, Von Nussbaum and Sussmuth hypothesized that just like in other lipid II-binding depsipeptides, the key binding interaction of teixobactin is that of the iminoimidazolidine moiety and the phosphate group of lipid II.⁵⁴ This implies that the high pKa on the iminimidazolidine group is essential for a successful interaction. It would be expected that replacing L-allo-End with lysine would be detrimental compared to replacement with arginine since lysine would end up getting deprotonated in the membrane.⁶² Wu et al. investigated the importance of the iminoimidazolidine group by making Arg10, Lys10, and His10, analogues. Their results showed that Lys10 has similar activity to Arg10, while use of histidine led to a dramatic reduction in activity.⁶³ The Arg10 analogue had lower activity than teixobactin, indicating that the shorter stature of allo-End10 could play a role in the activity. This appeared to support the hypothesis that a highly basic cationic group is required for the potent antimicrobial activity of teixobactin. Nowick et al. independently tested whether the

guanidinium group itself was required and compared the activity of Lys10 and Arg10.⁶⁴ Surprisingly, Lys-10-teixobactin had a higher antimicrobial activity than Arg-10-teixobactin. Still, the activity of both was lower than the activity of teixobactin with L-allo-enduracididine present. However, all these results did not put the question of L-allo-enduracididine's role in teixobactin to rest. In 2017, Nowick et al. performed an alanine scan on Lys10-teixobactin, by sequentially changing each peptide residue except D-Thr8 (to avoid perturbation of the 13-membered macrolactone ring), in order to identify modifiable residues. The result was quite surprising, as replacing lysine with alanine resulted in only moderate reduction in antimicrobial activity.⁶⁵ Given the role of cationic residues in the majority of antimicrobial peptides, a major decrease or abolishment of activity was expected. Encouraged by this unprecedented discovery, Jin et al. synthesized analogues of teixobactin incorporating 32 different non-isosteres of L-allo-enduracididine at position 10.⁶⁶ They subsequently reported that having cyclohexylglycine, norvaline or methionine (Figure 1-12) in position 10 led to lower MIC values compared to the naturally occurring teixobactin. At the time of this writing, it remains unclear why the removal of cationic amino acids from this peptide does not seem to impact its antimicrobial activity.

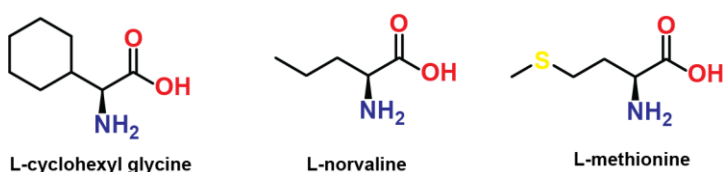


Figure 1-12. Non-isosteres of enduracididine incorporated in teixobactin which led to the highest antibacterial activity.

1.5.2 Enduracylinones

Despite the apparent lack of importance in the teixobactin pharmacophore, enduracididine remains an intriguing molecule. So far, the only antibiotics incorporating enduracididine were peptides, which are the focus of this review. However, in 2019, Monciardini et al. isolated two novel antibacterial aromatic polyketides that contain N-methyl enduracididine (NmEnd) (Figure 1-13).⁶⁷

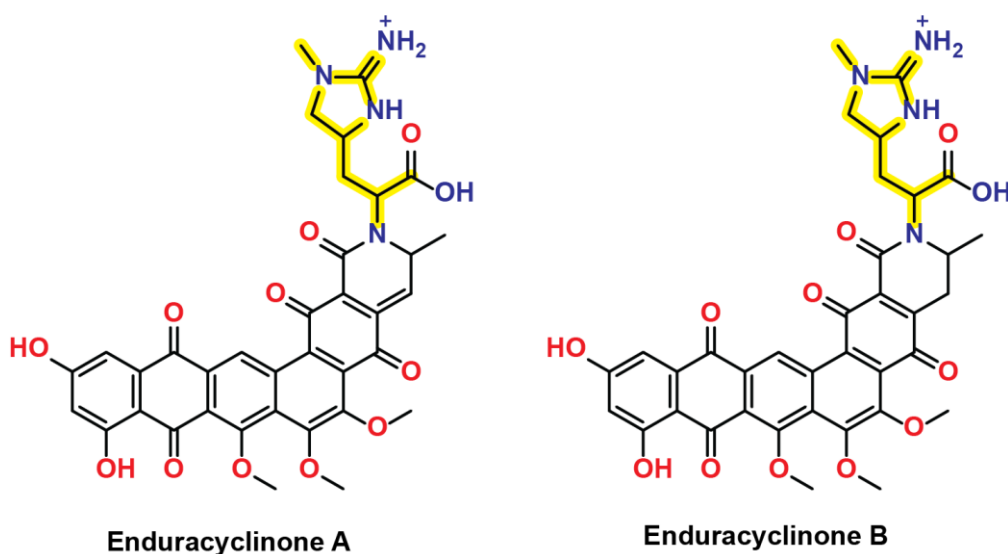


Figure 1-13. Structures of newly discovered aromatic polyketides containing N-methyl enduracididine.

This is the first time that enduracididine has been found in a polyketide and the methylated variant of enduracididine has not been observed in nature prior to this discovery. It remains to be seen what role it plays in these novel antibiotics. Gaining a full understanding of the mechanistic details of enduracididine biosynthesis has significant value given its presence in multiple antibiotics where it may play different roles.

1.5.3 Ramoplanin and Enduracidin

Ramoplanin, a cyclic lipoglycopeptide is an antibiotic that targets the synthesis of peptidoglycan by binding to the lipid I or lipid II precursors. It shows activity against drug-resistant Gram-positive bacteria like vancomycin-resistant *Enterococcus faecium* (VRE) and methicillin-resistant *S. aureus* (MRSA), making it an important target for structure-activity studies.⁶⁸ It was the first glycopeptide to enter advanced clinical trials for the treatment of

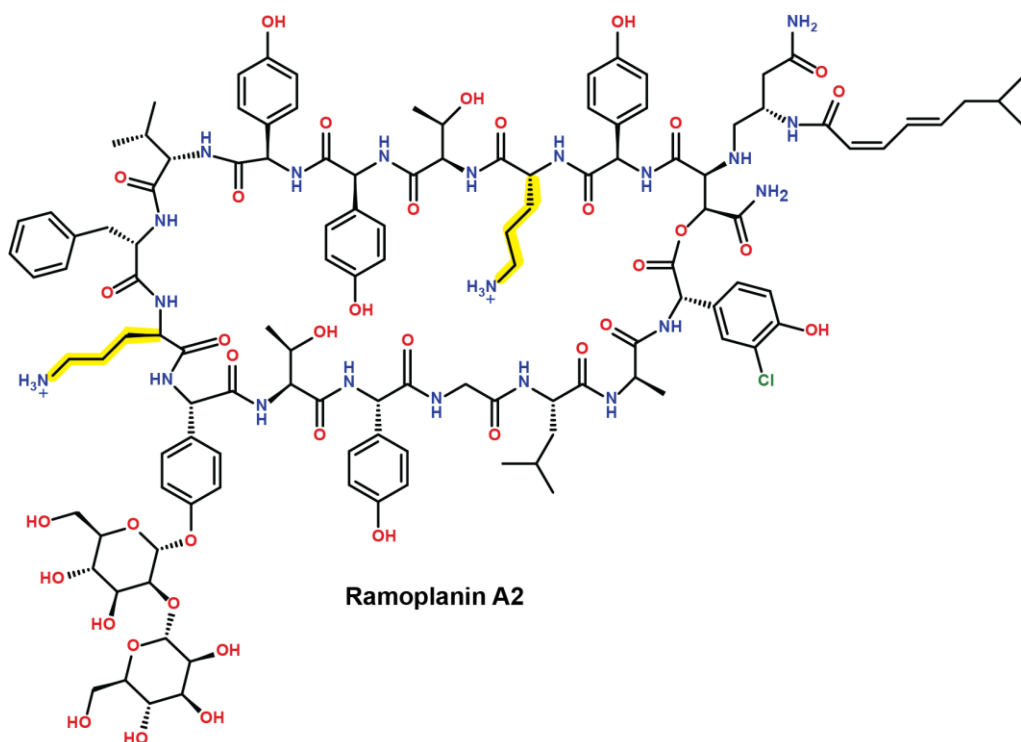


Figure 1-14. Structure of ramoplanin A2. Ornithine residues are highlighted in yellow.

Clostridium difficile infections, however, as of 2020 clinical trials involving ramoplanin have been discontinued. The positive charge of ramoplanin comes solely from its ornithine residues (Figure 1-14).

In order to test whether ornithine sidechains are necessary for activity, Cudic et al. probed the role of the ornithine residues by synthesizing analogues of ramoplanin where the primary amine of ornithine was replaced with guanidine (arginine), a secondary amine, or acetamide.⁶⁸ The resulting analogues all had lower activity, and the activity decreased going from guanidine to the secondary amine, showing the importance of positive charge at positions 4 and 10 of the peptide. However, when Helm et al. performed an alanine scan of ramoplanin they found that only Orn10 plays an essential role in binding.⁶⁹ In 2009, Hamburger et al. solved crystal structure of ramoplanin dimer which revealed its positioning with respect to the membrane and showed that ornithine-10 is positioned to interact with pyrophosphate of lipid II.⁷⁰

not been conducted for the enduracidins. So far, antibiotic resistance has not been observed toward these antimicrobial peptides. Theoretically bacteria could become resistant by lowering the net negative charge on their membranes via introduction of positively charged groups on the surface. It has been hypothesized that the lipophilic character of lipodepsipeptides can perhaps override unfavorable electrostatic interactions and still cause them to bind to the hydrophobic parts of the bacterial membranes.⁷²

1.5.4 Mannopectimycins

The mannopectimycins are glycopeptide antibiotics that show activity against VRE and MRSA.⁷²
⁷³ Five mannopectimycins (α - ϵ) have been discovered, all sharing the same hexapeptide core and differing in structure of disaccharide moieties (or lack thereof; Figure 1-16).

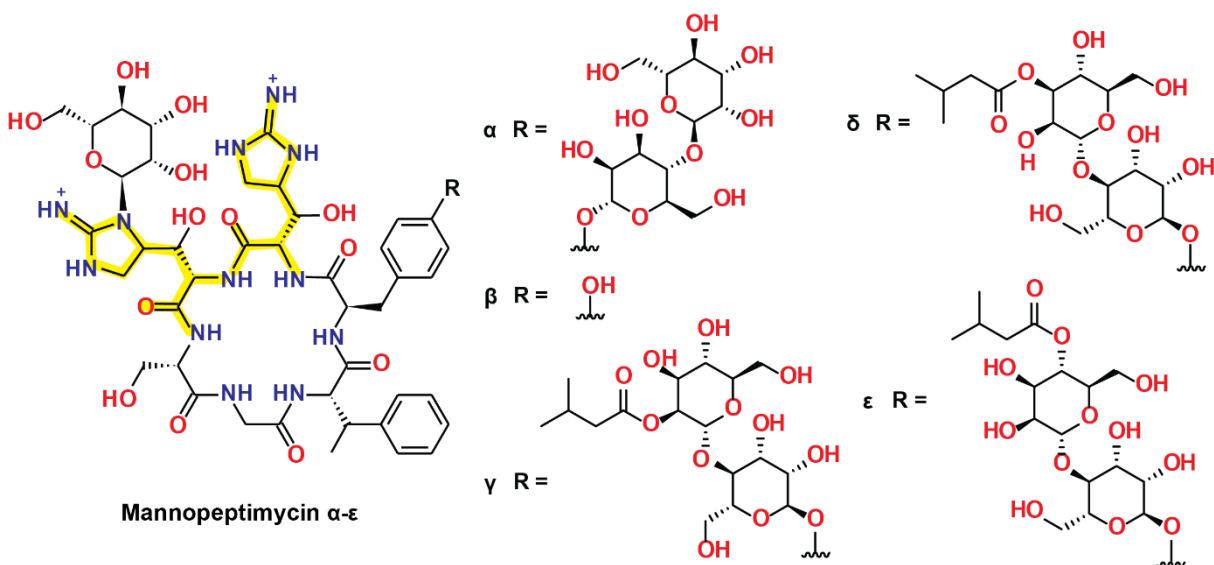


Figure 1-16. Structures of mannopectimycins.

The importance of the disaccharide moiety for the biological activity is obvious since mannopeptimycin β , which lacks any sugar moiety on D-Tyr₄, has very low antibacterial activity. Mannopeptimycin α , which lacks the isovaleryl group on the terminal mannose, has considerably lower activity than mannopeptimycin γ, δ , and ϵ .⁷⁴ Like enduracidin and teixobactin, the mannopeptimycins also contain L-End. In the case of the mannopeptimycins, however, both of these residues are hydroxylated at C β to give β -hydroxyenduracididine (β hEnd). This oxidation is catalyzed by the Fe(II)- and α -ketoglutarate-dependent oxygenase MppO in a tailoring step after formation of the peptide core of mannopeptimycin.⁷⁵ One of these residues, β hEnd₆, is N-glycosylated with mannopyranose on the iminoimidazolidine ring. In 2004, Ruzin et al. used a radioactive mannopeptimycin derivative to gain insight into its antibacterial mechanism. They found out that mannopeptimycin binds to the peptidoglycan synthesis intermediate lipid II, but in a different manner than vancomycin.⁷³ It also nonspecifically binds to lipoteichoic acid, thus accumulating near the cell membrane to interact with lipid II. Structure-activity relationship (SAR)

studies on the mannopeptimycins have mostly been focused on altering the saccharide portions of the molecule since these parts have been proven to play a role in biological activity.

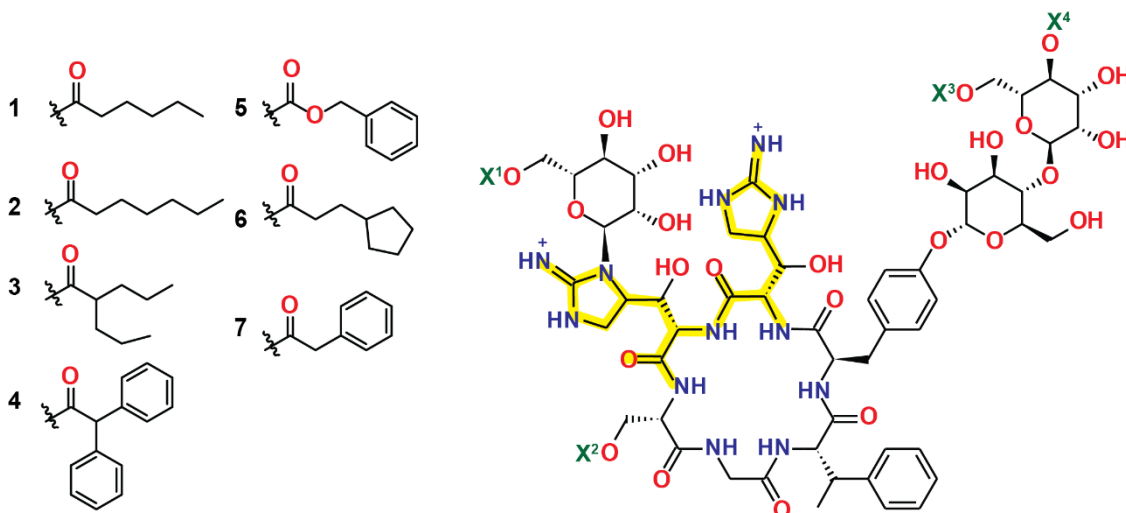


Figure 1-17. Ester and carbonate analogues of mannopeptimycin α .

It is possible that the reason why isovaleryl group on terminal mannose found in several mannopeptimycins plays a role in activity is that the hydrophobicity might help anchor the antibiotic in the membrane, analogous to the hydrophobic tails of lipodepsipeptides. Using acylation of terminal mannose, He et al. introduced additional hydrophobicity in derivatives (Figure 1-17).⁷⁴ It was observed that the location of the acylation played a key role in the biological activity of the derivatives. Functionalizing Ser1 or the N-linked mannose diminished activity, while adding a hydrophobic chain to the terminal mannose of the disaccharide enhanced it. Compounds with hydrophobic acyl groups **1,2**, and **3** on terminal mannose (X^4) exhibited higher activity against MRSA and VRE than any of the naturally occurring mannopeptimycins. Sum et al. have also tested introduction of bulky hydrophobic moieties to terminal mannose but with ether linkages instead (Figure 1-18).⁷⁶

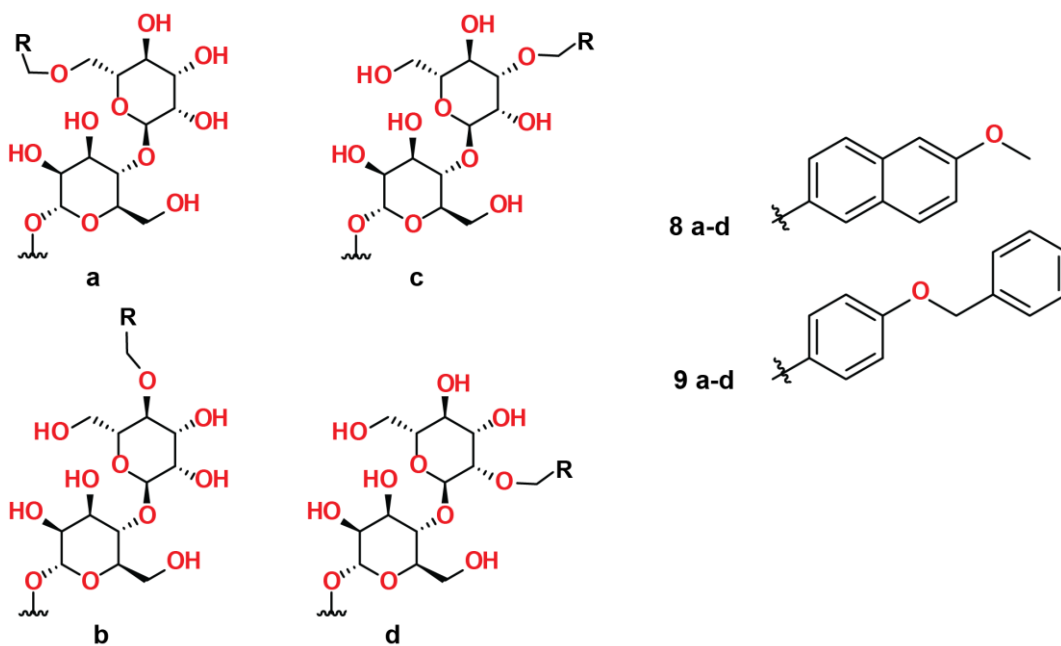


Figure 1-18. Ether analogues of mannopeptimycin.

Sum et al. also tested the effect of changing the character of the tyrosine core residue. They synthesized benzoxazole analogues that lacked the O-linked disaccharide on D-tyrosine, and in one analogue, also removed the N-linked mannose from β -hydroxy enduracididine to test whether the aglycone would have antibiotic activity (Figure 1-19).⁷⁷

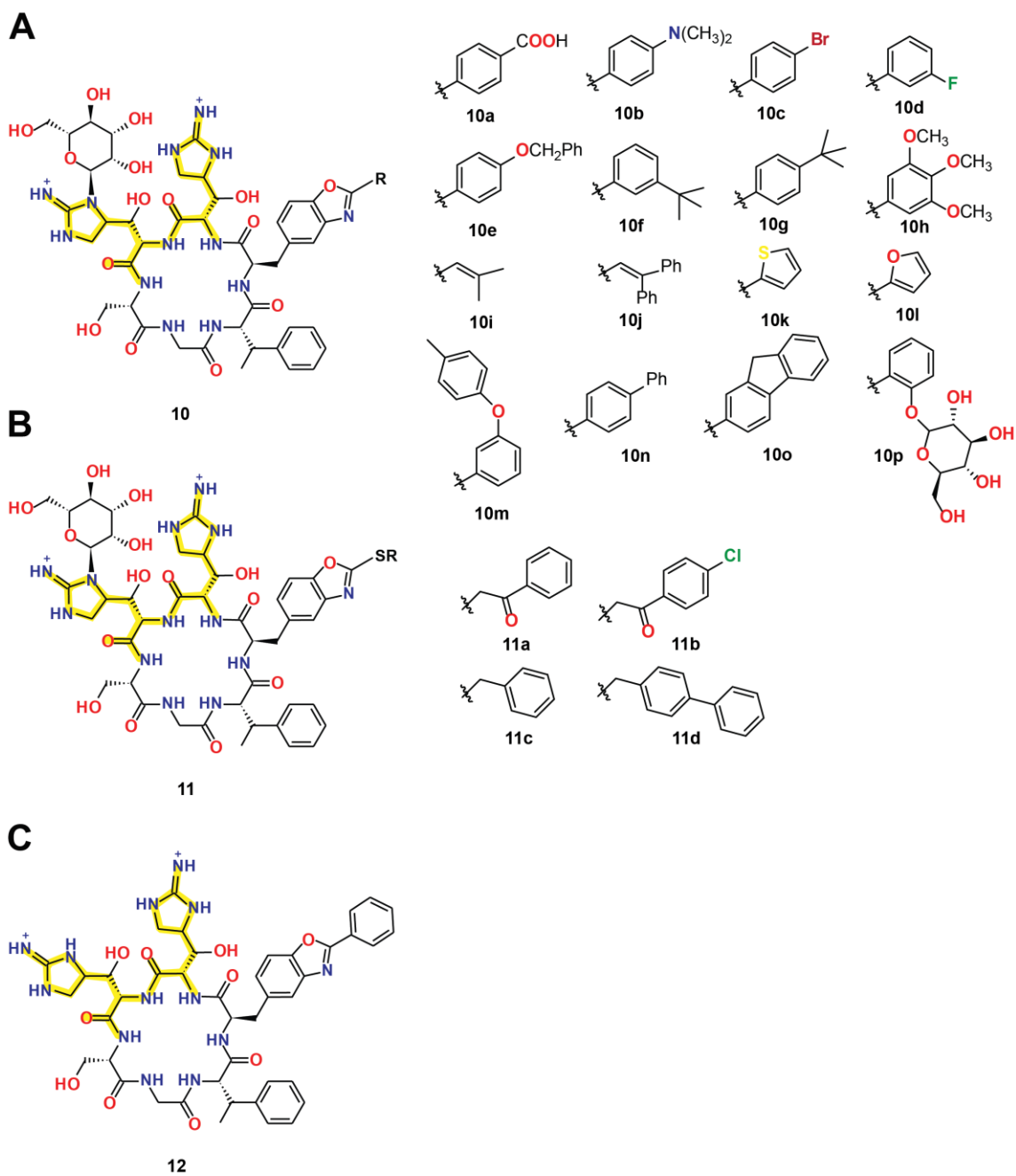


Figure 1-19. A) Substituted benzoxazole mannopeptimycin analogues B) Structures of 2-thio-substituted benzoxazole analogues C) Aglycone analogue of mannopeptimycin

The removal of the β hEnd6 N-linked mannose drastically diminished the activity. However, the Tyr4 O-linked disaccharide was found not to be essential for activity. In fact, several benzoxazoline derivatives yielded better antimicrobial activity than the parent compound (**10b**, **10d**, **10m** and **11b**) It is unclear whether the aromatic character of the phenyl rings of the benzoxazoline substituents interacted via ion-Pi stacking with anions of the membrane, or it was the result of fluorination/chlorination increasing the cell membrane penetration by the compounds. Interestingly, Sum et al. also halogenated the phenyl ring, which led to diminished activity. The importance of lipophilicity in these compounds was verified by studying analogues where lipophilic ether moieties were added to the terminal mannose of the disaccharide. All of the derivatives in this study led to increased activity. Despite such extensive SAR, no modifications have been done to either of the β hEnd residues. It would be interesting if future studies were to test different arginine analogs, including L-End (rather than the hydroxylated β hEnd) in that position.

1.5.5 The tuberactinomycins

Analogs of arginine are also present in the peptide-based antibiotics known as tuberactinomycins, due to their potent anti-tuberculosis activity. The first two tuberactinomycins to be characterized were viomycin and capreomycin. Both incorporate 2S,3R-capreomycinidene, which is, like L-End, a

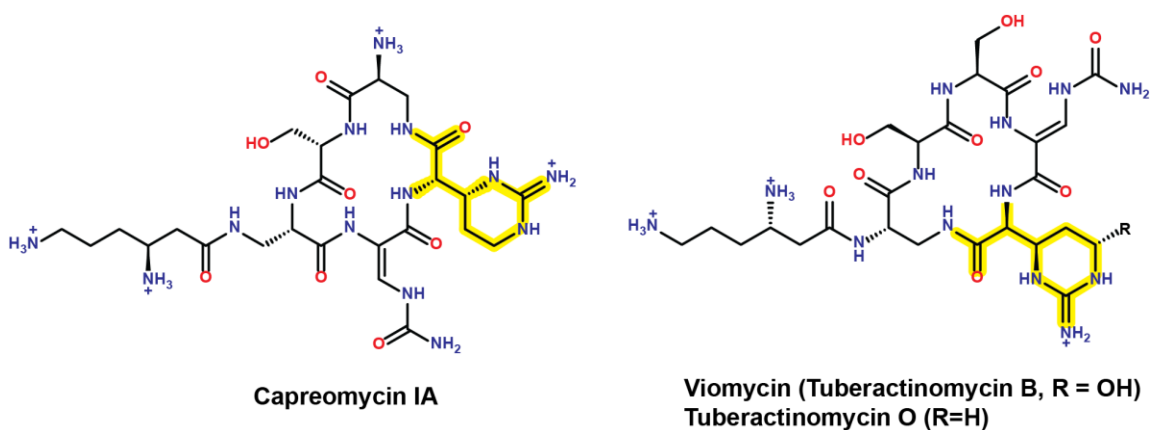
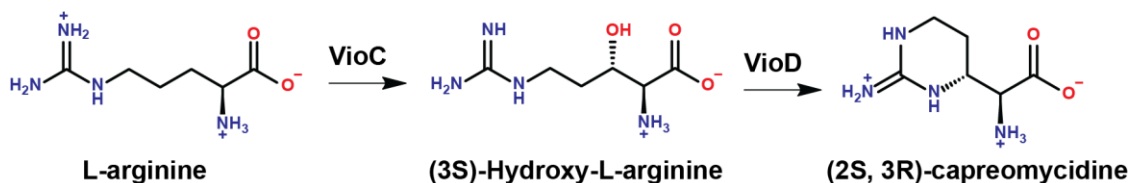


Figure 1-20. Structures of capreomycin IA, viomycin and tuberactinomycin O

cyclic arginine derivative (Figure 1-20). The 2S,3R-capreomycinidene synthesis in *Streptomyces* begins with oxidation of L-arginine by VioC, non-heme iron, α -ketoglutarate-dependent oxygenase. The resulting product (3S-hydroxy-L-arginine) is then cyclized by VioD, an enzyme possessing sequence similarity with PLP-dependent aminotransferases (Scheme 1-2).⁷⁸



Scheme 1-2. Biosynthetic pathway of 2S,3R-capreomycinidene.

The inhibitory mechanism of viomycin is based on its competition with elongation factor G for binding to the pre-translation ribosome. Binding of viomycin to the ribosome in place of elongation factor G prevents translocation of the mRNA, thus stalling protein synthesis.⁷⁹ A study by Nomoto

et al. has shown that the simple presence of a cationic charge in tuberactinomycin O is not sufficient for antibiotic activity. When capreomycin was replaced by L-Arg, or 3-guanidinoalanine, activity greatly decreased.⁸⁰ Interestingly, the L-Arg analogue had much lower activity than 3-guanidinoalanine one, leading to a conclusion that the shorter chain allows for better interaction with a bacterial target. Additionally both of them had inferior activity to capreomycin most likely because the linear chains have too much flexibility which negatively affects binding ability. In this case, the manner in which capreomycin promotes antibacterial activity was clearly determined when the crystal structures of viomycin and capreomycin in complexes with the 70s ribosome were solved by Stanley et al.⁸¹ The structure showed that the iminoimidazolidine group on capreomycin helps properly position the antibiotic by forming an electrostatic interaction with A1493 of the 16S rRNA. Capreomycin is currently used as a second-line treatment for drug resistant tuberculosis.

1.5.6 Pentaminomycins

In 2020, Kaweewan et al. isolated group of novel cyclic pentapeptides, pentaminomycins, from *Streptomyces cacaoi* subsp. *cacaoi* NBRC 12748T (Figure 1-21).⁸²

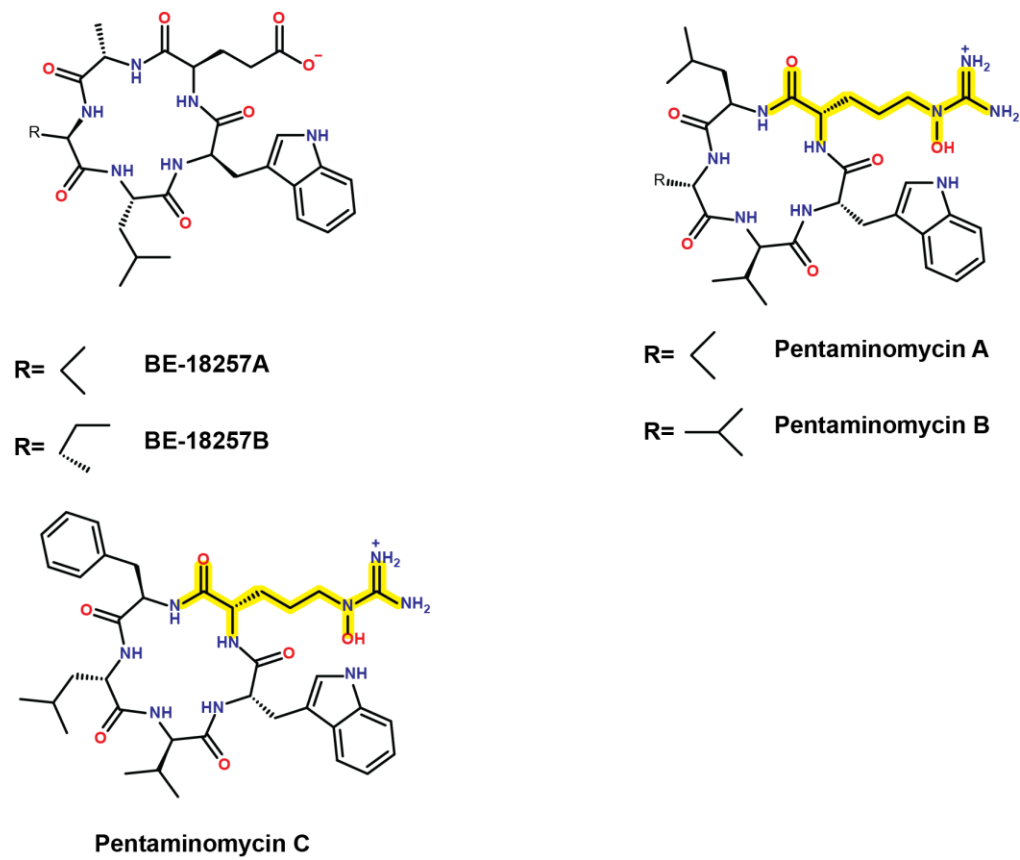
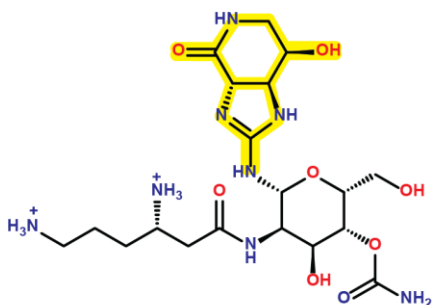


Figure 1-21. Structures of newly discovered pentaminomycins.

Pentaminomycins A, B, and C all contain a rare arginine analogue, 5N-hydroxy-arginine. The activity of pentaminomycins was compared with that of BE-18257A, a cyclopeptide that has no cationic residues and no antimicrobial activity as a control. Surprisingly, pentaminomycins A and B don't have antibacterial activity, while pentaminomycin C does, despite all having 5N-OH-Arg. However, this is not sufficient to dismiss the role that 5N-OH-Arg may play in the antibacterial activity. Pentaminomycins A and B also lack D-Phe, which makes them have a less lipophilic character. Considering how delicate interplay between lipophilicity and activity is, perhaps both D-Phe and 5N-OH-Arg are key parts of the pharmacophore, which warrants future SAR studies of these compounds.

1.5.7 Streptothricin F

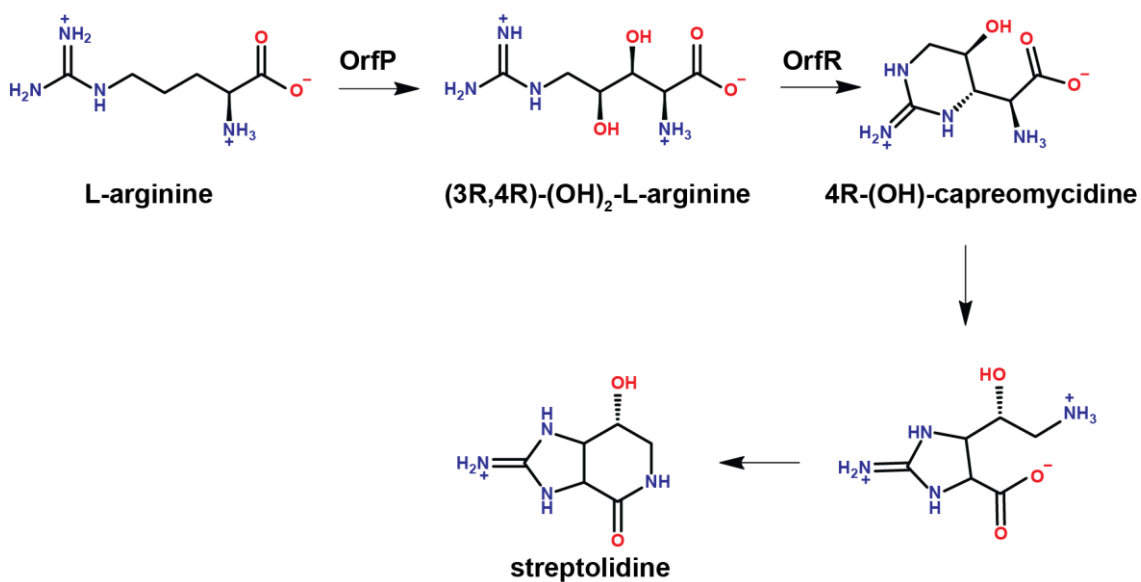
Although not a peptide based antibiotic, Streptothricin F has been included in this review to showcase exceptional role of arginine and its analogues as pharmacophore components in antibiotics. This aminoglycoside antibiotic possessing activity against both Gram-positive and Gram-negative bacteria, has an arginine analogue, streptolidine, incorporated in its structure (Figure 1-22).^{83, 84} The streptolidine bicyclic moiety appears essential for the activity which was determined by Hamano et al. In their study, hydrolysis of the lactam bond of streptolidine resulted in the loss of activity. The synthesis of streptolidin begins with dihydroxylation of L-Arg by OrfP,



Streptothricin F

Figure 1-22. Structure of Streptothricin F, an aminoglycoside antibiotic containing streptolidine.

non-heme iron, α -ketoglutarate-dependent oxygenase, followed by cyclization to 4R-OH-capreomycin, catalyzed by OrfR. This is followed by a rearrangement to streptolidine and subsequent lactam formation (Scheme 1-3).⁸³



Scheme 1-3. Streptolidine biosynthetic pathway.

This review has put on the display a variety of roles arginine and its analogues have in the antimicrobial peptides and also emphasized the heterogeneity in the ways they influence activity. It is therefore of crucial importance to investigate biosynthetic pathways of cryptic arginine analogues, in a quest to design more effective antibiotics.

The following chapters focus on characterizing the L-End biosynthetic enzymes MppP/R/Q from the mannopeptimycin-producing bacteria *Streptomyces hygroscopicus* and *S. wadayamensis*. This work should serve as a stepping stone toward combinatorial biosynthetic studies to produce novel mannopeptimycin derivatives.

1.6 References

1. Aslam, B.; Wang, W.; Arshad, M. I.; Khurshid, M.; Muzammil, S.; Rasool, M. H.; Nisar, M. A.; Alvi, R. F.; Aslam, M. A.; Qamar, M. U.; Salamat, M. K. F.; Baloch, Z., Antibiotic resistance: a rundown of a global crisis. *Infect Drug Resist* **2018**, *11*, 1645-1658.
2. Zaman, S. B.; Hussain, M. A.; Nye, R.; Mehta, V.; Mamun, K. T.; Hossain, N., A Review on Antibiotic Resistance: Alarm Bells are Ringing. *Cureus* **2017**, *9* (6), e1403.
3. Rice, L. B., Mechanisms of resistance and clinical relevance of resistance to beta-lactams, glycopeptides, and fluoroquinolones. *Mayo Clin Proc* **2012**, *87* (2), 198-208.
4. Stapleton, P. D.; Taylor, P. W., Methicillin resistance in *Staphylococcus aureus*: mechanisms and modulation. *Sci Prog* **2002**, *85* (Pt 1), 57-72.
5. Redgrave, L. S.; Sutton, S. B.; Webber, M. A.; Piddock, L. J., Fluoroquinolone resistance: mechanisms, impact on bacteria, and role in evolutionary success. *Trends Microbiol* **2014**, *22* (8), 438-45.
6. Leclercq, R., Mechanisms of resistance to macrolides and lincosamides: nature of the resistance elements and their clinical implications. *Clin Infect Dis* **2002**, *34* (4), 482-92.
7. Zhang, L. J.; Gallo, R. L., Antimicrobial peptides. *Curr Biol* **2016**, *26* (1), R14-9.
8. Borah, A.; Deb, B.; Chakraborty, S., A Crosstalk on Antimicrobial Peptides. *International Journal of Peptide Research and Therapeutics* **2020**.
9. Liou, J. W.; Hung, Y. J.; Yang, C. H.; Chen, Y. C., The antimicrobial activity of gramicidin A is associated with hydroxyl radical formation. *PLoS One* **2015**, *10* (1), e0117065.
10. David, J. M.; Rajasekaran, A. K., Gramicidin A: A New Mission for an Old Antibiotic. *J Kidney Cancer VHL* **2015**, *2* (1), 15-24.
11. Burkhardt, B. M.; Li, N.; Langs, D. A.; Pangborn, W. A.; Duax, W. L., The conducting form of gramicidin A is a right-handed double-stranded double helix. *Proc Natl Acad Sci U S A* **1998**, *95* (22), 12950-5.
12. Oh, D.; Shin, S. Y.; Kang, J. H.; Hahm, K. S.; Kim, K. L.; Kim, Y., NMR structural characterization of cecropin A(1-8) - magainin 2(1-12) and cecropin A (1-8) - melittin (1-12) hybrid peptides. *J Pept Res* **1999**, *53* (5), 578-89.
13. Hill, C. P.; Yee, J.; Selsted, M. E.; Eisenberg, D., Crystal structure of defensin HNP-3, an amphiphilic dimer: mechanisms of membrane permeabilization. *Science* **1991**, *251* (5000), 1481-5.
14. Hoover, D. M.; Chertov, O.; Lubkowski, J., The structure of human beta-defensin-1: new insights into structural properties of beta-defensins. *J Biol Chem* **2001**, *276* (42), 39021-6.
15. Sancho-Vaello, E.; Francois, P.; Bonetti, E. J.; Lilie, H.; Finger, S.; Gil-Ortiz, F.; Gil-Carton, D.; Zeth, K., Structural remodeling and oligomerization of human cathelicidin on membranes suggest fibril-like structures as active species. *Sci Rep* **2017**, *7* (1), 15371.
16. Pettersen, E. F.; Goddard, T. D.; Huang, C. C.; Couch, G. S.; Greenblatt, D. M.; Meng, E. C.; Ferrin, T. E., UCSF Chimera--a visualization system for exploratory research and analysis. *J Comput Chem* **2004**, *25* (13), 1605-12.
17. Brady, D.; Grapputo, A.; Romoli, O.; Sandrelli, F., Insect Cecropins, Antimicrobial Peptides with Potential Therapeutic Applications. *Int J Mol Sci* **2019**, *20* (23).
18. Seo, M. D.; Won, H. S.; Kim, J. H.; Mishig-Ochir, T.; Lee, B. J., Antimicrobial peptides for therapeutic applications: a review. *Molecules* **2012**, *17* (10), 12276-86.

19. Silvestro, L.; Axelsen, P. H., Membrane-induced folding of cecropin A. *Biophys J* **2000**, *79* (3), 1465-77.
20. Conlon, J. M.; Mechkarska, M.; King, J. D., Host-defense peptides in skin secretions of African clawed frogs (Xenopodinae, Pipidae). *Gen Comp Endocrinol* **2012**, *176* (3), 513-8.
21. Ganz, T., Defensins: antimicrobial peptides of innate immunity. *Nat Rev Immunol* **2003**, *3* (9), 710-20.
22. Zou, G.; de Leeuw, E.; Li, C.; Pazgier, M.; Li, C.; Zeng, P.; Lu, W. Y.; Lubkowski, J.; Lu, W., Toward understanding the cationicity of defensins. Arg and Lys versus their noncoded analogs. *J Biol Chem* **2007**, *282* (27), 19653-65.
23. Schmidt, N. W.; Tai, K. P.; Kamdar, K.; Mishra, A.; Lai, G. H.; Zhao, K.; Ouellette, A. J.; Wong, G. C., Arginine in alpha-defensins: differential effects on bactericidal activity correspond to geometry of membrane curvature generation and peptide-lipid phase behavior. *J Biol Chem* **2012**, *287* (26), 21866-72.
24. Mishra, A.; Lai, G. H.; Schmidt, N. W.; Sun, V. Z.; Rodriguez, A. R.; Tong, R.; Tang, L.; Cheng, J.; Deming, T. J.; Kamei, D. T.; Wong, G. C., Translocation of HIV TAT peptide and analogues induced by multiplexed membrane and cytoskeletal interactions. *Proc Natl Acad Sci U S A* **2011**, *108* (41), 16883-8.
25. Schmidt, N. W.; Lis, M.; Zhao, K.; Lai, G. H.; Alexandrova, A. N.; Tew, G. N.; Wong, G. C., Molecular basis for nanoscopic membrane curvature generation from quantum mechanical models and synthetic transporter sequences. *J Am Chem Soc* **2012**, *134* (46), 19207-16.
26. Seil, M.; Nagant, C.; Dehaye, J.-P.; Vandenbranden, M.; Lensink, M. F., Spotlight on Human LL-37, an Immunomodulatory Peptide with Promising Cell-Penetrating Properties. *Pharmaceuticals* **2010**, *3* (11), 3435-3460.
27. Durr, U. H.; Sudheendra, U. S.; Ramamoorthy, A., LL-37, the only human member of the cathelicidin family of antimicrobial peptides. *Biochim Biophys Acta* **2006**, *1758* (9), 1408-25.
28. Koziel, J.; Bryzek, D.; Sroka, A.; Maresz, K.; Glowczyk, I.; Bielecka, E.; Kantyka, T.; Pyrc, K.; Svoboda, P.; Pohl, J.; Potempa, J., Citrullination alters immunomodulatory function of LL-37 essential for prevention of endotoxin-induced sepsis. *J Immunol* **2014**, *192* (11), 5363-72.
29. Casanova, V.; Sousa, F. H.; Shakamuri, P.; Svoboda, P.; Buch, C.; D'Acremont, M.; Christophorou, M. A.; Pohl, J.; Stevens, C.; Barlow, P. G., Citrullination Alters the Antiviral and Immunomodulatory Activities of the Human Cathelicidin LL-37 During Rhinovirus Infection. *Front Immunol* **2020**, *11*, 85.
30. Wang, X.; Junior, J. C. B.; Mishra, B.; Lushnikova, T.; Epan, R. M.; Wang, G., Arginine-lysine positional swap of the LL-37 peptides reveals evolutionary advantages of the native sequence and leads to bacterial probes. *Biochim Biophys Acta Biomembr* **2017**, *1859* (8), 1350-1361.
31. Derakhshankhah, H.; Jafari, S., Cell penetrating peptides: A concise review with emphasis on biomedical applications. *Biomed Pharmacother* **2018**, *108*, 1090-1096.
32. Guidotti, G.; Brambilla, L.; Rossi, D., Cell-Penetrating Peptides: From Basic Research to Clinics. *Trends Pharmacol Sci* **2017**, *38* (4), 406-424.
33. Allolio, C.; Magarkar, A.; Jurkiewicz, P.; Baxova, K.; Javanainen, M.; Mason, P. E.; Sachl, R.; Cebecauer, M.; Hof, M.; Horinek, D.; Heinz, V.; Rachel, R.; Ziegler, C. M.; Schrofel, A.; Jungwirth, P., Arginine-rich cell-penetrating peptides induce membrane multilamellarity and subsequently enter via formation of a fusion pore. *Proc Natl Acad Sci U S A* **2018**, *115* (47), 11923-11928.

34. Lee, H.; Lim, S. I.; Shin, S.-H.; Lim, Y.; Koh, J. W.; Yang, S., Conjugation of Cell-Penetrating Peptides to Antimicrobial Peptides Enhances Antibacterial Activity. *ACS Omega* **2019**, *4* (13), 15694-15701.
35. Qvit, N.; Rubin, S. J. S.; Urban, T. J.; Mochly-Rosen, D.; Gross, E. R., Peptidomimetic therapeutics: scientific approaches and opportunities. *Drug Discov Today* **2017**, *22* (2), 454-462.
36. Lenci, E.; Trabocchi, A., Peptidomimetic toolbox for drug discovery. *Chem Soc Rev* **2020**, *49* (11), 3262-3277.
37. Perez, J. J., Designing Peptidomimetics. *Curr Top Med Chem* **2018**, *18* (7), 566-590.
38. Kuroda, K.; DeGrado, W. F., Amphiphilic polymethacrylate derivatives as antimicrobial agents. *J Am Chem Soc* **2005**, *127* (12), 4128-9.
39. Locock, K. E.; Michl, T. D.; Valentin, J. D.; Vasilev, K.; Hayball, J. D.; Qu, Y.; Traven, A.; Griesser, H. J.; Meagher, L.; Haeussler, M., Guanylated polymethacrylates: a class of potent antimicrobial polymers with low hemolytic activity. *Biomacromolecules* **2013**, *14* (11), 4021-31.
40. Perrier, S., 50th Anniversary Perspective: RAFT Polymerization—A User Guide. *Macromolecules* **2017**, *50* (19), 7433-7447.
41. Exley, S. E.; Paslay, L. C.; Sahukhal, G. S.; Abel, B. A.; Brown, T. D.; McCormick, C. L.; Heinhorst, S.; Koul, V.; Choudhary, V.; Elasri, M. O.; Morgan, S. E., Antimicrobial Peptide Mimicking Primary Amine and Guanidine Containing Methacrylamide Copolymers Prepared by Raft Polymerization. *Biomacromolecules* **2015**, *16* (12), 3845-52.
42. Yu, H. Y.; Tu, C. H.; Yip, B. S.; Chen, H. L.; Cheng, H. T.; Huang, K. C.; Lo, H. J.; Cheng, J. W., Easy strategy to increase salt resistance of antimicrobial peptides. *Antimicrob Agents Chemother* **2011**, *55* (10), 4918-21.
43. Goldman, M. J.; Anderson, G. M.; Stolzenberg, E. D.; Kari, U. P.; Zasloff, M.; Wilson, J. M., Human beta-defensin-1 is a salt-sensitive antibiotic in lung that is inactivated in cystic fibrosis. *Cell* **1997**, *88* (4), 553-60.
44. Baldassarre, L.; Pinnen, F.; Cornacchia, C.; Fornasari, E.; Cellini, L.; Baffoni, M.; Cacciatore, I., Synthesis of short cationic antimicrobial peptidomimetics containing arginine analogues. *J Pept Sci* **2012**, *18* (9), 567-78.
45. Levine, D. P., Vancomycin: a history. *Clin Infect Dis* **2006**, *42 Suppl 1*, S5-12.
46. Antonoplis, A.; Zang, X.; Wegner, T.; Wender, P. A.; Cegelski, L., Vancomycin-Arginine Conjugate Inhibits Growth of Carbapenem-Resistant *E. coli* and Targets Cell-Wall Synthesis. *ACS Chem Biol* **2019**, *14* (9), 2065-2070.
47. Delcour, A. H., Outer membrane permeability and antibiotic resistance. *Biochim Biophys Acta* **2009**, *1794* (5), 808-16.
48. Minnock, A.; Vernon, D. I.; Schofield, J.; Griffiths, J.; Parish, J. H.; Brown, S. B., Mechanism of uptake of a cationic water-soluble pyridinium zinc phthalocyanine across the outer membrane of *Escherichia coli*. *Antimicrob Agents Chemother* **2000**, *44* (3), 522-7.
49. Taevernier, L.; Wynendaele, E.; Gevaert, B.; Spiegeleer, B., Chemical Classification of Cyclic Depsipeptides. *Curr Protein Pept Sci* **2017**, *18* (5), 425-452.
50. Kitagaki, J.; Shi, G.; Miyauchi, S.; Murakami, S.; Yang, Y., Cyclic depsipeptides as potential cancer therapeutics. *Anticancer Drugs* **2015**, *26* (3), 259-71.
51. Moore, R. E., Cyclic peptides and depsipeptides from cyanobacteria: a review. *J Ind Microbiol* **1996**, *16* (2), 134-43.
52. Gang, D.; Kim, D. W.; Park, H. S., Cyclic Peptides: Promising Scaffolds for Biopharmaceuticals. *Genes (Basel)* **2018**, *9* (11).

53. Ling, L. L.; Schneider, T.; Peoples, A. J.; Spoering, A. L.; Engels, I.; Conlon, B. P.; Mueller, A.; Schaberle, T. F.; Hughes, D. E.; Epstein, S.; Jones, M.; Lazarides, L.; Steadman, V. A.; Cohen, D. R.; Felix, C. R.; Fetterman, K. A.; Millett, W. P.; Nitti, A. G.; Zullo, A. M.; Chen, C.; Lewis, K., A new antibiotic kills pathogens without detectable resistance. *Nature* **2015**, *517* (7535), 455-9.
54. von Nussbaum, F.; Sussmuth, R. D., Multiple attack on bacteria by the new antibiotic teixobactin. *Angew Chem Int Ed Engl* **2015**, *54* (23), 6684-6.
55. Atkinson, D. J.; Naysmith, B. J.; Furkert, D. P.; Brimble, M. A., Enduracididine, a rare amino acid component of peptide antibiotics: Natural products and synthesis. *Beilstein J Org Chem* **2016**, *12*, 2325-2342.
56. Burroughs, A. M.; Hoppe, R. W.; Goebel, N. C.; Sayyed, B. H.; Voegtline, T. J.; Schwabacher, A. W.; Zabriskie, T. M.; Silvaggi, N. R., Structural and functional characterization of MppR, an enduracididine biosynthetic enzyme from streptomyces hygrosopicus: functional diversity in the acetoacetate decarboxylase-like superfamily. *Biochemistry* **2013**, *52* (26), 4492-506.
57. Han, L.; Vuksanovic, N.; Oehm, S. A.; Fenske, T. G.; Schwabacher, A. W.; Silvaggi, N. R., Streptomyces wadayamensis MppP is a PLP-Dependent Oxidase, Not an Oxygenase. *Biochemistry* **2018**, *57* (23), 3252-3264.
58. Han, L.; Schwabacher, A. W.; Moran, G. R.; Silvaggi, N. R., Streptomyces wadayamensis MppP Is a Pyridoxal 5'-Phosphate-Dependent L-Arginine alpha-Deaminase, gamma-Hydroxylase in the Enduracididine Biosynthetic Pathway. *Biochemistry* **2015**, *54* (47), 7029-40.
59. Jad, Y. E.; Acosta, G. A.; Naicker, T.; Ramtahal, M.; El-Faham, A.; Govender, T.; Kruger, H. G.; de la Torre, B. G.; Albericio, F., Synthesis and Biological Evaluation of a Teixobactin Analogue. *Org Lett* **2015**, *17* (24), 6182-5.
60. Parmar, A.; Iyer, A.; Vincent, C. S.; Van Lysebetten, D.; Prior, S. H.; Madder, A.; Taylor, E. J.; Singh, I., Efficient total syntheses and biological activities of two teixobactin analogues. *Chem Commun (Camb)* **2016**, *52* (36), 6060-3.
61. Jin, K.; Sam, I. H.; Po, K. H. L.; Lin, D.; Ghazvini Zadeh, E. H.; Chen, S.; Yuan, Y.; Li, X., Total synthesis of teixobactin. *Nat Commun* **2016**, *7*, 12394.
62. Li, L.; Vorobyov, I.; Allen, T. W., The different interactions of lysine and arginine side chains with lipid membranes. *J Phys Chem B* **2013**, *117* (40), 11906-20.
63. Wu, C.; Pan, Z.; Yao, G.; Wang, W.; Fang, L.; Su, W., Synthesis and structure-activity relationship studies of teixobactin analogues. *RSC Advances* **2017**, *7* (4), 1923-1926.
64. Yang, H.; Chen, K. H.; Nowick, J. S., Elucidation of the Teixobactin Pharmacophore. *ACS Chem Biol* **2016**, *11* (7), 1823-6.
65. Chen, K. H.; Le, S. P.; Han, X.; Frias, J. M.; Nowick, J. S., Alanine scan reveals modifiable residues in teixobactin. *Chem Commun (Camb)* **2017**, *53* (82), 11357-11359.
66. Jin, K.; Po, K. H. L.; Kong, W. Y.; Lo, C. H.; Lo, C. W.; Lam, H. Y.; Sirinimal, A.; Reuven, J. A.; Chen, S.; Li, X., Synthesis and antibacterial studies of teixobactin analogues with non-isostere substitution of enduracididine. *Bioorg Med Chem* **2018**, *26* (5), 1062-1068.
67. Monciardini, P.; Bernasconi, A.; Iorio, M.; Brunati, C.; Sosio, M.; Campochiaro, L.; Landini, P.; Maffioli, S. I.; Donadio, S., Antibacterial Aromatic Polyketides Incorporating the Unusual Amino Acid Enduracididine. *J Nat Prod* **2019**, *82* (1), 35-44.
68. Cudic, P.; Behenna, D. C.; Kranz, J. K.; Kruger, R. G.; Wand, A. J.; Veklich, Y. I.; Weisel, J. W.; McCafferty, D. G., Functional analysis of the lipoglycopeptide antibiotic ramoplanin. *Chem Biol* **2002**, *9* (8), 897-906.

69. Helm, J. S.; Chen, L.; Walker, S., Rethinking ramoplanin: the role of substrate binding in inhibition of peptidoglycan biosynthesis. *J Am Chem Soc* **2002**, *124* (47), 13970-1.
70. Hamburger, J. B.; Hoertz, A. J.; Lee, A.; Senturia, R. J.; McCafferty, D. G.; Loll, P. J., A crystal structure of a dimer of the antibiotic ramoplanin illustrates membrane positioning and a potential Lipid II docking interface. *Proc Natl Acad Sci U S A* **2009**, *106* (33), 13759-64.
71. Fang, X.; Tiyanont, K.; Zhang, Y.; Wanner, J.; Boger, D.; Walker, S., The mechanism of action of ramoplanin and enduracidin. *Mol Biosyst* **2006**, *2* (1), 69-76.
72. Breukink, E.; de Kruijff, B., Lipid II as a target for antibiotics. *Nat Rev Drug Discov* **2006**, *5* (4), 321-32.
73. Ruzin, A.; Singh, G.; Severin, A.; Yang, Y.; Dushin, R. G.; Sutherland, A. G.; Minnick, A.; Greenstein, M.; May, M. K.; Shlaes, D. M.; Bradford, P. A., Mechanism of action of the mannopeptimycins, a novel class of glycopeptide antibiotics active against vancomycin-resistant gram-positive bacteria. *Antimicrob Agents Chemother* **2004**, *48* (3), 728-38.
74. He, H.; Shen, B.; Petersen, P. J.; Weiss, W. J.; Yang, H. Y.; Wang, T. Z.; Dushin, R. G.; Koehn, F. E.; Carter, G. T., Manno-peptimycin esters and carbonates, potent antibiotic agents against drug-resistant bacteria. *Bioorg Med Chem Lett* **2004**, *14* (1), 279-82.
75. Haltli, B.; Tan, Y.; Magarvey, N. A.; Wagenaar, M.; Yin, X.; Greenstein, M.; Hucul, J. A.; Zabriskie, T. M., Investigating beta-hydroxyenduracidin formation in the biosynthesis of the mannopeptimycins. *Chem Biol* **2005**, *12* (11), 1163-8.
76. Sum, P.-E.; How, D.; Torres, N.; Petersen, P. J.; Lenoy, E. B.; Weiss, W. J.; Mansour, T. S., Novel ether derivatives of mannopeptimycin glycopeptide antibiotic. *Bioorganic & Medicinal Chemistry Letters* **2003**, *13* (6), 1151-1155.
77. Sum, P. E.; How, D.; Torres, N.; Newman, H.; Petersen, P. J.; Mansour, T. S., Synthesis and activity of novel benzoxazole derivatives of mannopeptimycin glycopeptide antibiotics. *Bioorg Med Chem Lett* **2003**, *13* (15), 2607-10.
78. Yin, X.; McPhail, K. L.; Kim, K. J.; Zabriskie, T. M., Formation of the nonproteinogenic amino acid 2S,3R-capreomycin by VioD from the viomycin biosynthesis pathway. *Chembiochem* **2004**, *5* (9), 1278-81.
79. Holm, M.; Borg, A.; Ehrenberg, M.; Sanyal, S., Molecular mechanism of viomycin inhibition of peptide elongation in bacteria. *Proc Natl Acad Sci U S A* **2016**, *113* (4), 978-83.
80. S. Nomoto, T. T., T. Shiba, On the role of the ureido and guanidino groups in exhibition of antibacterial activity of tuberactinomycin. *Peptide Chemistry* **1977**, (15), 139-144.
81. Stanley, R. E.; Blaha, G.; Grodzicki, R. L.; Strickler, M. D.; Steitz, T. A., The structures of the anti-tuberculosis antibiotics viomycin and capreomycin bound to the 70S ribosome. *Nat Struct Mol Biol* **2010**, *17* (3), 289-93.
82. Kaweewan, I.; Hemmi, H.; Komaki, H.; Kodani, S., Isolation and structure determination of a new antibacterial peptide pentaminomycin C from *Streptomyces cacaoi* subsp. *cacaoi*. *J Antibiot (Tokyo)* **2020**, *73* (4), 224-229.
83. Chang, C. Y.; Lyu, S. Y.; Liu, Y. C.; Hsu, N. S.; Wu, C. C.; Tang, C. F.; Lin, K. H.; Ho, J. Y.; Wu, C. J.; Tsai, M. D.; Li, T. L., Biosynthesis of streptolidine involved two unexpected intermediates produced by a dihydroxylase and a cyclase through unusual mechanisms. *Angew Chem Int Ed Engl* **2014**, *53* (7), 1943-8.
84. Jackson, M. D.; Gould, S. J.; Zabriskie, T. M., Studies on the formation and incorporation of streptolidine in the biosynthesis of the peptidyl nucleoside antibiotic streptothricin F. *J Org Chem* **2002**, *67* (9), 2934-41.

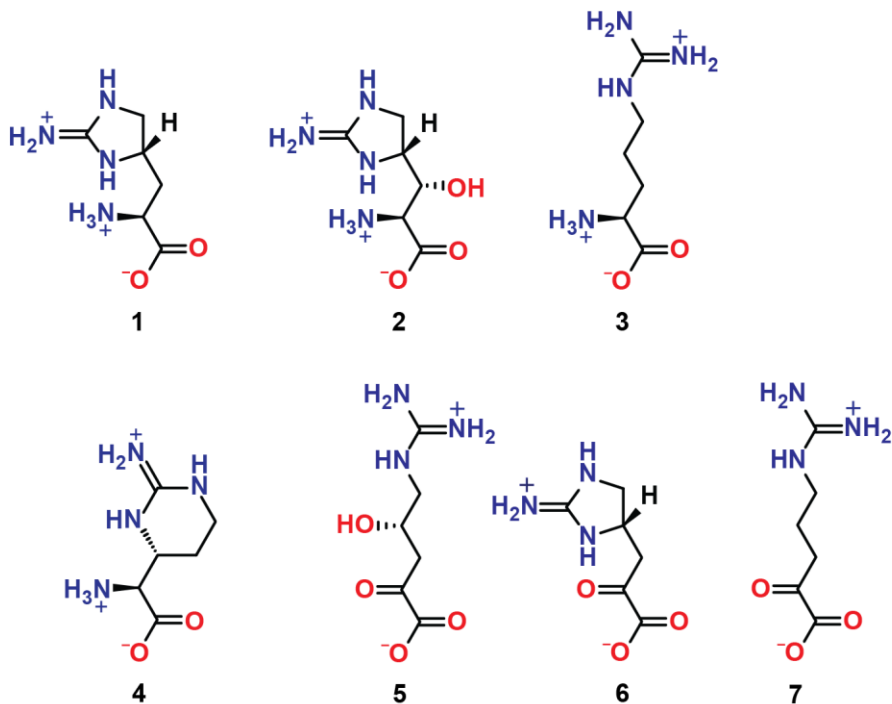
Chapter 2

Structural and Preliminary Biochemical Characterization of MppQ, a PLP-Dependent Aminotransferase from *Streptomyces hygroscopicus*

2.1 Introduction

Antibiotic-resistant pathogens are a continuing threat to public health. Mannopectimycin from *Streptomyces hygroscopicus* and enduracidin from *S. fungicidicus* are non-ribosomally produced peptide antibiotics with activity against a number of Gram-positive pathogens, including drug-resistant strains like methicillin-resistant *Staphylococcus aureus* (MRSA) and vancomycin-resistant enterococci (VRE)^{1,2}. Both these agents were discovered decades ago², but despite their promising potency against problem pathogens, they have proved too cytotoxic to be viable therapeutic agents.

The search for less toxic analogues, has been hampered by the difficulty of altering the core peptides of mannopectimycin and enduracidin since they both contain the unusual non-proteinogenic amino acid L-enduracididine (L-End, **1** in Scheme 2-1), or its hydroxylated derivative β -hydroxy enduracididine (β hEnd, **2**). This amino acid is not commercially available and, while synthetic routes have been developed³, they are multi-step processes starting from an advanced intermediate. The limited availability of this key building block has hampered efforts to



Scheme 2-1. Compounds discussed in this chapter. **1**, L-enduracididine (L-End); **2**, β -hydroxyenduracididine (β hEnd); **3**, L-arginine (L-Arg); **4**, L-capreomycin (L-Cap); **5**, 2-oxo-4-hydroxy-5-guanidinovaleric acid (i.e. 4-hydroxy-ketoarginine, 4HKA); **6**, 2-ketoenduracididine (2KE); **7**, 2-oxo-5-guanidinovaleric acid (i.e. 2-ketoarginine, 2KA).

make large groups of mannopeptimycin or enduracidin analogs. As a result, we have only a limited understanding of the structure-activity relationships in these compounds. A relatively inexpensive and facile route to L-End would facilitate the search for mannopeptimycin and enduracidin analogs with improved therapeutic properties.

Feeding experiments with radio-labelled amino acids⁴ showed that L-End biosynthesis originates with L-Arg (**3**). The biosynthetic clusters for both mannopeptimycin and enduracidin have been characterized^{1, 2}, and they share only 3 genes in common: *mpp/endP*, *Q*, and *R*. Disruption of any of these genes in *S. fungicidicus* abrogates enduracidin production. This defect can be rescued by addition of exogenous L-End to the growth medium.⁵ Thus, the Mpp/EndPQR gene products appear to convert L-Arg to L-End in the biosynthesis of mannopeptimycin and

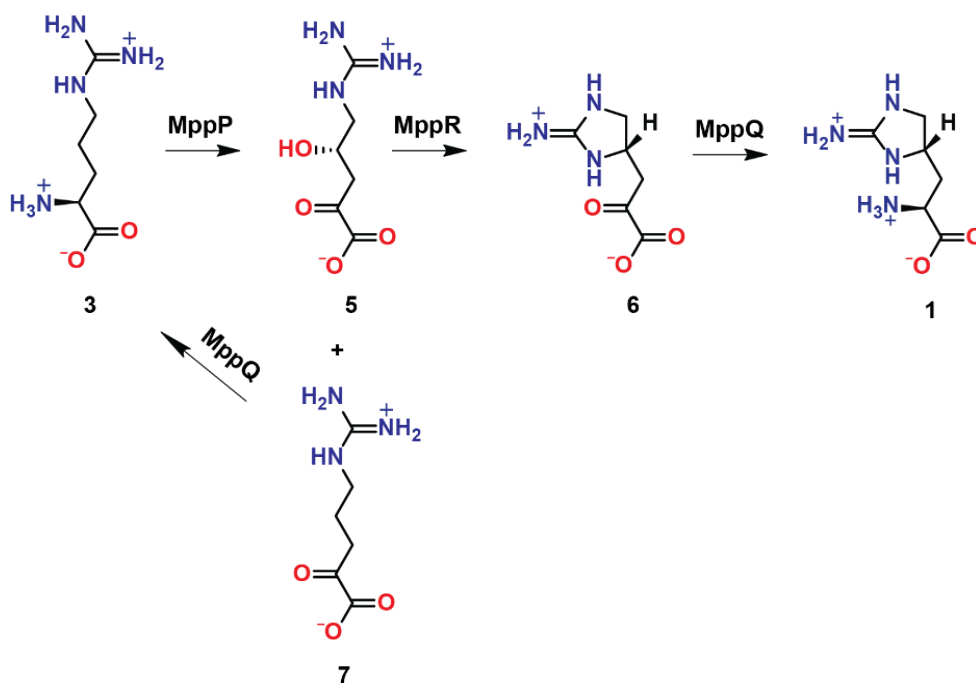
enduracidin, respectively. The mystery of how these three gene products produce L-End was only deepened by comparison to the biosynthetic pathway of a related, L-Arg-derived amino acid, L-capreomycidine (**4**).

Capreomycidine, a component of the antibiotic viomycin, is structurally similar to L-End and is produced by a two-enzyme system. VioC is a non-heme iron- and α -ketoglutarate-dependent oxygenase that hydroxylates L-Arg at the β -carbon atom.⁶ VioD is a fold type I PLP-dependent aminotransferase that catalyzes a unique intramolecular aminotransfer reaction to create the pyrimidinyl ring of **4**.⁶ This system uses one enzyme to activate the β -carbon for cyclization and a second enzyme to create the ring. L-End biosynthesis, by contrast, requires three enzymes. Two of these are PLP-dependent enzymes that could be capable of catalyzing the cyclization step (MppP and MppQ), and none of the three was expected, on the basis of amino acid sequence analysis, to have the catalytic power to activate the γ -carbon atom for cyclization.

The sequence of chemical steps leading from L-Arg to L-End and the intermediates involved became clearer when it was found that MppP from *S. wadayamensis* (SwMppP, a close homolog of the *S. hygroscopicus* enzyme and also in a mannopeptimycin biosynthetic cluster) is a novel type of PLP-dependent oxidase that catalyzes the oxidation of L-Arg to 2-oxo-4-hydroxy-5-guanidinovaleric acid (**5**).^{7, 8} This observation fit in well with previous work on MppR from *S. hygroscopicus* (ShMppR) that indicated this enzyme may operate on an oxidized arginine derivative like **5** to produce the ketone form of L-End (**6**).⁹ The PLP-dependent enzymes are a large group of proteins that catalyze a wide range of reactions, including racemization, decarboxylation, β - and γ -substitution/elimination, and transamination.¹⁰ This latter reaction accounts for a majority of PLP-dependent enzyme activities. Herein we report the X-ray crystal structure of *S. hygroscopicus* MppQ (ShMppQ), which shows that this enzyme is a fold type I

aminotransferase, matching both the tertiary structure and active site architecture of well characterized aminotransferases like aspartate aminotransferase from *E. coli* (EcAAT) and human kynurenine aminotransferase II (1X0M).¹¹

The steady state kinetic analysis of the transamination reaction between the possible substrate analog 2-oxo-5-guanidinovaleric acid (**7**) and L-alanine showed that the structural similarities are not surreptitious; ShMppQ catalyzes the aminotransfer reaction. Preliminary kinetic studies involving its physiological substrate, **6**, and L-alanine confirm the role of MppQ as a *bona fide* aminotransferase in the L-End pathway (Scheme 2-2). Based on the results of mass spectrometry based end-point assays, we have identified L-ornithine as the optimal amino group donor. These studies suggest a likely function for ShMppQ, completing our understanding of L-End biosynthesis.



Scheme 2-2. The proposed roles of MppP/R/Q in the biosynthetic pathway of L-End.

2.2 Materials and Methods

Protein expression and purification. The gene encoding *S. hygrosopicus* MppQ (UniProt accession code Q643B9) was synthesized by GenScript, Inc and subcloned into the pE-SUMOkan vector for expression in *E. coli* BL21 Star cells. Transformed cells were grown at 37 °C in 2-4 L of Luria-Bertani medium containing 50 µg ml⁻¹ kanamycin to an OD_{600nm} of ~1.0. Expression of MppQ was induced with 0.4 mM isopropyl β-D-1-thiogalactopyranoside (IPTG) and the temperature was reduced to 25 °C. After 18 hours, the cells were harvested by centrifugation at 6,000 rpm for 30 minutes. The pellets, approximately 10 g L⁻¹ of culture, were resuspended in 5ml of buffer A (25 mM TRIS pH 8.0, 300 mM NaCl, 10 mM imidazole, 200 µM PLP) per gram of cell pellet. The cells were lysed in a circulating ice bath using a Fisher Scientific Model 500 sonic dismembrator at 70% amplitude, for a total of 10 minutes (20 pulses of 30 seconds each, separated by 1-minute rest periods). The resulting lysate was clarified by centrifugation at 39,000 x g (18,000 rpm) for 1 hour. The clarified lysate was passed through a 0.45 µm syringe filter and loaded in 30 ml aliquots onto a 5 ml HisTrap FF column (GE LifeSciences) that had been pre-equilibrated with buffer A (without PLP). After washing with 10 column volumes of buffer A, the protein was washed further and ultimately eluted using a step gradient at 10%, 50%, and 100% buffer B (25 mM TRIS pH 8.0, 300 mM NaCl, 250 mM imidazole). Fractions containing significant amounts of SUMO-MppQ, as judged by a Coomassie-stained SDS-PAGE gel, were pooled and His₆-Ulp1 protease was added to a final concentration of 2.0 µM. The pooled HisTrap fractions were dialyzed overnight at 4 °C against 3.5 L of buffer C (50 mM TRIS pH 8.0, 150 mM NaCl, 0.5 mM DTT). The following day, the cleaved His₆-SUMO tag and protease were removed by passing the dialysate over the HisTrap FF column a second time. The flow-through fractions were collected and judged to be > 95% pure by SDS-PAGE. The protein concentration was quantified by A_{280nm}

using the calculated extinction coefficient of $37150 \text{ M}^{-1} \text{ cm}^{-1}$. The protein was dialyzed against 3.5 L of storage buffer (20 mM TRIS pH 8.0, 200 μM PLP) overnight at 4 °C, then concentrated to 11-15 mg ml⁻¹ and used directly or snap-frozen in liquid nitrogen.

Crystallization. Crystals of ShMppQ·PLP (internal aldimine) were grown by the hanging-drop vapor diffusion method over wells containing 15-25 % PEG 3350, and 0.1-0.2 M ammonium citrate trihydrate, trilithium citrate, or ammonium sulfate. Crystals appeared as clusters of thin needles after 3-7 days. The size and morphology of the crystals were improved by microseeding. The crystal used for the MppQ·PMP structure (external aldimine) was grown as above, except that the well solution contained 100mM L-arginine pH 8.0. Crystals were cryo-protected for data collection by soaking briefly in a sequence of solutions containing 30 % PEG 3350, 0.2 M ammonium citrate trihydrate, and 5, 10, or 20 % glycerol.

Data collection and processing. An initial data set was collected from an unliganded MppQ crystal at 100 K on beamline 21-ID-D of the Advanced Photon Source (Life Science Collaborative Access Team, LS-CAT) equipped with a MAR 300 CCD detector, using an oscillation angle of 1.0 ° over a total of 180 ° with an exposure time of 1 second, a crystal-to-detector distance of 250 mm, and wavelength of 0.97625 Å. Diffraction images were processed using iMOSFLM, POINTLESS, and SCALA as implemented in the CCP4 suite v7.0. This MppQ crystal diffracted to 2.1 Å-resolution. A higher-resolution data set was collected from a different crystal, also at LS-CAT beamline 21-ID-D, using an oscillation angle of 0.5 ° over a total of 140 ° at a distance of 220 mm. The exposure time and wavelength were the same as for the first data set. This crystal was essentially identical to the initial one but was larger and diffracted to 1.8 Å-resolution. These data were also processed using iMOSFLM,¹² POINTLESS,¹³ and SCALA.¹³ The final data set reported here was collected at LS-CAT beamline 21-ID-G equipped with a MAR 300 CCD

detector from an MppQ·L-Arg co-crystal. The X-ray wavelength was fixed at 0.97856, the oscillation range was 0.5 ° over a total of 120 °, the distance was 220 mm, and the exposure time was 1 second. This co-crystal diffracted to 1.5 Å-resolution. These data were processed with the HKL2000 package.¹⁴ Data processing statistics are given in Table 2-1.

Structure determination and model refinement. Initial phases were obtained by molecular replacement using PHASER (as implemented in the CCP4 suite v7.0)¹⁵ with the 2.1 Å-resolution unliganded data set and the structure of *Pyrococcus horikoshii* OT3 kynurenine aminotransferase II (PDB ID 1X0M¹¹; 31 % identical) with the 50 N-terminal residues, waters, and PLP-Lysine removed. The lower-resolution data set was used for structure determination, because the “a” cell edge of the crystal used to collect the 1.8 Å unliganded data set was oriented parallel to the spindle axis, resulting in poor sampling of the corresponding region of reciprocal space. The Matthews coefficient VM of 2.21 Å³ Da⁻¹ (41 % solvent) suggested that there were two molecules of MppQ (415 residues, 44.0 kDa) per asymmetric unit. While PHASER was able to find a viable solution (LLG=33, TFZ=9.5), it did not refine well. This poor molecular replacement model was subjected to density modification and automated rebuilding in PHENIX.AutoBuild¹⁶ to remove bias and improve the model. PHENIX.AutoBuild resulted in a model with 761 residues (740 with side chains placed; ~90 % complete) in 2 chains with R_{cryst} and R_{free} values of 20.0 % and 24.0 %, respectively. This model was used without refinement as the molecular replacement search model to obtain phases for the 1.8 Å-resolution data set (LLG=22,318; TFZ=135). After iterative rounds of restrained refinement in PHENIX.Refine¹⁷ and manual model building in COOT^{18, 19} the final model of the PLP-bound, internal aldimine form of ShMppQ contained two molecules of MppQ (774 total residues), 816 water molecules, and one molecule of PLP per chain covalently bound at Lys250. The final R_{cryst} and R_{free} values were 14.0 and 17.2 %, respectively.

Synthesis of 6. The starting material for **6**, 4(S)HKA, was produced enzymatically from L-Arg using the arginine oxidase MppP. A reaction containing 100 mM L-Arg and 200 μ M MppP was carried out in 20 mM ammonium acetate, pH 7.0. Bovine catalase (40 mg) was desalted in the reaction buffer (to remove the trehalose stabilizer that would complicate downstream NMR analysis) and added to the reaction mixture to prevent non-enzymatic decarboxylation of 4HKA by the hydrogen peroxide produced by the MppP reaction. The reaction was allowed to proceed overnight at 25 °C while shaking at 150 rpm. The reaction was quenched with 1 volume of methanol and centrifuged at 4,000 rpm for 5 minutes in order to remove the precipitated enzyme. The supernatant was collected and evaporated to dryness at 50 °C in a Centrifan PE Rotary Evaporator. Approximately 1 mg of dried material was resuspended in approximately 1 mL of water, centrifuged at 13 000 rpm for 5 minutes to remove any particulates and analyzed using a ZIC-HILIC column (3.5 μ m, 100 Å, 50 x 2.1 mm) paired with Shimadzu LC-MS/MS 8040. Mobile phases used were 20 mM ammonium formate pH 4.0 (designated as “A”) and acetonitrile with 0.1% formic acid (designated as “B”). The analytes were eluted via gradient method at 0.5 mL/min and 35 °C. 15 μ L of sample was injected. The following time program was used: hold at 90% B (3.0 min), decrease to 40% B (10 min), hold at 40% B (12 min), increase to 90% B (13 min), hold at 90% B (15). The sample was run in positive ESI mode with a sprayer positioned at 4 mm. The dwell times for products of 190 m/z precursor were set to 80 ms, while dwell time for products of 190 m/z was set to 247 ms. The mass chromatogram (Figure 2-1) shows the amount of 4HKA and 2KA produced. Note that the peak splitting and distortion has occurred because of column overloading as well as solvent mismatch making the integration less accurate. Based on this data, the sample contains approximately 78% 4(S)HKA and 22% 2KA.

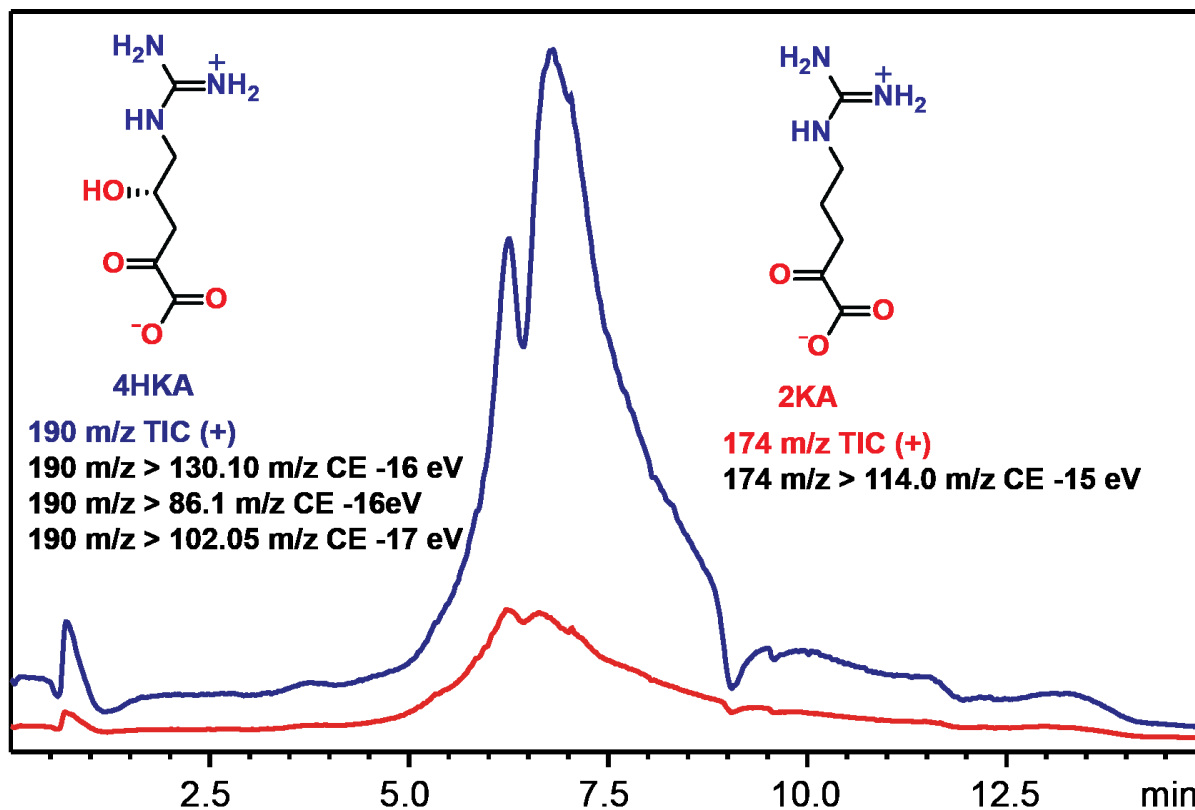


Figure 2-1. Chromatogram of enzymatically produced mixture of 4(S)HKA and 2KA in 20 mM ammonium acetate, pH 7.0.

The residue containing a mixture of 4HKA and 2KA (20 mg) was dissolved in a solution containing 180 μ M MppR stored in 20 mM sodium phosphate, pH 7.5. The reaction was allowed to proceed for 2 hours at 22 $^{\circ}$ C on a stir plate set at 100 rpm. The reaction was quenched with 1 volume of methanol and centrifuged at 4,000 rpm for 5 minutes to remove the precipitated enzyme. The supernatant was collected and evaporated to dryness at 50 $^{\circ}$ C in a Centrifan PE Rotary Evaporator. The reaction products were analyzed using a ZIC-HILIC column (3.5 μ m, 100 \AA , 50 x 2.1 mm) on a Shimadzu LC-MS/MS 8040. Mobile phases used were 20 mM ammonium formate

pH 4.0 (designated as “A”) and acetonitrile with 0.1% formic acid (designated as “B”). The analytes were eluted via gradient method at 0.5 mL/min and 35 C. Injection volume was 0.5 μ L. The following time program was used in each run: hold at 90% B (3.0 min), decrease to 40% B (4.5 min), hold at 40% B (6.5 min), increase to 90% B (7.0 min), hold at 90% B (9.0). The sample was run in positive ESI mode with a sprayer positioned at 4 mm. The dwell time for products of 172, 162, and 144 m/z precursors was set to 100 ms. The mass chromatogram (Figure 2-2) shows that most of 2KE is decarboxylated which most likely occurred during the heating stage at elevated temperature.

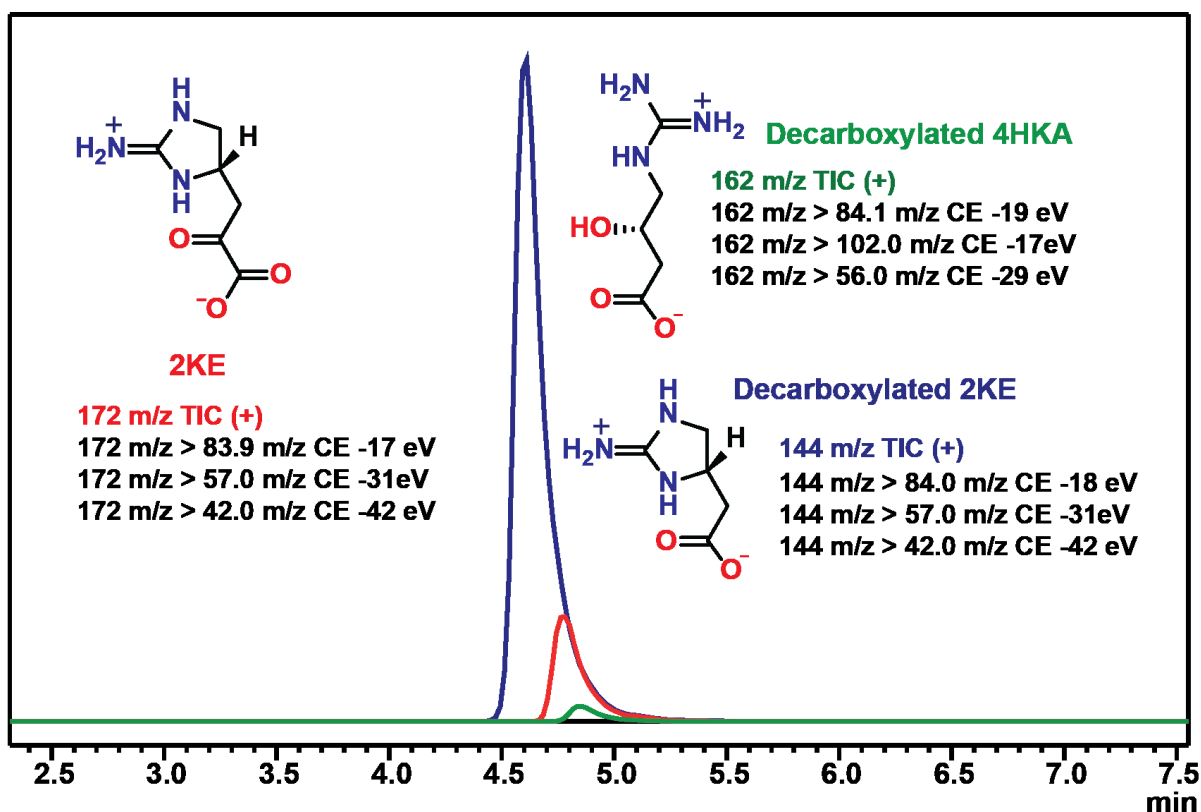


Figure 2-2. Chromatogram of enzymatically produced 2KE along with reaction by-products. The majority of 2KE appears to have been decarboxylated during the drying process, significantly decreasing product yield.

Assay of MppQ activity against 6. Snap-frozen MppQ stored in 50% glycerol, 25 mM TRIS pH 8.5, 200 μ M PLP, was thawed and glycerol was removed by buffer exchange with 20 mM TRIS, pH 8.5, 200 μ M PLP using a 10 kDa MWCO concentrator. The assay contained a nominal concentration of 50 μ M **6** (approximately 10% purity), 40 μ M MppQ and 100 mM L-Ala in 20 mM TRIS pH 8.5, 200 μ M PLP. The samples were manually quenched at 5, 10, 25, and 50 seconds using 1 volume of 0.1 M HCl. Measurements were conducted in triplicate. The reaction products were analyzed using a ZIC-HILIC column (3.5 μ m, 100 Å, 50 x 2.1 mm) on a Shimadzu LC-MS/MS 8040 using the 9 minute gradient described previously. Injection volume was 25 μ L for each sample. Dwell time of product ions 172 m/z and 173 m/z was 100 ms.

Synthesis of 7. The α -keto acid form of arginine was synthesized by enzymatic oxidation of L-arginine using a modified procedure developed by Meister,²⁰ and a purification method developed by Stalon et al.²¹ L-Arg (2 g, free base) was dissolved in 50 mL of water and the pH was adjusted using hydrochloric acid to 7.10-7.30. Lyophilized bovine catalase (50 mg) was dissolved in 3 mL of 5 mM sodium phosphate, pH 7.5, followed by buffer exchange using a 10 kDa MWCO concentrator. The sample was concentrated back down to 3 mL. L-Amino acid oxidase (LAAO) from *Crotalus atrox* (60 mg of dried venom) was dissolved in 10 mL water. One half of the catalase solution was added to the LAAO solution. The other half of the catalase solution was added to the L-Arg solution. The LAAO/catalase solution was then combined with the L-Arg/catalase solution, diluted to 100 mL with mqH₂O and placed in a 1000 mL Erlenmeyer flask and covered loosely with foil. The reaction flask was placed in a shaking incubator at 25 °C, 100 rpm, in the dark for 16 hr. The following day, the reaction was quenched with 100 mL of methanol and centrifuged at 4 °C, 3500 rpm for 10 min. The supernatant was collected. A 30 x 1 cm glass

column was packed with 20 g of Dowex 50WX8 200-400 mesh in hydrogen form. A peristaltic pump set to a flow rate of 8 mL/min was used to pass 300 mL of 0.5 M NaOH over the Dowex resin, followed by 300 mL 0.5 M HCl, 300 mL of 0.5 M NaCl, and finally 300 mL of water. The pH of the water issuing from the column must be 7.0 before loading the sample. The supernatant of the LAAO reaction was transferred to the column and the flow-through was collected in a round bottom flask. The column was then washed with 500 mL of water and the flow-through was collected in the same round bottom flask. The flow-through was evaporated to dryness using a rotavap at 40° C. Approximately 1 mg of sample was dissolved in 1 mL of deuterium oxide and centrifuged at 13 000 rpm for 5 minutes. The supernatant was collected and 700 µL of it was loaded into NMR tube. The sample was analyzed by ¹H, ¹³C and HSQC NMR. In aqueous solution, there are two forms of **7**: linear and cyclic (Appendix A). In the cyclic form the formation of a chiral center at C2 induces diastereotopic properties in the adjacent protons not seen in the linear form. In order to accurately integrate the spectrum, no standard such as acetonitrile was added, as it would overlap with the peaks of interest. The shift alignment was therefore done using the water solvent peak as a reference. This practice is not routinely used, since the shift of exchangeable water protons is dependent on factors such as temperature and pH value. . The solution should not be exposed to pH higher than 8.0 during purification, as this will lead to aldol condensation between two 2-ketoarginine molecules, yielding a conjugated product with a purple color.

ShMppQ spectrophotometric steady state assay. The steady state kinetics of ShMppQ-catalyzed transamination of L-Ala and **7** was studied by coupling the reaction to *E. coli* lactate dehydrogenase (EcLDH, EC 1.1.1.27). Pyruvate produced in the transamination reaction was reduced by EcLDH resulting in a loss of absorbance at 340 nm due to the oxidation of NADH ($\epsilon_{340\text{nm}} = 6220 \text{ M}^{-1}\text{cm}^{-1}$). The reactions contained 2 µM ShMppQ, 100 mM L-Ala, 20 U/ml EcLDH,

400 μM NADH, and concentrations of **7** in ranging from 2.5 – 320 μM . The reaction was carried out in 50 mM BICINE pH 7.8, 100 mM NaCl, 50 μM PLP. The absorbance at 340 nm was monitored using an Evolution 300 UV-Vis spectrophotometer (Thermo Scientific). The k_{cat} and K_{M} values were determined from the initial velocity data using Equation 1, where S is the concentration of **7**, v_0 is the initial velocity, V_{M} is the maximum velocity, and K_{M} is the Michaelis constant. Nonlinear regression analysis was performed in GraphPad Prism.

$$\text{Equation 1} \quad v_0 = \frac{V_{\text{M}}S}{(K_{\text{M}} + S)}$$

MppQ Amino Donor Screening. All reactions were carried out in 1 mL volumes of 20 μM ShMppQ, 50 mM bicine, pH 7.8, 150 mM NaCl, and 50 μM PLP. Three identical reactions with 1 mM **3** and 1 mM glyoxylate were manually quenched at 0.5, 1, 2, 5, 10, 15, and 20 minutes by mixing it with 1 volume of pure methanol. Two reactions with 1 mM glycine and 1 mM **7** were quenched in the same manner at 0.5, 10, and 20 minutes. The reactions with glycine and **7** were done in duplicate due to the limited amount of enzyme. The reaction products were analyzed using a ZIC-HILIC column on a Shimadzu LC-MS/MS 8040 using the 9 minute gradient elution method mentioned earlier. Injection volume was 15 μL for each sample. Dwell time for product ion of 174 m/z precursor was 247 ms.

Similar reactions with different amino donor substrates were carried out as end-point assays and contained 10 μM MppQ, 1 mM **7**, 1 mM L-His, L-Gln, L-Orn, L-Ala, L-Phe, L-Ile, or L-Thr, 50 mM bicine, pH 7.8, 10 mM NaCl, and 50 μM PLP. Samples of these reactions were quenched at 5 and 10 minutes with an equal volume of methanol. The reaction products were analyzed using

a ZIC-HILIC column (3.5 μm , 100 \AA , 50 x 2.1 mm) on a Shimadzu LC-MS/MS 8040 using the 9 minute gradient method mentioned earlier. Dwell time was 100 ms for every product ion resulting from 175 m/z precursor.

2.3 Results and discussion

Overall structure of *S. hygroscopicus* MppQ. The crystal structure of ShMppQ with the pyridoxal-5'-phosphate (PLP) cofactor covalently bound (internal aldimine) was determined by molecular replacement to a resolution of 1.7 \AA (Table 1-1). ShMppQ·PLP crystallized in space group P2₁2₁2₁ with unit cell dimensions a = 47.7, b = 114.3, and c = 133.4 \AA . The asymmetric unit contains two molecules. There are 14 residues at the N-terminus and 12 from the C-terminus of chain A that are not visible in the electron density. Chain B is similar, with 12 residues at each terminus missing from the model. Chain B also has a break between residues 325 and 329. Superposition of the two chains using Secondary Structure Matching (SSM)²² as implemented in COOT, gives a root mean square deviation (RMSD) of 0.32 \AA for 382 matched C α atoms. The two chains in the asymmetric unit form a homodimer (Figure 2-3; 2,974 \AA^2 buried surface area) that matches the quaternary structures observed for known fold type I aminotransferases.^{23, 24}

Superposition of the ShMppQ dimer onto the *E. coli* aspartate aminotransferase dimer (PDB ID 1ARS²⁵) gives an RMSD of 2.85 Å for 620 of the 775 C α atoms in the ShMppQ·PLP model.

The tertiary structure of ShMppQ, like its quaternary structure, matches that of typical fold type I aminotransferases like L-aspartate aminotransferase.^{10,23} The fold consists of an N-terminal extension (Met1 to Gly35) as well as a large domain (Leu49 to Ala324) and a small domain (Val36 to Leu48 and Met325 to Ser415). The large domain is comprised of a 7-stranded mixed β -sheet flanked by 10 α -helices (α - β - α sandwich), while the small domain has a mixed α - β topology. The large and small domains are linked by a 25-residue-long (~ 40 Å) helix that serves as the “backbone” of the enzyme. The active site is located at the interface between the large domains of

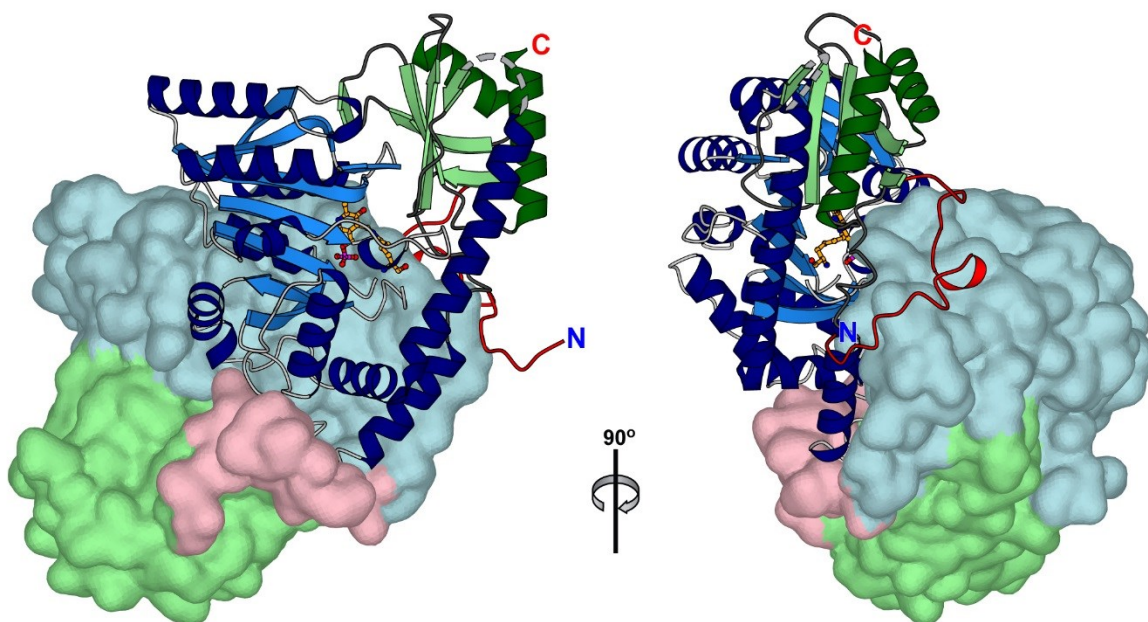


Figure 2-3. ShMppQ homodimer, with one monomer shown as ribbon representation and other shown as surface representation.

each protomer. As in all known fold type I aminotransferases, the cofactor is held in a cleft between

the central β -sheet, and helices $\alpha 3$ and $\alpha 4$ of one subunit, and helix $\alpha 8$ from the other subunit of the dimer (Figure 2-3).

In addition to the *E. coli* aspartate aminotransferase, a PDBeFold^{22, 26} search using chain A of the ShMppQ-PLP model returned 388 unique structures having Q scores of at least 0.14, the threshold value that implies significant structural similarity.²⁶ Of these, several had Q scores well above 0.4, implying very strong structural similarity.²⁶ These included the human kynurenine aminotransferase II homolog from *Pyrococcus horikoshii* OT3 (PhKAT-II; PDB ID 1X0M¹¹; 31 % identical, 2.1 Å RMSD) and the glutamine-phenylpyruvate aminotransferase from *Thermus thermophilus* HB8 (TtGlnAT; PDB ID 1V2D²⁷; 29 % identical, 2.2 Å RMSD). The former catalyzes the production of kynurenic acid and glutamate from kynurenine and α -ketoglutarate,²⁸ while the latter has been shown to catalyze aminotransfer between a number of aromatic amino acids and α -ketoglutarate.²⁷

Comparison of PLP- and PMP-bound MppQ. The Structure of ShMppQ-PLP shows clear electron density for the covalent attachment of PLP to the catalytic Lys250. The side chains surrounding the cofactor are typical of aspartate aminotransferase (Figure 2-4). The residues N187 and Y218 are hydrogen bonded to the oxygen atom attached to the pyridinium ring of PLP. D215 forms a salt bridge with the nitrogen of the pyridinium, thus stabilizing it and allowing PLP to act as an electron sink in the reaction with the substrate. The phosphate group of the PLP is within hydrogen bonding distances of S109, R257, S249, S247, as well as Y72 of the other monomer chain (Figure 2-4C). Most side chains lining the active site in EcAAT active site are identical (Y225, N194, D222, R266, S257, S255), except for subtle differences (PDB Entry: 1ARS).²⁵ In EcAAT, it is Trp140 which forms interactions with the PLP aromatic ring via pi-pi stacking, while

in MppQ, Y133 is found in this location. EcAAT also has T109 interacting with the phosphate moiety instead of S109.

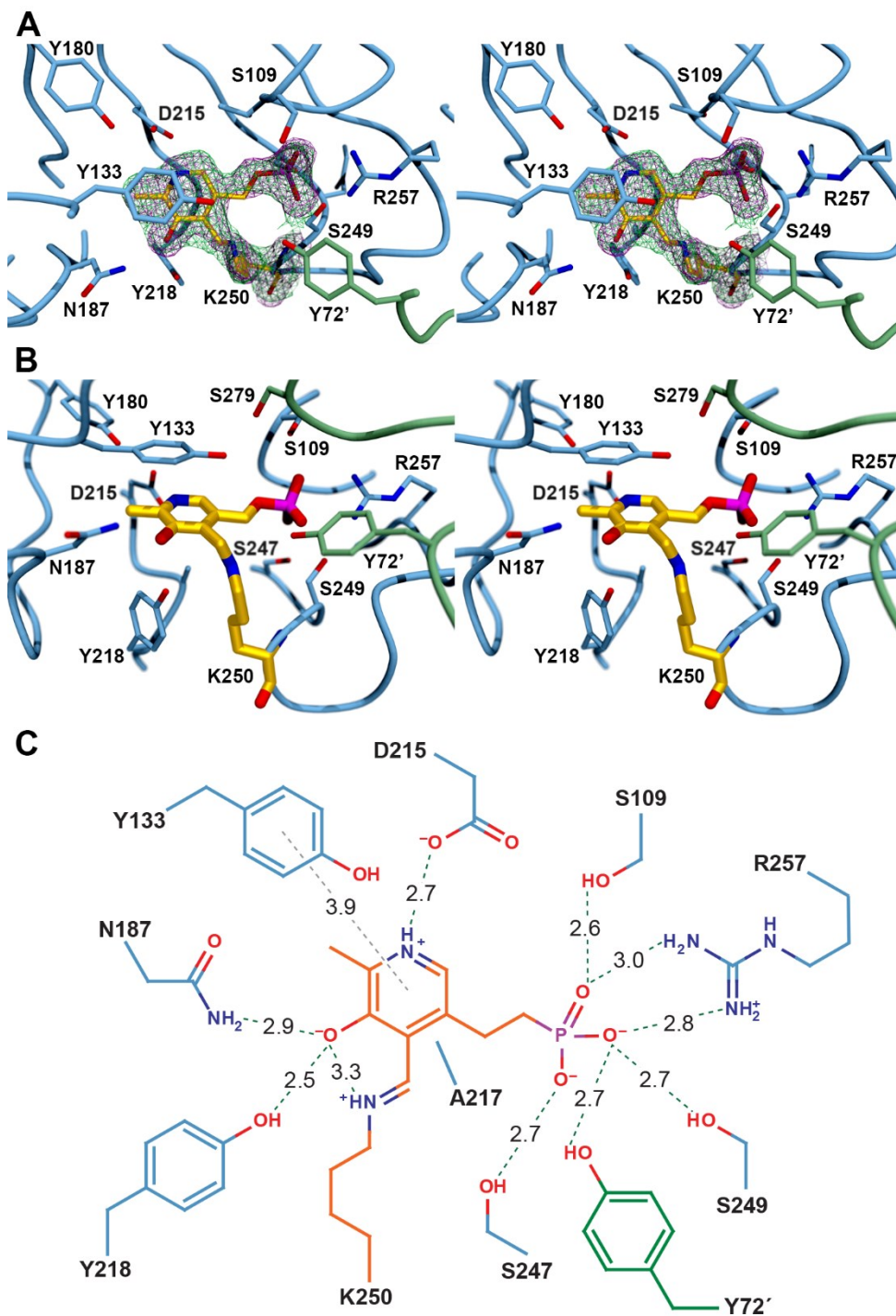
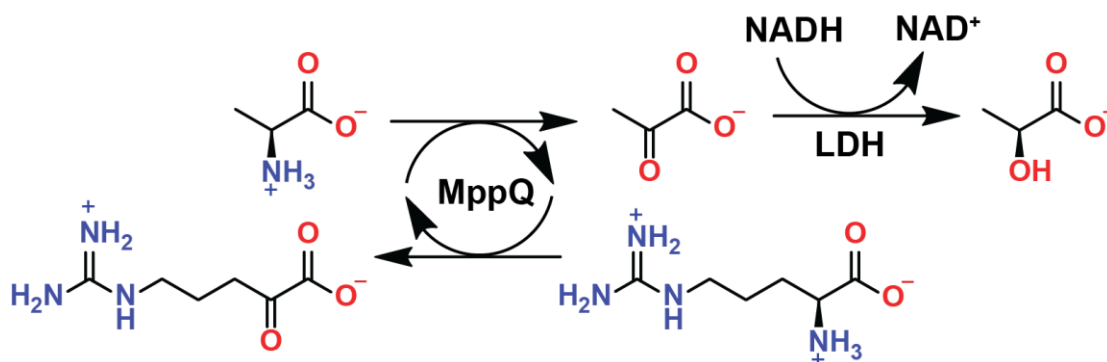


Figure 2-4. The $2|F_o| - |F_c|$ (magenta mesh) and simulated annealing composite omit (green mesh) electron density maps are shown for the K250-PLP adduct at 1.2σ (map radius 2.5 \AA) in a stereoview of the ShMppQ active site (A). A second stereoview of the active site (B) is shown without electron density and in a different orientation (rotated $\sim 60^\circ$ in the horizontal) to give a clearer picture of the linkage between K250 and the cofactor. A schematic representation of the active site (C) shows the interactions of active site functional groups with the cofactor and each other (associated distances are given in \AA).

Co-crystallization of the PLP-bound enzyme with 10 mM L-Arg resulted in trapping of the noncovalent complex between ShMppQ and pyridoxamine-5'-phosphate (PMP). The PMP-bound form of the enzyme was isomorphous with the ShMppQ·PLP complex. These crystals diffracted to 1.6 Å resolution and contained two molecules in the asymmetric unit, arranged in the same quaternary structure observed for the PLP-bound form of the enzyme (0.295 Å RMSD). The disordered regions in each chain are identical to those seen in the ShMppQ·PLP model.

The active site clearly contains PMP, as evidenced by the lack of continuous electron density to Lys250 (Figure 2-5). Aside from the presence of PMP in the active site, there is virtually no difference between the active sites of the PLP- and PMP-bound forms of ShMppQ. It will be interesting to find out if the change to a “closed” conformation (rotation of the small domain relative to the large domain) observed in some ATases does not happen in MppQ, or if the crystal simply captured an “open” conformation in each case.

Preliminary analysis of MppQ catalytic activity. The typical transamination reaction begins with the attack of the deprotonated amine of an amino acid on the C4' imine of PLP to form the external aldimine. Hydrolysis of this adduct releases the keto-acid and leaves PMP in the enzyme active site. A different α -keto acid, often α -ketoglutarate, binds and reacts with PMP, forming a second external aldimine. Given the structural evidence that ShMppQ is an aminotransferase, and that it operates in the biosynthesis of L-End from L-Arg, we used steady state kinetics to assess the reaction of the enzyme with a number of amino group donor and acceptor.



Scheme 2-3. An assay of MppQ reaction with 7 and L-Ala, coupled with LDH reaction with pyruvate produced by MppQ.

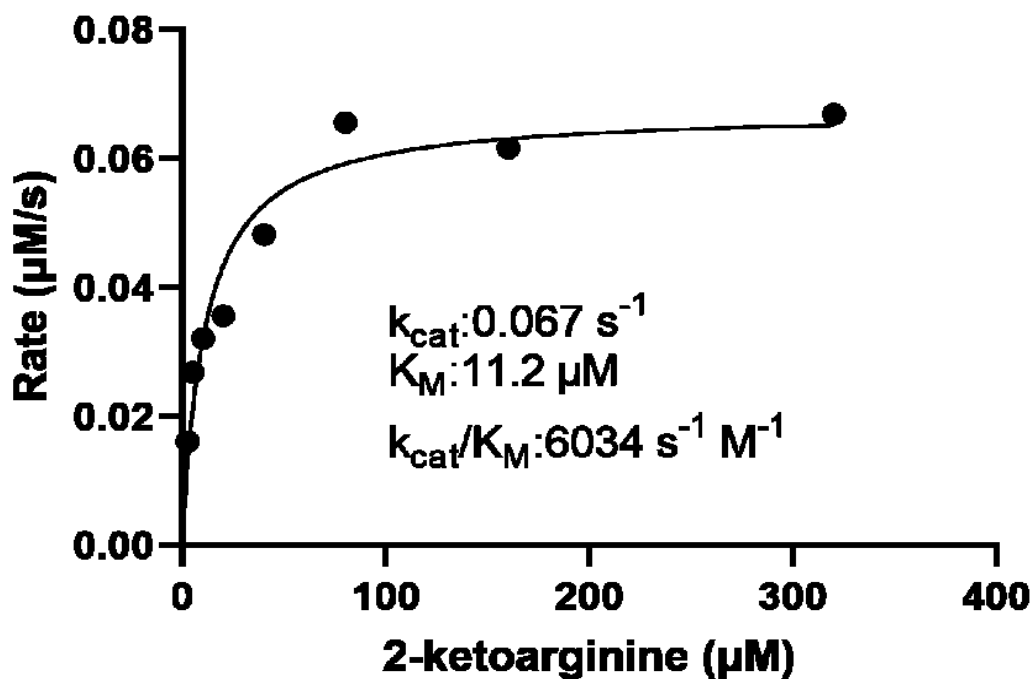


Figure 2-6. Michaelis-Menten curve for the reaction of ShMppQ with 7 and L-Ala.

In order to observe the aminotransferase activity of MppP, a coupled assay with lactate dehydrogenase (LDH) was designed. This assay relied on L-alanine as an amino group donor being converted to pyruvate, which is then reduced to lactate, while oxidizing NADH in the process (Scheme 2-3). Through following the decay of NADH at 340 nm, preliminary steady state kinetics data was collected. It was shown that MppQ catalyzes transamination of **7** and L-alanine (Figure 2-6), as well as its proposed physiological substrate, **6**, and L-alanine. The low K_M values indicates that MppQ has a high affinity for **7**. It is plausible that this serves a physiological role, as it would allow MppQ to recycle the “shunt product” **7**, back to L-arginine, thus providing MppP with more substrate and increasing the yield of L-End produced. The reactions of MppQ with 2KE and L-Ala manually quenched and analyzed using MS, have confirmed the substrate turnover (Figure 2-7, Figure 2-8).

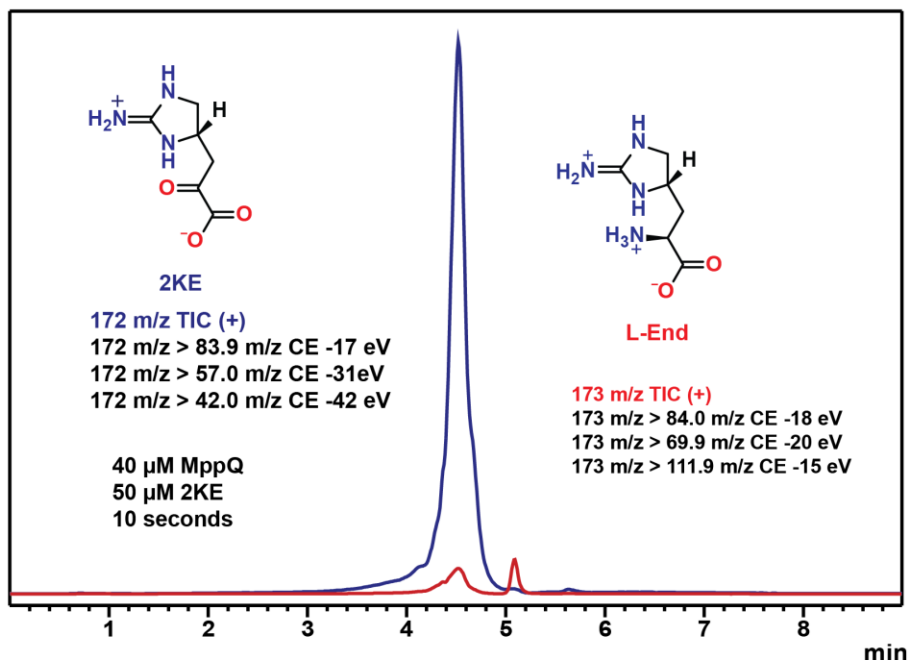
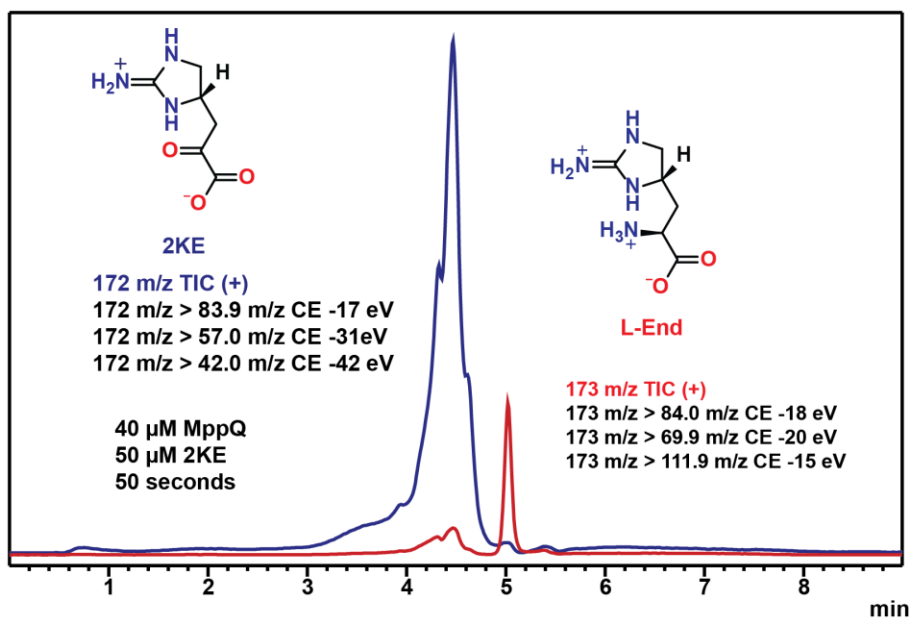
A**B**

Figure 2-7. MS chromatograms of MppQ reaction with **5** and L-Ala at 10 (A) and 50 seconds (B).

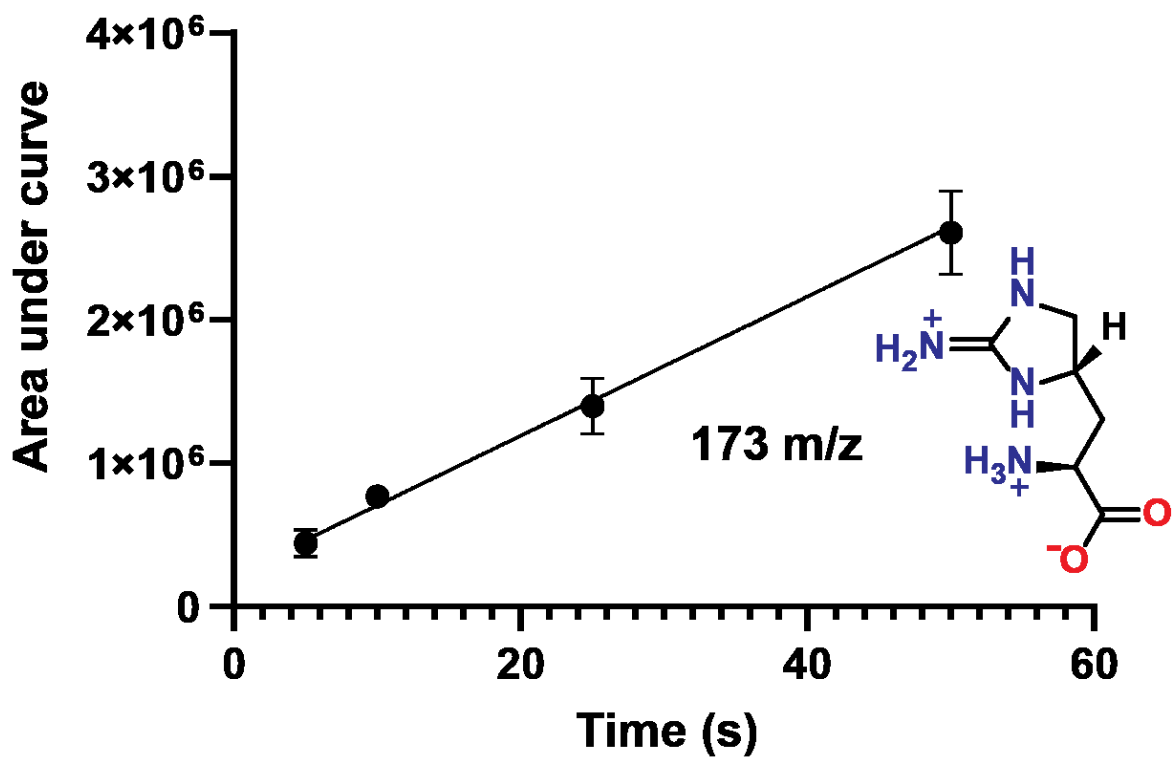


Figure 2-8. Production of 1 in a reaction of ShMppQ with 6 and L-Ala. The peaks corresponding to all fragments generated from 173 m/z precursor ion were integrated and areas under the curve plotted on the y-axis.

However, L-Ala is a very poor substrate ($K_M > 50$ mM, data not shown), leading to difficulty in obtaining accurate kinetic parameters. Previous HPLC-based end-point assays have indicated that MppQ reacts with L-Arg and glyoxylate, and that this reaction proceeds more rapidly than the analogous reaction with pyruvate as the amino group acceptor. However, it appears that this reaction is irreversible, as the reaction of ShMppQ with **7** and glycine produced no L-Arg (Figure 2-9).

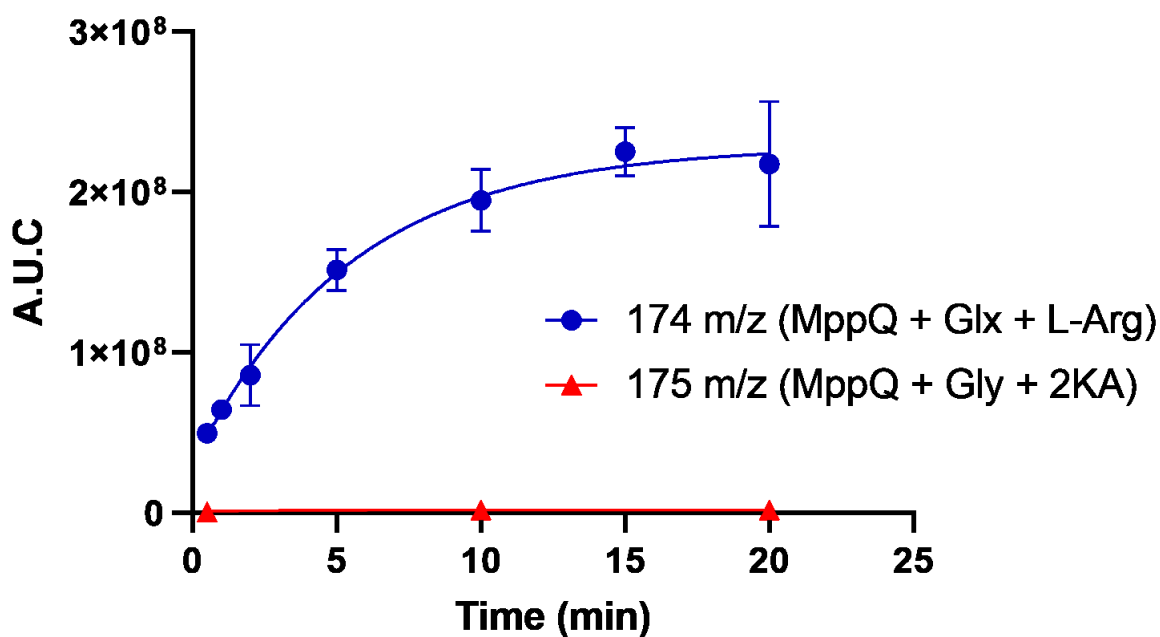


Figure 2-9. Production of 2KA (174 m/z) and lack of produced L-Arg (175 m/z) in reactions of MppQ with glyoxylate and glycine, respectively. The coupling partner in each reaction was **7**.

This is most likely due to glycine's lack of a side chain which makes it more difficult to be properly oriented for catalysis. Using MS-based end-point assays, different amino group donors were tested, and the best donor substrate was shown to be L-ornithine (Figure 2-10).

The fact that the sidechain of L-ornithine possesses a charged amine may explain its exceptional activity with MppQ as an amino group donor since MppQ's physiological substrate, **6**, possesses a positively charged iminoimidazolidine moiety.

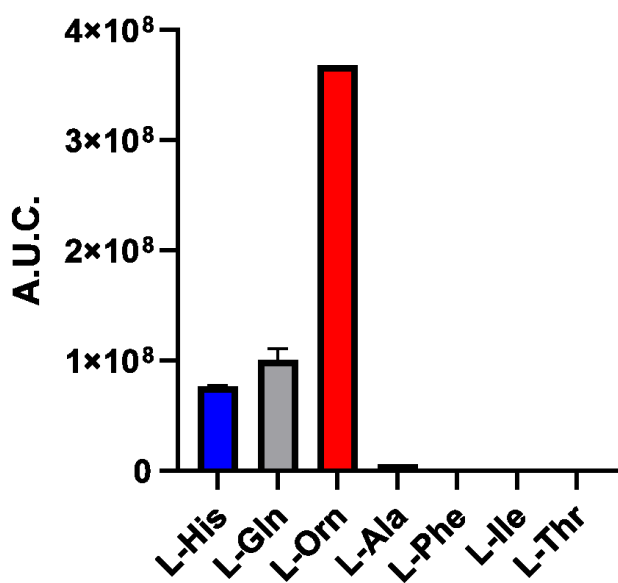


Figure 2-10. Reactivity of MppQ and 7 with various amino donor substrates.

Table 2-1. Crystallographic data collection and refinement statistics of MppQ-PLP and MppQ-PMP

	MppQ-PLP	MppQ-PMP
Data collection		
Space group	P 2 ₁ 2 ₁ 2 ₁	P 212121
Unit cell dimensions (Å)	47.7, 114.4, 133.3	47.7, 114.6, 133.4
Resolution (Å) ^a	44.08 - 1.74 (1.80-1.74)	38.82 - 1.64 (1.70-1.64)
R _{symm} ^b	0.093 (0.822)	0.058 (0.590)
R _{meas}	0.102 (0.899)	0.064 (0.672)
R _{pim}	0.041 (0.360)	0.029 (0.317)
CC _{1/2}	0.998 (0.729)	0.999 (0.798)
<I/σ(I)>	14.0 (2.1)	17.7 (2.2)
Completeness (%)	99.0 (97.2)	99.9 (99.0)
Multiplicity	5.8 (5.9)	4.9 (4.2)
No. of reflections	75,373 (3,677)	90,523 (4,415)
Wilson B-factor (Å ²)	17.0	16.9
Model Refinement		
R _{work} / R _{free} ^c	0.140 / 0.172	0.141 / 0.166
Ave. B factors (non-H atoms; Å ²) ^d	22.0	22.7
Protein	20.7 (5,902)	21.6 (5844)
PLP/PMP	15.4 (30)	16.8 (32)
Solvent	31.2 (816)	32.1 (698)
R.M.S. deviations		
Bond lengths (Å)	0.011	0.010
Bond angles (°)	1.41	1.42
Coordinate error (Å)	0.17	0.14
Ramachandran statistics		
Favored/allowed/outliers (%)	97.8/2.2/0.0	97.3/2.7/0.0
Rotamer outliers (%)	0.34	0.00
Clashscore	2.96	3.48
Number of TLS groups	8	7

^a Values in parenthesis relate to the highest-resolution shell.

^b R_{symm} = $\sum |I - \langle I \rangle| / \sum I$, where I is the observed intensity and $\langle I \rangle$ is the average intensity from multiple measurements.

^c R_{work} = $\sum |F_o| - |F_c| / \sum |F_o|$, for reflections contained in the working set. R_{free} is calculated in the same manner using data from the test set (2,000 reflections, 2.7% of the MppQ-PLP data set and 2.2% of the MppQ-PMP data set).

^d The average B factors reported are those calculated by phenix.model_vs_data and contain contributions from both local isotropic atomic vibrations and TLS motions.

2.4 References

1. Magarvey, N. A.; Haltli, B.; He, M.; Greenstein, M.; Hucul, J. A., Biosynthetic pathway for mannopeptimycins, lipoglycopeptide antibiotics active against drug-resistant gram-positive pathogens. *Antimicrob Agents Chemother* **2006**, *50* (6), 2167-77.
2. Fang, X.; Tiyanont, K.; Zhang, Y.; Wanner, J.; Boger, D.; Walker, S., The mechanism of action of ramoplanin and enduracidin. *Mol Biosyst* **2006**, *2* (1), 69-76.
3. Atkinson, D. J.; Naysmith, B. J.; Furkert, D. P.; Brimble, M. A., Enduracididine, a rare amino acid component of peptide antibiotics: Natural products and synthesis. *Beilstein J Org Chem* **2016**, *12*, 2325-2342.
4. Ruzin, A.; Singh, G.; Severin, A.; Yang, Y.; Dushin, R. G.; Sutherland, A. G.; Minnick, A.; Greenstein, M.; May, M. K.; Shlaes, D. M.; Bradford, P. A., Mechanism of action of the mannopeptimycins, a novel class of glycopeptide antibiotics active against vancomycin-resistant gram-positive bacteria. *Antimicrob Agents Chemother* **2004**, *48* (3), 728-38.
5. Goebel, N. Biosynthesis and modification of the antibiotic enduracidin. Oregon State University, Oregon State University, 2012.
6. Yin, X.; McPhail, K. L.; Kim, K. J.; Zabriskie, T. M., Formation of the nonproteinogenic amino acid 2S,3R-capreomycin by VioD from the viomycin biosynthesis pathway. *Chembiochem* **2004**, *5* (9), 1278-81.
7. Han, L.; Vuksanovic, N.; Oehm, S. A.; Fenske, T. G.; Schwabacher, A. W.; Silvaggi, N. R., Streptomyces wadayamensis MppP is a PLP-Dependent Oxidase, Not an Oxygenase. *Biochemistry* **2018**, *57* (23), 3252-3264.
8. Han, L.; Schwabacher, A. W.; Moran, G. R.; Silvaggi, N. R., Streptomyces wadayamensis MppP Is a Pyridoxal 5'-Phosphate-Dependent L-Arginine alpha-Deaminase, gamma-Hydroxylase in the Enduracididine Biosynthetic Pathway. *Biochemistry* **2015**, *54* (47), 7029-40.
9. Burroughs, A. M.; Hoppe, R. W.; Goebel, N. C.; Sayyed, B. H.; Voegtline, T. J.; Schwabacher, A. W.; Zabriskie, T. M.; Silvaggi, N. R., Structural and functional characterization of MppR, an enduracididine biosynthetic enzyme from streptomyces hygrosopicus: functional diversity in the acetoacetate decarboxylase-like superfamily. *Biochemistry* **2013**, *52* (26), 4492-506.
10. Eliot, A. C.; Kirsch, J. F., Pyridoxal phosphate enzymes: mechanistic, structural, and evolutionary considerations. *Annu Rev Biochem* **2004**, *73*, 383-415.
11. Chon, H.; Matsumura, H.; Koga, Y.; Takano, K.; Kanaya, S., Crystal structure of a human kynurenine aminotransferase II homologue from Pyrococcus horikoshii OT3 at 2.20 Å resolution. *Proteins* **2005**, *61* (3), 685-8.
12. Battye, T. G.; Kontogiannis, L.; Johnson, O.; Powell, H. R.; Leslie, A. G., iMOSFLM: a new graphical interface for diffraction-image processing with MOSFLM. *Acta Crystallogr D Biol Crystallogr* **2011**, *67* (Pt 4), 271-81.
13. Evans, P., Scaling and assessment of data quality. *Acta Crystallogr D Biol Crystallogr* **2006**, *62* (Pt 1), 72-82.
14. Otwinowski, Z.; Minor, W., Processing of X-ray diffraction data collected in oscillation mode. *Methods Enzymol* **1997**, *276*, 307-26.
15. Winn, M. D.; Ballard, C. C.; Cowtan, K. D.; Dodson, E. J.; Emsley, P.; Evans, P. R.; Keegan, R. M.; Krissinel, E. B.; Leslie, A. G.; McCoy, A.; McNicholas, S. J.; Murshudov, G. N.; Pannu, N. S.; Potterton, E. A.; Powell, H. R.; Read, R. J.; Vagin, A.; Wilson, K. S., Overview of the CCP4 suite and current developments. *Acta Crystallogr D Biol Crystallogr* **2011**, *67* (Pt 4), 235-42.
16. Adams, P. D.; Afonine, P. V.; Bunkoczi, G.; Chen, V. B.; Davis, I. W.; Echols, N.; Headd, J. J.; Hung, L. W.; Kapral, G. J.; Grosse-Kunstleve, R. W.; McCoy, A. J.; Moriarty, N. W.; Oeffner, R.; Read, R.

- J.; Richardson, D. C.; Richardson, J. S.; Terwilliger, T. C.; Zwart, P. H., PHENIX: a comprehensive Python-based system for macromolecular structure solution. *Acta Crystallogr D Biol Crystallogr* **2010**, *66* (Pt 2), 213-21.
17. Afonine, P. V.; Mustyakimov, M.; Grosse-Kunstleve, R. W.; Moriarty, N. W.; Langan, P.; Adams, P. D., Joint X-ray and neutron refinement with phenix.refine. *Acta Crystallogr D Biol Crystallogr* **2010**, *66* (Pt 11), 1153-63.
 18. Emsley, P.; Cowtan, K., Coot: model-building tools for molecular graphics. *Acta Crystallogr D Biol Crystallogr* **2004**, *60* (Pt 12 Pt 1), 2126-32.
 19. Emsley, P.; Lohkamp, B.; Scott, W. G.; Cowtan, K., Features and development of Coot. *Acta Crystallogr D Biol Crystallogr* **2010**, *66* (Pt 4), 486-501.
 20. Meister, A., Enzymatic preparation of alpha-keto acids. *J Biol Chem* **1952**, *197* (1), 309-17.
 21. Stalon, V.; Mercenier, A., L-arginine utilization by *Pseudomonas* species. *J Gen Microbiol* **1984**, *130* (1), 69-76.
 22. Krissinel, E.; Henrick, K., Secondary-structure matching (SSM), a new tool for fast protein structure alignment in three dimensions. *Acta Crystallogr D Biol Crystallogr* **2004**, *60* (Pt 12 Pt 1), 2256-68.
 23. Schneider, G.; Kack, H.; Lindqvist, Y., The manifold of vitamin B6 dependent enzymes. *Structure* **2000**, *8* (1), R1-6.
 24. Kwon, S.; Park, H. H., Structural Consideration of the Working Mechanism of Fold Type I Transaminases From Eubacteria: Overt and Covert Movement. *Comput Struct Biotechnol J* **2019**, *17*, 1031-1039.
 25. Okamoto, A.; Higuchi, T.; Hirotsu, K.; Kuramitsu, S.; Kagamiyama, H., X-ray crystallographic study of pyridoxal 5'-phosphate-type aspartate aminotransferases from *Escherichia coli* in open and closed form. *J Biochem* **1994**, *116* (1), 95-107.
 26. Evgeny Krissinel, K. H., Multiple Alignment of Protein Structures in Three Dimensions. *Computational Life Sciences* **2005**, *3695*, 67-78.
 27. Goto, M.; Omi, R.; Miyahara, I.; Hosono, A.; Mizuguchi, H.; Hayashi, H.; Kagamiyama, H.; Hirotsu, K., Crystal structures of glutamine:phenylpyruvate aminotransferase from *Thermus thermophilus* HB8: induced fit and substrate recognition. *J Biol Chem* **2004**, *279* (16), 16518-25.
 28. Okada, K.; Angkawidjaja, C.; Koga, Y.; Takano, K.; Kanaya, S., Characteristic features of kynurenine aminotransferase allosterically regulated by (alpha)-ketoglutarate in cooperation with kynurenine. *PLoS One* **2012**, *7* (7), e40307.

Chapter 3

Engineering a more specific *E. coli* glyoxylate/hydroxypyruvate reductase for coupled steady state kinetics assays

3.1 Introduction

The non-proteinogenic amino acid L-enduracididine (Figure 3-1, **5**) is a component of several non-ribosomally produced peptide natural products, including the antibiotic mannopeptimycin.¹ As a part of our work on L-enduracididine biosynthesis,²⁻⁴ it became necessary to develop a coupled assay to measure the kinetics of the putative 2-ketoenduracididine aminotransferase MppQ. In addition to its proposed role in the last step of L-enduracididine biosynthesis, MppQ is also capable of returning the dead-end product 2-ketoarginine (Figure 3-1, **3**) back to the starting material, L-Arg. Preliminary experiments showed that, in reactions with L-Arg and a selection of amino acceptor substrates (*e.g.* glyoxylate, pyruvate, oxaloacetate and α -ketoglutarate, Scheme 1), MppQ was most efficient using glyoxylate as the acceptor substrate (manuscript in preparation). This led to the idea that, in the more biosynthetically relevant transamination of 2-ketoenduracididine or 2-ketoarginine to the corresponding amino acids, glycine would be an efficient amino donor substrate. Since these reactions would result in the production of glyoxylate, we selected GhrA from *E. coli* (EcGhrA) as a potential coupling enzyme in a spectrophotometric assay for the transamination of 2-ketoarginine or 2-ketoenduracididine and glycine. This particular enzyme was

chosen over other enzymes previously used in assays of glyoxylate-producing reactions, such as porcine L-lactate dehydrogenase or the glyoxylate reductase from *Spinacea oleracea*,⁵ because it could be produced very efficiently and inexpensively in house.

The D-2-hydroxyacid dehydrogenases (2HAD) family contains enzymes with diverse substrate affinities that show significant potential for use in the industrial synthesis of chiral D-2-hydroxy acids.⁶ Members of the 2HAD family are known to be promiscuous, and EcGhrA also catalyzes the reduction of 2-hydroxypyruvate.⁷ Surprisingly, the promiscuity of EcGhrA extended to the much larger and positively charged 2-ketoarginine, which would, of course, preclude its use in monitoring the reaction we wished to study.

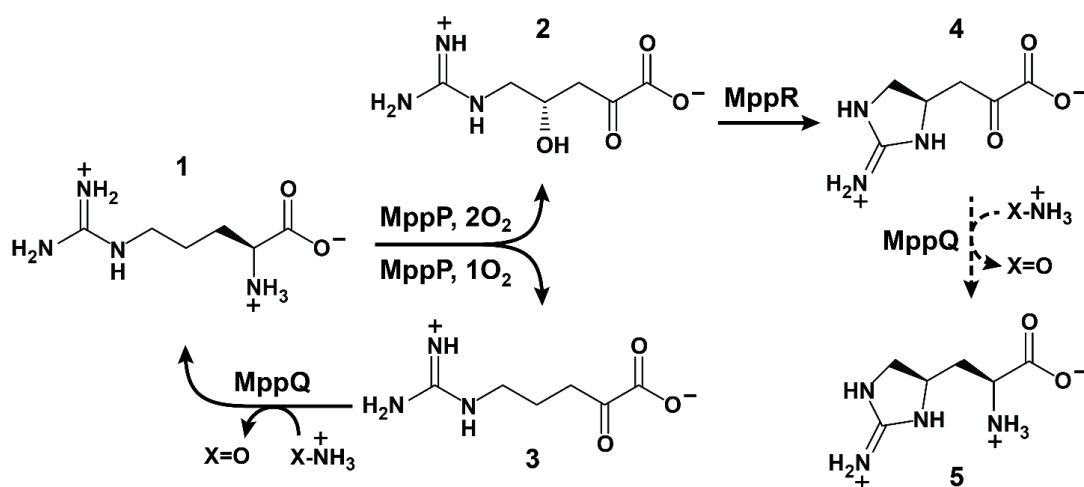
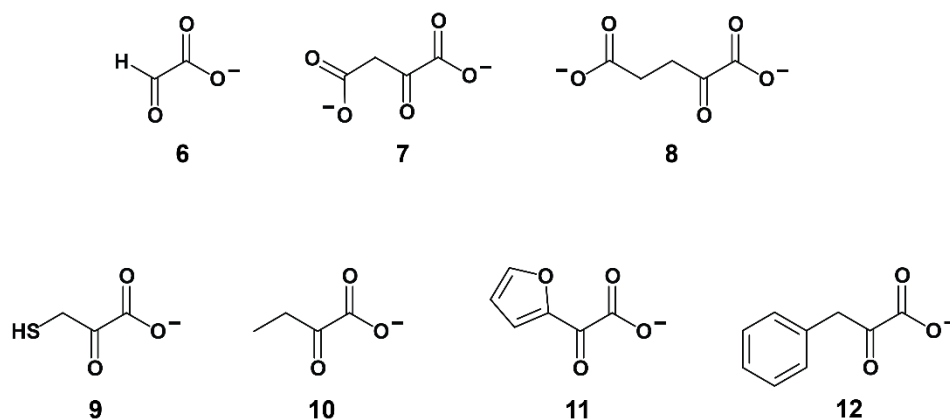


Figure 3-1. The L-enduracididine biosynthetic pathway begins with L-arginine (1), which is oxidized by the unusual PLP-dependent L-Arg oxidase, MppP, to 4(R)-hydroxy-2-ketoarginine (2). MppP, at least in vitro, releases the partially oxidized dead-end product 2-ketoarginine (3) in about 40% of catalytic cycles. The oxidized arginine derivative 2 is cyclized by MppR to create the iminoimidazolidine ring of the intermediate 4 (i.e. 2-ketoenduracididine). MppQ is thought to catalyze the transamination of 4 with an as-yet-unidentified amino donor substrate to yield the finished amino acid L-enduracididine (5). MppQ also catalyzes the transamination of the dead-end product 3 to regenerate L-Arg, though it has not been ascertained if this is a physiologically relevant catalytic activity or an adventitious in vitro phenomenon.



Scheme 3-1. *EcGhrA* substrates investigated in this work.

This observation led us to wonder what other α -keto acids are substrates for EcGhrA. The substrate specificities of other GhrA homologs have been examined and it was found that oxaloacetate is a substrate for the *Euglena gracilis*⁸ and *Saccharomyces cerevisiae*⁹ enzymes, succinic semialdehyde is a substrate for the *Arabidopsis thaliana* homolog¹⁰, *Neurospora crassa* GhrA reacts with phenylpyruvate¹¹ and α -ketoglutarate is a slow substrate for the *E. gracilis* GhrA⁸. To extend the knowledge of EcGhrA promiscuity, we investigated additional α -keto acids (Scheme 3-1, 7-12) that, to our knowledge, have not been tested previously. The results of these studies (*vide infra*) together with the structural work described herein suggested that it might be possible engineer an EcGhrA variant with increased specificity for glyoxylate in order to develop a suitable coupling enzyme for use in future steady state kinetics work.

Rational engineering of 2HAD enzymes to alter substrate specificity has been described in the literature. In 2007, Shinoda et al. transformed formate dehydrogenase into a glyoxylate reductase by mutating two catalytic residues¹². In 2013, Zhen et al. rationally engineered D-lactate dehydrogenase to reduce phenylpyruvic acid, α -ketobutyric acid, α -ketovaleric acid, and α -hydroxypyruvic acid via a single Y52L mutation.¹³ At the time of this writing, rational engineering of a GhrA homolog to make it more specific for glyoxylate has not been attempted.

Herein we describe the crystal structures of wild-type EcGhrA in ternary complexes with NADP⁺ and either glyoxylate or **3** that were the basis of our (ir)rational design of a more specific glyoxylate reductase. These structures suggested that making a limited number of mutations near the outer edge of the active site could reduce the affinity of EcGhrA for **3**. Steady state kinetics of the wild-type and variant EcGhrA enzymes shows that a single mutation, W45F, leads to a 10-fold decrease in the specificity constant (k_{cat}/K_M) for **3**. This new variant of EcGhrA may be useful for studying the kinetics of glyoxylate-producing enzymes where the promiscuity of the wild-type EcGhrA is problematic.

3.2 Materials and Methods

Cloning, expression and purification of wild-type and mutant EcGhrA

The EcGhrA gene was amplified from *E. coli* genomic DNA using primers containing NdeI and BamHI restriction sites (underlined; forward, 5'-GGATTCCCATATGGAAACCTGTATTTTCAGGGTATGGATATCATCTTTTATCACCCAA-3'; reverse, 5'-CGGGATCCTTAGTAGCCGCGTGCGC-3'). The forward primer also encoded a tobacco etch virus (TEV) protease cleavage site (*italic*, MENLYFQG). The PCR reaction was carried out using Phusion PCR High Fidelity PCR Master Mix (Thermo Scientific) and the genomic DNA was extracted from *E. coli* BL21 Star (DE3) (Invitrogen) using genomic the Blood and Cell Culture DNA mini kit (Qiagen). The amplified PCR product was digested in one step using NdeI and BamHI HF (New England Biolabs) and ligated into similarly treated pET-15b to create plasmid pET15b-EcGhrA. Site-directed mutagenesis to create the EcGhrA^{W45F} variant was performed using the Q5 Site-Directed Mutagenesis Kit (New England Biolabs) using the

mutagenic primers 5'-TGCTTTAGTCTTTTCATCCTCCTG-3' (forward) and 5'-TAATCAGCAGAGTCATTATC-3' (reverse).

The His₆-tagged wild-type EcGhrA was expressed from *E. coli* BL21 Star (DE3) cells carrying the pET15b-EcGhrA plasmid grown at 37 °C in Luria-Bertani broth with 100 µg/mL ampicillin. Protein expression was induced with 0.4 mM IPTG when the OD_{600nm} reached 0.6. The temperature was reduced to 25 °C and the cells were grown overnight with shaking at 250 rpm. Cells were harvested via centrifugation and resuspended in 5 mL of buffer A [25 mM TRIS (pH 8.0), 300 mM NaCl, 10 mM imidazole] containing 0.1 mg/mL Dnase I (Worthington Biochemical Corp.) per gram of wet cell paste. Cells were lysed using a Branson Sonifier S-450 cell disruptor (Branson Ultrasonics Corp.) at 60% amplitude with 30 s pulses separated by 50 s rest periods for a total of 10 min of sonication. The temperature of the lysate was maintained below 4 °C by keeping the steel beaker suspended in an ice bath over a stir bar. The lysate was clarified via centrifugation at 39,000 x g for 45 min before loading it onto a 5 mL HisTrap column (GE Lifesciences) and the His₆-tagged protein was purified using a 4-step gradient of increasing concentrations of Buffer B [25 mM TRIS (pH 8.0), 300 mM NaCl, and 250 mM imidazole; 5 column volumes each at 5, 15, 50, and 100% B]. The elution was monitored spectroscopically at 280 nm. His₆-EcGhrA eluted at 50% Buffer B, and these fractions were collected and analysed using Coomassie-stained SDS-PAGE. In order to remove the His₆ tag, the pooled fractions were dialyzed overnight against 10 µM TEVpM2 (an optimized TEV protease variant)¹⁴ in 50 mM TRIS (pH 8.0), 100 mM NaCl, 1 mM DTT, and 0.25 mM EDTA at 4 °C. The dialysate was passed through the same HisTrap column, but less than 10% of the protein had the His₆ tag removed. The protein was desalted into 10 mM HEPES pH 7.5, 1 mM DTT, by dialyzing overnight at 4 °C. EcGhrA^{W45F} was expressed and purified in the same manner as the wild type EcGhrA.

EcGhrA Steady state enzyme kinetics

The initial velocities of wild-type and mutant EcGhrA-catalyzed reduction of varied concentrations of glyoxylate, and concomitant oxidation of NADPH, under steady state conditions were monitored at 340 nm ($\epsilon_{340\text{nm}} = 6220 \text{ M}^{-1}\text{cm}^{-1}$) using a Shimadzu UV-2600 double beam UV-visible spectrophotometer. All the reactions were carried out in triplicate under identical conditions. The enzyme (0.5 μM) was incubated with NADPH (200 μM) for 30 seconds in 50 mM HEPES, pH 7.5 at 22 °C before initiating the reaction by the addition of substrate. The substrate concentrations ranged from 0.2 to 40 mM for **6** and **3**, 0.6 to 40 mM for **7** and **8**.

The steady state kinetic constants for the reactions with evidence of substrate inhibition (e.g. wild-type EcGhrA with **6**) were estimated by fitting the initial velocity vs substrate concentration data to Equation 1:

Equation 1
$$v_o = \frac{V_{\max}S}{K_M + S(1 + \frac{S}{K_i})}$$

where v_o is the initial velocity, V_{\max} is the maximum velocity, S is the substrate concentration, K_M is the Michaelis constant, and K_i is the inhibition constant for reversible substrate inhibition. Reactions showing no evidence of substrate inhibition were analyzed using the standard Michaelis-Menten equation (Equation 2):

Equation 2
$$v_o = \frac{V_{\max}S}{K_M + S}$$

Crystallization of the EcGhrA·NADP⁺ binary complex and EcGhrA·NADP⁺·6 ternary complex

Diffraction quality crystals were obtained after screening 16.6 mg/mL EcGhrA against the Index HT screen (Hampton Research). The optimized crystallization buffer consisted of 1.26 M sodium phosphate monobasic monohydrate, 0.14 M potassium phosphate dibasic, pH 5.6, and 1.8 mM

NADP⁺. Hanging drop vapor diffusion experiments were initiated by mixing 1 μ L of ~16 mg/mL wild-type EcGhrA in 10 mM HEPES pH 7.5, 1 mM DTT with 1 μ L of the crystallization solution on a siliconized glass cover slip and sealing this above a well containing 500 μ L of the crystallization solution in a 24-well VDX plate (Hampton Research). Hexagonal prisms of approximate dimensions 200 x 50 x 50 μ m formed after 1 day. For the binary complex, crystals were cryo-protected by a brief soak in the crystallization buffer supplemented with 20 % glycerol. For the ternary complex, crystals were soaked overnight in 10 μ L of crystallization solution containing 100 mM sodium glyoxylate and 5 mM NADP⁺. Substrate-soaked crystals were prepared for flash-cooling by soaking them briefly in the same solution supplemented with 20 % glycerol before being plunged into liquid nitrogen.

Crystallization of the ternary complexes of EcGhrA with NADP⁺ and **3** or **8**

Since we have determined that phosphate significantly inhibits EcGhrA activity at the concentrations used for crystallization (data not shown), and is therefore likely to compete with the substrate in binding to the active site, we identified an alternative, phosphate-free crystallization condition. After optimization of another condition from the initial Index HT screen, diffraction quality crystals were obtained from hanging drop vapor diffusion experiments where the well solution consisted of 17% PEG 3350, 0.2 lithium sulfate, 0.1 M BIS-TRIS, pH 5.5, and 1.8 mM NADP⁺. The crystals were soaked overnight in 10 μ L of a solution containing 50 mM **3**, 5 mM NADP⁺, 30% PEG 3350, 0.2 M lithium sulfate, and 0.1 M BIS-TRIS, pH 5.5. Paratone N (Hampton Research) was used to cryo-protect the crystals before being flash-cooled plunging in liquid nitrogen.

Crystallization of EcGhrA^{W45F} with NADP⁺

Diffraction quality crystals were obtained from the initial LMB screen at 295 K, in a sitting drop vapor diffusion experiment where the well solution consisted of 16% PEG 4000, 0.1 ammonium sulfate, 0.1 M sodium citrate, pH 5.8, 20% glycerol and 1 mM NADP⁺. The crystals were taken directly out a drop and flash-cooled by plunging in liquid nitrogen, without further cryo-protection since glycerol was present in the crystallization mixture.

Data collection and structure solution

X-Ray diffraction data for the EcGhrA·NADP⁺·**6** ternary complex and EcGhrA·NADP⁺·**8** ternary complex were collected at the Life Sciences Collaborative Access Team (LS-CAT) beamline 21-ID-F at the Advanced Photon Source (APS). The crystal-to-detector distances for the EcGhrA·NADP⁺·**6** ternary complex and EcGhrA·NADP⁺·**8** ternary complex were 215 and 300 mm, respectively. Diffraction data for the EcGhrA·NADP⁺·**3** ternary complex and the EcGhrA·NADP⁺ binary complex were collected using LS-CAT beamline 21-ID-G. Both beamlines were equipped with MAR 300 CCD detectors and 50 x 50 μm beams at wavelengths of 0.97872 Å and 0.97856 Å, respectively. In all cases, data were collected for full 180 ° oscillations of the crystals in 0.5° increments exposed for 1.0 s each. The crystal-to-detector distances for the EcGhrA·NADP⁺·**3** ternary complex and the EcGhrA·NADP⁺ binary complex were 250 and 260 mm, respectively. The data for EcGhrA^{W45F}·NADP⁺ binary complex was collected on LS-CAT beamline 21-ID-D. This beamline was equipped with Dectris Eiger 9M detector and 50 x 50 μm beam at wavelength of 1.12723 Å. A total of 900 frames were collected from φ = 0 to 180 °, 5 %/sec, 5 images collected per degree, at detector distance of 200 mm. All X-ray diffraction data sets were indexed, integrated and scaled using HKL2000¹⁵.

Initial phase estimates for all five structures were determined by molecular replacement in PHASER¹⁶ as implemented in the CCP4¹⁷ suite. The structure of the binary complex of EcGhrA with NADP⁺ was determined using the coordinates of chain A of GhrA from *Salmonella typhimurium* (PDB ID 3KBO, unpublished) as the search model, with all non-protein atoms removed and all isotropic B-factors set to 20 Å². After refinement of this model (see below), it was used as the search model for phasing the three ternary complex structures and the EcGhrA^{W45F} structure. The EcGhrA·NADP⁺ structure was prepared for molecular replacement by removing all hydrogen atoms, solvent molecules, and NADP⁺ and setting all isotropic B-factors to 20.0 Å². Model refinement was performed using phenix.refine from the PHENIX suite^{18, 19} and model building was done with COOT^{20, 21}. Iterative rounds of model building and refinement were done until the R-factors converged, at which point the substrates were modeled into the ternary complex structures. The optimal number of translation-libration-screw (TLS) groups was determined using phenix.find_tls_groups (P. V. Afonine, unpublished). The final models were validated using MolProbity²², as implemented in the PHENIX suite. Residues lacking defined electron density for the sidechain were modeled without the sidechains in order to avoid interpretational bias. The geometric restraints for **3** were calculated using phenix.elbow²³. The restraints for NADP⁺, **6**, and **8** distributed with the CCP4 package were used in their respective refinements. The model refinement statistics as well as data collection parameters are listed in Table 3-1. Coordinates have been deposited in the Protein Data Bank, and the accession codes for each structure are also given in Table 3-1.

3.3 Results and Discussion

Structure determination of EcGhrA with NADP⁺ alone and in the presence of α -keto acid substrates.

Since there were no crystal structures of the *E. coli* glyoxylate/hydroxypyruvate reductase available, we began by determining the structure of the EcGhrA·NADP⁺ complex. This form of the enzyme crystallized with two molecules per asymmetric unit arranged as a homodimer (Figure 3-2A) as observed in the structures of homologous glyoxylate/hydroxypyruvate reductases^{24, 25}. GhrA homologs from other organisms are known to be active as homodimers^{26, 27}. Both the overall fold (Figure 3-2A) and active site architecture of EcGhrA are very similar to those of enzymes like *Sinorhizobium meliloti* GhrA (PDB ID 5UOG²⁴) and *Pyrococcus furiosus* GhrA (PDB ID 5AOV²⁷). The main differences lie in the conformations of the dimerization loops (residues 111-136, EcGhrA numbering) and the C-terminal section beginning at residue 296.

The question driving this work—can we generate an EcGhrA variant that does not accept α -keto acids having large side chains (*e.g.* **8** and **3**) without abrogating activity with glyoxylate (**6**)—demanded that we determine how **6**, **8**, and **3** bind to the wild-type enzyme by determining structures of the ternary complexes of EcGhrA with NADP⁺ and **3** or **6**. A challenge we encountered in this effort was that the crystallization conditions identified via high-throughput screening invariably contained high concentrations of phosphate, sulfate, or tartrate salts. We have observed that, at high concentrations, phosphate significantly inhibits EcGhrA activity (data not shown). Phosphate can be observed bound to R227 in the structure of the binary complex of EcGhrA with NADP⁺, and thus these ions likely prevent binding of substrates. To solve this problem, we sequentially soaked crystals in solutions containing increasing concentrations of PEG 3350% and decreasing concentrations of salt to back-soak salts from of the active site. These back-soaked crystals were subsequently soaked with the substrates **6**, **8**, and **3**. While the treatment did

reduce the concentration of competing salts enough for us to determine the structures of several ternary EcGhrA complexes, some salt remained. The partial occupancies of phosphate or sulfate in these structures complicated the electron density for the α -keto acid moieties of **6**, **8**, and **3** which was, in all three cases, not fully planar as would be expected for 2-keto acids (see below; Figure 3-3, Figure 3-4).

The EcGhrA·NADP⁺·**6** ternary complex structure (Figure 3-3A) was determined to elucidate the binding mode of the preferred substrate, glyoxylate. The amides of A65 and G66 mainchain form hydrogen bonds with the carboxylic moiety, properly positioning it in the active site. The ketone is positioned 3.5 Å above the nicotinamide ring of NADP⁺. When reacted with NADPH, this allows for hydride transfer via nucleophilic attack on carbonyl carbon, followed by deprotonation of H275. Carbonyl group of **6** also hydrogen bonds to R227, ensuring proper substrate orientation (Figure 3-3C).

The structure of the ternary complex between EcGhrA, NADP⁺, and α -ketoglutarate (**8**) shows well defined electron density for **8** near the nicotinamide ring of NADP⁺, in the same position occupied by glyoxylate in the structure of the EcGhrA·NADP⁺·**6** complex (Figure 3-4). The α -keto acid makes the same interactions observed in the complex with glyoxylate: the carboxylic acid forms hydrogen bonding interactions with the mainchain amides of A65 and G66, the guanidinium group of R227 bridges the carboxylate and ketone groups, and the imidazole group of H275 forms a hydrogen bonding interaction with the ketone of **8**. Interestingly, there is no clear indication from the structure why the activity with **8** is so much lower than the activity against glyoxylate. Likely this difference in reactivity has more to do with differences in the equilibrium of the keto-enol tautomerization in these two substrates.

The crystal structure of the EcGhrA·NADP⁺·**3** ternary complex was the most important with respect to informing our efforts to engineer EcGhrA to *not* accept **3** as a substrate. The structure shows that the keto acid moiety of **3** overlays quite well with glyoxylate from the EcGhrA·NADP⁺·**6** ternary complex. Surprisingly, the guanidinium group of **3** makes no clear contacts with the enzyme. While the guanidinium group of **3** is well defined in the electron density, there is little or no density for the methylene carbon atoms of the side chain. This suggests that there is considerable mobility in the side chain and binding is mediated primarily by the interactions of the α -keto acid moiety with the main chain amides of A65 and G66, and the side chains of R227 and H275 (Figure 3-3B,D). It should be noted that even these ternary complex structures appear to be “open” when compared to those of other EcGhrA homologs with substrates bound. It is conceivable that the indole nitrogen atom of W45 and/or the imidazole group of H46 could make strong contacts with the side chain of **3** if the substrate-binding domain were fully closed. The tryptophan would likely interact with the charged guanidinium group solely via cation- π interaction^{28, 29}, while the histidine could accept a hydrogen bond from the protonated nitrogen atoms of the guanidinium group of **3**. Based mostly on the possibility that these two residues are important for binding in a presumed “closed” conformation of EcGhrA, we set out to generate the W45F and W45F/H46S variants of the enzyme.

Substrate specificity of EcGhrA.

The kinetics of glyoxylate reduction catalyzed by wild-type EcGhrA was studied first to establish a basis of comparison with other, more thoroughly characterized, GhrA homologs. EcGhrA exhibits a strong preference for NADPH over NADH (data not shown), so all kinetic analyses were done in the presence of saturating (200 μ M) NADPH. The k_{cat} value for the reaction

of EcGhrA with glyoxylate (40.0 ± 23.0 ; Table 3-2) is similar to the values reported for the reaction of the *Homo sapiens* and *A. thaliana* homologs (27.0 and 25.5 s^{-1} , respectively)^{30, 31}. The K_M value for glyoxylate ($2.2 \pm 1.7 \text{ mM}$) was significantly different from those observed for the *H. sapiens* and *A. thaliana* enzymes (0.24 mM and $34 \text{ }\mu\text{M}$, respectively)^{30, 31}. This difference may reflect differences in the structures and activities of these enzymes, or it may result from the acute substrate inhibition we observed (Figure 3-5; $K_I = 1.5 \pm 1.1 \text{ mM}$). The simple modified Michaelis-Menten equation (Equation 1) used to fit these data resulted in poor fits, as evidenced by the large standard uncertainties on the kinetic parameters. However, more nuanced models with additional parameters either failed to converge or resulted in absurdly large standard uncertainties.

Unlike glyoxylate (**6**), 2-ketoarginine (**3**) showed no sign of substrate inhibition. The turnover number for the reaction of EcGhrA with **3** ($6.6 \pm 0.4 \text{ s}^{-1}$) is only 6-fold lower than that for **6** and the K_M value for **3** is only 4-fold higher than that for **6**. The ratio of the pseudo-second order rate constants for **6** and **3** is 24 ± 4 , giving some quantitative idea of the relative preference of EcGhrA for these two substrates.

We used this ratio as a “selectivity factor” to compare the other substrates tested here (Table 3-2). Of compounds **7** – **12**, only oxaloacetate (**7**) and α -ketoglutarate (**8**) proved to be substrates for the enzyme. Oxaloacetate is nearly as efficient a substrate as **6**, and shows some evidence of substrate inhibition, though it is very weak ($K_I^7 = 52 \pm 15$). The turnover number for **7** ($1.9 \pm 0.1 \text{ s}^{-1}$) is approximately 20-fold lower than k_{cat}^6 ; K_M^6 is roughly half of the K_M for **6**. The selectivity factor for oxaloacetate is only 13 ± 3 , which underscores the similar catalytic efficiencies of oxaloacetate and glyoxylate. Conversely, α -ketoglutarate is a much poorer substrate, having a selectivity factor of 266 ± 50 . With a K_M value only twice that for **6**, most of the difference between **8** and **6** comes in the turnover number. The value of k_{cat}^8 (0.3 ± 0.02) is approximately 130-fold

lower than the turnover number for glyoxylate. The K_M values for **8** and **3** are not significantly different, which is consistent with the close agreement between the positioning of **6** and **8** in the crystal structures.

The W45F variant of EcGhrA is more selective for glyoxylate.

The W45F and H46S mutations were chosen as the most conservative changes that would still disrupt any potential interactions with substrate **3**. The W45F and W45F/H46S variants both expressed and purified similarly to the wild-type enzyme. There was no indication that mutation(s) had any effect on the stability of the enzyme. Steady state kinetic studies of both variants showed that the double mutant W45F/H46S did not behave differently from the single W45F variant. Therefore, only the W45F variant will be discussed here. EcGhrA^{W45F} exhibited a roughly 10-fold decrease in k_{cat}/K_M for **3**, while the k_{cat}/K_M for **6** turned out to be statistically within the range of the values for the wild-type (Table 3-2). Thus, the W45F mutation somewhat decreased the catalytic efficiency of the reaction with **3**, while leaving the reaction with **6** essentially untouched. The selectivity factor for **6** with respect to **3** increased 5-fold for the mutant (119 vs 24 for the wild-type). It is also important to mention that the K_M values for both **6** and **3** are likely overestimates, since **6** exists predominantly in a hydrated gem-diol form³², while **3** is in equilibrium with the cyclic pyrrolidine-1-amidino-2-hydroxy-2-carboxylic acid³³.

The crystal structure of the single mutant showed no conformational changes of the mutated residues, or the catalytic residues R227 and H275 (Figure 3-6), suggesting that the substrate binding modes remain unchanged. We have also tested whether additional mutation of His46 to Ser46 had any additional effect on substrate specificity, but this double mutant did not lead to any enhancement over the EcGhrA^{W45F}. These site-directed mutations suggest that implementing

minimal perturbations to the active site can lead to a significant improvement in substrate specificity of EcGhrA.

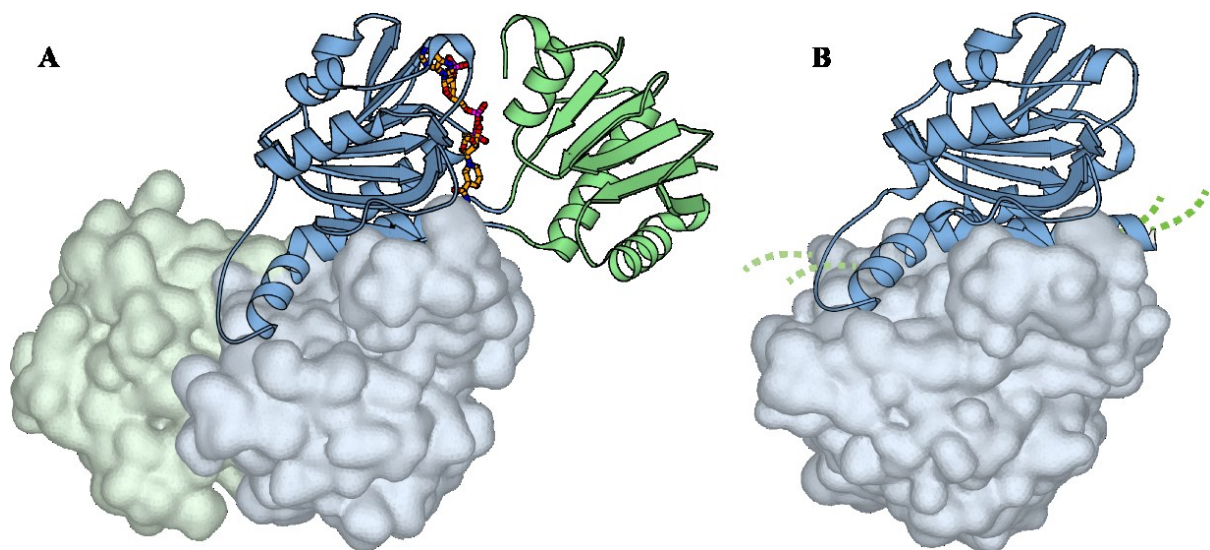


Figure 3-2. EcGhrA is active as a dimer of 35 kDa protomers as shown in (A). One protomer is shown in cartoon representation, and the other as a solvent-accessible surface. Each protomer is comprised of two domains: a nucleotide binding domain (blue) and a substrate binding domain (green). In the absence of NADP(H), the substrate binding domain is disordered (B). This figure was generated using the POVSCRIPT+ modification of MOLSCRIPT^{34, 35}

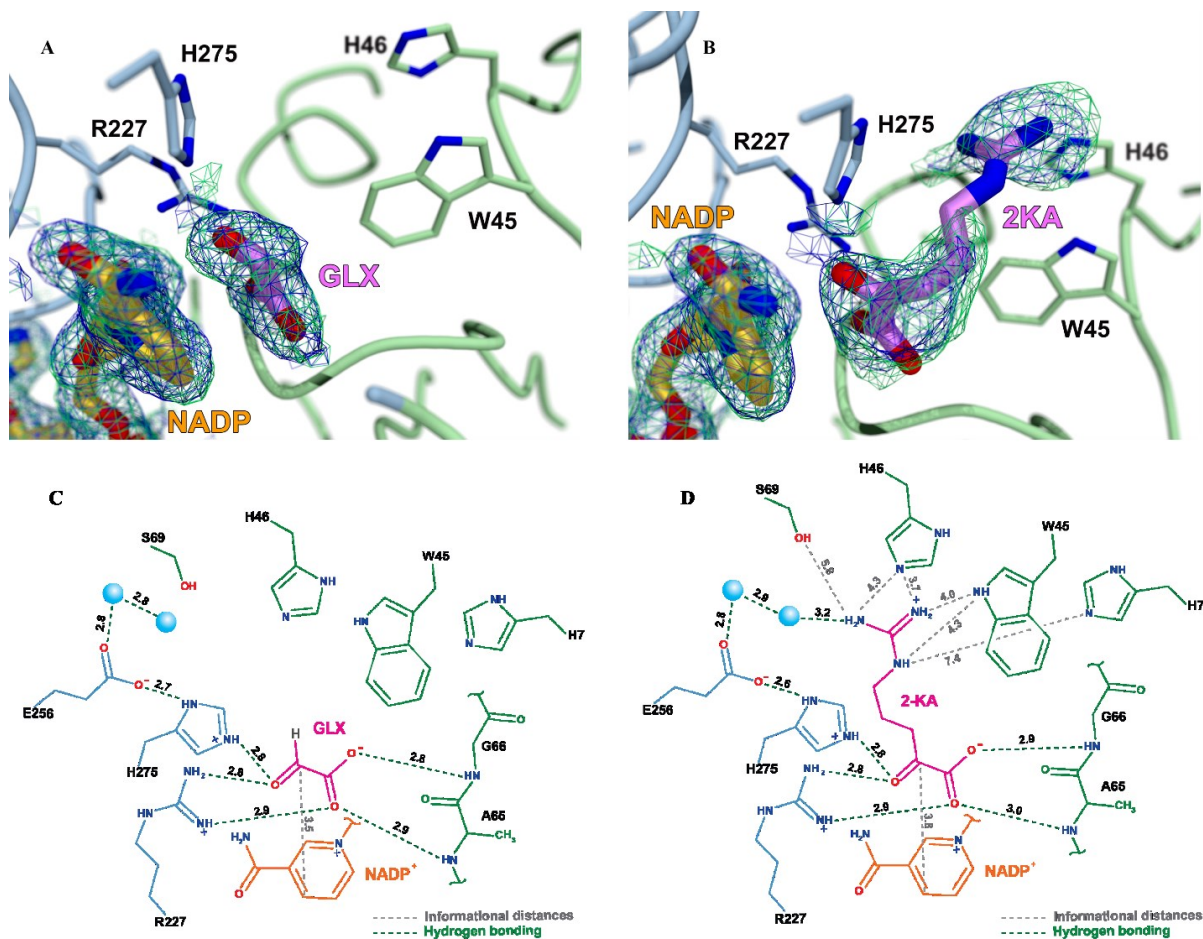


Figure 3-3. The view of EcGhrA active site with glyoxylate (A) and 2-ketoarginine (B) bound. The $2|F_o| - |F_c|$ electron density map contoured at 1.0σ is shown as blue mesh, and the $2|F_o| - |F_c|$ composite omit map, also contoured at 1.0σ , is shown as green mesh. The (A) and (B) were prepared using the POVSCRIPT+ modification of MOLSCRIPT. The 3D views were displayed in 2D in (C) and (D) to clearly show distances between ligands and the active site residues. All distances were calculated using tools provided in COOT.

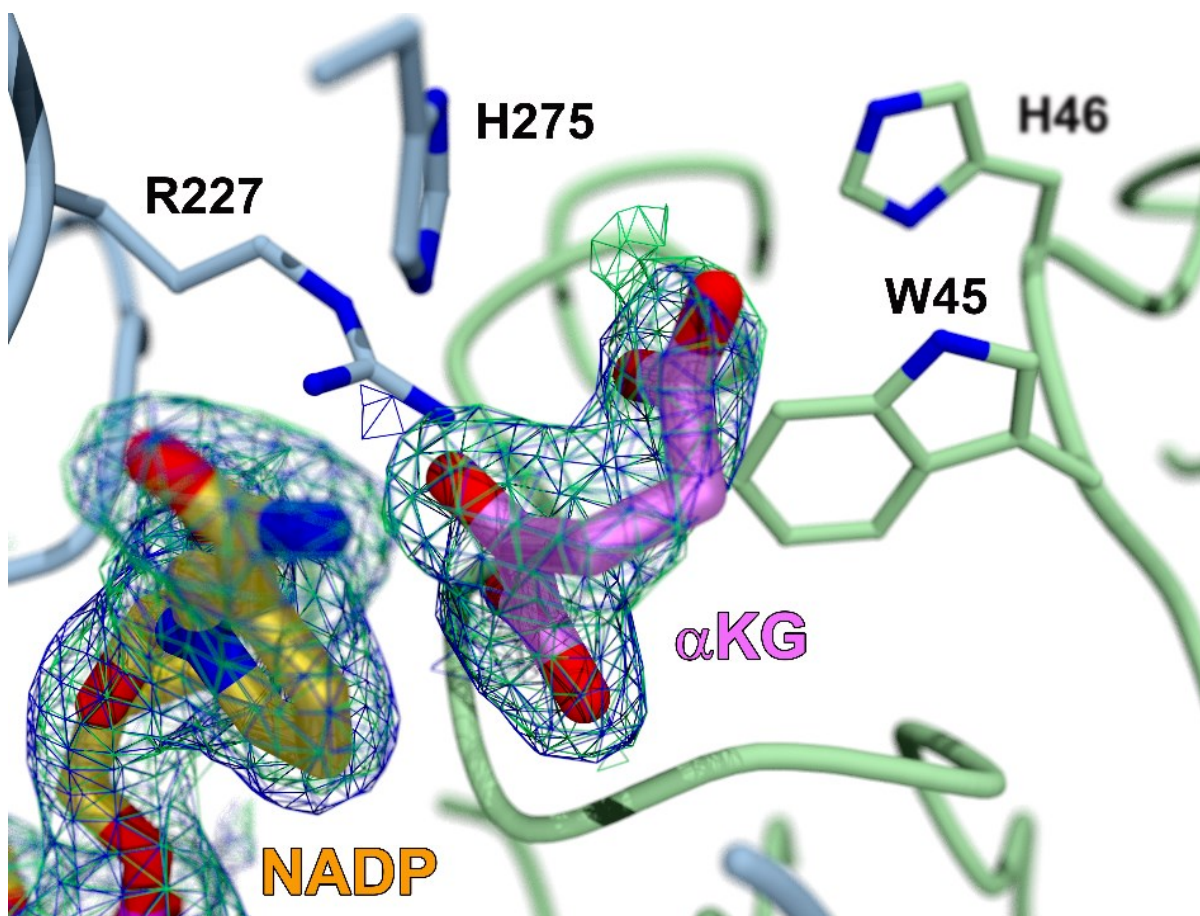


Figure 3-4 The view of wild-type EcGhrA active site with α -ketoglutarate bound. The $2|F_o| - |F_c|$ electron density map contoured at 1.0σ is shown as blue mesh, and the $2|F_o| - |F_c|$ composite omit map, also contoured at 1.0σ , is shown as green mesh. The image was generated using the POVSCRIPT+ modification of MOLSCRIPT.

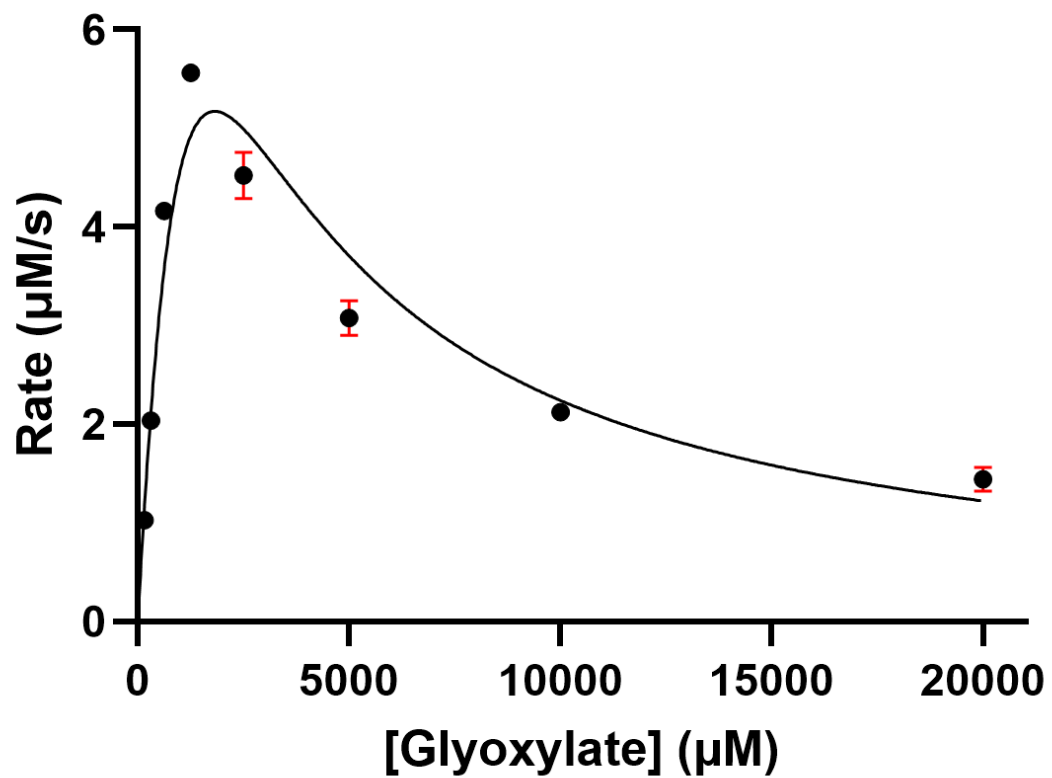


Figure 3-5. Michaelis-Menten (with substrate inhibition) curve for reaction of wild-type EcGhrA with glyoxylate.

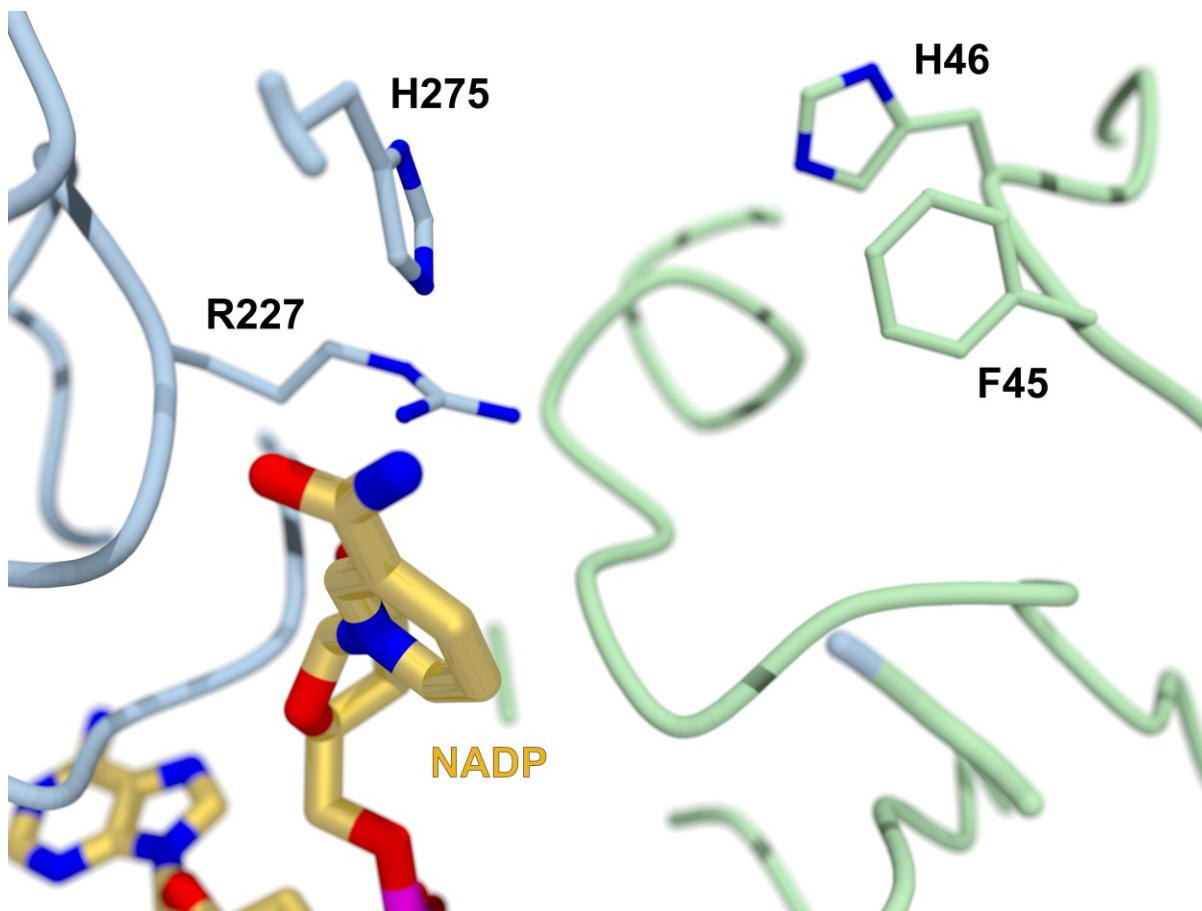


Figure 3-6. The view of *EcGhrA*^{W45F} active site. The image was generated using the POVSCRIPT+ modification of MOLSCRIPT.

Table 3-1. Crystallographic tables for GR and ligand complexes

	WT GR	WT GR·2KA	WT GR·KG	WT GR·GLX	W45F GR
PDB Entry	7JQH	6P35	7JQI	6OVL	7JQJ
Data collection					
Resolution (Å) (last shell) ^a	46.03 – 1.999 (2.07 - 1.999)	45.78 – 2.5 (2.589 – 2.5)	45.87 – 2.399 (2.485 – 2.399)	36.73 – 2.1 (2.175 -2.1)	35.24 – 2.204 (2.283 – 2.204)
Space group	P 65 2 2	P 65 2 2	P 65 2 2	P 65 2 2	P 65 2 2
a, b, c (Å)	158.768, 158.768, 97.699	158.578, 158.578, 98.285	158.887, 158.887, 96.091	158.82, 158.82, 96.71	159.177, 159.77, 95.709
α, β, γ (°)	90, 90, 120	90, 90, 120	90, 90, 120	90, 90, 120	90, 90, 120
R _{merge} ^a	0.1228 (0.7386)	0.1459 (0.8655)	0.1079 (0.3597)	0.09166 (0.7968)	0.116 (0.5544)
R _{meas} ^a	0.1257 (0.7557)	0.1495 (0.8901)	0.1148 (0.382)	0.09453 (0.8394)	0.1201 (0.5903)
R _{pim} ^a	0.02673 (0.1594)	0.03261 (0.2057)	0.03891 (0.1277)	0.02256 (0.2548)	0.03031 (0.1956)
CC _{1/2} ^a	0.998 (0.942)	0.998 (0.903)	0.995 (0.948)	0.999 (0.897)	0.998 (0.853)
No. of unique reflections ^a	49390 (4836)	25704 (2516)	28341 (2727)	42222 (3925)	36363 (2919)
Completeness (%) ^a	99.95 (99.77)	99.83 (99.88)	99.44 (97.77)	99.09 (94.62)	97.28 (81.59)
Multiplicity ^a	22.1 (22.3)	20.5 (18.4)	8.5 (8.7)	16.2 (9.6)	15.1 (8.3)
$\langle I/\sigma(I) \rangle^a$	26.24 (4.65)	24.37 (3.57)	22.70 (6.32)	29.83 (3.51)	16.11 (2.33)
Model Refinement					
Reflections used in refinement ^a	49371 (4836)	25669 (2516)	28324 (2723)	41937 (3925)	35509 (2920)
Reflections used for R _{free} ^a	2000 (196)	1992 (196)	1403 (157)	2121 (214)	1763 (148)
R _{cryst} (R _{free}) ^a	0.1735 (0.2095)	0.2057 (0.2585)	0.1965 (0.2135)	0.1835 (0.2451)	0.1950 (0.2479)
Wilson B-factor (Å ²)	24.25	36.50	34.92	27.74	32.44
Average B factor (Å ²)	28.46	41.52	39.56	32.67	37.77
Protein atoms	27.34	41.44	39.43	31.67	37.54
Ligand atoms	23.00	49.19	33.27	29.78	26.23
Solvent	38.75	36.92	42.86	42.34	43.15
Root-mean-square (RMS) deviations					

Bond lengths (Å)	0.014	0.012	0.011	0.004	0.005
Bond angles (°)	1.15	1.33	1.13	0.99	1.01
Coordinate error (Å) ^b	0.14	0.26	0.20	0.19	0.20
Ramachandran statistics					
Favored/allowed/outliers (%)	97.43/2.25/0.32	97.74/1.61/0.65	96.77/2.90/0.32	97.43/2.25/0.32	97.06/2.94/0.00
Rotamer outliers (%)	0.00	2.64	0.00	0.38	0.00
Clashscore	1.00	2.94	1.60	0.20	1.02
TLS groups	7	3	10	1	4

^aValues in parentheses apply to the high-resolution shell indicated in the resolution row

^b Maximum-likelihood based estimates of coordinate error

Table 3-2. Steady state parameters of EcGhrA and EcGhrA^{W45F} with GLX, 2KA, OA, and α KG

	EcGhrA	EcGhrA^{W45F}
k_{cat}^6 (s ⁻¹)	40.0 ± 23.0	120.0 ± 63.0
K_M^6 (mM)	2.2 ± 1.7	10.8 ± 6.1
k_{cat}^6/K_M^6 (M ⁻¹ s ⁻¹)	(2.0 ± 1.8) x 10 ⁴	(1.1 ± 0.9) x 10 ⁴
K_I^6 (mM)	1.5 ± 1.1	4.3 ± 2.9
k_{cat}^2 (s ⁻¹)	6.6 ± 0.4	4.0 ± 0.7
K_M^2 (mM)	8.8 ± 0.8	43.2 ± 8.4
k_{cat}^2/K_M^2 (M ⁻¹ s ⁻¹)	(8.3 ± 1.0) x 10 ²	92.5 ± 24.0
K_I^2 (mM)	NA	NA
Selectivity factor ^a	24 ± 4	119 ± 32
k_{cat}^7 (s ⁻¹)	1.9 ± 0.1	1.8 ± 0.04
K_M^7 (mM)	1.3 ± 0.2	6.3 ± 0.2
k_{cat}^7/K_M^7 (M ⁻¹ s ⁻¹)	(1.5 ± 0.3) x 10 ³	290 ± 17
K_I^7 (mM)	52 ± 15	NA
Selectivity factor ^a	13 ± 3	38 ± 4
k_{cat}^8 (s ⁻¹)	0.30 ± 0.02	0.26 ± 0.01
K_M^8 (mM)	4.0 ± 0.4	11.5 ± 0.8
k_{cat}^8/K_M^8 (M ⁻¹ s ⁻¹)	75.2 ± 12.5	22.6 ± 2.3
K_I^8 (mM)	NA	NA
Selectivity factor ^a	266 ± 50	487 ± 64

^a The selectivity factor is taken as the ratio of the pseudo-second order rate constant for **6** to those of the other substrates tested here.

3.4. References

1. Haltli, B.; Tan, Y.; Magarvey, N. A.; Wagenaar, M.; Yin, X.; Greenstein, M.; Hucul, J. A.; Zabriskie, T. M., Investigating beta-hydroxyenduracididine formation in the biosynthesis of the mannopeptimycins. *Chem Biol* **2005**, *12* (11), 1163-8.
2. Han, L.; Vuksanovic, N.; Oehm, S. A.; Fenske, T. G.; Schwabacher, A. W.; Silvaggi, N. R., Streptomyces wadayamensis MppP is a PLP-Dependent Oxidase, Not an Oxygenase. *Biochemistry* **2018**, *57* (23), 3252-3264.
3. Han, L.; Schwabacher, A. W.; Moran, G. R.; Silvaggi, N. R., Streptomyces wadayamensis MppP Is a Pyridoxal 5'-Phosphate-Dependent L-Arginine alpha-Deaminase, gamma-Hydroxylase in the Enduracididine Biosynthetic Pathway. *Biochemistry* **2015**, *54* (47), 7029-40.
4. Burroughs, A. M.; Hoppe, R. W.; Goebel, N. C.; Sayyed, B. H.; Voegtline, T. J.; Schwabacher, A. W.; Zabriskie, T. M.; Silvaggi, N. R., Structural and functional characterization of MppR, an enduracididine biosynthetic enzyme from streptomyces hygrosopicus: functional diversity in the acetoacetate decarboxylase-like superfamily. *Biochemistry* **2013**, *52* (26), 4492-506.
5. Pineda, M.; Piedras, P.; Cardenas, J., A continuous spectrophotometric assay for ureidoglycolase activity with lactate dehydrogenase or glyoxylate reductase as coupling enzyme. *Anal Biochem* **1994**, *222* (2), 450-5.
6. Matelska, D.; Shabalin, I. G.; Jablonska, J.; Domagalski, M. J.; Kutner, J.; Ginalska, K.; Minor, W., Classification, substrate specificity and structural features of D-2-hydroxyacid dehydrogenases: 2HADH knowledgebase. *BMC Evol Biol* **2018**, *18* (1), 199.
7. Nunez, M. F.; Pellicer, M. T.; Badia, J.; Aguilar, J.; Baldoma, L., Biochemical characterization of the 2-ketoacid reductases encoded by ycdW and yiaE genes in Escherichia coli. *Biochem J* **2001**, *354* (Pt 3), 707-15.
8. Yokota, A.; Haga, S.; Kitaoka, S., Purification and some properties of glyoxylate reductase (NADP+) and its functional location in mitochondria in Euglena gracilis z. *Biochem J* **1985**, *227* (1), 211-6.
9. Tochikura, T.; Fukuda, H.; Moriguchi, M., Purification and properties of glyoxylate reductase I from baker's yeast. *J Biochem* **1979**, *86* (1), 105-10.
10. Allan, W. L.; Simpson, J. P.; Clark, S. M.; Shelp, B. J., Gamma-hydroxybutyrate accumulation in Arabidopsis and tobacco plants is a general response to abiotic stress: putative regulation by redox balance and glyoxylate reductase isoforms. *J Exp Bot* **2008**, *59* (9), 2555-64.
11. Fukuda, H.; Moriguchi, M.; Kimura, A.; Tochikura, T., Purification and Properties of Glyoxylate Reductase from Neurospora crassa. *Agricultural and Biological Chemistry* **1981**, *45* (5), 1153-1158.
12. Shinoda, T.; Arai, K.; Taguchi, H., A highly specific glyoxylate reductase derived from a formate dehydrogenase. *Biochem Biophys Res Commun* **2007**, *355* (3), 782-7.
13. Zheng, Z.; Sheng, B.; Gao, C.; Zhang, H.; Qin, T.; Ma, C.; Xu, P., Highly stereoselective biosynthesis of (R)-alpha-hydroxy carboxylic acids through rationally re-designed mutation of D-lactate dehydrogenase. *Sci Rep* **2013**, *3*, 3401.
14. Wei, L.; Cai, X.; Qi, Z.; Rong, L.; Cheng, B.; Fan, J., In vivo and in vitro characterization of TEV protease mutants. *Protein Expr Purif* **2012**, *83* (2), 157-63.
15. Otwinowski, Z.; Minor, W., Processing of X-ray diffraction data collected in oscillation mode. *Methods Enzymol* **1997**, *276*, 307-26.

16. McCoy, A. J.; Grosse-Kunstleve, R. W.; Adams, P. D.; Winn, M. D.; Storoni, L. C.; Read, R. J., Phaser crystallographic software. *J Appl Crystallogr* **2007**, *40* (Pt 4), 658-674.
17. Winn, M. D.; Ballard, C. C.; Cowtan, K. D.; Dodson, E. J.; Emsley, P.; Evans, P. R.; Keegan, R. M.; Krissinel, E. B.; Leslie, A. G.; McCoy, A.; McNicholas, S. J.; Murshudov, G. N.; Pannu, N. S.; Potterton, E. A.; Powell, H. R.; Read, R. J.; Vagin, A.; Wilson, K. S., Overview of the CCP4 suite and current developments. *Acta Crystallogr D Biol Crystallogr* **2011**, *67* (Pt 4), 235-42.
18. Afonine, P. V.; Mustyakimov, M.; Grosse-Kunstleve, R. W.; Moriarty, N. W.; Langan, P.; Adams, P. D., Joint X-ray and neutron refinement with phenix.refine. *Acta Crystallogr D Biol Crystallogr* **2010**, *66* (Pt 11), 1153-63.
19. Adams, P. D.; Afonine, P. V.; Bunkoczi, G.; Chen, V. B.; Davis, I. W.; Echols, N.; Headd, J. J.; Hung, L. W.; Kapral, G. J.; Grosse-Kunstleve, R. W.; McCoy, A. J.; Moriarty, N. W.; Oeffner, R.; Read, R. J.; Richardson, D. C.; Richardson, J. S.; Terwilliger, T. C.; Zwart, P. H., PHENIX: a comprehensive Python-based system for macromolecular structure solution. *Acta Crystallogr D Biol Crystallogr* **2010**, *66* (Pt 2), 213-21.
20. Emsley, P.; Cowtan, K., Coot: model-building tools for molecular graphics. *Acta Crystallogr D Biol Crystallogr* **2004**, *60* (Pt 12 Pt 1), 2126-32.
21. Emsley, P.; Lohkamp, B.; Scott, W. G.; Cowtan, K., Features and development of Coot. *Acta Crystallogr D Biol Crystallogr* **2010**, *66* (Pt 4), 486-501.
22. Chen, V. B.; Arendall, W. B., 3rd; Headd, J. J.; Keedy, D. A.; Immormino, R. M.; Kapral, G. J.; Murray, L. W.; Richardson, J. S.; Richardson, D. C., MolProbity: all-atom structure validation for macromolecular crystallography. *Acta Crystallogr D Biol Crystallogr* **2010**, *66* (Pt 1), 12-21.
23. Moriarty, N. W.; Grosse-Kunstleve, R. W.; Adams, P. D., electronic Ligand Builder and Optimization Workbench (eLBOW): a tool for ligand coordinate and restraint generation. *Acta Crystallogr D Biol Crystallogr* **2009**, *65* (Pt 10), 1074-80.
24. Kutner, J.; Shabalin, I. G.; Matelska, D.; Handing, K. B.; Gasiorowska, O.; Sroka, P.; Gorna, M. W.; Ginalski, K.; Wozniak, K.; Minor, W., Structural, Biochemical, and Evolutionary Characterizations of Glyoxylate/Hydroxypyruvate Reductases Show Their Division into Two Distinct Subfamilies. *Biochemistry* **2018**, *57* (6), 963-977.
25. Booth, M. P.; Connors, R.; Rumsby, G.; Brady, R. L., Structural basis of substrate specificity in human glyoxylate reductase/hydroxypyruvate reductase. *J Mol Biol* **2006**, *360* (1), 178-89.
26. Ogino, H.; Nakayama, H.; China, H.; Kawata, T.; Doukyu, N.; Yasuda, M., Characterization of recombinant glyoxylate reductase from thermophile *Thermus thermophilus* HB27. *Biotechnol Prog* **2008**, *24* (2), 321-5.
27. Lassalle, L.; Engilberge, S.; Madern, D.; Vauclore, P.; Franzetti, B.; Girard, E., New insights into the mechanism of substrates trafficking in Glyoxylate/Hydroxypyruvate reductases. *Sci Rep* **2016**, *6*, 20629.
28. Gallivan, J. P.; Dougherty, D. A., Cation-pi interactions in structural biology. *Proc Natl Acad Sci U S A* **1999**, *96* (17), 9459-64.
29. Dougherty, D. A., Cation-pi interactions involving aromatic amino acids. *J Nutr* **2007**, *137* (6 Suppl 1), 1504S-1508S; discussion 1516S-1517S.
30. Mdluli, K.; Booth, M. P.; Brady, R. L.; Rumsby, G., A preliminary account of the properties of recombinant human Glyoxylate reductase (GRHPR), LDHA and LDHB with glyoxylate, and their potential roles in its metabolism. *Biochim Biophys Acta* **2005**, *1753* (2), 209-16.
31. Simpson, J. P.; Di Leo, R.; Dhanoa, P. K.; Allan, W. L.; Makhmoudova, A.; Clark, S. M.; Hoover, G. J.; Mullen, R. T.; Shelp, B. J., Identification and characterization of a plastid-localized Arabidopsis glyoxylate reductase isoform: comparison with a cytosolic isoform and implications for cellular redox homeostasis and aldehyde detoxification. *J Exp Bot* **2008**, *59* (9), 2545-54.

32. Duncan, R. J.; Tipton, K. F., The oxidation and reductn of glyoxylate by lactic dehydrogenase. *Eur J Biochem* **1969**, *11* (1), 58-61.
33. Cooper, A. J.; Meister, A., Cyclic forms of the alpha-keto acid analogs of arginine, citrulline, homoarginine, and homocitrulline. *J Biol Chem* **1978**, *253* (15), 5407-10.
34. T. D. Fenn, D. R. G. A. P., POVScript+: a program for model and data visualization using persistence of vision ray-tracing. *Journal of Applied Crystallography* **2004**, *36*, 944-947.
35. Kraulis, P. J.; lucr, MOLSCRIPT: a program to produce both detailed and schematic plots of protein structures. *Journal of Applied Crystallography* **1991**, *24* (5), 946-950.

Chapter 4

A general quench-flow LC-MS/MS-based method for the study of enzyme kinetics

4.1 Introduction

Many enzymatic reactions involving chromo- or fluorogenic substrates or products can be directly monitored by UV-visible or fluorescence spectroscopy.¹ When this is not the case, the enzymatic reactions can often be coupled with a spectrophotometrically active enzymatic reaction, allowing for product formation or substrate consumption to be observed indirectly (a so-called “coupled assay”).^{2,3} However, developing an elegant continuous assay is not always an achievable goal. The only way to observe intermediates and gain information about enzyme kinetics in cases where it is impossible to monitor the reaction in real time is to quench the reaction at various time points and quantify the species present using analytical chemistry techniques.⁴ To date, kinetic studies of the enzymes in the biosynthetic pathway of L-enduracididine (L-End) have been limited to the kinetic characterization of MppP,^{5,6} the first enzyme in the biosynthesis of L-End, since its formation and decay of spectrophotometrically active intermediates can be monitored directly using stopped-flow techniques and steady state kinetics can be measured by following oxygen consumption using a Clark electrode. However, the two subsequent enzymes in the pathway, MppR and MppQ, have remained elusive targets for kinetic studies due to a lack of adequate coupled continuous assays. MppR is a putative cyclase, responsible for cyclization of 4S-hydroxy 2-ketoarginine (4HKA) forming 2-ketoenduracididine (2KE),⁷ while MppQ is a fold type I PLP-dependent aminotransferase forming L-End by transaminating 2KE in the presence of an amino

group donor (*i.e.* an amino acid). In order to understand the kinetic parameters of these enzymes, I have developed a discontinuous quenched-flow LC/MS-MS method that can measure the kinetics of MppR, MppQ, and likely many other enzymes that lack adequate spectrophotometric or fluorescence assays.

4.1.1 Quench-Flow Methods in Enzymology

While it is possible to do discontinuous assays by manually quenching reactions, this method lacks reproducibility and leaves sub-second times inaccessible. It is also difficult to trap intermediates by manual quenching owing to the often-rapid timescales of their formation and decay. The limitations inherent in manual-quench experiments motivated the development of rapid quench-flow (QF) instruments. The first use of the rapid quench-flow technique was by Ferguson and Roughton in 1934,⁸ to estimate the concentrations of carbamino compounds resulting from the reaction of CO₂ with hemoglobin. In 1960s, Barman and Gutfreund developed sophisticated quench-flow methods to kinetically characterize enzymatic mechanisms of trypsin and chemotrypsin.⁹ Lynn and Taylor were able to kinetically study the hydrolysis of ATP by the

myosin ATPase using quench-flow and ^{32}P -labeled ATP, illustrating the great versatility of quench-flow methods.¹⁰ Figure 4-1 shows the QF instrument design used by Lynn and Taylor.

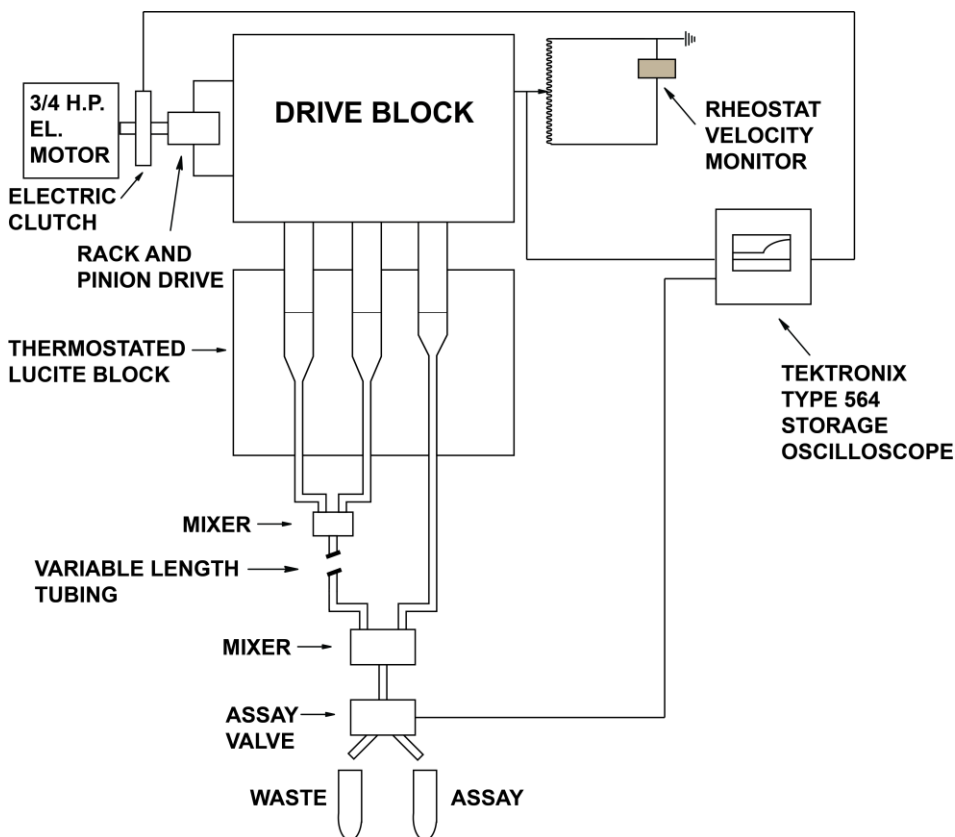


Figure 4-1. Schematic representation of quench-flow instrument adapted from Lynn and Taylor, 1970.

This instrument contained enzyme and substrate in two syringes, while the quencher was in the third syringe. The quenching times could be varied either by changing the tubing length between the two mixers or by changing the flow rate. All solutions would be mixed via push of the single drive block. This design had limitations, most notably, the inability to obtain quench times beyond the millisecond time scale. Lowering the flow rate beyond a certain point inevitably leads to inaccuracies caused by poor mixing. This challenge led to the development of time-delay (pulse-flow) QF instruments (Figure 4-2).¹¹ This design uses two independent drives to mix the samples. Substrate and enzyme are mixed using drive 1 and allowed to age in a delay loop until drive 2 is

activated and mixes the reaction with a quencher. This type of instrument allows quenching at very long timescales and is essentially the same as current QF instruments.

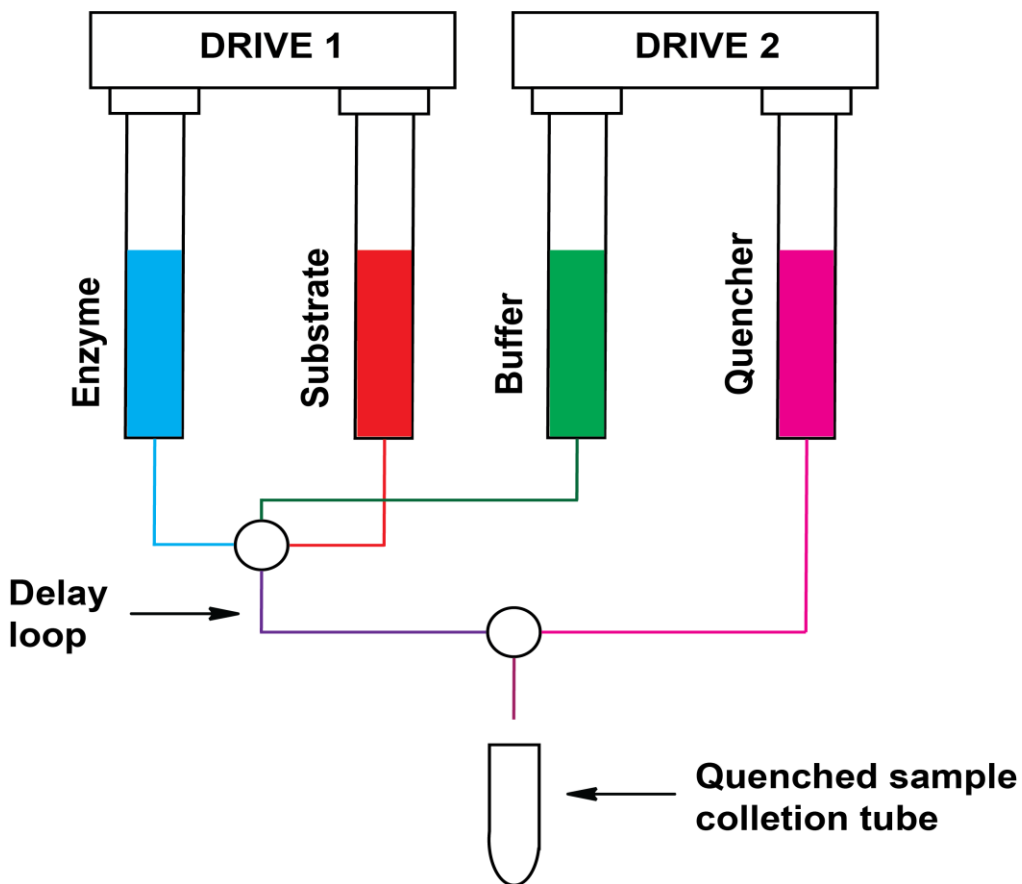


Figure 4-2. Schematic representation of a time-delay quench flow apparatus (Adaptation from Barman et al. 2006)

The most laborious part of the early QF methods was analysis of each individual quenched sample, but the development of autosamplers, in particular the ones coupled with HPLC systems, has provided a relatively easy way to analyze large numbers of QF samples.

The great improvement in mass-spectrometry instrumentation over the past two decades has spurred significant progress in developing rapid-mixing quench-flow/mass spectrometry-based

methods to study enzyme kinetics. These methods, while often labor-intensive, do not rely on chromophores, radiolabeled substrates, or substrate analogues. Pre-steady state kinetic data in the millisecond range can be successfully obtained using quench-flow systems interfaced with a mass spectrometer. While such time-resolved mass spectrometry (TRMS) methods involving custom-built quench-flow devices directly connected to mass spectrometers represent a powerful tool, they require significant effort in terms of building or modifying the necessary devices.¹² Additionally, the use of on-line quench-flow devices coupled with electrospray ionization (ESI) requires use of volatile, mass spectrometry-friendly buffers. However, many enzymes require significant amounts of salt for stability, which, when subjected to ESI, causes significant ion suppression. For enzymologists who lack the expertise in development of these methods and are primarily interested in collecting steady state kinetic data or screening different substrates for activity, this may pose a major obstacle. An alternative is to combine flow injection analysis with ESI, as described by Norris et al. In this method, tandem mass spectrometry eliminates the signal from contaminant ions by relying on multiple reaction monitoring (MRM).¹³

In this chapter, I report the development of a method using the qPod quench-flow module installed on an SF-61DX2 stopped-flow instrument, both manufactured by TgK Scientific (Bradford-on-Avon, UK). The quench-flow device is coupled off-line with LC/MS-MS to obtain quantitative information about the kinetics of enzymes in the L-End biosynthetic pathway. Hydrophilic interaction liquid chromatography (HILIC) was able to fully separate the analytes in the reaction mixtures, provide enhanced peak reproducibility, and limit of quantitation compared to direct-injection methods, all while minimizing matrix effects.

The advantages of using a qPod module over a dedicated quench-flow instrument are its low-cost and easy installation on an existing stopped-flow instrument, which allows for convenient

anaerobic experiments. To the best of our knowledge, there have been no reports in the literature of this device being used for any quantitative mass spectrometry-based kinetic studies of enzymes, though Conrad et al published a method using the qPod for quantifying intermediates in the oxidative half-reaction of the FAD-dependent thymidylate synthase by HPLC analysis.¹⁴ The limitation of the qPod is that it does not offer exceptionally high temporal resolution, since the dead-time of the quench-flow module is ~20 ms, making it unsuitable for very fast reactions. Furthermore, the manual ejection of the reaction mixture from the mixing chamber is a potential source of error. To account for this, I used *p*-nitrophenol as an internal standard to determine exact dilution factors. This standard was chosen because our efforts to find a mass spectrometry-compatible internal standard did not yield satisfying results in terms of being chromatographically separated from the analytes of interest. It is likely that different enzyme systems will require identification of other suitable internal standards. Since mass spectrometry is not an inherently quantitative technique, standard curves were prepared by analyzing standards of each analyte in the same solution matrix as the enzymatic reaction products. The ability to obtain reproducible quantitative data for a number of enzymatic products not measurable spectrophotometrically showed that, if suitable standards are available, the qPod module can be a low-cost alternative to a dedicated quench-flow apparatus or time-consuming and expensive fabrication of custom devices.

4.1.2 Hydrophilic Interaction Liquid Chromatography

HILIC is a normal phase chromatography technique employing a polar stationary phase and typically used for separation of highly polar molecules that exhibit poor retention on reverse phase C18 columns.¹⁵ Therefore, in HILIC, an organic solvent such as acetonitrile is the “weak” solvent,

while the aqueous phase is the “strong” solvent, eluting the analytes from the column. A portion of the aqueous mobile phase forms a layer over the stationary phase, allowing analytes to partition between the stationary and mobile phase.^{16, 17} For this reason, it is necessary to have at least some aqueous phase at all times in order to ensure adequate hydration of the column. HILIC employs a complex mechanism of separation compared to normal phase chromatography. Partitioning between the stationary and mobile phases occurs through multiple modes of interactions including dipole-dipole, and ionic interactions. This is possible due to a variety of stationary phases used in HILIC ranging from plain silica to silica functionalized with amines, amides, saccharides, peptides, or other functional groups that may contribute additional interactions with analytes (Figure 4-3A, 3B).¹⁵ A HILIC column with sulfobetaine-type groups grafted on a silica support

(ZIC HILIC, Figure 4-3C) proved most effective for HPLC separation and analysis of compounds encountered while studying enzymes in the L-End biosynthetic pathway.

The zwitterionic character of the stationary phase provided by the sulfonic acid and quaternary ammonium groups provides additional selectivity to the column. In cases when charged stationary phases are used, it is necessary to have salts in the mobile phase in order to displace charged analytes. For methods combining HPLC with MS, volatile buffers such as ammonium acetate or ammonium formate are typically used. A typical LC/MS-MS chromatogram of the MppP reaction products separated using ZIC-HILIC is shown in Figure 4-4. Note the presence of decarboxylated

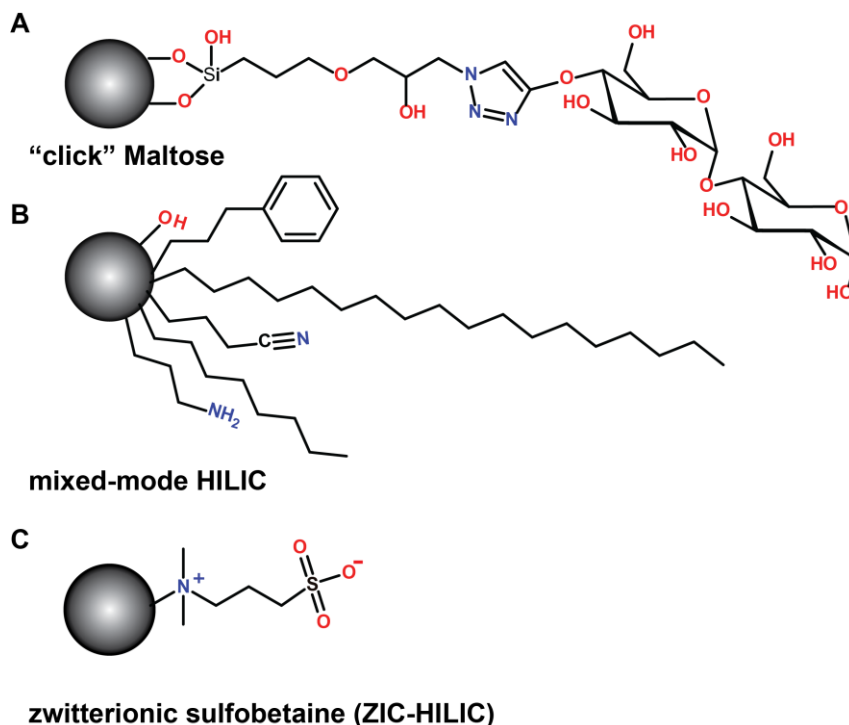


Figure 4-3. A) HILIC “click” saccharide stationary phase. B) Mixed mode HILIC stationary phase. C) Structure of the sulfobetaine functional group of the ZIC-HILIC stationary phase. Adapted from Buszewski and Noga, 2011.

2KA and 4HKA due to generation of hydrogen peroxide during the reaction. Under the 5-minute

gradient method, non-decarboxylated 2KA and 4HKA peaks are not resolved. For this reason, in quench flow experiments where MppP products were quantified using LC/MS-MS, additional hydrogen peroxide was added in order to ensure full decarboxylation and achieve full compound separation.

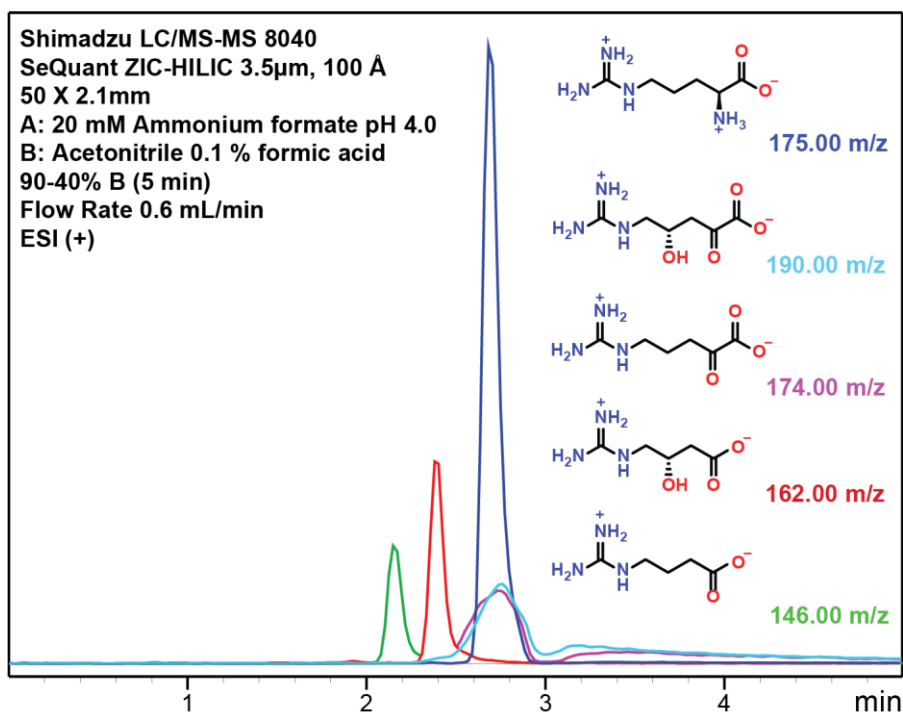


Figure 4-4. Separation of MppP reactant and products using ZIC-HILIC.

4.1.3 Mass Spectrometry

Mass spectrometry is one of the most commonly used and powerful methods to detect analytes at very low concentrations. High-resolution mass spectrometers have provided chemists with novel ways to study increasingly complex mixtures.¹⁸ These developments were particularly helpful for studying biological systems where myriad solution components make analysis via techniques such as NMR quite difficult. Mass spectrometry (MS) requires molecules to be ionized and mass analyzers detect analytes based on their mass-to-charge ratios (m/z). The two most popular ionization methods in MS are electrospray ionization (ESI) and atmospheric pressure chemical ionization (APCI). ESI is commonly used to study polar molecules, and this method ionizes molecules by applying high voltage to the capillary through which charged droplets exit. Aided by drying gas and high temperature, the droplets diminish in size until the point at which ions on the

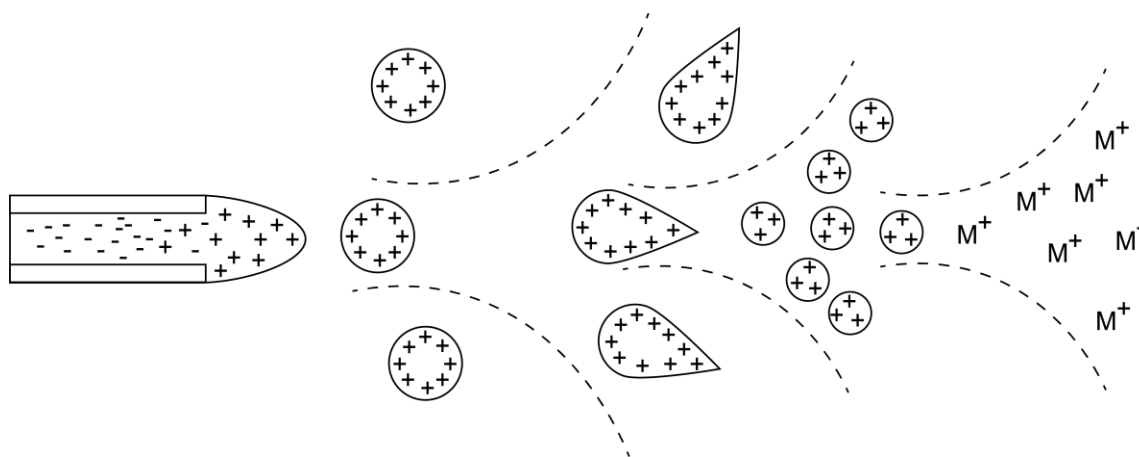


Figure 4-5. Graphical representation of ionization mechanism employed by electrospray ionization (ESI) (adapted from Ho et al., 2003)

droplet surface transition into the gas phase and can be analyzed (Figure 4-5).¹⁹ APCI uses corona discharge to form singly charged ions in the gas phase. Molecules prone to thermal degradation

tend to fragment during APCI, making analysis more complex. It is commonly used to study non-polar molecules and in cases where lack of ion suppression during APCI outweighs the higher m/z range offered by ESI.

ESI does not result in any fragmentation and is considered a “soft” ionization method, simplifying analysis since only molecular ions are observed. Under ESI, however, a variety of adducts can form that can complicate the resulting spectra. Protonation of the molecular ion, $[M+H]^+$, is commonly seen, and all the precursor ions studied in this work are protonated adducts.²⁰ However, ESI MS suffers when analyzing complex matrices with molecules that, after ionization, have very similar m/z to the analyte(s) or isobaric molecules. Any isobaric ions (ions with identical masses but with different atomic compositions) analyzed using ESI would appear indistinguishable. Triple

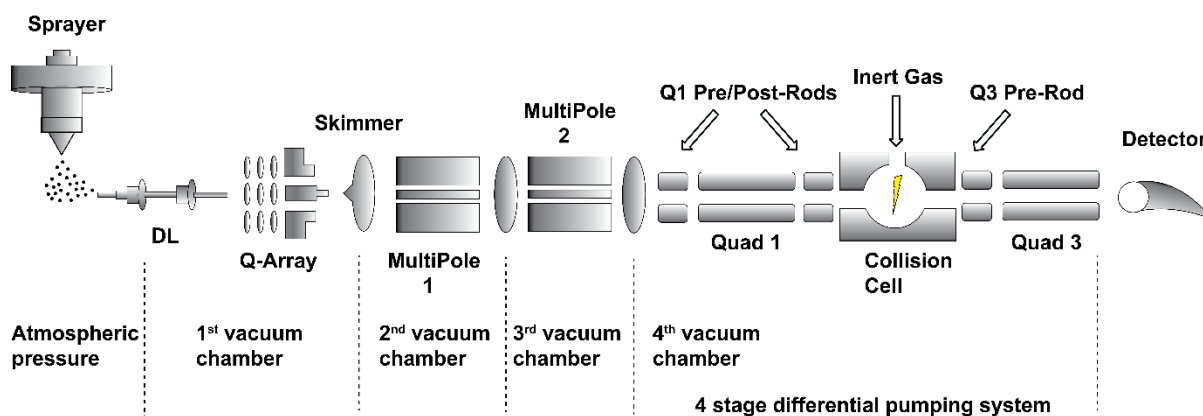


Figure 4-6. Schematic representation of a triple quadrupole mass spectrometer (Shimadzu LCMS-8040). Adapted from LCMS 8040 Brochure, Shimadzu Corporation, 2012.

quadrupole mass spectrometers were developed to combine the convenience of detecting molecular ions and the specificity of molecular fragmentation. Triple quadrupole mass spectrometry represents a powerful tool for identifying and quantifying reaction products. It typically uses collision-induced dissociation (CID) to fragment precursor ions into product ions. In cases where multiple precursor ions have similar m/z values, fragmentation aids in distinguishing between them.

Triple quadrupole instruments employ two quadrupole mass analyzers and a collision chamber to analyze precursor and product ions. Figure 4-6 shows a schematic representation of the Shimadzu LCMS 8040 used in this work. The ions formed by applying voltage to the tip of the capillary needle (ESI) are sprayed orthogonally to a desolvation line (DL) at the atmospheric pressure. This geometry minimizes the amount of molecules coating the desolvation line and potentially clogging it.²¹ Under vacuum, ions go through a Qarray RF ion guide, to focus them on the skimmer. Two multi-poles provide additional ion guidance before the ions enter the first quadrupole (Q1). Inert gas, such as argon or nitrogen, is used for collision with precursor ions inside the collision cell.²² Product ions then go through another quadrupole (Q3) before reaching the detector. Each quadrupole (Figure 4-7) consists of two pairs of parallel rods. RF (alternating) voltage and DC voltage are applied to the rods; the rods in each pair have opposite polarity.²³ This applied current produces a fluctuating electric field, which plays a key role in selecting ions with certain mass-to-charge ratios. By adjusting the current, only ions with certain m/z values can have a trajectory that allows them to reach the detector successfully. Other ions will collide with the rods and will not be detected. This selection of both fragments and precursor ions, referred to as mass transitions, is the basis for single-reaction monitoring (SRM).²⁴ The SRM involves selection a single precursor ion using the 1st quadrupole and then monitoring a single product ion selected by 3rd quadrupole. Multiple reaction monitoring (MRM) can be used in a similar manner to select a single precursor

ion and monitor multiple product ions, or select multiple precursors and observe a single product.¹⁸ In this work, all the quantitative MS experiments relied on multiple-reaction monitoring (MRM).

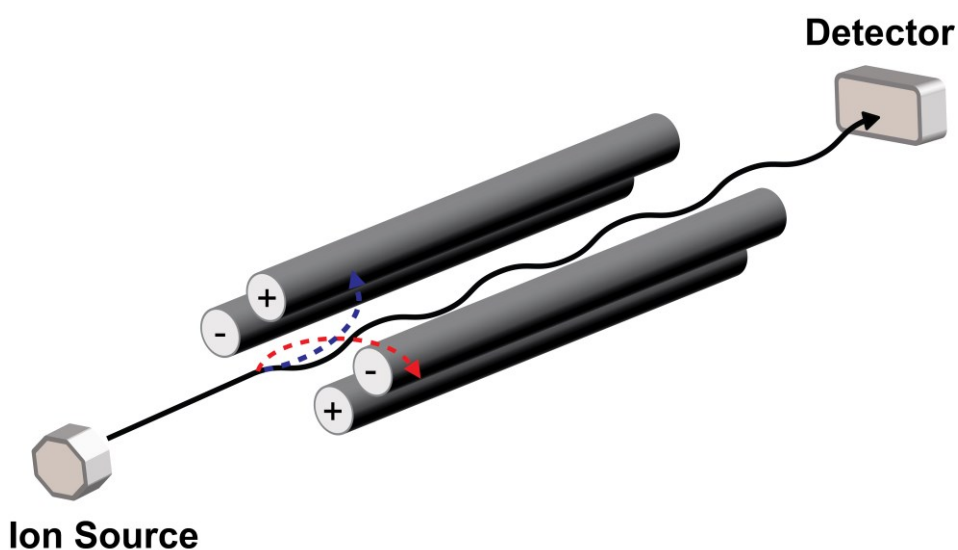


Figure 4-7. Schematic representation of a quadrupole mass-analyzer. Adapted from El-Aneed et al., 2009

The high selectivity and sensitivity of ESI-MS/MS may give the false impression that sample purification and preparation is unnecessary, since impurities present in the sample matrix are not visible on the MS chromatogram. This is not the case, because whenever ESI-MS is employed as a method to quantify specific analytes, the user must be aware of the adverse effects of ion suppression on the validity and reproducibility of the assay.^{25,26} In ESI, ion suppression is caused by a competition between the analytes and matrix components at the ionization source, leading to less efficient ionization of the analytes. Even without impurities being present in the sample matrix, at high sample concentrations, analytes can suppress their own ionization. When running

samples with the analyte increasing in concentration, there is a threshold, specific to each analyte, where the linearity of the detector response breaks down. There are multiple approaches to eliminate or at least fully account for ion suppression. Running a sample through a column that can separate analytes from other matrix components ensures that they do not enter the ionization source simultaneously. If feasible, this is the best way to prevent ion suppression. Another option is to lower the sample injection volume or dilute the sample. However, when working with trace amounts of analytes, this method could lead to problems with detection and quantification. In certain cases, when it is impossible to chromatographically separate analytes and sample purification techniques prove inadequate, careful design of calibration standards can be used to compensate for ion suppression. The internal standards used in quantitative MS typically employ isotopically labeled analytes with physicochemical properties identical to those of the analytes in the sample matrix. This allows for accurate quantitation since both analytes and the standards are exposed to the same level of ion suppression. The isotopically labeled analogues must be stable and at least 3 mass units heavier than the analyte.²⁷ It is not an absolute requirement to use an isotopically labeled analogue as an internal standard. If a structurally similar analogue can be found that behaves identically to the analyte in the chromatographic separation and has the same physicochemical properties, it is suitable for use as an internal standard. When working with complex biological matrices, such as blood, plasma, or urine, the use of isotopically labeled stable analogues is the preferred method. However, when dealing with relatively simple matrices, such as samples containing products of a single enzymatic reaction in buffer, external matrix-matched standards or the standard addition method will suffice. The standard addition method involves spiking the sample with multiple concentrations of the same analyte.²⁸ Since the actual sample matrix is used to make standards this method yields a very high degree of accuracy. The problem with this method

is that a relatively large amount of sample is required.²⁹ The work described in this chapter used external matrix-matched standards to generate calibration curves.

4.2 Materials and Methods

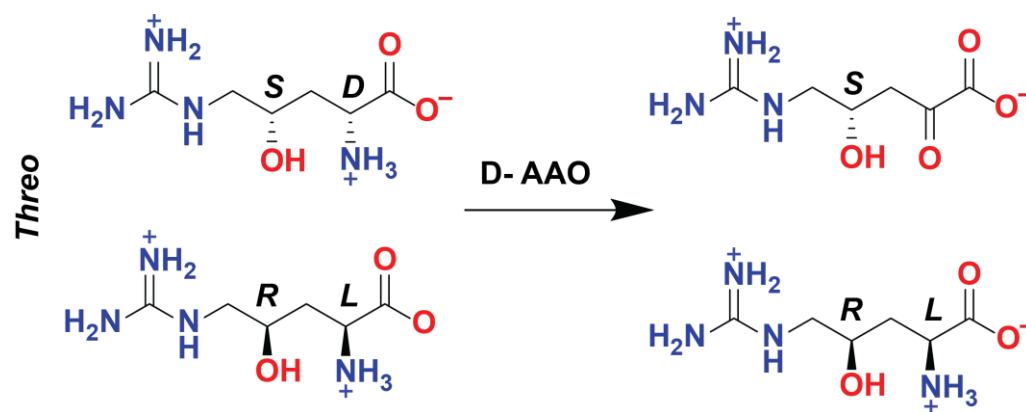
4.2.1 Cloning, Purification, and Expression of *Streptomyces hygroscopicus* MppR

The gene encoding *Streptomyces hygroscopicus* MppR was codon optimized and synthesized by GenScript, Inc. The gene was subcloned into the pE-SUMO_{kan} vector, expressed, and purified according to the protocol described by Burroughs et al[REF]. Briefly, the His₆-tagged SUMO-MppR fusion protein was expressed from *E. coli* BL21 Star (DE3) cells (Invitrogen, Inc.) carrying the pE-SUMO-MppR plasmid. Cultures were grown at 37 °C in 2 L of Luria-Bertani medium with 50 µg/mL kanamycin to an O.D._{600nm} of 0.8-1.0, at which point protein expression was induced with 0.4 mM IPTG. The temperature was reduced to 25 °C and the cultures were grown overnight. Cells were harvested by centrifugation, resuspended in 5 mL/g of buffer A (25 mM TRIS pH 8.0, 300 mM NaCl, 10 mM imidazole) and 0.1 mg/mL DNase. Cells were lysed using a Branson Sonifier S-450 cell disruptor (Branson Ultrasonics Corp.). The sonication program included 10 minutes total of sonication at 60% amplitude with 30s pulses separated by 30 s rest periods. The lysate was clarified by centrifugation at 39,000 × g for 45 minutes and then applied to a 5 mL HisTrap column (GE Lifesciences) at a flow rate of 5 mL/min to isolate the His₆-SUMO-MppR fusion protein. The protein was eluted by a 4-step gradient of buffer B (25 mM TRIS pH 8.0, 300 mM NaCl, 250 mM imidazole; 5, 15, 50, and 100 % buffer B). The His₆-SUMO-MppR fusion protein eluted in the third and fourth steps. Peak fractions were pooled and dialyzed overnight against 4 L of 25 mM TRIS pH 8.0, 150 mM NaCl in the presence of ~2 µM SUMO protease.

MppR was desalted into 5 mM phosphate pH 7.5 and 75 mM NaCl using a 2 x 5 mL HiTrap desalting column (GE Lifesciences), aliquoted, and flash-frozen in a dry ice/ethanol bath.

4.2.2 Cloning, Expression and purification of *Arthropobacter protoformiae* D-Amino Acid Oxidase (D-AAO)

Characterizing the kinetic behavior of MppR requires a supply of pure 4S-hydroxy-2-ketoarginine. The Schwabacher group at UWM has developed a route to 4-hydroxy-arginine that results in a mixture of all four possible diastereomers of this compound. They also developed a separation scheme that was able to separate the erythro diastereomers from the threo diastereomers (Hagemann et al., unpublished work). The threo-4(R/S)-hydroxy-D,L-arginine mixture (Scheme 4-1) was treated with the D-amino acid oxidase (DAAO) from *Arthropobacter protoformiae* (Genbank accession code AY306197), which selectively oxidized the threo-4S-hydroxy-D-arginine to the corresponding ketoacid. This preparation of the MppR substrate is contaminated with ~50% of threo-4R-hydroxy-L-arginine, which may or may not inhibit MppR. The *A.*



Scheme 4-1. Reaction of *Arthropobacter protoformiae* D-amino acid oxidase with the diastereomeric mixture of threo-4(R/S)-hydroxy-D,L-arginine.

protophormiae DAAO was chosen for to its very favorable substrate profile compared to mammalian DAAOs, which had poor activity with arginine.³⁰

The *A. protophormiae* DAAO gene was synthesized and subcloned into the pET-28a vector by GenScript Inc.(Piscataway, NJ). The glycerol stock of BL21 DE3 (Star) cells carrying the p28a-DAAO plasmid was used to inoculate 20 mL starter cultures in Luria Bertani medium with 50 µg/mL kanamycin. These starter cultures were grown overnight at 37 °C with agitation at 250 rpm. The following day, each 20 mL starter culture was used to inoculate 1 L of Luria-Bertani medium with 50 µg/mL kanamycin. The large-scale cultures were allowed to grow until they reached OD_{600nm} of 0.8-1.0. Protein expression from the pET-28a plasmid was induced with 0.4 mM IPTG and the cultures were grown overnight at 22 °C with agitation at 250 rpm. The cells were then harvested by centrifugation, resuspended in 5 mL of buffer A (25 mM TRIS pH 8.0, 300 mM NaCl, 10 mM imidazole), 50 µM FAD disodium salt, 1 mg/mL lysozyme, and 0.1 mg/mL DNase per gram of wet cell paste. The cells were lysed using a Branson Sonifier S-450 cell disruptor (Branson Ultrasonics Corp.). The sonication program consisted of 10 minutes total of sonication at 60% amplitude in 30s pulses separated by 30 s rest periods. The resulting cell lysate was clarified by centrifugation at 39,000 × g for 45 minutes and then applied to a 5 mL HisTrap column (GE Lifesciences) at a flow rate of 5 mL/min to isolate the His₆-tagged DAAO. The protein was eluted by a 4-step gradient of buffer B (25 mM TRIS pH 8.0, 300 mMNaCl, 250 mM imidazole; 5, 15, 50, and 100 % buffer B). The His₆-tagged DAAO eluted in the third and fourth steps. The His₆ tag was not removed as it does not affect the enzymatic activity of DAAO (data not shown). The enzyme was desalted in 50 mM ammonium bicarbonate pH 7.6 (pH was not adjusted via acid/base titration) using 2 x 5 mL HiTrap desalting column (GE Lifesciences).

4.2.3 Reaction of DAAO with threo-4(R/S)-hydroxy-D,L-arginine mixture

Bovine catalase (40 mg; Sigma Aldrich) was desalted into 50 mM ammonium bicarbonate, pH 7.6, to remove the trehalose stabilizer (20% w/w) added by the manufacturer. A pre-washed 10 kDA MWCO concentrator (washed 3 times with mqH₂O) was used to wash catalase with an

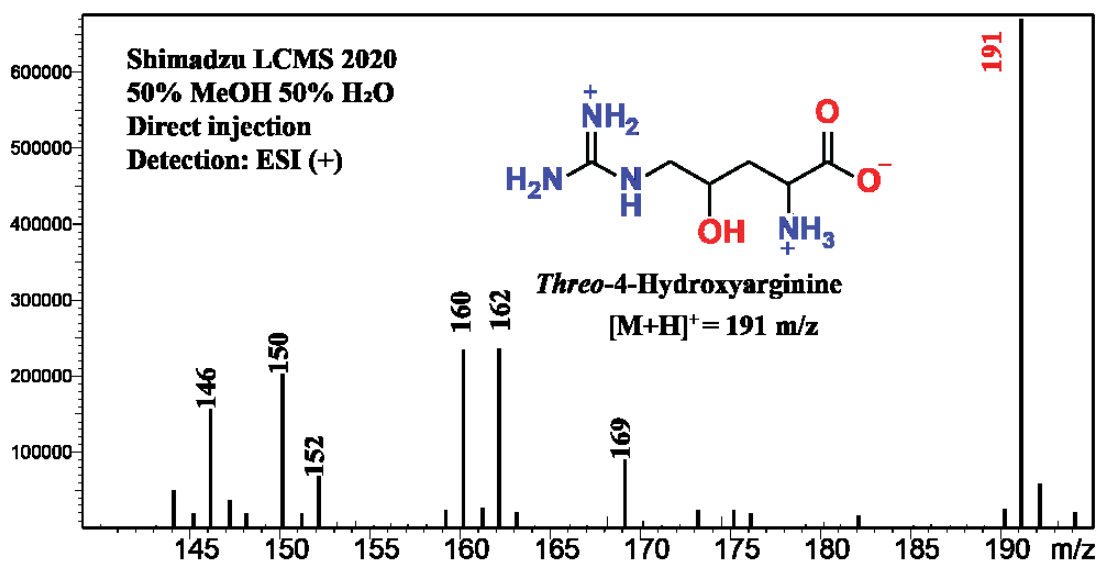


Figure 4-8. Mass spectrum of threo-4(R/S)-hydroxy-D,L-arginine mixture in the precursor ion scan mode.

additional 50 mL of ammonium bicarbonate buffer (to remove any residual trehalose) and concentrate the enzyme. The purity of threo-4(R/S)-hydroxy-D,L-arginine mixture was verified using Shimadzu LC-MS 2020 (direct injection, Figure 4-8). Since the threo-4(R/S)-hydroxy-D,L-arginine mixture is extremely hygroscopic, it was not feasible to remove it from the round bottom flask provided by the Schwabacher lab and weigh out an exact amount. The material turns into a gel almost upon exposure to the air and adheres to both the spatula and the glassine weighing paper. There was approximately 30-40 mg in the flask, and I decided to conduct the reaction directly in the 100 mL round bottom flask above a stirring plate. The washed and concentrated

catalase preparation (2 mL) was mixed with 6 mL of 490 μ M DAAO. This enzyme mixture was added to the substrate in the flask and used to dissolved it. Upon dissolution of the threo-4(R/S)-hydroxy-D,L-arginine mixture, the color of the enzyme solution changed instantly from yellow to a pale blueish gray transition occurs: from yellow to faint gray due to reduction of the FAD in DAAO. The enzyme-substrate mix was diluted to a final volume of 20 mL with 50 mM ammonium bicarbonate. The reaction stood overnight at room temperature (23.5 C, 30% RH), uncovered with stirring at 150 rpm to maintain oxygen saturation in the reaction mixture. The following day, an aliquot of the reaction was taken and mixed with an equal volume of neat acetonitrile. This sample

was centrifuged at 13,000 rpm for 10 min and analyzed by ESI-MS on a Shimadzu 8040 LC/MS (direct injection; Figure 4-9A). An additional 6 mL of DAAO was added to the reaction to ascertain whether the reaction had reached completion. The reaction ran for another 3 hours after the second DAAO addition, at which point a second sample was taken for ESI-MS analysis

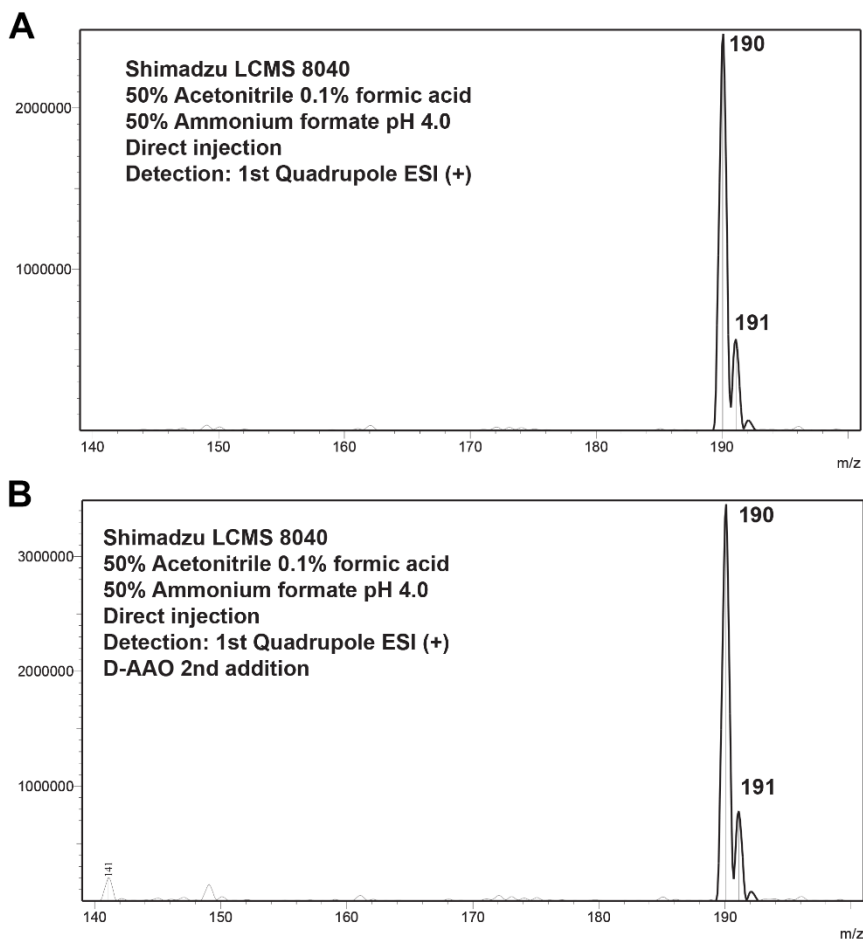


Figure 4-9. MS precursor ion scan of DAAO after overnight reaction with the threo-4(R/S)-hydroxy-D,L-arginine mixture (A). A similar MS precursor ion scan after the second addition of DAAO (B).

(Figure 4-9B). There was no increase in the amount of 4HKA produced after the second addition. The entire solution was quenched with an equal volume of neat acetonitrile and dried overnight at 40 °C in a Centrifan PE Rotary Evaporator (KD Scientific).

4.2.4 Preparation of 4(S)-hydroxy-2-ketoarginine standards

A solution of 4(S)-hydroxy-2-ketoarginine (4(S)HKA) was prepared by dissolving three mixture in mqH₂O. Insoluble particulates were removed by centrifugation at 4000 rpm for 10 min. A 100 µL aliquot was taken and mixed with 100 µL of acetonitrile to minimize solvent mismatch. The sample was analyzed on a ZIC-HILIC column (Merck) connected to a Shimadzu LCMS-8040 for MS/MS analysis. The exact concentration of 4(S)HKA was determined using a MS calibration curve prepared using a decarboxylated 4HKA solution of known concentration produced enzymatically as described below.

SwMppP reacts with L-arginine to produce 4(S)HKA and the partially oxidized, abortive product 2KA. Having 2KA in the mixture is problematic when studying the kinetics of MppR, because previous structural work has shown that MppR binds 2KA and reacts to form a Schiff base. 2KA is potentially a competitive inhibitor of MppR. However, this mixture can still be used as a

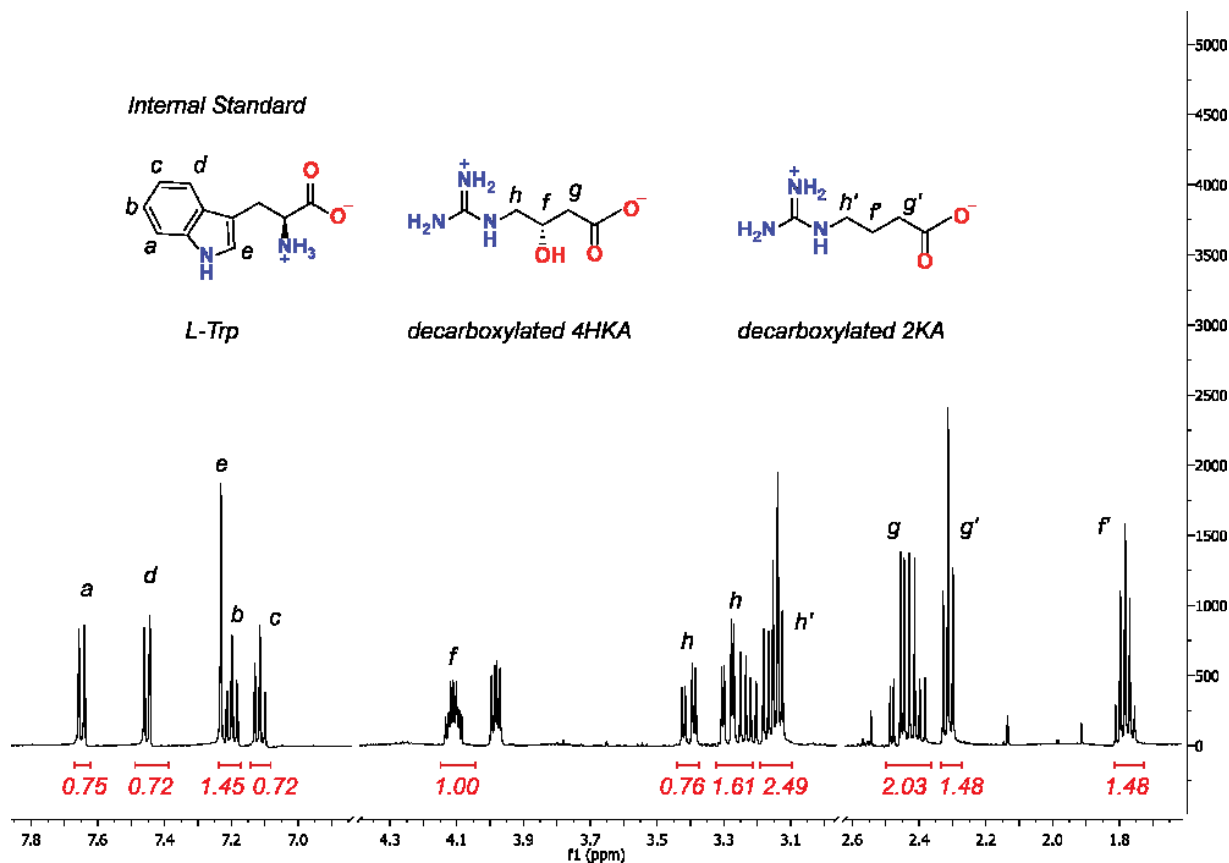


Figure 4-10. ^1H NMR spectrum of enzymatically produced 4(S)HKA doped with L-Trp in deuterium oxide.

4(S)HKA/2KA standard for quantitative MS studies. While it would be more straightforward to simply quantify the DAAO-derived 4(S)HKA using ^1H NMR, this could not be done owing to the very limited quantity of this material available.

To avoid having nonvolatile salts in the samples, the SwMppP reaction with L-arginine was carried out in 50 mM ammonium bicarbonate, pH 9.0. Upon heating, this buffer rapidly decomposes into ammonia and carbon dioxide. Typically, catalase would be added to the reaction to prevent

decarboxylation of products by hydrogen peroxide. However, lyophilized bovine catalase from Sigma Aldrich is stored with a significant amount of trehalose as a stabilizer. Despite buffer exchanging catalase several times, our experiments have shown that traces of trehalose remained in the ^1H NMR samples, complicating analysis and preventing accurate quantification. To generate material for quantitation, the reaction was carried out in an uncapped 50 mL conical tube holding 5 mL of 500 μM SwMppP, 22.8 mM of L-Arg hydrochloride, and 50 mM ammonium bicarbonate pH 9. The reaction was shaken at 100 rpm overnight at 22 $^\circ\text{C}$. The following day, hydrogen peroxide (2%) was added to the reaction mixture and the reaction was left to incubate for 2 h at room temperature. The enzyme was precipitated with 1 volume of acetonitrile and the precipitate was removed via centrifugation at 4000 rpm for 10 minutes. The supernatant was collected and evaporated to dryness using a Centrifan PE rotary evaporator at 40 $^\circ\text{C}$ overnight.

To determine the exact concentration of 4(S)HKA via ^1H NMR, the sample was doped with L-Trp as an internal standard. L-Trp was chosen as the internal standard due to presence of aromatic protons that are lacking in the other compounds present in the reaction mixture. The L-Trp concentration is also readily obtained by UV-Vis spectroscopy. This facilitates accurate determination of peak integral ratios between the L-Trp protons and 4(S)HKA protons, as shown in Figure 4-10.

The solution of 4(S)HKA was prepared by dissolving 6.51 mg of the powder in 1000 μL deuterium oxide. The solution was then doped with 2.04 mg L-Trp. The solution was then vortexed to solubilize all the powder and centrifuged to remove any insoluble particles. The exact concentration of L-Trp in the solution was determined using UV-Vis absorbance by mixing 10 μL of the solution with 990 μL of mQH_2O in a quartz cuvette. The UV-Vis absorbance at 280 nm was measured and the concentration of L-Trp was determined to be 9.19 mM ($\epsilon_{280\text{nm}} = 5690 \text{ M}^{-1} \text{ cm}^{-1}$

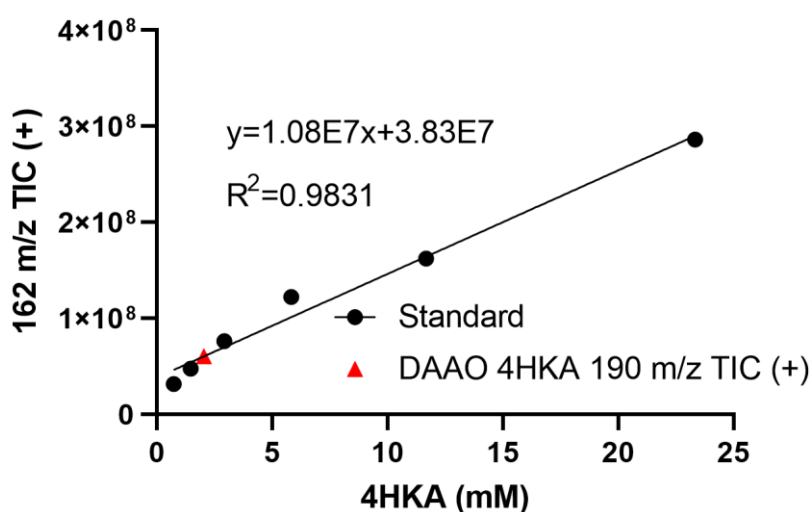


Figure 4-11. Decarboxylated 4(S)HKA standard curve used to determine the concentration of DAAO-derived 4(S)HKA.

¹). The solution was then transferred to an NMR tube and the ¹H NMR spectrum was collected on a Bruker Avance III 500 MHz spectrometer equipped with a Prodigy 5mm X-nuclei optimized cryo probe. Data was processed with MestreNova, including manual phase correction and baseline correction to a 3rd degree Bernstein polynomial. The peak areas of the aromatic protons of L-Trp were averaged to obtain the response of a single proton at 9.19 mM concentration. The concentration of 4(S)HKA was determined by comparing the integral of the C4 peak of 4(S)HKA to the average single-proton integral of L-Trp. It was found to be 11.7 mM 4(S)HKA.

The enzymatically produced 4(S)HKA was serially diluted to obtain a set of accurate concentration standards. The standard samples were dissolved in 50% m_qH₂O/50% LCMS-grade acetonitrile and run through the ZIC-HILIC column on the LCMS-8040 for MS/MS analysis. The MS data were collected in the MRM (multiple reaction monitoring) mode, and all the product ions produced from 162 m/z parent ion were monitored. The method was optimized for detection of product ions. The areas under peaks were manually integrated in the LabSolutions software package (Shimadzu). Blank samples consisting of 50% m_qH₂O/50% acetonitrile were run between each standard sample. The summed responses of all fragments (total ion counts) for each concentration of 4(S)HKA were used to build a standard curve. DAAO-derived 4(S)HKA samples were dissolved in 50% m_qH₂O/50 % acetonitrile and analyzed in the same way as the standards. The responses from the unknowns were used to estimate the concentration of 4(S)HKA from the standard curve (Figure 4-11).

4.2.5 Quench Flow and LC-MS/MS analysis of *MppR* kinetics with 4(S)HKA

The qPod attachment for the SF-61DX2 stopped-flow instrument was installed in place of the spectrophotometer flow cell according to the manufacturer's instructions. Enzyme and substrate were loaded in syringes A and B, respectively, while the quencher was loaded in syringe C. Syringe D was loaded with water to push the quencher and mix it with the aged reaction mixture. The stop

syringe volume was set to 240 μL , as required for double-mixing mode on the SF-61DX2. The maximum volume of a quenched reaction solution that can be recovered from the qPod chamber is 70 μL . The first drive step pushes 150 μL (total) from syringes A and B through the first mixing chamber (M1), filling the age loop while displacing the previous contents into a waste container. The second drive step is timed to give the desired age time of the reaction mixture in the age loop and pushes enough quencher into the second mixing chamber (M2) to immediately stop the reaction. Rather than leaving the second mixer and entering the optical cell as in Figure 4-12, the quenched sample is retained inside the qPod. The quenched sample must then be ejected from the qPod manually, and consequently, variable volumes of the sample are recovered. This poses an issue when

Figure 4-12. Schematic representation of a quenched-flow qPOD double-mixing experiment.

Figure 4-12 is a schematic diagram of a quenched-flow qPOD double-mixing experiment. It shows a flow system with four syringes (Enzyme, Substrate, Quencher, Buffer) at the bottom, each with a fill valve. The Enzyme and Substrate syringes are connected to a first mixing chamber (Mix 1). The Quencher and Buffer syringes are connected to a second mixing chamber (Mix 2). The output of Mix 1 goes to a Sample loop, which then leads to a qPod chamber. A Pushing Syringe is connected to the qPod chamber. A Waste Valve is connected to the top of the qPod chamber. A Stop Syringe and Stop Block are also shown. The system is driven by two drive steps, Drive 1 and Drive 2.

quantifying compounds in the quenched sample that can only be addressed by including an internal standard in the quencher. The sample is recovered by injecting water using a luer lock syringe (Figure 4-13A). During operation, the qPod collection valve is set to DRIVE (Figure 4-13B, left); when recovering samples, it is set to COLLECT (Figure 4-13B, right). It is of crucial importance that there is no air present anywhere in the system, as this will compress and prevent proper displacement of the reactant and quench solutions. Prior to data collection the qPod is carefully flushed with buffer or water and several dummy shots are executed.

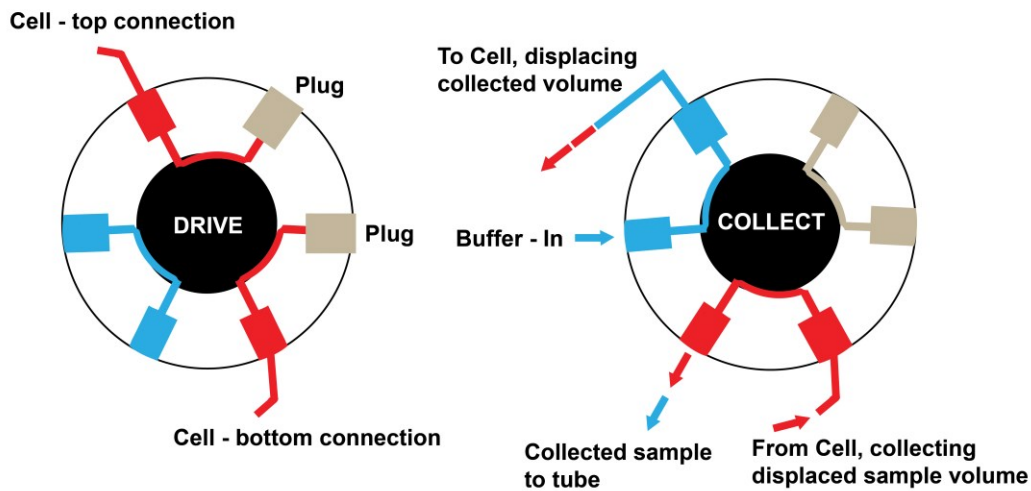
A**B**

Figure 4-13. Side view of the qPod device showing the “pushing syringe” (grey) and the collection valve in the DRIVE position (A). Schematic diagram of the qPod collection valve showing the sample path in both the DRIVE and COLLECT positions (B). Diagram adapted from qPOD manual (TgK Scientific, 2007)

The best way to tell whether there is air in the system is to monitor the flow rates for both drives

in the qPod software module. If there is air in the system, the compression will result in very low flow rates for the drives. In this case, it is necessary to keep flushing the system until the flow rates are in the range of 5 - 10 mL/s for both drives. All quenched-flow experiments used a 10 mL luer lock syringe for recovering samples. This “pushing syringe” should not be removed from the qPod unless the syringe is empty. The removal of the syringe results in unavoidable introduction of air in the system, and several test shots need to be done after replacing the pushing syringe.

MppR was thawed at room temperature and the storage buffer (5 mM sodium phosphate, pH 7.5, 75 mM NaCl) was replaced by 5 mM HEPES, pH 7.5 by cycles of dilution and concentration using a 10 kDa MWCO concentrator. This was done in order to minimize the amount of non-volatile salts that could decrease the sensitivity of the ESI-MS through ion suppression. Prior to buffer exchange, the concentrator was washed with 50 mL of mqH₂O to remove glycerol, which is used as a stabilizer in concentrator membrane. Glycerol impurities could alter the reaction kinetics (unpublished result) and, at sufficient concentrations, could affect mixing in the quenched-flow instrument. Buffer exchange was performed by washing 1 mL of enzyme (160 μM) with 20 mL of 5 mM HEPES pH 7.5. The concentration was determined by measuring absorbance at 280 nm using a Shimadzu 2600 UV-VIS spectrometer. After buffer exchange, the enzyme was diluted to 8 μM using 5 mM HEPES pH 7.5. The 4(S)HKA solutions were prepared in water. The quencher

consisted of 0.5 M hydrochloric acid, 33% acetonitrile, and 2348.6 μM p-nitrophenol (PNP). The concentration of p-nitrophenol was determined by absorbance at 400 nm ($\epsilon_{400\text{nm}} = 18330 \text{ cm}^{-1} \text{ M}^{-1}$).³¹ This was done by mixing 10 μL of the quench solution with 990 μL of 0.1 M

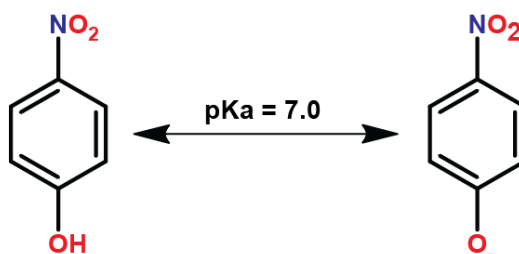


Figure 4-14. Only the deprotonated form of p-nitrophenol absorbs UV light at 400 nm.

sodium hydroxide in a quartz cuvette. This is necessary because PNP is spectrophotometrically active only in its deprotonated form (Figure 4-14). Adding a strong base ensures that all the PNP is deprotonated. The addition of acetonitrile to the quencher may seem redundant, but it is done to prevent solvent mismatch in the LC separation, ensuring symmetrical peak shapes and reproducible peak areas. While strong base would also be a highly effective quencher, it was not chosen out of concern that running a large number of strongly basic samples would degrade the ZIC-HILIC column, which is only stable from pH 3 - 8. The neutralization of basic samples was not an option as the resulting increase in non-volatile salt concentration would also decrease the MS sensitivity. The syringe in position D was filled with mqH₂O. The chosen quench time points were: 5, 15, 30, and 60 s. All solutions were equilibrated to room temperature prior to the experiment to prevent outgassing. The temperature of the solutions in the syringes was maintained at 25 °C with a circulating water bath. The quenched samples were recovered using a water-filled syringe deliver a total volume of approximately 500 µL. The displaced samples were collected in clean 1.5 mL centrifuge tubes. An additional 200 µL of neat acetonitrile was added to minimize solvent mismatch during LC/MS-MS experiments. The concentration of p-nitrophenol in each diluted sample was determined by UV-VIS, combining 100 µL of sample and 900 µL of 0.1 M sodium hydroxide. Each sample was incubated for at least 30 seconds prior to measurement of absorbance at 400 nm. All samples were auto-zeroed prior to measurements.

To maximize sensitivity for the particular mobile phase and samples used in these experiments, several rounds of optimization of the MS instrument parameters were performed prior to data collection. The collision energy (for collision-induced dissociation (CID)), the pre-rod voltage, and the detector voltage were all optimized. To optimize the sprayer position for maximum sensitivity, test samples were run in direct injection mode at different sprayer positions ranging

from 0.5 - 5 mm). For the Shimadzu LCMS 8040, the optimum sprayer position was determined to be 4 mm. Separation of analytes was done using ZIC-HILIC column (3.5 μm , 100 \AA , 50 x 2.1 mm). Mobile phases used were 20 mM ammonium formate pH 4.0 (designated as “A”) and acetonitrile with 0.1% formic acid (designated as “B”). The analytes were eluted via gradient method at 0.5 mL/min and 35 $^{\circ}\text{C}$. The following time program was used in each run: hold at 90% B (0.5 min), decrease to 40% B (2.0 min), hold at 40% B (4.0 min), increase to 90% B (4.5 min), hold at 90% B (5.0). Dwell time for all quantified fragments was 100 ms.

The MS chromatograms showed that MppR reacts with 4(S)HKA to produce 2-ketoenduracididine (2KE). Full separation of 2KE and 4(S)HKA was achieved using the ZIC-HILIC column (Figure 4-15A,B). The major 2KE fragment (83.9 m/z) was used to quantify the amount of 2KE produced by MppR. The decrease in the concentration of 4(S)HKA could not be accurately monitored, because the acidic condition used to quench the reactions promotes formation of a beta-lactone from 4(S)HKA (Scheme 4-2).

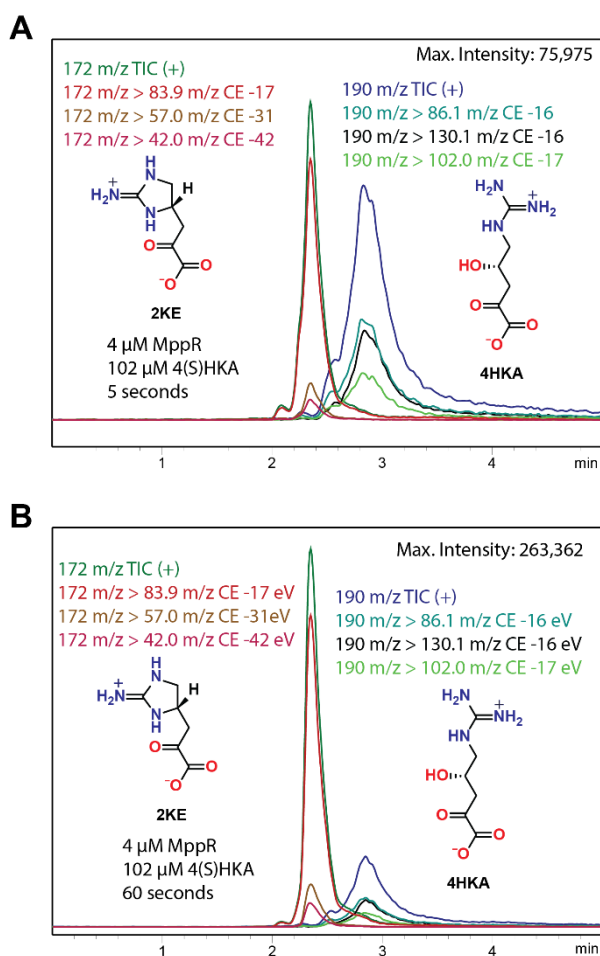
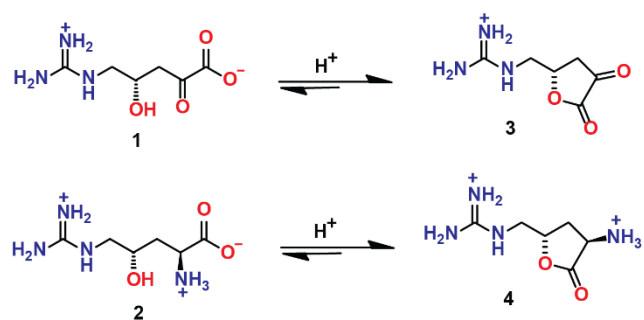


Figure 4-15. LC-MS chromatograms showing an increase in the production of 2KE over a period of 60 seconds. The CE values represent collisional energies used to generate the product ions.

The integrals of 2-KE major fragment were corrected for dilution and converted to concentration using a standard curve generated by running decarboxylated 4(S)HKA standard produced as described in Section X, which were run on the same day as the quench-flow samples. Due to possibility of the instrument desolvation line getting clogged over time, and the subsequent loss of sensitivity, it is of crucial importance that the standards are run at the same time as the samples. The sample sequence was interspersed with blanks, which showed that there was no carry-over between the runs. All measurements were collected as biological triplicates. The MS data analysis yielded steady state parameters for MppR reaction with 4(S)HKA (Figure 4-16).



Scheme 4-2. Both **1** and **2** lactonize under acidic conditions.

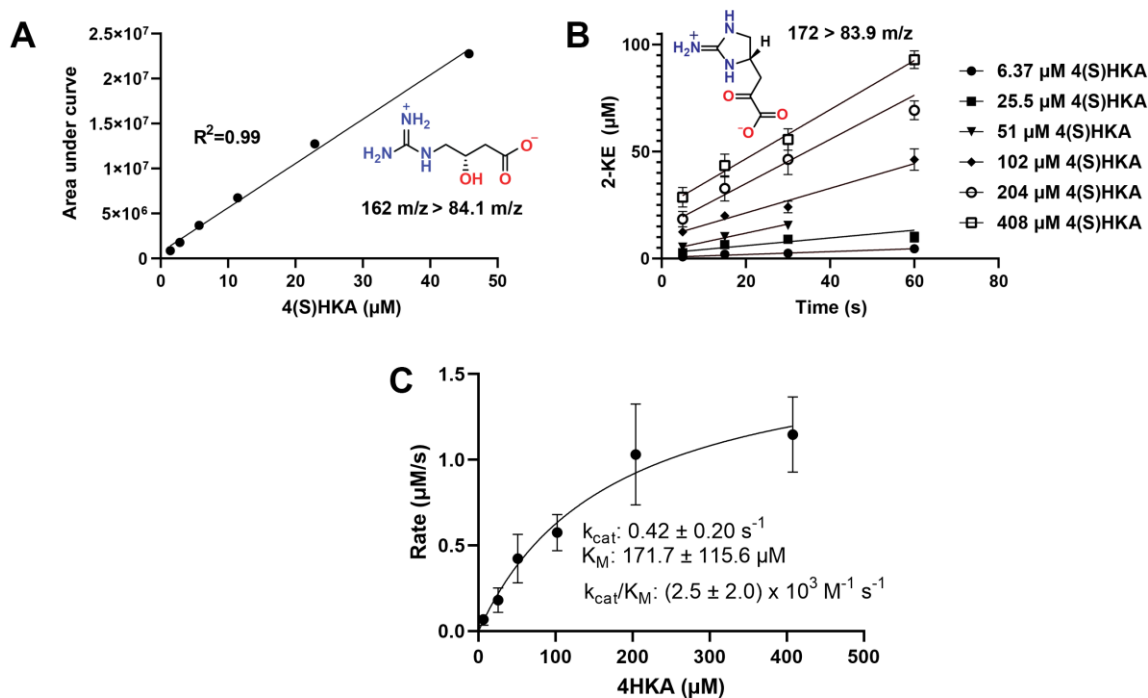


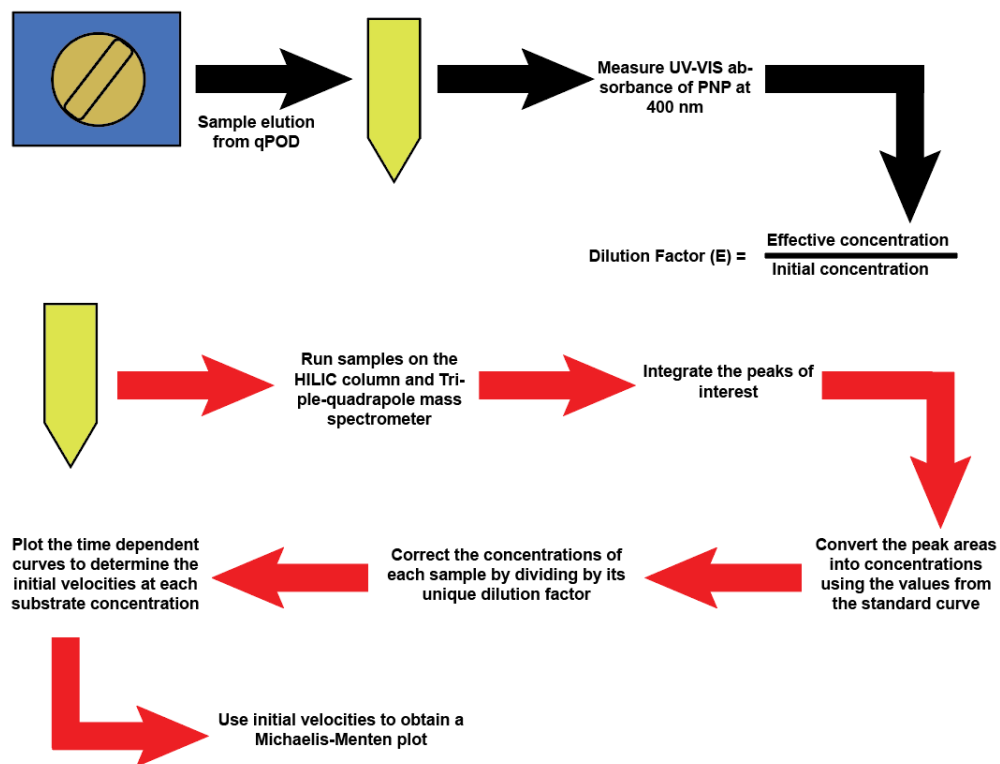
Figure 4-16. Calibration curve used to determine concentrations of 2KE produced by MppR (A). Time-dependent production of 2KE at various concentrations of 4(S)HKA (B). Michaelis-Menten curve for a reaction of MppR with 4(S)HKA (C). For panels B and C, the weighted ($1/Y^2$) non-linear regression fit with outliers detected and removed was performed in GraphPad Prism. The 95% CI (symmetric) of 2KE concentration or initial rates is represented by error bars.

4.3 Discussion

The results of a steady state kinetic analysis of MppR with 4(S)HKA as a substrate are shown in Figure 13. The calibration curve was designed to cover the entire possible range of 2KE concentrations produced by MppR (Figure 4-16A). Regarding the rate dependence on 4(S)HKA concentration, it can be seen that the rate at which 2KE is produced increases together with

4(S)HKA concentration (Figure 4-16B). At each concentration of 4(S)HKA, the increase in 2KE concentration over a period was linear, indicating effective quenching of the reaction. The error relating to the rate measured at 204 μM 4(S)HKA is higher than for other concentrations, and this significantly increases uncertainty related to the Michaelis-Menten constant (K_M) (Figure 4-16C). The turnover number (k_{cat}) value of MppR is comparable to the published k_{cat} of MppP, the enzyme producing 4(S)HKA ($0.2025 \pm 0.0061 \text{ s}^{-1}$).⁵ From an evolutionary perspective, it seems reasonable to assume that MppR did not need to become significantly faster at turning over 4(S)HKA compared to MppP turnover of L-arginine.

In addition to observing turnover of 4(S)HKA by MppR, this discontinuous assay (Scheme 4-3) has allowed us to investigate feasibility of using qPOD module coupled with LC-MS/MS. The use of qPOD seem to be a viable option to study enzyme kinetics in cases where quenching times below 20 ms are not necessary.



Scheme 4-3. Graphical representation of the quench-flow method coupled with LC-MS/MS described in this chapter.

4.4 References

1. Bisswanger, H., Enzyme assays. *Perspectives in Science* **2014**, *1* (1-6), 41-55.
2. McClure, W. R., A kinetic analysis of coupled enzyme assays. *Biochemistry* **1969**, *8* (7), 2782-6.
3. Hendricks, C. L.; Ross, J. R.; Pichersky, E.; Noel, J. P.; Zhou, Z. S., An enzyme-coupled colorimetric assay for S-adenosylmethionine-dependent methyltransferases. *Anal Biochem* **2004**, *326* (1), 100-5.
4. Lento, C.; Wilson, D. J., Unravelling the mysteries of sub-second biochemical processes using time-resolved mass spectrometry. *Analyst* **2017**, *142* (10), 1640-1653.
5. Han, L.; Vuksanovic, N.; Oehm, S. A.; Fenske, T. G.; Schwabacher, A. W.; Silvaggi, N. R., Streptomyces wadayamensis MppP is a PLP-Dependent Oxidase, Not an Oxygenase. *Biochemistry* **2018**, *57* (23), 3252-3264.
6. Han, L.; Schwabacher, A. W.; Moran, G. R.; Silvaggi, N. R., Streptomyces wadayamensis MppP Is a Pyridoxal 5'-Phosphate-Dependent L-Arginine alpha-Deaminase, gamma-Hydroxylase in the Enduracididine Biosynthetic Pathway. *Biochemistry* **2015**, *54* (47), 7029-40.
7. Burroughs, A. M.; Hoppe, R. W.; Goebel, N. C.; Sayyed, B. H.; Voegtline, T. J.; Schwabacher, A. W.; Zabriskie, T. M.; Silvaggi, N. R., Structural and functional characterization of MppR, an enduracididine biosynthetic enzyme from streptomyces hygroscopicus: functional diversity in the acetoacetate decarboxylase-like superfamily. *Biochemistry* **2013**, *52* (26), 4492-506.
8. Ferguson, J. K.; Roughton, F. J., The direct chemical estimation of carbamino compounds of CO(2) with haemoglobin. *J Physiol* **1934**, *83* (1), 68-86.
9. Barman, T. E.; Gutfreund, H., The application of the rapid-flow sampling technique to the chemical identification of intermediates in trypsin-catalyzed reactions. *Proc Natl Acad Sci U S A* **1965**, *53* (6), 1243-5.
10. Lymn, R. W.; Taylor, E. W., Transient state phosphate production in the hydrolysis of nucleoside triphosphates by myosin. *Biochemistry* **1970**, *9* (15), 2975-83.
11. Barman, T. E.; Bellamy, S. R.; Gutfreund, H.; Halford, S. E.; Lionne, C., The identification of chemical intermediates in enzyme catalysis by the rapid quench-flow technique. *Cell Mol Life Sci* **2006**, *63* (22), 2571-83.
12. Clarke, D. J.; Stokes, A. A.; Langridge-Smith, P.; Mackay, C. L., Online quench-flow electrospray ionization Fourier transform ion cyclotron resonance mass spectrometry for elucidating kinetic and chemical enzymatic reaction mechanisms. *Anal Chem* **2010**, *82* (5), 1897-904.
13. Norris, A. J.; Whitelegge, J. P.; Faull, K. F.; Toyokuni, T., Analysis of enzyme kinetics using electrospray ionization mass spectrometry and multiple reaction monitoring: fucosyltransferase V. *Biochemistry* **2001**, *40* (13), 3774-9.
14. Conrad, J. A.; Ortiz-Maldonado, M.; Hoppe, S. W.; Palfey, B. A., Detection of intermediates in the oxidative half-reaction of the FAD-dependent thymidylate synthase from *Thermotoga maritima*: carbon transfer without covalent pyrimidine activation. *Biochemistry* **2014**, *53* (32), 5199-207.
15. Buszewski, B.; Noga, S., Hydrophilic interaction liquid chromatography (HILIC)--a powerful separation technique. *Anal Bioanal Chem* **2012**, *402* (1), 231-47.
16. Dejaegher, B.; Vander Heyden, Y., HILIC methods in pharmaceutical analysis. *J Sep Sci* **2010**, *33* (6-7), 698-715.
17. McCalley, D. V., Understanding and manipulating the separation in hydrophilic interaction liquid chromatography. *J Chromatogr A* **2017**, *1523*, 49-71.
18. Glish, G. L.; Vachet, R. W., The basics of mass spectrometry in the twenty-first century. *Nat Rev Drug Discov* **2003**, *2* (2), 140-50.

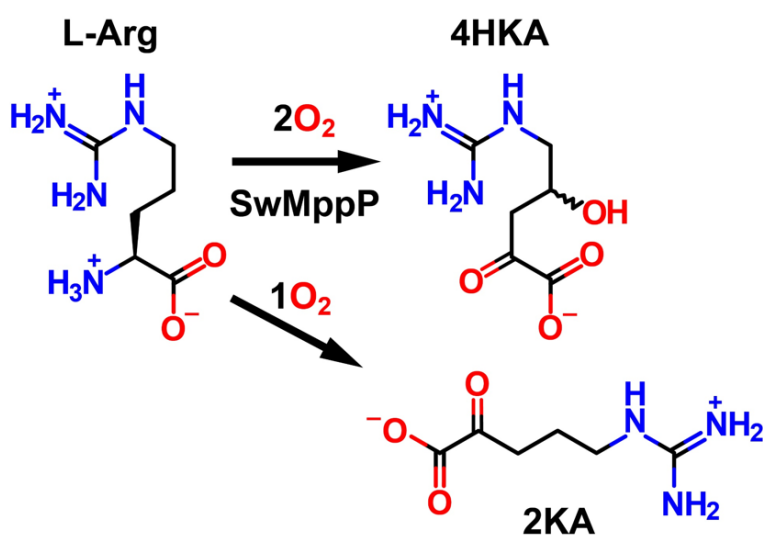
19. Ho, C. S.; Lam, C. W.; Chan, M. H.; Cheung, R. C.; Law, L. K.; Lit, L. C.; Ng, K. F.; Suen, M. W.; Tai, H. L., Electrospray ionisation mass spectrometry: principles and clinical applications. *Clin Biochem Rev* **2003**, *24* (1), 3-12.
20. Krueve, A.; Kaupmees, K., Adduct Formation in ESI/MS by Mobile Phase Additives. *J Am Soc Mass Spectrom* **2017**, *28* (5), 887-894.
21. Banerjee, S.; Mazumdar, S., Electrospray ionization mass spectrometry: a technique to access the information beyond the molecular weight of the analyte. *Int J Anal Chem* **2012**, *2012*, 282574.
22. Roger Giles, D. P. Ion Analysis Apparatus and Method of Use. US8610054B2, 2013.
23. El-Aneed, A.; Cohen, A.; Banoub, J., Mass Spectrometry, Review of the Basics: Electrospray, MALDI, and Commonly Used Mass Analyzers. *Applied Spectroscopy Reviews* **2009**, *44* (3), 210-230.
24. Lange, V.; Picotti, P.; Domon, B.; Aebersold, R., Selected reaction monitoring for quantitative proteomics: a tutorial. *Mol Syst Biol* **2008**, *4*, 222.
25. Annesley, T. M., Ion suppression in mass spectrometry. *Clin Chem* **2003**, *49* (7), 1041-4.
26. Remane, D.; Meyer, M. R.; Wissenbach, D. K.; Maurer, H. H., Ion suppression and enhancement effects of co-eluting analytes in multi-analyte approaches: systematic investigation using ultra-high-performance liquid chromatography/mass spectrometry with atmospheric-pressure chemical ionization or electrospray ionization. *Rapid Commun Mass Spectrom* **2010**, *24* (21), 3103-8.
27. Clarke, W., Mass spectrometry in the clinical laboratory: determining the need and avoiding pitfalls. In *Mass Spectrometry for the Clinical Laboratory*, 2017; pp 1-15.
28. Cimetiere, N.; Soutrel, I.; Lemasle, M.; Laplanche, A.; Crocq, A., Standard addition method for the determination of pharmaceutical residues in drinking water by SPE-LC-MS/MS. *Environ Technol* **2013**, *34* (21-24), 3031-41.
29. Gergov, M.; Nenonen, T.; Ojanpera, I.; Ketola, R. A., Compensation of matrix effects in a standard addition method for metformin in postmortem blood using liquid chromatography-electrospray-tandem mass spectrometry. *J Anal Toxicol* **2015**, *39* (5), 359-64.
30. Geueke, B.; Weckbecker, A.; Hummel, W., Overproduction and characterization of a recombinant D-amino acid oxidase from *Arthrobacter protophormiae*. *Appl Microbiol Biotechnol* **2007**, *74* (6), 1240-7.
31. Bowers, G. N., Jr.; McComb, R. B.; Christensen, R. G.; Schaffer, R., High-purity 4-nitrophenol: purification, characterization, and specifications for use as a spectrophotometric reference material. *Clin Chem* **1980**, *26* (6), 724-9.

Chapter 5

On the mechanism of the L-arginine oxidase MppP from *Streptomyces wadayamensis*

5.1 Introduction

Before this laboratory began working to learn the details of L-enduracididine biosynthesis, all that was known was that the starting material was L-arginine and that the products of the *mppP*, *mppQ*, and *mppR* genes were responsible for the chemical transformations. The exact natures of these transformations—the biochemical activities of these three enzymes and the order in which they act—were completely unknown. Sequence analysis suggested that MppP and MppQ were both Fold Type I PLP-dependent aminotransferases, and that MppR was annotated as an acetoacetate decarboxylase. If the sequence-based function assignments were correct, L-End biosynthesis



Scheme 5-1. MppP produces 4HKA and a partially oxidized abortive product 2KA

would indeed be a puzzling affair. How could two aminotransferases and a decarboxylase cyclize the sidechain of L-Arg? The answer, of course, is that the sequence-based function assignments are entirely fictitious. The first indication of this was our determination that MppR does not catalyze the decarboxylation of any alpha- or beta-keto acid we tested, though an X-ray crystal structure did show that the tertiary structures of MppR and acetoacetate decarboxylase are nearly identical. When crystals of MppR were soaked in a solution containing 4(R/S)-hydroxy-2-ketoarginine, the resulting crystal structure showed that the 4(R/S)-hydroxy-2-ketoarginine had been cyclized and was bound as a Schiff base to the catalytic K156. This species would be 2-ketoenduracididine upon hydrolysis of the Schiff base and release from the enzyme. Thus, at this point it was clear that MppR forms the iminoimidazolidine ring of L-End from the highly oxidized arginine derivative 4(R/S)-hydroxy-2-ketoarginine. Assuming that one of the putative aminotransferases, MppP or MppQ, was a *bona fide* aminotransferase, that enzyme would likely be responsible for converting the 2-ketoenduracididine to L-End. Events proved the fact and we demonstrated that MppQ is a very typical Fold Type I PLP-dependent aminotransferase. The answer to the obvious question of where the 4(R/S)-hydroxy-2-ketoarginine comes from seemed equally obvious, but also puzzling, for how could an enzyme that looks so much like a typical transaminase at the primary sequence level possibly catalyze a 4-electron oxidation of arginine?

The early functional and structural studies of MppP by Han et al. in 2015 quickly dispelled the notion that MppP is an aminotransferase and revealed an enzyme with a rather unique activity. It was observed that, in the presence of L-Arg, MppP consumes dioxygen at a rate that is proportional to both the enzyme and L-Arg concentrations. Product analyses using NMR and mass spectrometry determined that MppP oxidizes L-Arg to a mixture consisting of about 60% of the fully oxidized 4-hydroxy-2-ketoarginine and about 40% of the partially-oxidized, abortive product 2-

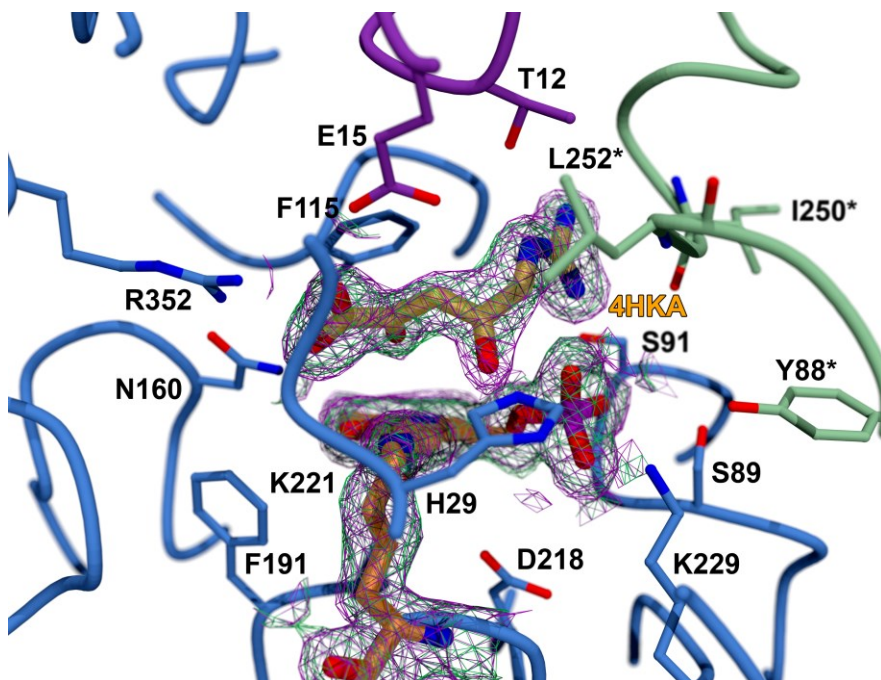


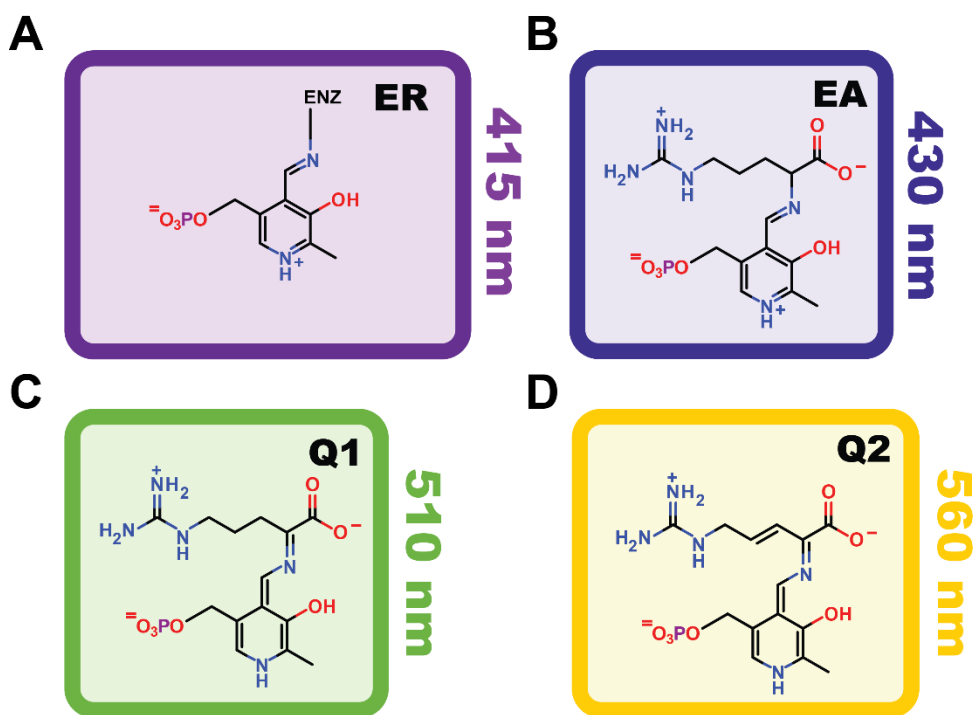
Figure 5-1. Structure of *MppP* active site with 4(*S*)HKA bound. (Han et al., 2018)

ketoarginine. A crystal structure of the enzyme with product bound showed that *MppP* installs the 4-hydroxyl group in the *S* configuration (Figure 5-1). On the basis of these findings, *MppP* was designated as a PLP-dependent hydroxylase (Scheme 5-1).¹ Further investigation by Han et al. in 2018, used $^{18}\text{O}_2$ and H_2^{18}O to determine that both oxygen atoms incorporated into 4HKA derive from water and not from dioxygen.² This result refined the function assignment from hydroxylase (which implies oxygenase activity) to L-arginine oxidase.

5.1.1 Preliminary *MppP* mechanism

Like most PLP-dependent enzymes, *MppP* progresses through a number of intermediates with distinct spectral properties. In both the apoenzyme and the enzyme-substrate complex, the PLP cofactor is covalently attached at C4' to the ϵ -amino group of the catalytic K221. This “internal

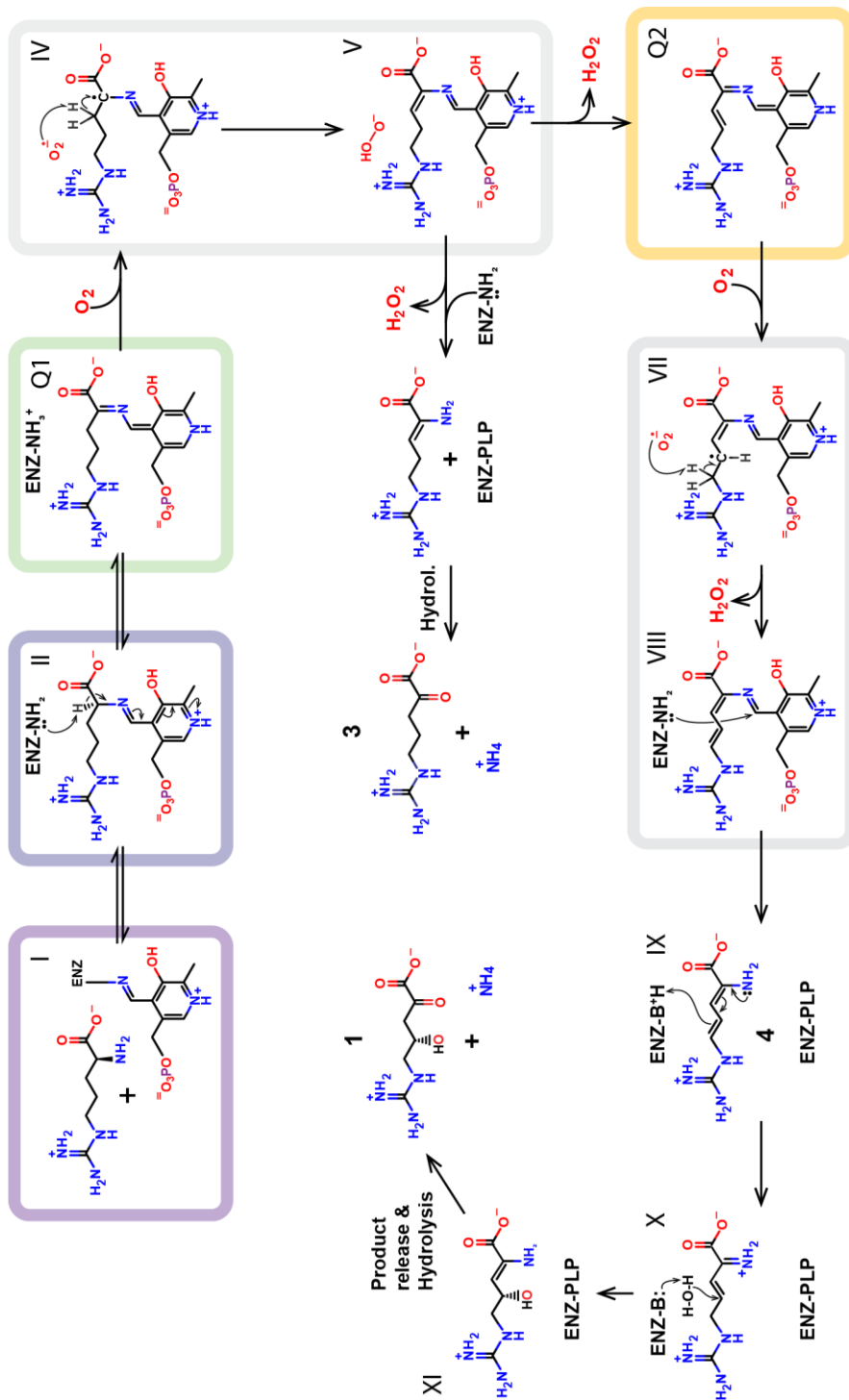
aldimine” species absorbs UV light at 415 nm. Upon attack of the substrate amino group on C4’ of the cofactor, K221 is displaced and the substrate becomes covalently linked to PLP, forming the “external aldimine”, which absorbs light at 425-430 nm. Finally, there are two quinonoid intermediates, Q1 and Q2, which absorb light at 510 and 560 nm, respectively (Scheme 5-2). The accumulation and decay of these intermediates, and the dependencies on the L-Arg and dioxygen concentrations were investigated in pre-steady state kinetics experiments. A preliminary mechanism of MppP was proposed on the basis of these data (Scheme 5-3).



Scheme 5-2. Spectroscopically active intermediates in the MppP reaction with L-arginine. A) Internal aldimine. B) External aldimine. C) First quinonoid intermediate. D) Second quinonoid intermediate

Many PLP-dependent enzymes form quinonoid intermediates like Q1, but these species are generally short-lived. What sets MppP apart is that the active seems designed to stabilize this form of the cofactor to the point that, in the absence of dioxygen, it will persist for several hours. The preliminary MppP mechanism had the external aldimine progress to the first quinonoid. The electron-rich quinonoid then transfers an electron to dioxygen, presumably forming superoxide

and a substrate-centered radical (IV). Abstraction of a proton from C3 of arginine generates peroxy anion and the 2,3-unsaturated species (V), followed by release of hydrogen peroxide. Intermediate V represents the bifurcation point in the mechanism: If a proton is abstracted from C4 of arginine, then the second quinonoid intermediate (Q2) is formed and turnover will result in the fully oxidized product 4HKA. If, on the other hand, K221 attacks at C4' of the cofactor, then the 2-electron oxidized enamine would be released and rapidly deaminated in solution to give 2-ketoarginine. Once Q2 is formed, it can transfer an electron to dioxygen, generating a second substrate-centered radical (VII) and a second equivalent of superoxide. It was envisioned that this molecule of superoxide would abstract a proton from C5 of the substrate to give the 4,5-unsaturated intermediate (VIII). The catalytic K221 would then complete the cycle by attack at C4' of PLP to release the 2,3,4,5-unsaturated enamine. The timing of the installation of the hydroxyl group was conjectural at this stage and remains so. While it is not definitive, the observation of 4(S)-hydroxy-2-ketoarginine in the product-bound crystal structure with no evidence of the 4(R) enantiomer suggests that the hydroxylation is stereospecific and thus occurs on the enzyme. It may even occur before the release of intermediate VIII from the cofactor. It should also be noted that the steps depicted at IV/V and VII/VIII could also be explained as peroxo intermediates at C2 of the substrate. The outstanding questions at this stage were (1) what structural features of the MppP active site are responsible for the extreme stability of the first quinonoid intermediate and (2) how is dioxygen activated for catalysis?

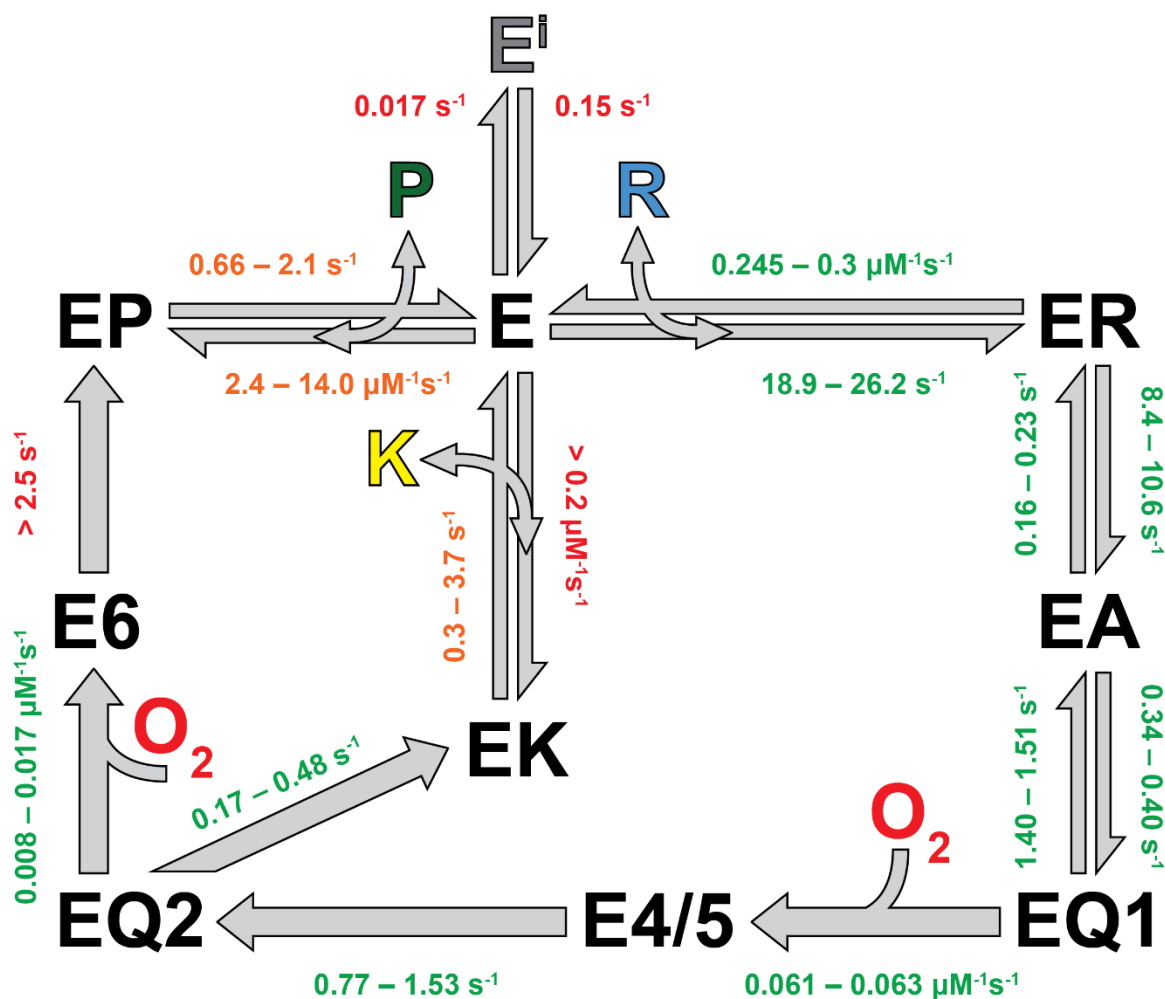


Scheme 5-3. The initially proposed mechanism of L-arginine oxidation catalyzed by MppP.

5.1.2 Determination of microscopic rate constants

Assigning rate constants to particular steps in a complex mechanism like the one proposed for MppP using traditional non-linear least squares fitting would be exceedingly difficult. Indeed, the early attempts to extract mechanistic information from the early pre-steady state kinetic experiments resulted in very limited conclusions. The data for the accumulation and decay of Q2 were impossible to fit at all using standard exponentials. For this reason, we turned to the KinTek Explorer software to simultaneously fit all of the pre-steady state data by simulation^{3, 4}. Upon entering the kinetic model and rough estimates of the various rate constants involved, the software generates and solves the entire set of differential equations in order to calculate the concentrations of species involved in the model and, thus, to estimate the rate constants of each individual step. Of course, entering a very complex model and fitting parameters without any constraint could lead to an excellent fit, but it would represent a non-unique mathematical solution, insufficient for validating the mechanism. In other words, the range of parameter values that could give the same “excellent” fit would be very large. The FitSpace algorithm provides a measure of the reliability of the kinetic parameters for each step in the model.⁵ FitSpace does this by calculating “confidence contours” that provide a range of parameter values that would lead to the same fit. The narrower the range of parameter values, the better the quality of the model.

The preliminary model used to fit the stopped flow data in KinTek Explorer is shown in Scheme 5-4. The numbers associated with each step are the rate constant ranges determined by FitSpace. Those with narrow parameter constraints (< ~25% difference) are colored green, those with much



Scheme 5-4. The Kintek Explorer model with rate constants for the first proposed MppP mechanism.

wider ranges are not as well constrained and are colored orange. The numbers in red represent either lower limits or parameters that were fixed and not refined during the fitting. The fully oxidized product 4HKA is denoted by a “P” and the partially oxidized 2KA product by a “K”. In this scheme it is obvious that the steps leading up to Q2 are reasonably well constrained, but the rate constants for the later steps are not well defined. Obtaining narrow parameter constraints for

every step in the model is challenging, because of a combination of the complexity of the MppP mechanism and a lack for measurable signals for steps following the breakdown of Q2.

5.1.3 Outstanding questions regarding the MppP mechanism

Given that only four intermediates in the model have been experimentally observed and studied, the steps between the quinonoid intermediates and those following breakdown of the second quinonoid remain speculative. The involvement of superoxide has not been experimentally confirmed, and neither has the nature of the proposed substrate radical(s). The involvement of the 4,5-unsaturated intermediate (VIII in Scheme 5-3) is based on chemical intuition and not on any empirical observation. The factors controlling the partitioning down the 4HKA and 2KA branches of the mechanism also remain to be identified. Finally, obtaining additional data regarding the appearance and decay of species proposed in the second half of the mechanism would likely improve the parameter constraints and increase confidence in the proposed model. The work presented in this chapter is aimed at answering these questions and providing a better understanding of the MppP mechanism.

5.1.4 Superoxide oxide detection using electron paramagnetic resonance (EPR)

Electron paramagnetic resonance (EPR) is a spectroscopic technique analogous to nuclear magnetic resonance (NMR) that relies on the interaction of an external magnetic field with unpaired electrons in the sample. When an unpaired electron is subjected to an external magnetic field, the degeneracy of its two spin states is affected and two energetically different spin states form. The lower energy spin state is aligned with the magnetic field, while the higher energy spin

state is oriented against it. An unpaired electron in an external magnetic field can absorb electromagnetic radiation of the associated energy corresponding to the energy between the two spin states. This phenomenon is known as the Zeeman Effect and is described by Equation 1:

$$\Delta E = g\beta B \quad (1)$$

In this equation, B represents the strength of the external magnetic field, β is the Bohr magneton and g is a constant which depends on the environment of the unpaired electron.⁶ This constant is analogous to the chemical shift observed in NMR. The interaction of unpaired electrons with neighboring nuclei leads to hyperfine coupling and additional lines in the spectrum. The number of lines resulting from this coupling is given by Equation 2, where n represents the number of neighboring nuclei and I represents their nuclear spins.⁶

$$\text{Number of lines} = 2nI + 1 \quad (2)$$

The fact that EPR can detect and characterize unpaired electrons, while detecting no signal from diamagnetic species, makes it the method of choice for studying free radicals. However, most free radicals are transient, which leads to very weak EPR signals. The “spin trapping” method was developed to circumvent this issue. Most commonly used spin traps are nitrones (Figure 5-2) which can form stable radical adducts with free radicals.^{6, 7} If the newly formed adduct is long-lived, it can accumulate in solution, making characterization possible.

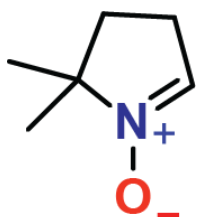


Figure 5-2. The structure of DMPO, a nitron compound commonly used in spin trapping.

The adducts formed with different radicals can be easily distinguished by their characteristic hyperfine lines in the EPR spectra. However, one disadvantage of this technique is that it may complicate characterization of the original free radical, as the signals from coupling with nuclei of the spin trap may obscure the signals from the nuclei on the original free radical.⁶

Due to its roles in biology and disease, a variety of spin traps have been developed to detect and quantify superoxide both *in vivo* and *in vitro*. Superoxide reacts very rapidly with water to form EPR-silent diamagnetic species, making its quantification somewhat challenging. It is less of a problem for *in vitro* experiments, but spin-trapping superoxide can be difficult *in vivo*, since nitron traps do not have sufficient affinity for superoxide to out-compete other reactive species in these complex samples. Additionally, radical adducts could be reduced to diamagnetic species by ascorbate, transition metal ions, or flavoenzymes.⁸

This led to the development of cyclic hydroxylamine probes. Unlike spin traps, spin probes do not trap a free radical. Hydroxylamine-based spin probes, for example, are oxidized by superoxide to form very stable nitroxide radicals. A significant advantage of using cyclic hydroxylamines is that their reactivity with hydrogen peroxide is negligible unless in the presence of transition metal ions.⁹ Given these advantages, a hydroxylamine, 1-Hydroxy-3-methoxycarbonyl-2,2,5,5-tetramethylpyrrolidine (CMH) was used to detect the production of superoxide in the reaction of MppP with L-arginine. Oxidation of CMH by superoxide yields the stable radical CM• (Figure 5-3).

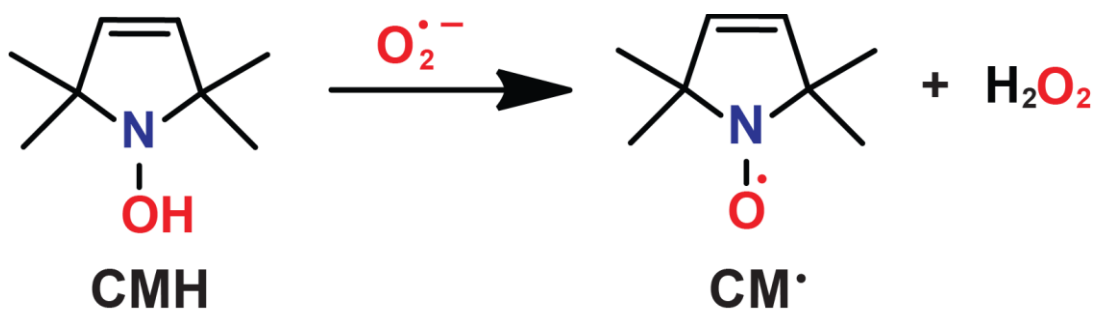


Figure 5-3. Reaction of CMH with superoxide generates the stable nitron radical CM•

5.1.5 Characterizing the carbon-centered radical intermediate

While I have confirmed the involvement of superoxide radical in the reaction via EPR spin-probing, the identity of the free radical produced after proton abstraction by superoxide from the first quinonoid intermediate (Q1) has remained hypothetical. It would be exceedingly difficult to use EPR to identify the carbon-centered radical intermediate. To this end I have designed an experiment relying on formation of a stable adduct that can be characterized using mass spectroscopy.

Since the MppP active site allows molecular oxygen to enter and react with Q1, I hypothesized that a highly reactive radical species such as nitric oxide would be small enough to enter the active

site as well. The nitric oxide could potentially react with a short-lived carbon-centered radical to form a stable adduct that could be detected by mass spectroscopy. The highly reactive nature of NO, of course, presents certain challenges. For one, the reaction of nitric oxide with molecular oxygen is a higher order process¹⁰ and would likely out-compete the desired reaction at high reactant concentrations. However, keeping nitric oxide at sub-micromolar concentration could slow the reaction with dioxygen enough to allow NO a chance to react with an organic radical as well. We took advantage of the fact that catalase, which is usually added to the MppP assay solution to prevent product decarboxylation, forms a complex with nitric oxide ($\text{Cat}(\text{Fe}^{3+})\text{NO}$) with a K_a of $8.7 \times 10^6 \text{ M}^{-1}$.¹¹ This complex would allow for NO to be released gradually into solution. In order to keep the dioxygen concentration low, the reaction was carried out under an inert atmosphere in a glove box. All solution components except for the MppP stock solution were thoroughly degassed. Handling gaseous nitric oxide is impractical and dangerous, so we used a nitric oxide generator, 2-(N,N-diethylamino)-diazonolate-2-oxide (DEANO; Figure 5-4), instead. DEANO rapidly decomposes into 2 equivalents of nitric oxide under acidic conditions. Our previous spin-probing EPR experiments did not confirm whether the superoxide generated during the reaction leaves the MppP active site. If superoxide does leave the MppP active site (which seems unlikely), it could also react with nitric oxide. To prevent this possibility, superoxide

dismutase (SOD) was included in the reaction mixture as well. The metal center of SOD does not bind nitric oxide so SOD does not affect the reaction.

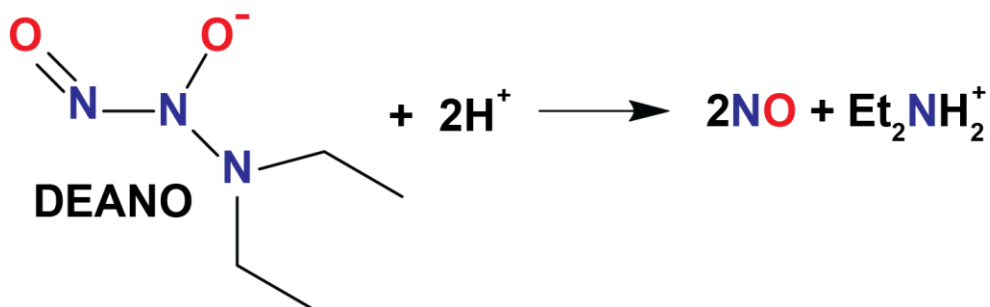


Figure 5-4. Decomposition of DEANO under acidic conditions produces two molecules of nitric oxide and one of diethylamine.

5.1.6 Mechanistic studies of MppP using nuclear magnetic resonance (NMR)

The previously proposed mechanism for the MppP-catalyzed conversion of L-arginine to 4-hydroxy-2-ketoarginine involved a 4,5-unsaturated intermediate generated by proton abstraction at C5 (VIII, Scheme 5-3). However, there was no experimental data to prove the existence of this intermediate and its inclusion in the mechanism was entirely speculative.

To determine whether such a 4,5-unsaturated intermediate is involved in the mechanism, I designed a ¹H NMR experiment in which the MppP reaction would be carried out in deuterium oxide. In such an experiment, the signals from exchangeable protons would diminish or disappear due to hydrogen-deuterium exchange during catalysis. If a proton at C5 were abstracted, this signal would be expected to decrease if reaction were conducted in deuterium oxide. The diastereotopic

protons at C3 would also be expected to diminish in signal since the proposed mechanism includes a step in which superoxide abstracts a proton at C3. Proton abstraction at C3 can occur non-enzymatically as well, since α -keto acids undergo keto-enol tautomerization in solution. In water (or D₂O), the equilibrium lies far toward the ketone, because the carbonyl group is stabilized by hydrogen bonding interactions with the solvent. However, once trifluoroacetic acid is added to the NMR sample, the acidic condition will favor the enol form and one would certainly expect some non-enzymatic hydrogen-deuterium exchange at C3.

5.1.7. Single turnover kinetic experiments with MppP

The preliminary model of the MppP mechanism was derived from a global fit of all available stopped flow pre-steady state data in KinTek Explorer. All the stopped-flow measurements were carried out under quasi-pseudo-first order conditions, where the substrate concentration was at least 2-fold higher than the enzyme concentration. Since KinTek Explorer performs global fits by

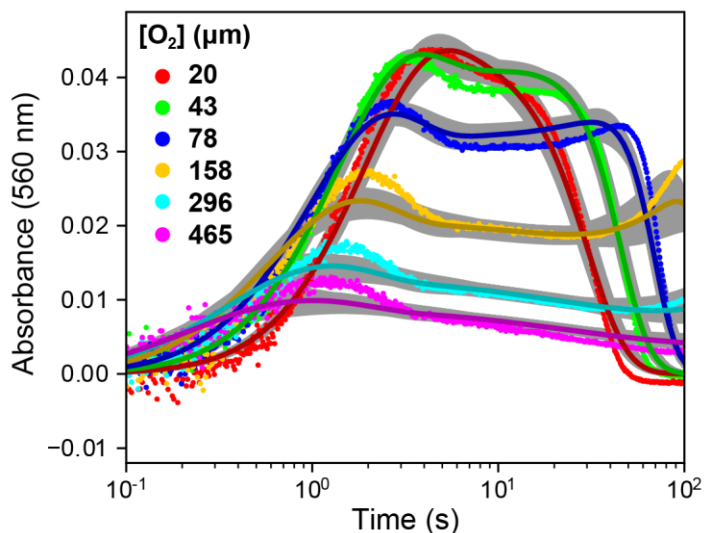


Figure 5-5. Pseudo first-order double-mixing reaction of MppP and L-Arg. Note the multiple phases and broad range of parameters as indicated by gray area around every simulated fit.

simulation, as opposed to traditional non-linear least squares fitting of exponential equations, there

is no need for true pseudo-first order conditions. However, fitting some of the pseudo-first order data was particularly challenging. For example, the data from a double-mixing experiment in which the dependence of the accumulation and decay of the second quinonoid species on the dioxygen concentration was studied via absorbance at 560 nm (Figure 5-5). The presence of multiple, perhaps overlapping, phases makes fitting these data globally with other experiments difficult, which is indicated by significant uncertainty of the simulated fit lines (the gray areas mark the FitSpace parameter boundaries). I hypothesized that the multiphasic behavior of the pseudo-first order data was caused by the enzyme, with its bifurcated mechanism, going through multiple turnover cycles.

To “simplify” the data and improve the signal to noise ratio, I carried out a series of single-turnover experiments on the previously studied intermediates of the MppP catalytic cycle (ER, 415 nm; EA, 430 nm; Q1, 510 nm; Q2, 560 nm). In a single turnover experiment, a very large concentration of enzyme relative to the substrate is used, such that every enzyme molecule undergoes just one catalytic cycle. Single-turnover experiments could not be carried out to observe the decay of the internal aldimine via fluorescence (excitation of the internal aldimine, EA, at 415 nm) due to the fact that the large amount of the internal aldimine (*i.e.* the resting state of the enzyme) saturated the fluorescence detector.

5.1.8. Single turnover experiments with 3,4-dehydro L-arginine

In order to be gain access to the second quinonoid intermediate (Q2) for in-depth kinetic characterization, I carried out single turnover experiments with 3,4-dehydro-L-arginine (DHR) synthesized by the Schwabacher Lab (Figure 5-6). When reacting with MppP, DHR will proceed from the external aldimine directly to the second quinonoid (Scheme 5-5). The kinetic studies

described here were aimed at estimating the rate constants for the accumulation and decay of Q2, and to determine which products result for turnover by MppP.

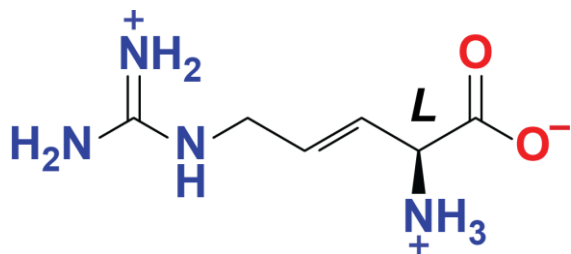
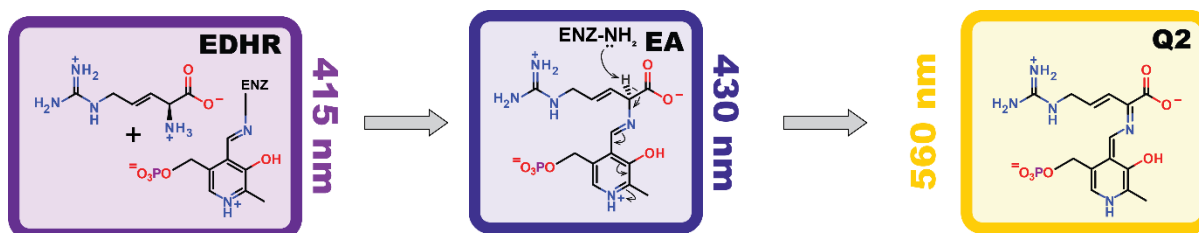


Figure 5-6. Structure of DHR



Scheme 5-5. Reaction of MppP with 3,4-dihydroarginine leads to the formation of external aldimine and then proceeds directly to quinonoid 2 (Q2) intermediate.

5.1.9 Determining the extinction coefficient of the first quinonoid intermediate (Q1)

Herein I present a method for measuring the extinction coefficient of the first quinonoid intermediate (Q1) in the MppP mechanism. Input of experimentally determined extinction coefficient for Q1 can help improve the accuracy of fitting by simulation in KinTek Explorer by removing a variable from the model.

5.1.10 Inhibition of MppP by vinylglycine

Vinylglycine (VG) and its analogues are known to inhibit a number of PLP-dependent enzymes, as the relatively small size of VG allows it to enter a variety of active sites.^{12, 13} VG is proposed to inhibit PLP-dependent enzymes by Michael addition, forming a covalent adduct between the catalytic lysine and the vinyl group of the inhibitor.¹⁴ Given that the MppP active site is significantly different from other PLP-dependent enzymes, this section investigates whether VG can inhibit its activity. This was done by following the rate of formation of Q1 in the presence of VG as monitored by the absorbance at 510 nm.

5.1.11 Solvent isotope effects on MppP catalysis

The measurement of solvent kinetic isotope effects (KIE) represents a powerful tool for studying enzymatic reactions. When a reaction involves solvent-sensitive steps, such as nucleophilic attacks by water molecules, or protonation, the rate constants for those steps will differ when the reaction is conducted in deuterium oxide.¹⁵⁻¹⁷ Solvent KIEs can be described by Equation 3. If the rate constant is higher in water, that is considered a normal solvent KIE, while the opposite case is called an inverse solvent KIE. Studies of solvent KIEs have helped support the mechanisms of enzymes such as β -lactamases,¹⁸ and helped improve our understanding of conformational dynamics of ribonuclease A.¹⁹ However, when multiple steps involve solvent, or there are multiple catalytic residues that could be affected by proton/deuterium exchange, the deconvolution of the effects becomes exceedingly difficult.

$$\text{Kinetic isotope effect} = \frac{k_{HOH}}{k_{DOD}} \quad \text{Equation (3)}$$

Since the proposed mechanism of MppP involves protonation by a lysine residue which can undergo rapid hydrogen-deuterium exchange of hydrogens on the amino group, solvent KIEs could be used as a tool to gain more insight into the mechanism of MppP. This section presents preliminary stopped flow experiments to verify the existence of solvent KIEs on the MppP reaction. Future work will elaborate on these results and extend to the use of specifically labeled L-Arg substrates to gain mechanistic insights.

5.1.11 Factors affecting the ratio of MppP products

Wild-type MppP always produces both the fully oxidized 4-hydroxy-2-ketoarginine (4HKA) and the partially oxidized 2-ketoarginine (2KA). Since MppP is most active under basic conditions (pH > 8.0), all NMR experiments were carried out in sodium phosphate, pH 8.4. Phosphate was the chosen buffer, because it does not produce any signal in NMR spectra. The ratio of the two products under this condition was approximately 60 % 4HKA and 40 % 2KA. However, in the NMR analysis of reactions run in deuterium oxide and in water discussed earlier in this chapter (see Section 5.3.4) it was observed that this ratio was perturbed in the reaction run in D₂O, which contained more than 80 % 4HKA. This apparent influence of pH and/or ionic strength on the partitioning of the reaction between the two branches of the mechanism led us to investigate further into factors that affect the ratio of products produced by MppP.

5.1.12 Using quenched-flow LC-MS/MS to accurately determine the product ratio at early times in the oxidation of L-arginine by SwMppP

Previously, our lab determined the ratio between the 4(S)HKA and 2KA produced by MppP in the reaction with L-arginine indirectly by measuring the amount of oxygen consumed by the enzyme in a Clark electrode-based assay. Using this assay, it was determined SwMppP catalyzes the oxidation of L-Arg and O₂ into 4HKA and 2KA with a ratio of approximately 1.7:1 when carried

out in BTP pH 9.0. Direct analysis of the products was also performed using ^1H NMR. Both these methods are imperfect, because neither can provide direct product measurements on a timescale of seconds. The previously described quenched-flow LC-MS/MS method can solve these problems and elucidate the kinetics of 4HKA and 2KA production at short reaction times.

5.2 Materials and Methods

5.2.1 CMH reaction with MppP.

The MppP reaction was conducted in 20 mM potassium phosphate, pH 8.4, 20 μM wild-type MppP, 500 μM L-Arg and 10 mM freshly prepared CMH. The CMH solution was prepared in MiliQ water. Out of concern that closure of the N-terminus over the active site could preclude CMH from accessing the catalytic center, an identical reaction was set up using MppP $^{\Delta 1-22}$, an N-terminal truncation mutant where the first 22 residues of the protein have been removed. Immediately after mixing, the reaction contents were transferred to a glass capillary tube via syringe. Data collection was initiated immediately upon placing the capillary tube into the sample holder. Data were collected at room temperature using a Bruker EMX spectrometer. Data acquisition was performed at 9.47 GHz, microwave power of 2.08 mW, attenuation of 20.0 dB, field sweep of 140 G, amplitude modulation of 1 G at 100 kHz, time constant of 5.12 ms, and a delay time of 3.0 s.

5.2.2 NMR of MppP reaction in the presence of CMH

The total volume of the reaction was 5 mL and it was carried out in a 50 mL polypropylene tube. The reagent concentrations were 2.5 mM CMH, 20 μM wild type MppP, and 2 mM L-Arg in 20 mM phosphate, pH 8.4. A control reaction lacking CMH was also carried out. Both reactions were

run overnight at 25 °C, while shaking at 220 rpm. Reactions were quenched using 5 mL of methanol and evaporated to dryness in a Centrifan PE centrifugal evaporator (KD Scientific). The dried residue was dissolved in 1 mL of deuterium oxide and centrifuged at 4000 rpm for 10 minutes to remove insoluble material (e.g. precipitated enzyme). A 700 µL portion of the supernatant was loaded into an NMR tube for analysis.

5.2.3 Reaction of MppP in the presence of nitric oxide

To ensure that all of generated nitric oxide was bound in the Cat(Fe³⁺)NO complex, a 2.6-fold molar excess of catalase was used. The exact concentration of catalase was determined using the absorbance at 405 nm ($\epsilon_{\text{tetramer}} = 420 \text{ mM}^{-1} \text{ cm}^{-1}$). The complex of catalase and nitric oxide absorbs strongly at 570 nm ($\epsilon_{\text{cat}\cdot\text{NO}} = 30 \text{ mM}^{-1} \text{ cm}^{-1}$). Thus, by monitoring the absorbance at 570 nm, we could ensure that catalase was not saturated. All solution preparation steps were carried out inside a glovebox, under a nitrogen atmosphere. Lyophilized bovine catalase was dissolved in 100 mM bis-tris propane, pH 7. A 20 mM DEANO stock was prepared in 0.1 M sodium hydroxide. Lyophilized SOD (bovine, > 2500 U/mg) was dissolved in 10 mM potassium phosphate, pH 7.4, at a concentration of 200 µM. The solutions were added to a quartz cuvette at the following concentrations: 21 µM catalase, 8 µM DEANO, 500 nM SOD, 2 mM L-arginine, 20 µM MppP, and 100 mM bis-tris propane, pH 7. The reaction mixture was allowed to stand under inert atmosphere for 1 hour, and then quenched with 1 volume of methanol. The sample was centrifuged for 5 minutes at 13,000 rpm and then analyzed by direct injection on an LCMS 8040 triple quadrupole instrument (ESI (+) mode, 1st quadrupole scan). A control sample was prepared as described above, save for the omission of MppP.

5.2.4 Reaction of MppP and L-Arg in deuterium oxide

The wild-type SwMppP used in these experiments was buffer exchanged into deuterium oxide (99.8% atom D, Sigma Aldrich) using a 10 kDa MWCO centrifugal concentrator. The reaction contained 20 μ M enzyme and 2 mM L-arginine monohydrochloride. A 500 mM arginine stock was prepared by dissolving the powder in deuterium oxide. The reaction (5 mL total volume) was conducted in a 50 mL polypropylene tube placed in a shaking incubator set to 200 rpm overnight at RT. The reaction was protected from light by draping the vessel in aluminum foil so that oxygen exchange would not be restricted. A control reaction was conducted in mqH_2O in exactly the same manner as the deuterium oxide reaction. The next day, the reactions were quenched using 1 volume of acetonitrile, centrifuged for 10 minutes at 4000 RPM and then evaporated to dryness using a Centrifan PE centrifugal evaporator (KD Scientific). The dried residue was dissolved in 700 μ L of deuterium oxide and 0.1% trifluoroacetic acid (TFA). In previous studies of MppP reaction products using 1H NMR, I had observed that the diastereotopic protons at C3 appear as a doublet, instead of appearing as a multiplet due to coupling with each other and the neighboring proton on C4. In order to split the doublet of diastereotopic C3 protons into a multiplet, I tested various methods of perturbing the environment. One attempt included introducing metal ions such as calcium into the NMR sample in the hope that the salt formed with the carboxylic acid would perturb the environment of the diastereotopic protons. This method proved ineffectual. However, addition of 0.1% trifluoroacetic acid resolved the doublet into a multiplet, and I was able to measure the coupling constants for the diastereotopic protons at C3. The NMR data were collected using a Bruker DRX500 500 MHz spectrometer.

5.2.5 Wild-type MppP single turnover with L-Arg

Double-mixing single-turnover experiments monitoring absorbance at 510 nm and 560 nm were carried out using an SF-61DX2 stopped-flow instrument manufactured by TgK Scientific

(Bradford-on-Avon, UK) equipped with a photomultiplier tube detector. Single-mixing, single-turnover experiments monitoring absorbance at 510 nm were carried out on the same instrument equipped with a charge-coupled device (CCD) array detector.

Prior to all experiments, approximately 10 mL of anaerobic solution containing 20 mM HEPES, pH 7.5, and 10 mM glucose were prepared and loaded into the body of a tonometer; 150 μ L of 1000 U/mL glucose oxidase stock (*Aspergillus niger*, prepared in 20 mM HEPES, pH 7.5) were placed in the sidearm. Dioxygen was removed from the solutions by connecting the tonometer to a Schlenk line and performing 45 purge-flush cycles (~5 s under vacuum and 30 s under argon). Once the solution was anaerobic, the buffer in the body of the tonometer was allowed to mix with the glucose oxidase stock in the sidearm. The stopped flow instrument was flushed with the anaerobic solution and to stand overnight to “scrub” the residual oxygen from the Teflon components. The following day, MppP solution was prepared in a similar way. The enzyme was purified as described by Han et al.¹ and stored in 20 mM MES, pH 6.7, 20 μ M PLP. The body of the tonometer was filled with 5-10 mL of solution containing enzyme (in 20 mM MES, pH 6.7, 20 μ M PLP) and 200 μ M glucose. To one of the two sidearms were added 30 μ L of glucose oxidase (from the same 1000 U/mL stock). Since MppP is light sensitive, the tonometer was covered with aluminum foil during preparation. In order to prevent outgassing and bubble formation during stopped flow analysis, the tonometer was prepared at room temperature. After making the tonometer anaerobic via 45 purge-flush cycles, the glucose oxidase solution in the side arm was mixed with the enzyme solution in the body of the tonometer. The glucose/glucose oxidase removed any remaining traces of dioxygen left after the purge-flush cycles.²⁰ Arginine solutions in 200 mM bis-tris propane (BTP), pH 9.0, with 200 μ M glucose were placed in a glass syringe, sparged with argon for 5 minutes, and injected with 10 μ L of 1000 U/mL glucose oxidase. All the

enzyme and L-Arg concentrations are diluted 2-fold after single-mixing, and 4-fold in the case of double-mixing. Concentrations after mixing are inside the parentheses. All experiments were carried out at room temperature (22 °C).

510 nm single-mixing experiment: 854 (427) μM of enzyme was anaerobically mixed with 3.12 – 50 μM (1.56 – 25 μM) L-Arg. The reaction was monitored for 25 seconds, determined by the time necessary for the signal to plateau.

415 nm single-mixing experiment: 20 (10) μM of enzyme was anaerobically mixed with 40 (20) – 1280 (640) μM L-Arg. The fluorescence signal was monitored for 10 seconds.

510 and 560 nm double mixing experiments: In order to study the dependence of the MppP reaction rate on the concentration of dioxygen, an anaerobic solution containing enzyme and L-Arg mixed in 1:1 was reacted with an oxygenated buffer containing a range of dioxygen concentrations. The oxygenated buffer was prepared using a Maxtec Maxblend gas blender to mix oxygen and nitrogen. The Clarke electrode was used to measure the oxygen levels in the buffer and adjust the mixing valve to achieve the desired concentrations. In the first mixing step, 1360 (340) μM MppP was mixed with 40 (10) μM L-Arg and aged for 30 seconds to allow time for Q1 to accumulate fully. In the second mixing step, the MppP/L-Arg reaction from the first mixing step was mixed with an equal volume of oxygenated 100 mM BTP, pH 9.0 (40 – 325 μM dioxygen after mixing) with 100 μM glucose (to prevent viscosity mismatch between the various solutions that could give artifacts (Schlieren lines) in the spectrophotometer cuvette). The buffer used to push the dioxygen solution and the substrate/enzyme mix in the second mixing step was anaerobic 100 mM BTP, pH 9.0, 100 μM glucose. The reactions were monitored for 100 seconds.

5.2.6 Wild-type MppP single turnover with DHR

A 1 mM stock solution of DHR in water was prepared from DHR powder (2.3 % purity). All enzyme, substrate, and buffer concentrations mentioned are post single/double mixing.

560 nm single-mixing: 1170 (585) μ M MppP in 10 mM MES, pH 6.7, 10 μ M PLP, 100 μ M glucose was reacted with 6.24 (3.12) – 100 (50) μ M DHR in 100 mM BTP, pH 9.0, 100 μ M glucose. Absorbance at 560 nm was monitored for 100 seconds.

560 nm double-mixing: 1148 (287) μ M MppP in 5 mM MES, pH 6.7, 5 μ M PLP, 100 μ M glucose was reacted with 40 (10) μ M DHR for 0.2 seconds and then mixed with oxygenated buffer to yield final dioxygen concentrations of 0 – 315 μ M. The sample was not aged because it decays in the absence of oxygen as well, and I wanted it to decay primarily due to added oxygen. The relative rates of Absorbance at 560 nm was monitored for 100 seconds.

5.2.7 MppP and DHR product analysis

A 1 mL solution of MppP (295 μ M) in 5 mM MES pH 6.7, 5 μ M PLP and 100 μ M glucose was added to a tonometer. A solution of 200 μ L glucose oxidase (1000 U/mL in 20 mM HEPES pH 7.5) and 200 μ L of 5 mM DHR (in 800 mM BTP pH 9) was then added to one of the tonometer bulbs. A high concentration of bis-tris propane was used, so that after mixing, the concentration of bis-tris propane, pH 9.0, would be 114 mM, more than 20 times concentration of the enzyme storage buffer (5 mM MES, pH 6.7). After 45 purge-flush cycles with argon (See the MppP and L-Arg single-turnover section above), the enzyme was mixed with the glucose oxidase and DHR in the sidearms. The concentration of DHR in the resulting solution was 714 μ M. This solution was kept under positive argon flow during the reaction for a period of 10 minutes. The reaction was quenched using 5 mL of pure methanol (previously sparged with argon for 10 min) which was

injected through the septum (Figure 5-4B). The solution was then exposed to air and centrifuged at 4000 rpm for 10 minutes to remove the denatured enzyme. The sample was placed in a MS vial. Data were collected on a Shimadzu LC-MS 2020 via direct injection (mobile phase A: water, mobile phase B: methanol, 0.1% formic acid). Injections consisted of 50 μL of sample. The scan range was from 130-200 m/z .

5.2.8 Determination of Quinonoid 1 extinction coefficient

Enzyme and substrate solutions were prepared in two separate tonometers. The first tonometer contained 2 mL of 500 μM MppP in 20mM MES, pH 6.7, 20 μM PLP, and 200 μM glucose; 30 μL of glucose oxidase (1000 U/mL) were placed in a sidearm. The second tonometer contained 5 mL of 12.5 μM L-Arginine in 200 mM BTP, pH 9.0, and 200 μM glucose, with 50 μL glucose oxidase in a sidearm. Both tonometers were made anaerobic with 45 purge/flush cycles as described earlier. After mixing, the MppP concentration was 100 μM and the L-arginine concentration was 10 μM . The enzyme concentration was kept ten-fold higher than the substrate concentration to ensure that most of the substrate would be bound to the enzyme. UV-VIS spectra were collected on a Varian Cary 50 UV-VIS spectrometer inside a nitrogen glovebox (MBraun). The spectrometer was blanked with L-arginine in BTP pH 9.0, prior to adding the enzyme to the cuvette. Scans were collected at 30-second intervals. Once it was established that Q1 was stable, the 3 scans were averaged and Beer's Law (Equation 4), where A is absorbance, ϵ is extinction coefficient, b is path length and c is concentration, was used to calculate the extinction coefficient

for Q1. The path length of the quartz cuvette was 1 cm. which was found to be 29173.63 ± 470.46 $M^{-1} \text{ cm}^{-1}$.

$$A = \epsilon bc \quad (\text{Equation 4})$$

5.2.9 Wild-type MppP reaction with L-Arg in the presence of vinyl glycine

Two identical reactions of MppP and L-Arg in the presence of L-VG were set up in quartz cuvettes. In one, the enzyme was preincubated with VG for 15 minutes prior to data collection, while the other had no preincubation period. The reactions both contained 1 mM L-Arg, 1 mM VG, 10 μ M MppP, 100 mM BTP, pH 9.0. The control reaction contained 1 mM L-Arg, 10 μ M MppP and no VG. Data were collected at room temperature. The UV-VIS spectra were collected on a Hewlett-Packard 845 diode array spectrophotometer. The volume of all three reactions was 1 mL.

5.2.10 Wild-type MppP single turnover of L-Arg in deuterium oxide

The bis-tris propane (BTP) and MES buffers used in these experiments were prepared by dissolving the dry powders in deuterium oxide and adjusting the pD value using deuterium chloride. The pD value was measured using a standard pH electrode and corrected for pD using Equation 4.²¹

$$pD = pH + 0.44 \quad (4)$$

MppP was desalted in 20 mM MES, pD 6.3, 20 μ M PLP by washing the enzyme with 20 volumes of deuterated buffer in a 10 kDa MWCO concentrator. An L-Arg stock was prepared in deuterium oxide and diluted using 200 mM BTP, pD 8.6, 200 μ M glucose (prepared from a 1 M stock in

deuterium oxide). An *Aspergillus niger* glucose oxidase (Millipore-Sigma) stock was prepared by dissolving lyophilized enzyme in deuterium oxide to 1000 U/mL.

Single-turnover double-mixing at 510 and 560 nm: 920 (230) μ M MppP and 40 (10) μ M L-Arg were reacted with 38 (19) – 366 (183) μ M dioxygen in deuterium oxide. Anaerobic 100 mM BTP, pH 9.0, 100 μ M glucose was used to push solutions into the second mixer (syringe D). Prior to the second mixing step, the sample was aged for 50 seconds. The absorbance at 510 or 560 nm was monitored for 500 seconds.

Single-turnover single-mixing at 510 nm: 606 (303) μ M MppP was mixed anaerobically with 3.0 (1.5) – 50 (25) μ M L-Arg in 100 mM BTP, pD 8.6, 100 μ M glucose (post-mixing concentrations). The absorbance at 510 nm was monitored for 50 seconds.

Pseudo first-order single-mixing fluorescence: 20 (10) μ M MppP and 40 (20) – 640 (320) μ M L-Arg in 100 mM BTP, pD 8.6, 100 μ M glucose (post-mixing concentrations) were mixed anaerobically. The internal aldimine was excited at 415 nm and the total emission was monitored for 50 seconds.

5.2.11 Wild-MppP reactions with L-Arg at different pH and temperature values

Reactions comparing different pH values were carried out in water (pH \approx 7.0), 20 mM phosphate, pH 8.4, and 10 mM 2-[(2-amino-2-oxoethyl)-(carboxymethyl)amino]acetic acid (ADA), pH 6.4. Each reaction contained 20 μ M MppP and 2 mM L-Arg. Reactions were incubated overnight at 22 $^{\circ}$ C with shaking at 220 rpm. Reactions were quenched with 1 volume of neat methanol, centrifuged at 4,000 rpm for 10 minutes to remove the precipitated protein, and evaporated to dryness in a CentrifanTM PE centrifugal evaporator (KD Scientific). To test the effect of temperature on the product ratio, two identical reactions containing 20 μ M MppP, 2 mM L-Arg in 10 mM phosphate,

pH 8.4, were carried out at 37 °C and 4 °C. In order to minimize the effect of the storage buffer on activity, the protein was desalted in 10 mM phosphate, pH 8.4, using a 10 kDa MWCO concentrator. The reactions (5 mL) were carried out in 50 mL polypropylene tubes while shaking at 220 rpm overnight. Reactions were quenched, centrifuged, and evaporated to dryness as described above.

5.2.12 Quench-flow LC-MS/MS of wild-type MppP reaction with L-Arg

The quenched-flow experiments and sample preparation was done as described in Chapter 4. Separation of analytes was done using ZIC-HILIC column (3.5 μm , 100 Å, 50 x 2.1 mm) and MS analysis was carried out on Shimadzu LC-MS/MS 8060. Mobile phases used were 20 mM ammonium formate pH 4.0 (designated as “A”) and acetonitrile with 0.1% formic acid (designated as “B”). The analytes were eluted via gradient method at 0.5 mL/min and 40 °C. Injection volume was 0.7 μL . The following time program was used in each run: hold at 90% B (0.5 min), decrease to 40% B (2.0 min), hold at 40% B (4.0 min), increase to 90% B (4.5 min), hold at 90% B (5.0). The highest sensitivity for the mobile phases used was determined to be at a sprayer position of 0.5 mm. The concentrations listed are after single-mixing (2-fold dilution). 20 μM of MppP (in 2.5 mM MES, pH 6.7, 10 μM PLP) and 480 μM L-Arg (10 mM BTP, pH 9.0) were quenched using 0.5 M hydrochloric acid, 33% acetonitrile, and 2348.6 μM p-nitrophenol (PNP). The samples were quenched at 0.94, 1.87, 3.75, 7.5, and 15 seconds in triplicate. Elution from the qPOD attachment was done using pure acetonitrile. The samples were fully decarboxylated using the method described in Chapter 4. The 4HKA and 2KA used to make the standard curves were prepared in the same matrix as the samples. Decarboxylated 4HKA and 2KA obtained from the MppP reaction were used as standards (Figure X). The concentrations of standards were roughly approximated by NMR (Figure 5-), using the relative ratio of the two products.

5.3 Results

5.3.1 MppP reaction with L-Arg generates superoxide

As shown in Figure 5-7, as the reaction of wild type MppP with L-arginine proceeds, there is a linear increase in superoxide concentration as indicated by an increase in the EPR signal with hyperfine splitting characteristic of a stable nitroxide radical. The reaction of the truncated MppP^{Δ1-22} followed the same pattern (data not shown). This result confirms that the Mpp-catalyzed reaction proceeds through a free radical mechanism involving superoxide. However, this experiment was not quantitative, so it provided no information about the kinetics of the reaction.

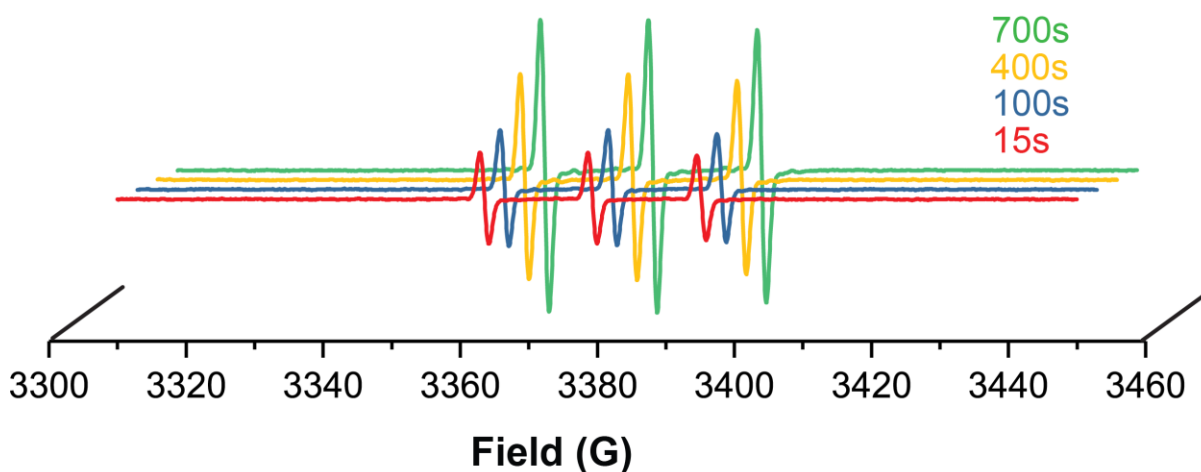


Figure 5-7. First-derivative plots of the time-dependent EPR spectra of the MppP reaction with L-Arg in the presence of CMH (selected time points chosen for clarity).

A question that was not addressed by this experiment was whether the spin probe CMH enters the MppP active site to react with superoxide or reacts only with superoxide that has left the active site. The best way to test this would be to repeat the experiment in the presence of superoxide dismutase. Superoxide dismutase converts two molecules of superoxide into one molecule each of dioxygen and hydrogen peroxide. Therefore, CMH should be EPR silent if it only reacts with superoxide that has left the MppP active site. However, due to limited access to EPR instrumentation, I instead attempted to determine whether CMH enters the active site using NMR.

The rationale behind the NMR experiment was that if CMH does enter the active site, it could perturb the rate of the MppP reaction as well as the ratio of products ratio by consuming superoxide. Since it is not a highly selective spin probe, it could perhaps react with carbon-centered radical as well, thus poisoning the reaction, and preventing it from going to completion.

5.3.2. NMR analysis of MppP reaction in the presence of CMH

The ¹H NMR spectrum in Figure 5-8A shows the ratio of products of the control reaction containing MppP and L-arginine in the absence of CMH. There is approximately 60% 4-hydroxy-2-ketoarginine and 40% 2-ketoarginine, consistent with previous measurement of MppP reaction products from reactions in the same buffer at room temperature. The NMR spectrum in Figure 5-3b shows that in the presence of CMH the ratio of products shifts in favor of the fully oxidized product 4HKA (73% vs 60% in the control). Since the factors governing the ratio between these two products are currently under investigation, it is not clear that this shift was the result of CMH

interaction. For instance, it is possible that a modest difference in ionic strength when CMH is added could have altered the ratio. However, our preliminary studies have shown that conditions that slow down enzyme turnover, such as lowering the pH or the temperature, shift the ratio in favor of 4-hydroxy-2-ketoarginine. Thus, it is plausible that CMH has entered the active site and slowed the reaction by reacting with superoxide.

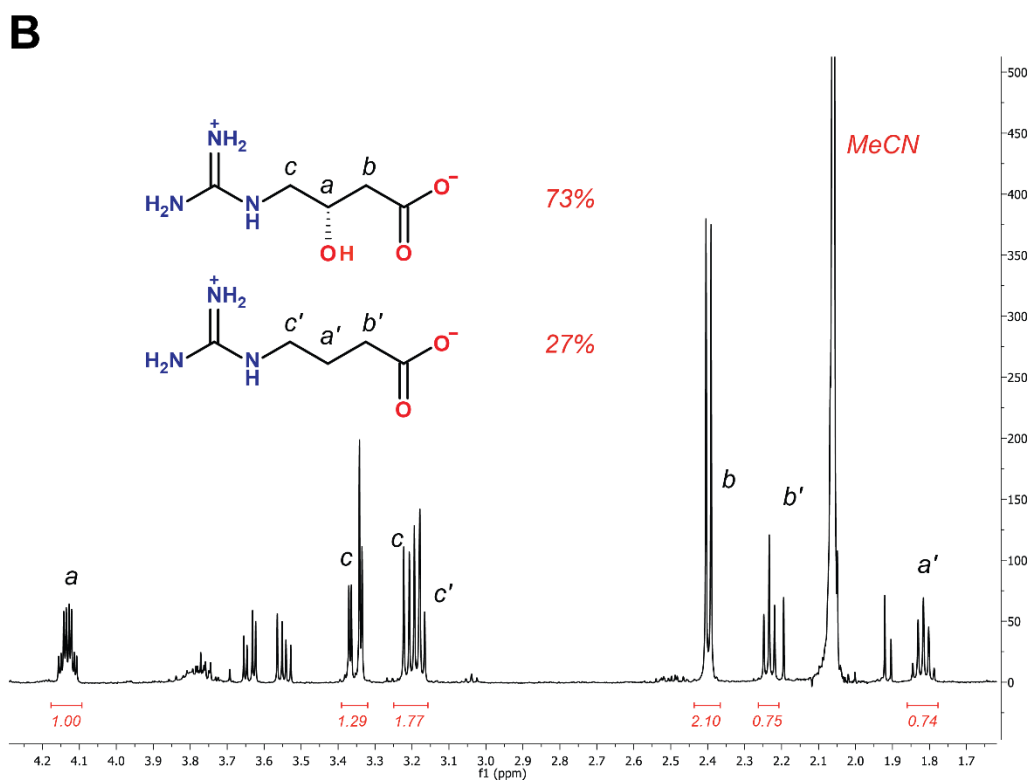
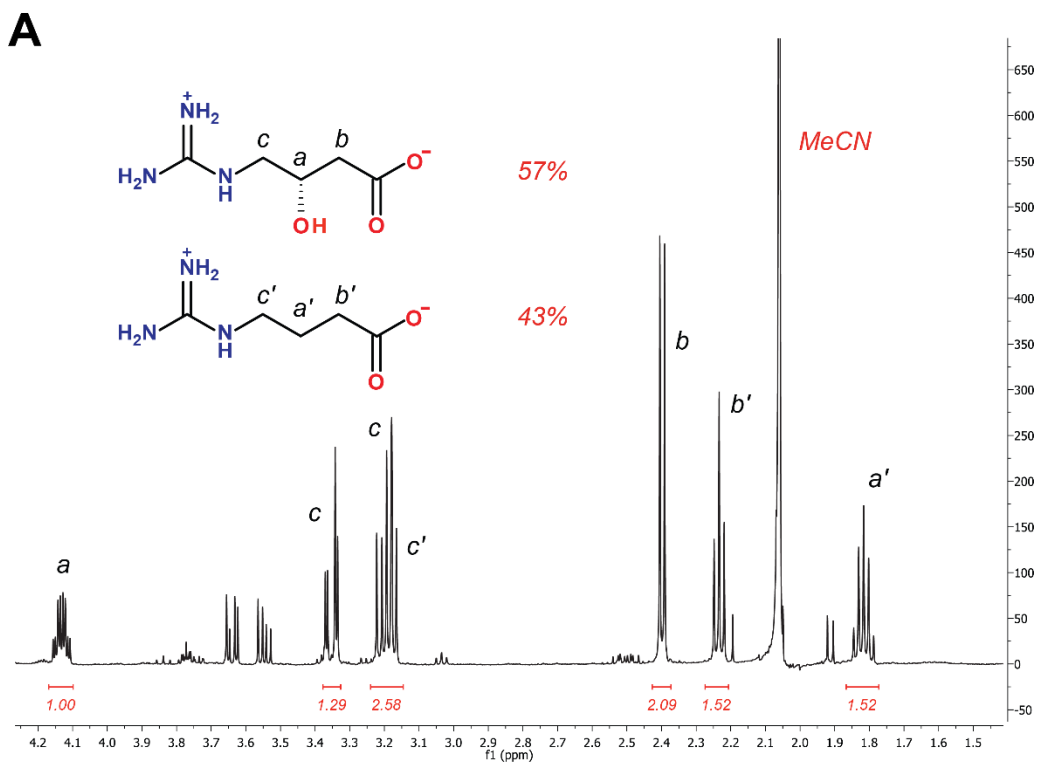


Figure 5-8. ^1H NMR spectra from reaction mixtures containing MppP and L-arginine in the absence of CMH (a) and in the presence of CMH (b).

5.3.3 Capturing nitric oxide adduct

Given the high reactivity of nitric oxide, numerous adducts could possibly form with the reaction components. A potential adduct with a hypothetical arginine-derived, carbon-centered radical is shown in Figure 5-9. Since nitrogen dioxide is also a product of the reaction of nitric oxide with dioxygen, formation of an adduct involving this species is also a possibility. The results of the ESI-MS analysis of the reaction and control samples are displayed in Figure 5-10. The peak at 205 m/z, which is missing in the control reaction, could indicate an adduct forming at C2 (Figure 5-10B). Further studies will include optimization of reagent concentrations as well fragment analysis using MS/MS to confirm the identity of the adduct.

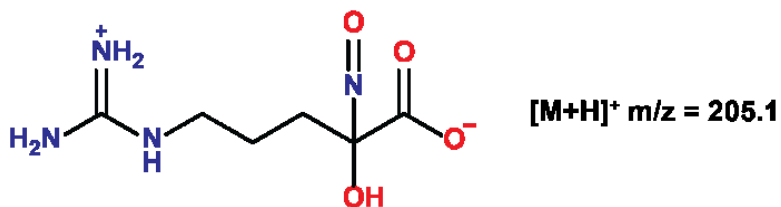


Figure 5-9. Potential adduct formed by MppP reaction intermediate and nitric oxide

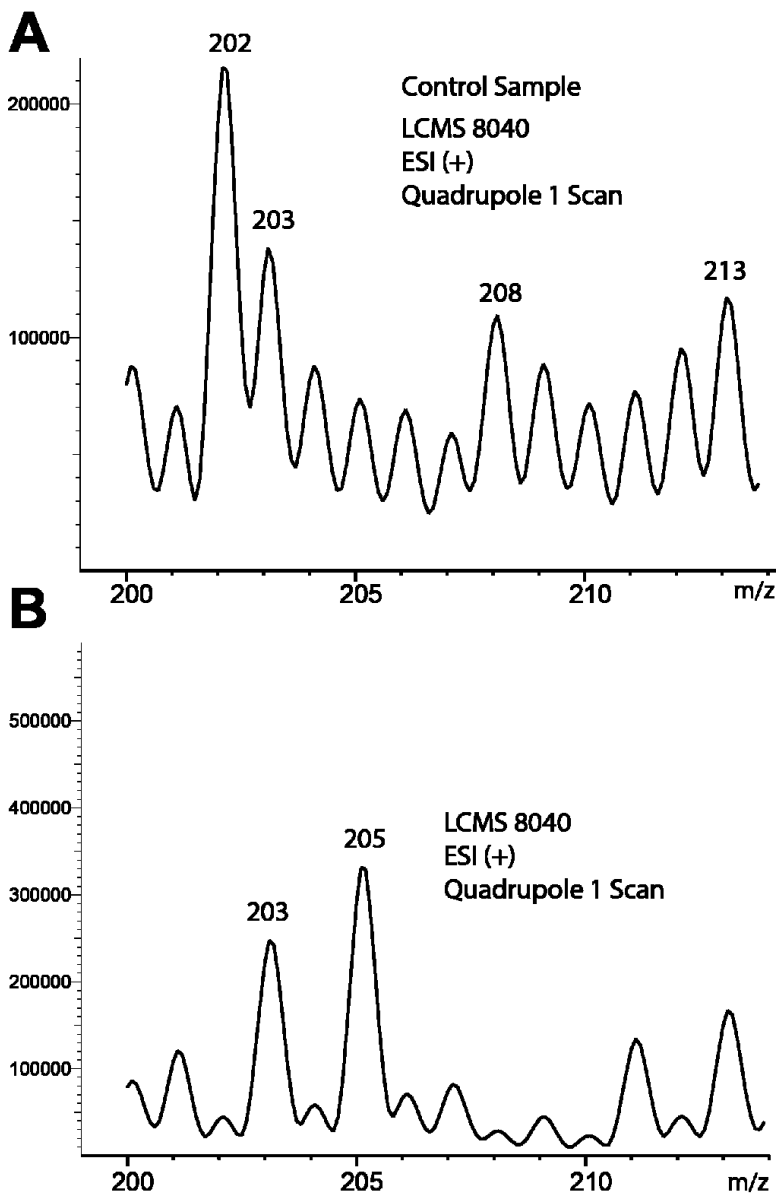


Figure 5-10. First quadrupole scan of the L-Arg, DEANO, Cat(Fe^{3+})NO control sample in positive ESI mode (a). First quadrupole scan of the test sample containing L-Arg, DEANO, Cat(Fe^{3+})NO, and MppP.

5.3.4 MppP mechanism does not involve 4,5 unsaturated intermediate

The resulting integrated spectra show that hydrogen/deuterium exchange occurs for the protons on C3 (Note that this refers to C3 of amino acid, which corresponds to C2 on the decarboxylated acid seen in NMR spectra) as reflected by the diminished integrals and collapsing of the multiplet caused by the negligible coupling with deuterium atoms (Figure 5-11A). The C4 multiplet also became “simplified” in deuterium oxide, due to reduced coupling constants with the C3 deuterium

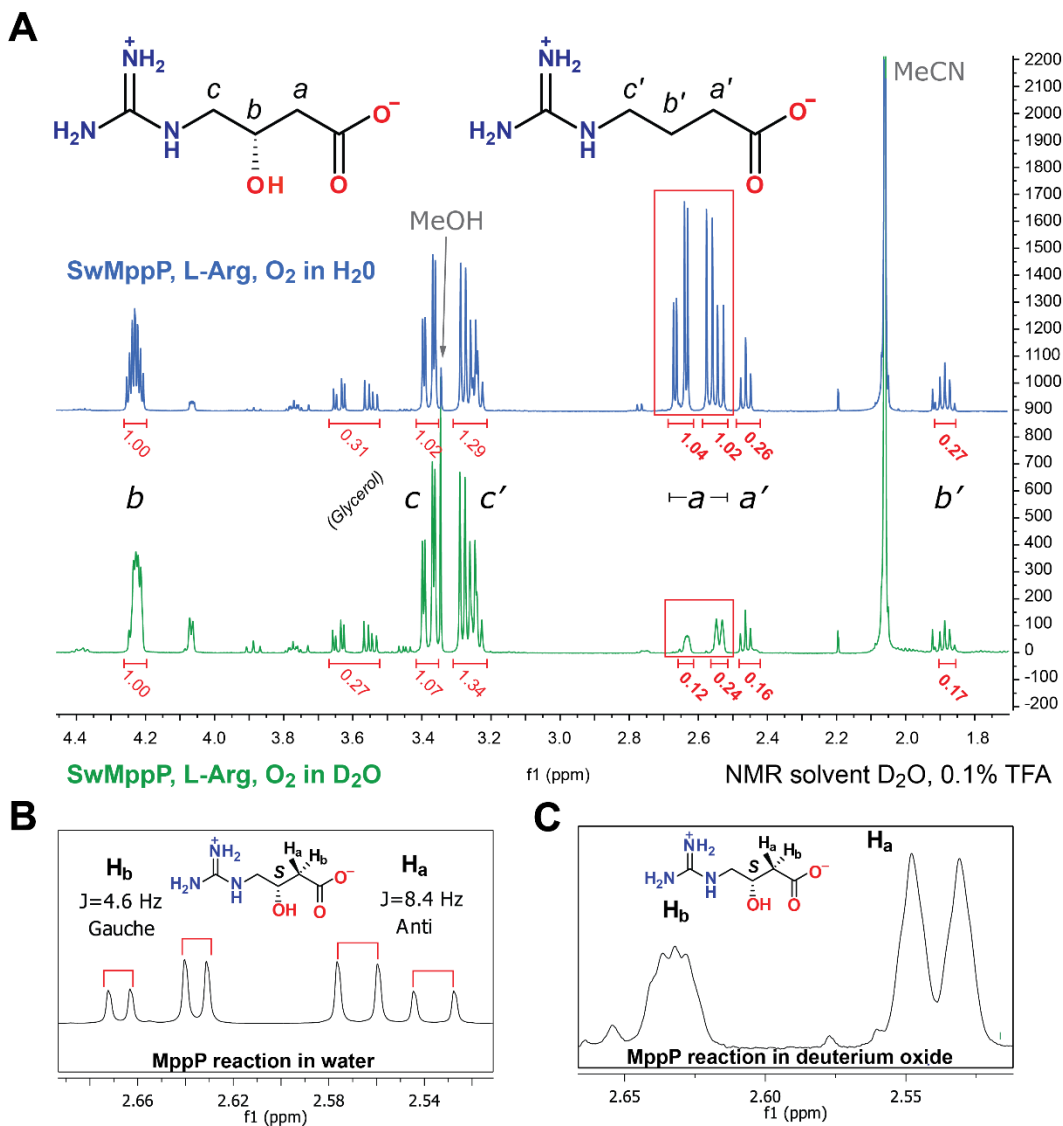


Figure 5-11. ¹H NMR spectra of MppP reaction with L-arginine carried out in deuterium oxide (bottom) and water (top) (A). Zoomed in ¹H NMR spectra of MppP and L-Arg reactions in deuterium oxide and water, showing only the diastereotopic protons on alpha carbon. (B) Measured J-constants for anti and gauche protons. (C) “Simplified” peaks due to smaller J-constants of deuterium exchanged protons.

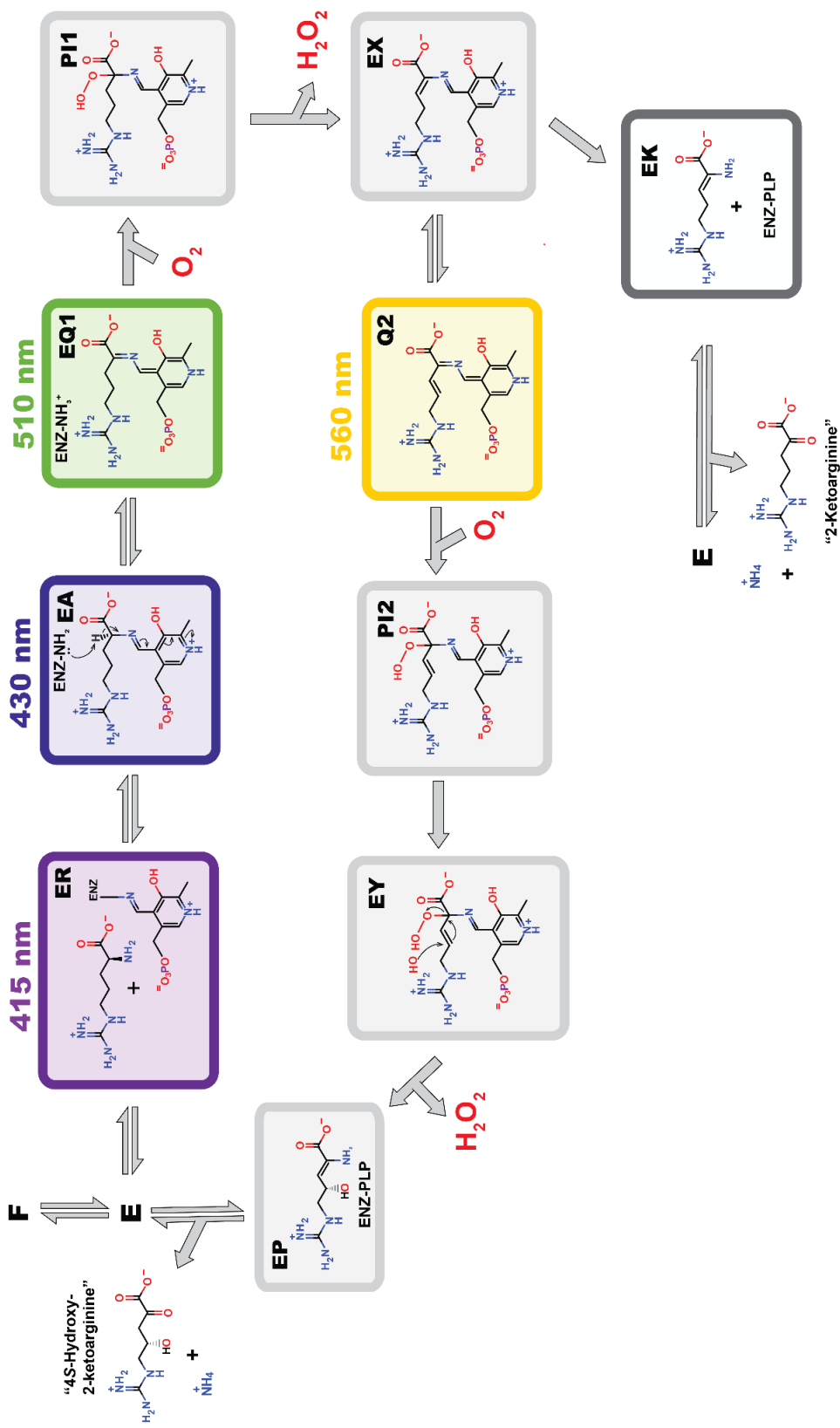
atoms. However, the signal from the C5 diastereotopic protons did not diminish at all, leading to the conclusion that proton abstraction did not occur at this site. In addition to ruling out the involvement of a 4,5-unsaturated intermediate in the mechanism, this experiment provided information about the stereoselectivity of proton abstraction at C3.

Figure 5-11B shows the NMR spectrum zoomed in on the signal from the C3 diastereotopic protons for the MppP reaction in water. The protons in gauche conformation relative to the hydroxyl group on C4 exhibit smaller coupling constants (J constant) than protons in the anti conformation. As seen in Figure 5-11B, the C3 diastereotopic protons do not show evidence of non-enzymatic hydrogen-deuterium exchange (D_2O was used as the solvent for all NMR measurements to reduce the signal from water), indicating that even in the acidic environment due to the 0.1% TFA in the NMR sample, the ketone form is favored over the enol. Therefore, any hydrogen-deuterium exchange observed at C3 for the reaction run in deuterium oxide can be attributed to the enzymatic activity of MppP.

In deuterium oxide (Figure 5-11C) exchange of the gauche proton has been approximately two-fold higher than the exchange of proton in anti conformation. This unequal extent of hydrogen-deuterium exchange for the diastereotopic protons on C3 indicates that stereoselective proton abstraction of the gauche proton is occurring. The identity of the species abstracting the C3 proton remains speculative at this point, although the reactive nucleophiles such as superoxide or hydroperoxide anion generated from its reaction with water, are plausible candidates.

5.3.5 Revised MppP mechanism

Since the results of the NMR experiment carried out in deuterium oxide showed that no proton abstraction occurs at C5, the MppP mechanism needed to be revised to remove the 4,5-unsaturated intermediate (Scheme 5-3, VIII). In the revised mechanism (Scheme 5-6), the steps originally envisioned as involving the direct abstraction of a proton from the substrate have been reworked as a series of peroxy intermediates resulting from the attack of hydroperoxide anion at C2 of the substrate (Scheme 5-6, PI1 and PI2). In PI2, the C3-C4 bond has been oxidized and the hydroxide ion generated from the reaction of superoxide with water to generate the hydroperoxide anion could then perform a Michael addition at C4. This would lead to the release of hydrogen peroxide and creation of a 2,3-unsaturated enamine (now hydroxylated at C4; *e.g.* EP in Scheme 5-6) that is subsequently deaminated after release from the enzyme to give 4-hydroxy-2-ketoarginine. It is not clear at this point whether the keto acid (4HKA) or the enamine is the favored substrate for the next enzyme in the pathway, MppR. Given the rapidity of the non-enzymatic deamination, it would be difficult, but perhaps not impossible, to answer this question.



Scheme 5-6. Revised MppP mechanism without 4,5-unsaturated intermediate

5.3.6 Single turnover experiments improved Kintek Explorer fit

The single-turnover, double-mixing data at 560 nm show a “simpler” curve, with just one peak (Figure 5-12), that provided a fit with better-constrained parameters compared to the pseudo first-order experiment. The revised model with the rate constants calculated by KinTek Explorer is shown in Scheme 5-7. As seen from the FitSpace plots (Figure 5-13), the first half of the model is well constrained, while the second half contains several steps with few, if any constraints. Despite this shortcoming, the revised model has an improved global fit, particularly for quinonoid 2, and is in agreement with the NMR experiments that indicate that a 4-5 unsaturated intermediate is not involved in the mechanism.

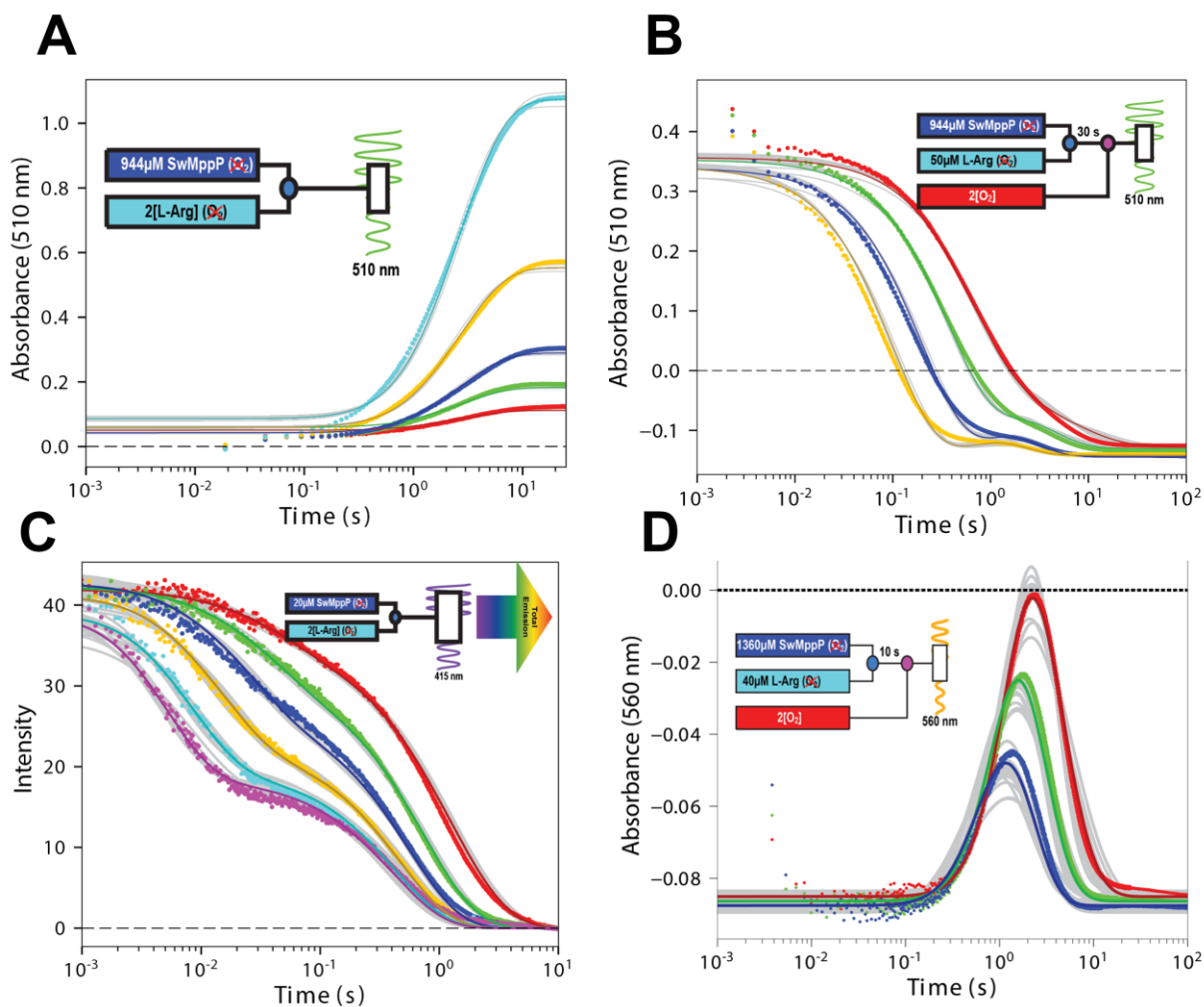
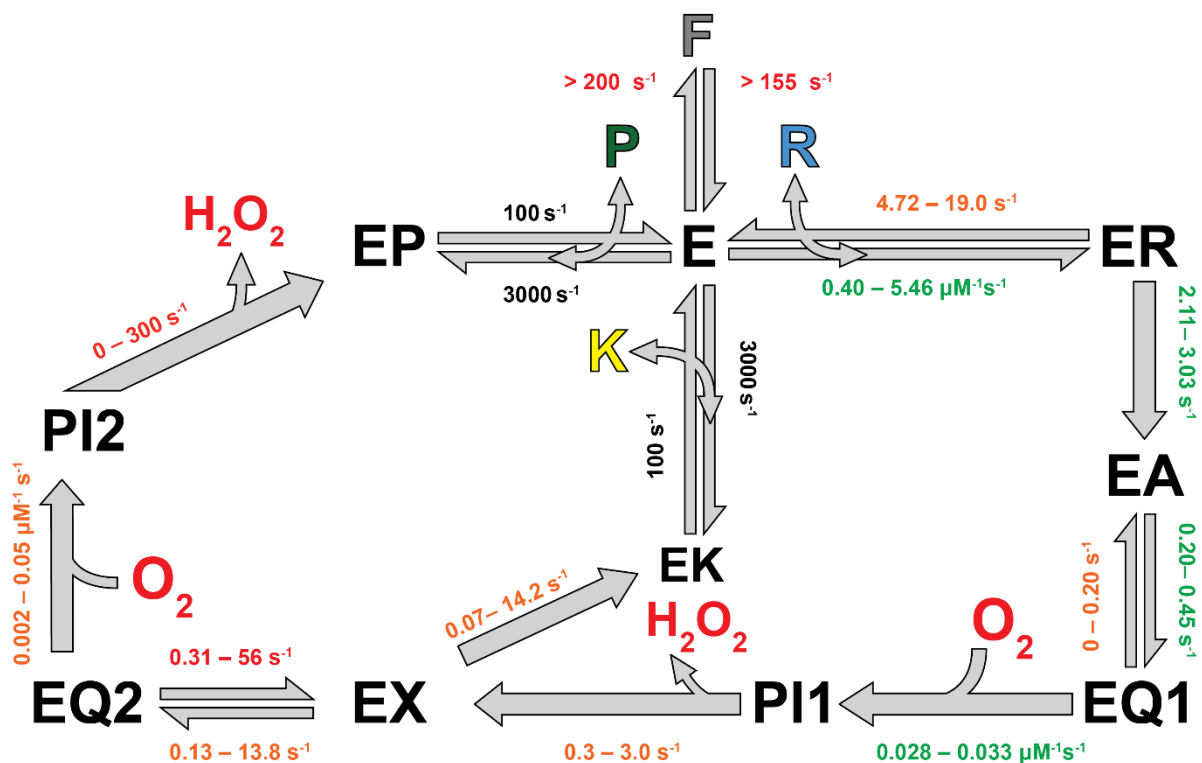


Figure 5-12. (A,B,D) Single-turnover experiments of MppP and L-Arg. The double-mixing experiment monitoring absorbance at 560 nm shows just one peak, unlike when carried out under pseudo first-order conditions. (C) Pseudo first-order experiment monitoring fluorescence produced by excitation at 415 nm.



Scheme 5-7. The revised kinetic model for MppP fit using KinTek Explorer. The peroxo intermediates (PI1 and PI2) were included based on the NMR experiments that eliminated any 4-5 unsaturated species from the mechanism as described earlier. The green rate constants are relatively well constrained based on the FitSpace results (see Figure 5-11). Orange constants have broader parameter ranges, while red ones are poorly constrained. The black constants have been fixed during global fitting as they were assumed to involve rapid equilibrium.

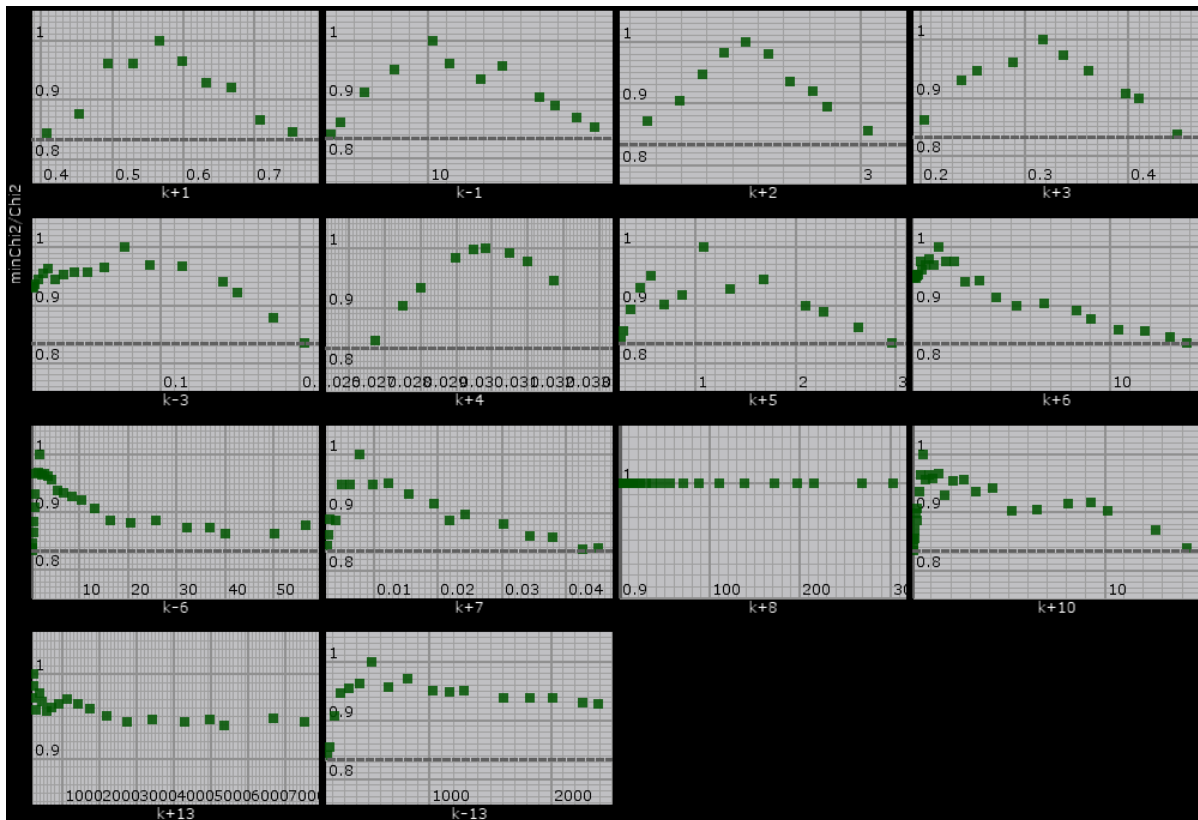


Figure 5-13. Two-dimensional FitSpace plots showing the range of values for each rate constant in the kinetic model that are consistent with the data. Single, sharp peaks indicate well constrained estimates. A sharp rise followed by a plateau signifies that the lower limit is well defined, while the opposite pattern, a plateau followed by a sharp drop, defines an upper limit on the rate constant. Flat lines (e.g. $k+8$) show that the rate constant is completely unconstrained by the data. No plots are calculated for rate constants that were fixed in the model (e.g. the irreversible steps for the reactions with dioxygen).

5.3.7. Product analysis of MppP reaction with DHR

Upon mixing the enzyme and the substrate, the solution turned purple for approximate 10 seconds (Figure 5-14), after which it became dark yellow. The mass spectroscopic product analysis of the reaction of anaerobic MppP with DHR showed that the Q2 decays to 2-ketoarginine (Figure 5-15).

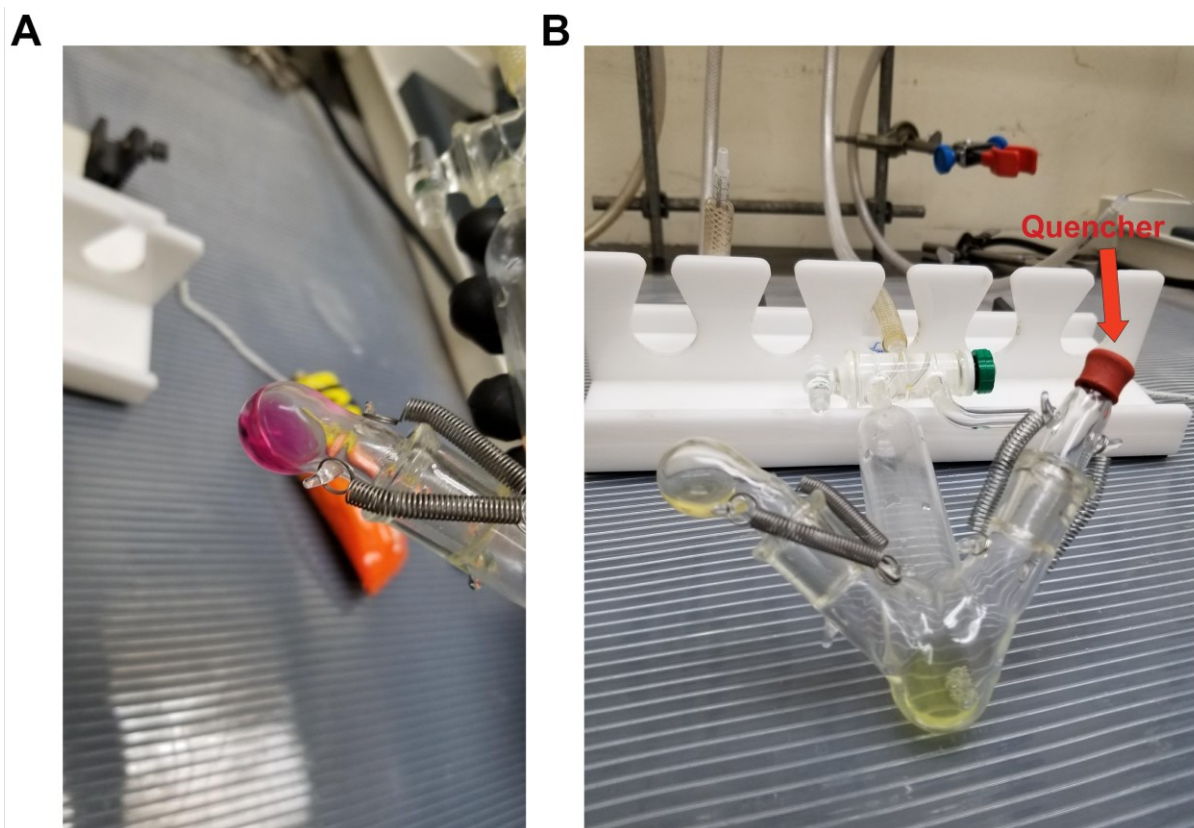


Figure 5-14. (A) upon mixing with enzyme, DHR solution briefly turns purple, confirming formation of a highly conjugated quinonoid 2. (B) The tonomer used for anaerobic reaction of MppP and DHR. The side arm on the right has a septum in order to allow for injection of methanol to quench the reaction, while maintaining anaerobic environment.

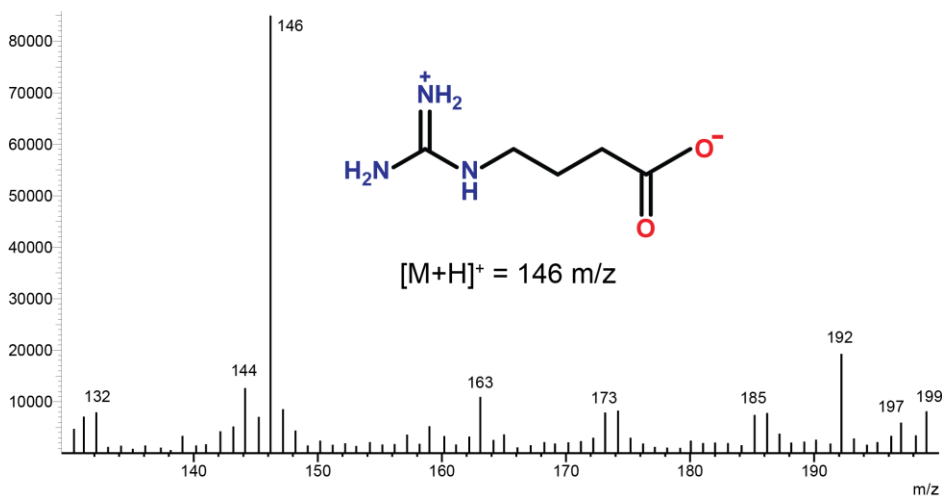


Figure 5-15. MS scan of reaction of MppP and DHR. The most intense peak corresponds to decarboxylated 2-ketoarginine

The single-turnover experiments with DHR show that, even under anaerobic conditions, the second quinonoid intermediate will decay (Figure 5-16A). This was a surprising observation, as we had expected Q2 to require oxygen to proceed to 4HKA and would thus be stable in the absence of oxygen. The biphasic decay in Figure 5-16A is convincing, however; there is no plateau at 560

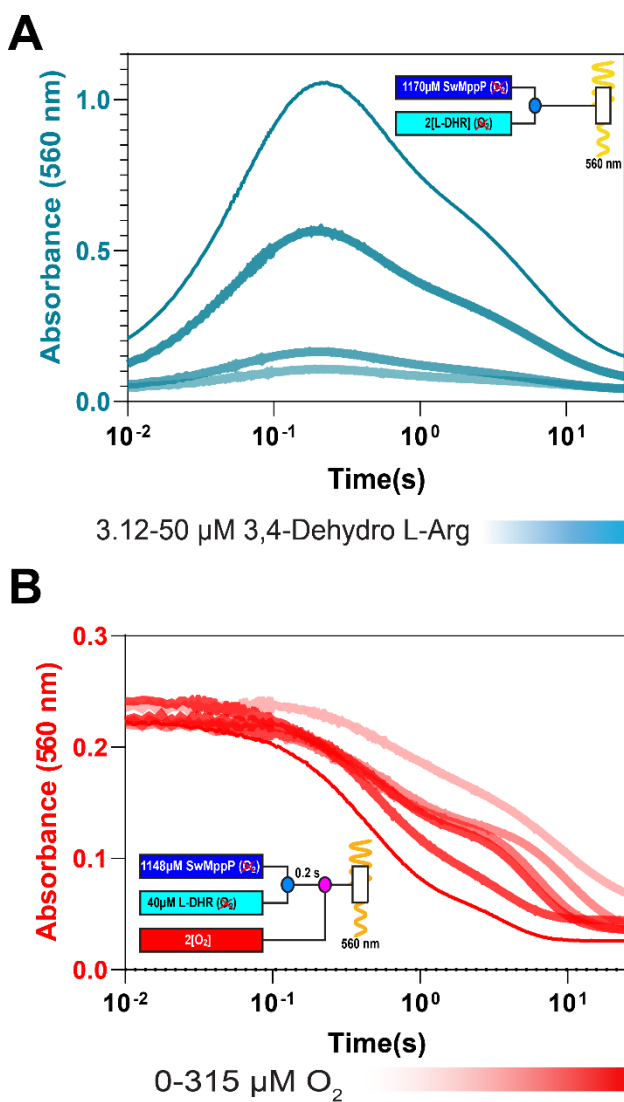


Figure 5-16. (A) The single-turnover single-mixing reaction of MppP and DHR monitored via absorbance at 560 nm. Under anaerobic condition, the quinonoid 2 accumulates followed by rapid decay phase. (B) Single-turnover double-mixing reaction of MppP and DHR with a range of added dioxygen concentrations.

nm. Mass spectrometric analysis of reaction products revealed that Q2 decayed to give 2-

ketoarginine. This confirms the placement of the bifurcation point before Q2, as suggested by modelling the mechanism in KinTek Explorer. Thus far, we have been unable to satisfactorily fit the DHR data by simulation in KinTek Explorer. A number of different models have been tested, but none result in a robust fit to these complicated, multiphasic data.

5.3.8 Determination of Q1 extinction coefficient

As seen in Figure 5-17, there is no decay at 510 nm, indicating that there is no oxygen present in the reaction. Using the method described in Section 5.2.8, the extinction coefficient of quinonoid 1 was determined to be which was found to be $29173.63 \pm 470.46 \text{ M}^{-1} \text{ cm}^{-1}$ (at 95 % confidence interval)

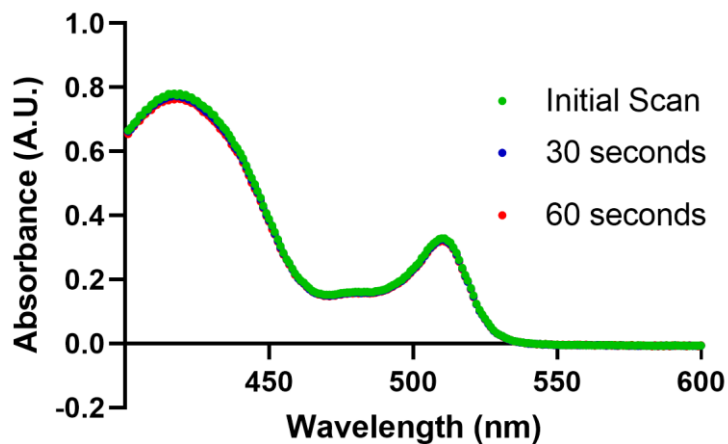


Figure 5-17. UV-VIS scans of MppP reaction with L-Arg under anaerobic conditions leading to accumulation of quinonoid 1 intermediate. The subsequent scans show that the absorbance at 510 nm is stable meaning that all arginine is bound, and no oxygen is present to allow decay of quinonoid 1.

5.3.9 Vinyl glycine inhibits MppP activity

The inhibition of MppP by VG is seen in Figure 5-18. In the control reaction, the accumulation of

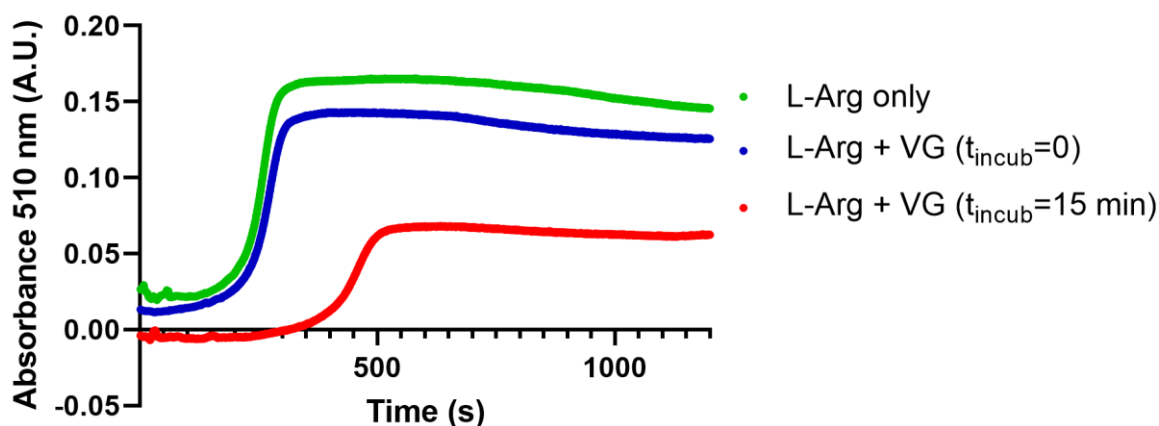


Figure 5-18. Inhibition curves for MppP reaction in the presence of vinylglycine. The green curve represents the reaction of MppP and L-Arg without vinylglycine. The blue curve represents the reaction of MppP and L-Arg in the presence of vinylglycine without first incubating enzyme and vinylglycine. Red curve was obtained for the experiment incubating enzyme and vinylglycine for 15 minutes prior to adding L-Arg.

the Q1 peak at 510 nm begins at approximately 200 s. This is the time required for 10 μ M SwMppP to consume all of the dioxygen in the cuvette. Without preincubation with VG, there is no significant inhibition, since L-Arg can likely out-compete VG due to its higher binding affinity. However, when MppP is preincubated with VG, the enzyme takes longer to consume the available dioxygen, presumably because the active enzyme concentration has been reduced by the inhibitor. The peak at 510 nm in the presence of VG with preincubation is also only 40% of that observed in the control reaction.

5.3.10 Analysis of solvent isotope effects

There are several significant differences in the spectra obtained from the single-turnover reactions that appear to be caused by solvent isotope effects. The pseudo-first order fluorescence experiment shows a muted first phase compared to the experiment in H₂O (Figure 5-19A) which is not the case in the absence of deuterium oxide (Figure 5-12C). In the single-mixing experiment monitored at 510 nm, where MppP reacts with L-Arg in the absence of dioxygen, one typically sees Q1 accumulate and then plateau as the enzyme is “stuck” waiting for dioxygen. When there are traces of oxygen (*i.e.* the system is not completely anaerobic) the plateau will not be perfectly horizontal and the absorbance at 510 nm will decrease slightly after the peak. However, even though oxygen was absent in this experiment, a marked decay of Q1 was observed. It is currently difficult to explain how deuterium oxide apparently destabilizes Q1, but it could be that the energetics of proton/deuteron transfers favor the decay of Q1, presumably back to the external aldimine. Overall, these preliminary experiments confirm the presence of significant normal solvent KIEs in MppP catalysis, which can be helpful in future mechanistic studies.

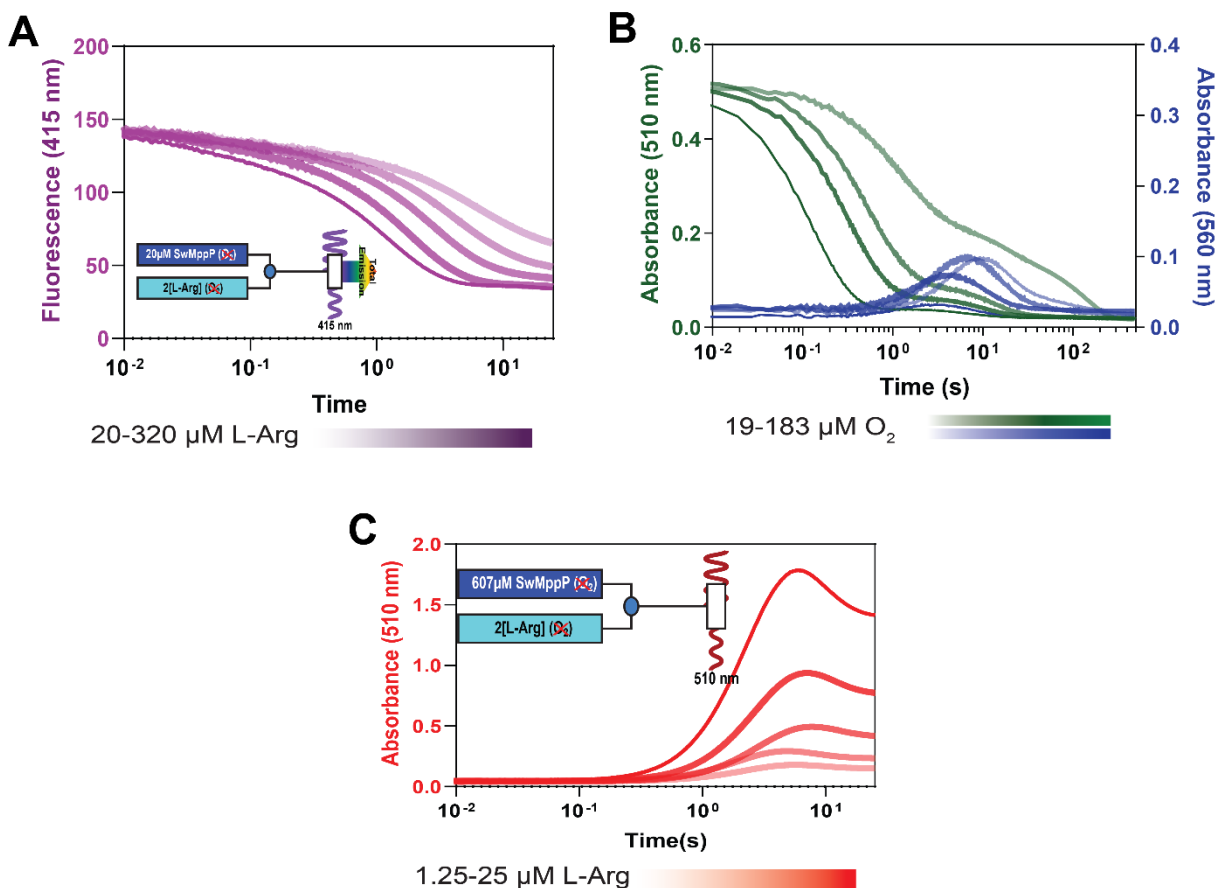


Figure 5-19. (A) Single-mixing 415 nm excitation fluorescence experiment of MppP and L-Arg in the presence of deuterium oxide. (B) Double-mixing experiments at 510 and 560 nm of MppP and L-Arg in the presence of deuterium oxide. (C) Single-mixing experiment at 510 nm of MppP and L-Arg in the presence of deuterium oxide.

5.3.11 Ratio of 4HKA/2KA varies with pH and temperature

The NMR spectra in Figure 5-20 show that lowering the pH increases the amount of 4HKA produced, despite reducing the reaction rate (as measured by dioxygen consumption, see Han, Lanlan, "Structure-Function Relationships in Bacterial Regulatory Proteins and an Enzyme Involved in Antibiotic Biosynthesis" (2017). *Theses and Dissertations*). However, it appears that even in phosphate at pH 8.4, the ratio can fluctuate, as in this experiment, the amount of 4HKA was 14 % higher than expected. This may not be a direct result of any influence on MppP catalysis,

but rather a consequence of the non-linear NMR baseline leading to less accurate integrals. The reason for the consistently increased preference for 4HKA production at lower pH values is currently unknown. It could be that pH has an influence on the dynamics of the enzyme. Since the N-terminus is known to transition from disordered to ordered upon substrate binding, and to make key contacts with the substrate,² it is tempting to speculate that pH can affect the conformational dynamics in this part of the protein. The effect might also be due to alterations in the dynamics of the catalytic lysine, since attack of the Lys221 at C4' of the PLP in the EX intermediate (Scheme 5-6) could lead to premature release of the oxidized imine (Scheme 5-6, EK). Partitioning down the two branches of the mechanism may be a function of keeping the catalytic lysine away from the cofactor until the second oxidation step has occurred. It could also be that the enzyme is running unnaturally fast at alkaline pH, since *in vivo* it would presumably function closer to pH 7.0. Perhaps the increased rate deranges the relative timings of events in the active site, creating opportunities for the enzyme to release the partially oxidized product. The NMR experiments also show that lowering the temperature increases the amount of 4HKA produced (Figure 5-21), even at pH 8.4 where the enzyme reaches its maximum turnover number. Temperature could also clearly affect the conformational dynamics of the protein, and if the N-terminus is more mobile at higher temperatures, one could imagine that premature “opening” of the active site by disordering of the N-terminus might allow water to enter the active site and prematurely hydrolyze a post-Q1 reaction intermediate to 2KA. Presumably, at lower temperatures, the active site is better able to shield itself from water.

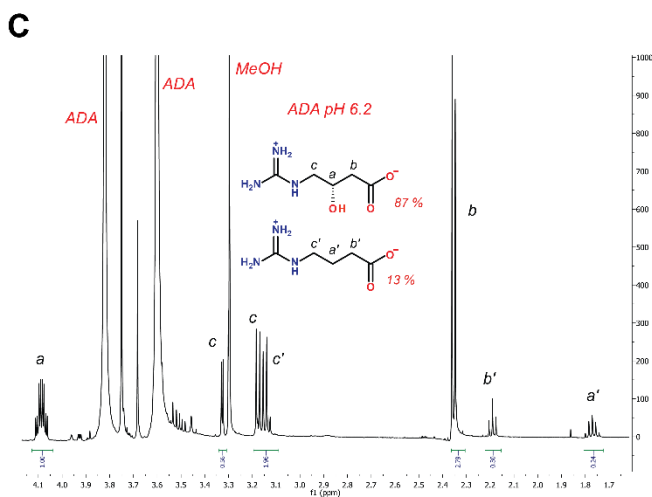
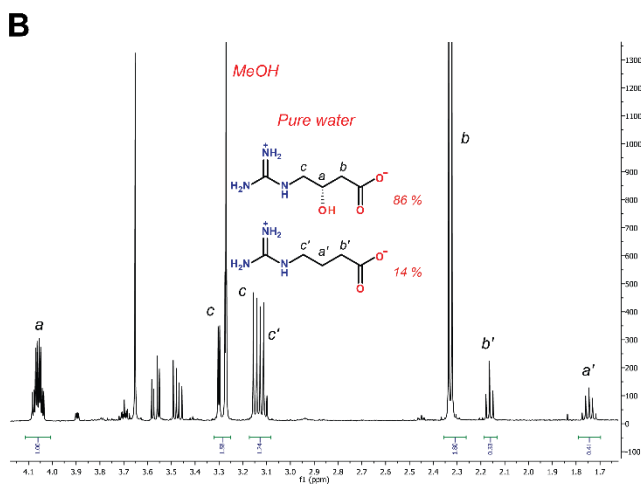
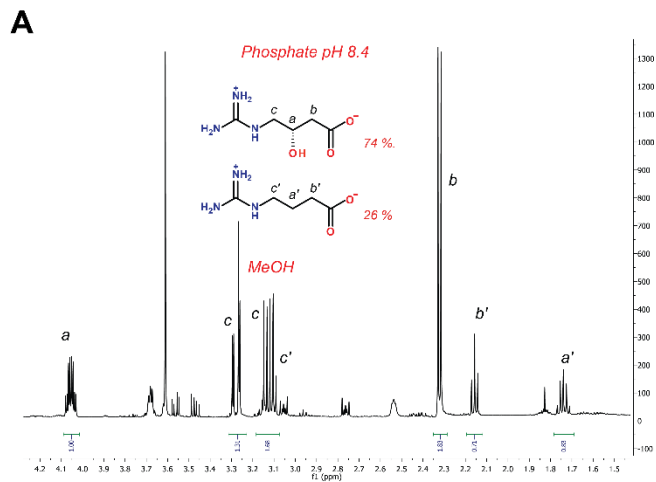


Figure 5-20. (A) ^1H NMR spectrum of MppP reaction with L-Arg carried out in phosphate pH 8.4. (B) ^1H NMR spectrum of MppP reaction with L-Arg carried out in water. (C) ^1H NMR spectrum of MppP reaction with L-Arg carried out in ADA pH 6.2.

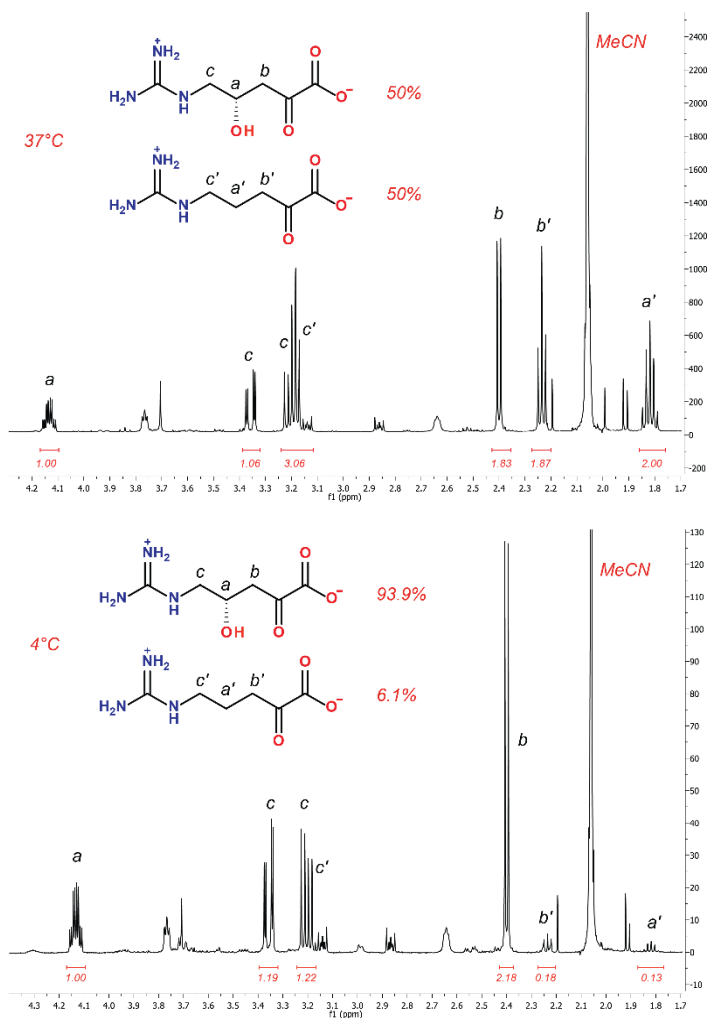


Figure 5-21. (A) ¹H NMR spectrum of MppP reaction with L-Arg in 10 mM phosphate pH 8.4 at 37 °C. (B) ¹H NMR spectrum of MppP reaction with L-Arg in 10 mM phosphate pH 8.4 at 4 °C.

5.3.12 The ratio of 4HKA/2KA determined using quench-flow based method

The quenched-flow LC-MS/MS experiments provided direct insight into the production of 4HKA and 2KA at early reaction times, as opposed to the end-point measurements done by NMR (Figure 5-25A). The average ratio of 4HKA to 2KA at 7s and 15s is 1.48 (Figure 5-25B), compared to approximately 1.45 determined using ¹H NMR (Figure 5-22). However, below 5 seconds, the ratio is closer to 1:1. Such behavior was not expected and future studies will be aimed at gaining better understanding of it.

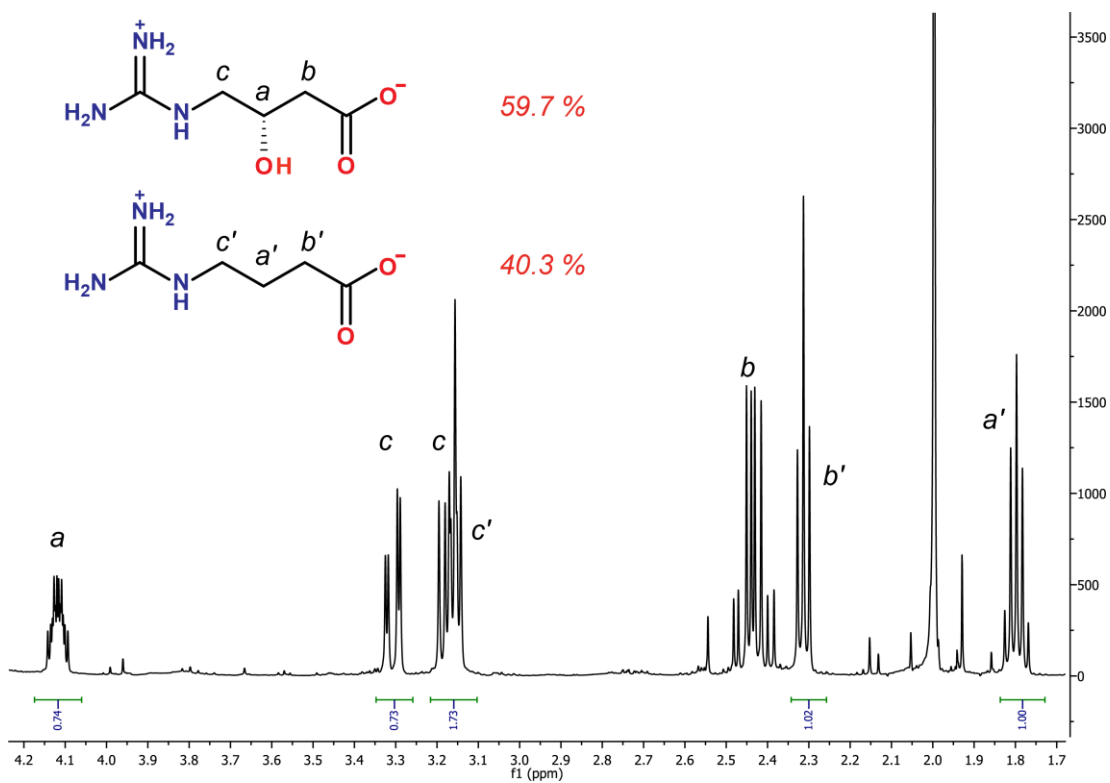


Figure 5-22. ^1H NMR spectrum of reaction of MppP and L-Arg. The relative ratio between 4HKA and 2KA was used to quantify standards used in LC-MS/MS experiments.

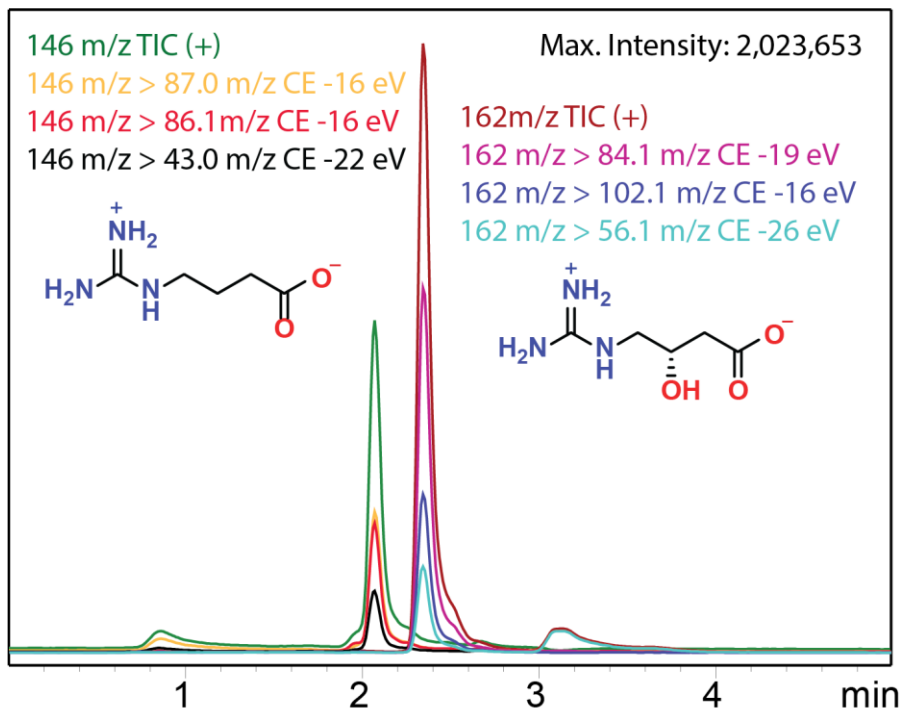


Figure 5-23. Separation of decarboxylated 4HKA and 2KA using ZIC HILIC on Shimadzu LCMS 8060 for a reaction of 20 μ M MppP and 480 μ M L-Arg quenched after 15 seconds

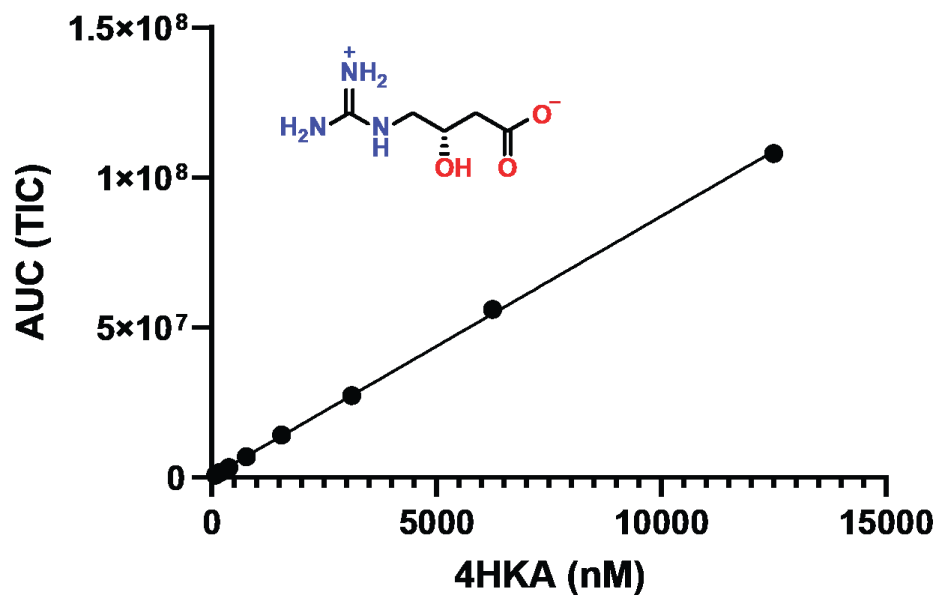
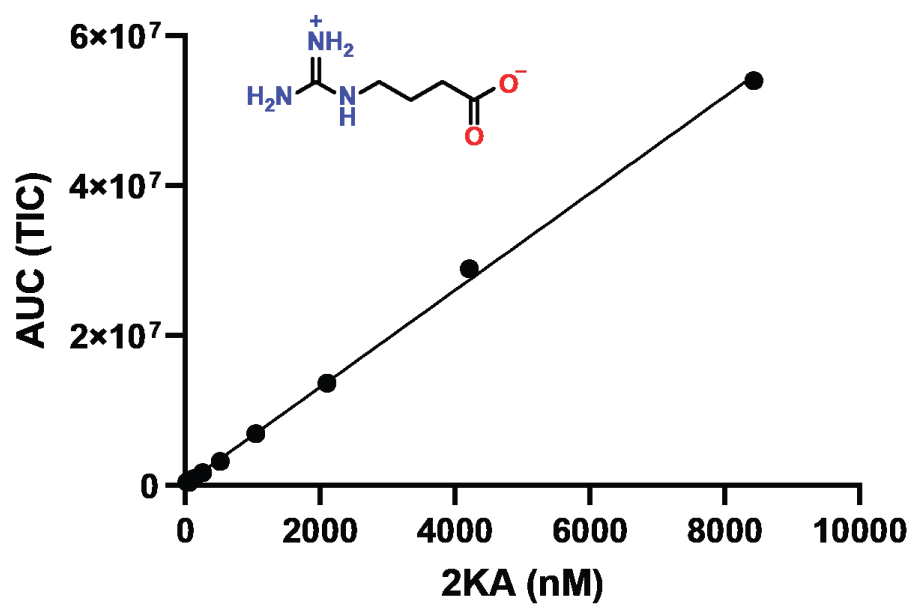
A**B**

Figure 5-24. (A) Standard curve for 4HKA. (B) Standard curve for 2KA

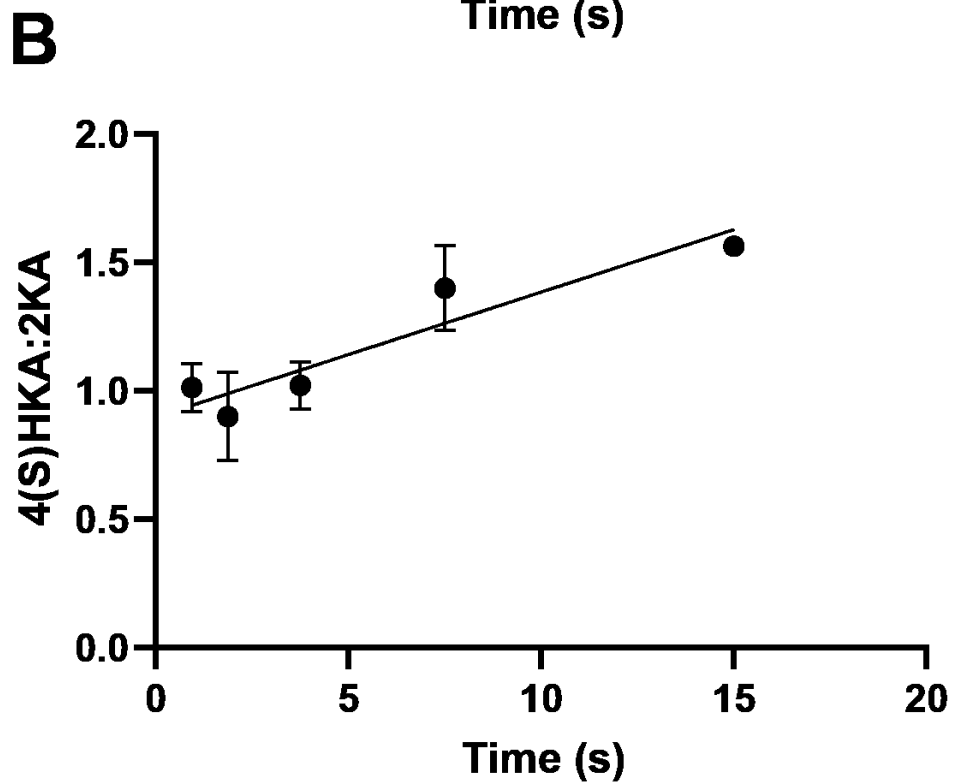
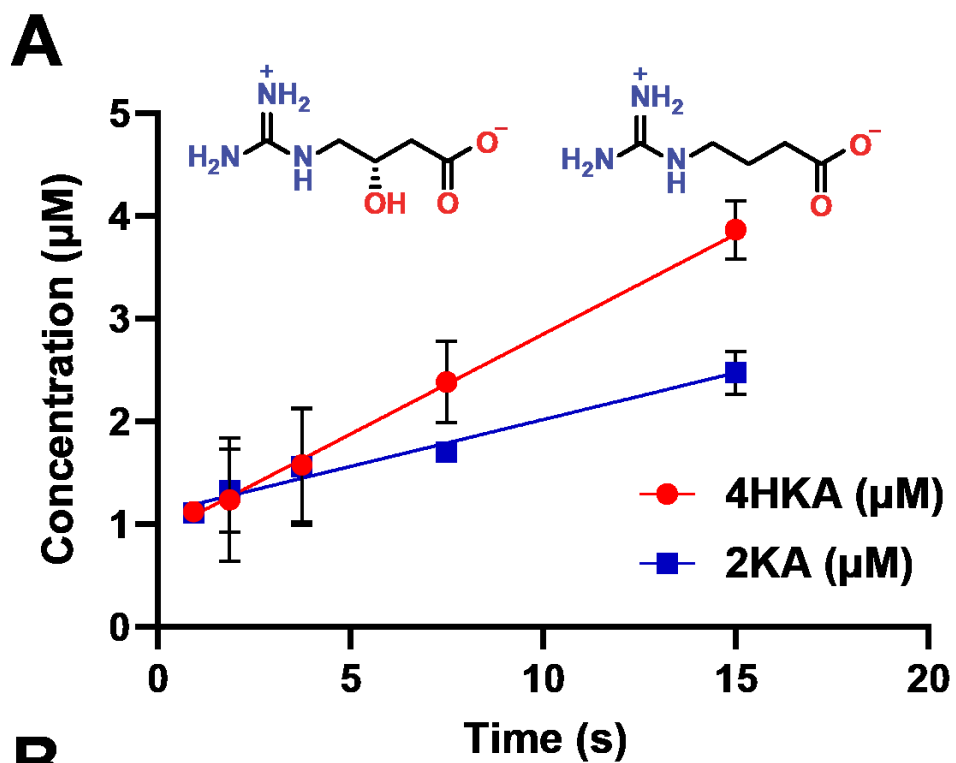


Figure 5-25. (A) The production of 4HKA and 2KA by MppP in a reaction with 480 μM L-Arg. (B) The ratio between 4HKA and 2KA over time.

5.4 Conclusions

The work shown in this chapter led to a revised mechanism of MppP, since NMR experiments in deuterium oxide showed that a 4,5-unsaturated intermediate is not involved in the mechanism. Involvement of superoxide has been confirming using EPR, and preliminary MS data indicates a possibility of trapping the carbon-centered radical intermediate. In addition to answering existing questions, some of the experiments discussed in this chapter have raised new ones, such as questions regarding a shift in product ratios observed in quenched-flow experiments. Looking forward, the future work on the MppP mechanism will focus on the attempt to capture the proposed peroxy intermediate as well as finding a way to exclusively produce 4HKA.

5.5 References

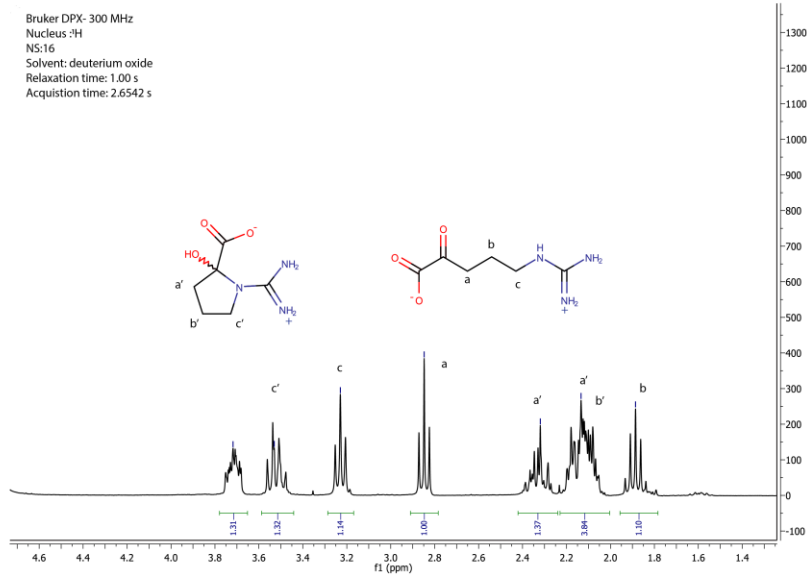
1. Han, L.; Schwabacher, A. W.; Moran, G. R.; Silvaggi, N. R., Streptomyces wadayamensis MppP Is a Pyridoxal 5'-Phosphate-Dependent L-Arginine alpha-Deaminase, gamma-Hydroxylase in the Enduracididine Biosynthetic Pathway. *Biochemistry* **2015**, *54* (47), 7029-40.
2. Han, L.; Vuksanovic, N.; Oehm, S. A.; Fenske, T. G.; Schwabacher, A. W.; Silvaggi, N. R., Streptomyces wadayamensis MppP is a PLP-Dependent Oxidase, Not an Oxygenase. *Biochemistry* **2018**, *57* (23), 3252-3264.
3. Johnson, K. A., Fitting enzyme kinetic data with KinTek Global Kinetic Explorer. *Methods Enzymol* **2009**, *467*, 601-626.
4. Johnson, K. A.; Simpson, Z. B.; Blom, T., Global kinetic explorer: a new computer program for dynamic simulation and fitting of kinetic data. *Anal Biochem* **2009**, *387* (1), 20-9.
5. Johnson, K. A.; Simpson, Z. B.; Blom, T., FitSpace explorer: an algorithm to evaluate multidimensional parameter space in fitting kinetic data. *Anal Biochem* **2009**, *387* (1), 30-41.
6. Davies, M. J., Detection and characterisation of radicals using electron paramagnetic resonance (EPR) spin trapping and related methods. *Methods* **2016**, *109*, 21-30.
7. Villamena, F. A., EPR Spin Trapping. In *Reactive Species Detection in Biology*, 2017; pp 163-202.
8. Dikalov, S. I.; Polienko, Y. F.; Kirilyuk, I., Electron Paramagnetic Resonance Measurements of Reactive Oxygen Species by Cyclic Hydroxylamine Spin Probes. *Antioxid Redox Signal* **2018**, *28* (15), 1433-1443.
9. Babić, N.; Peyrot, F., Molecular Probes for Evaluation of Oxidative Stress by In Vivo EPR Spectroscopy and Imaging: State-of-the-Art and Limitations. *Magnetochemistry* **2019**, *5* (1).
10. Solc, M., Kinetics of the Reaction of Nitric Oxide with Molecular Oxygen. *Nature* **1966**, *209*, 706.
11. Purwar, N.; McGarry, J. M.; Kostera, J.; Pacheco, A. A.; Schmidt, M., Interaction of nitric oxide with catalase: structural and kinetic analysis. *Biochemistry* **2011**, *50* (21), 4491-503.
12. Berkowitz, D. B.; Charette, B. D.; Karukurichi, K. R.; McFadden, J. M., alpha-Vinyl Amino Acids: Occurrence, Asymmetric Synthesis and Biochemical Mechanisms. *Tetrahedron Asymmetry* **2006**, *17* (6), 869-882.
13. Eliot, A. C.; Kirsch, J. F., Pyridoxal phosphate enzymes: mechanistic, structural, and evolutionary considerations. *Annu Rev Biochem* **2004**, *73*, 383-415.
14. Capitani, G.; Tschopp, M.; Eliot, A. C.; Kirsch, J. F.; Grutter, M. G., Structure of ACC synthase inactivated by the mechanism-based inhibitor L-vinylglycine. *FEBS Lett* **2005**, *579* (11), 2458-62.
15. Schowen, K. B.; Schowen, R. L., Solvent isotope effects of enzyme systems. *Methods Enzymol* **1982**, *87*, 551-606.
16. Schowen, R. L., The use of solvent isotope effects in the pursuit of enzyme mechanisms. *Journal of Labelled Compounds and Radiopharmaceuticals* **2007**, *50* (11-12), 1052-1062.
17. Fernandez, P. L.; Murkin, A. S., Inverse Solvent Isotope Effects in Enzyme-Catalyzed Reactions. *Molecules* **2020**, *25* (8).
18. Sharma, N. P.; Hajdin, C.; Chandrasekar, S.; Bennett, B.; Yang, K. W.; Crowder, M. W., Mechanistic studies on the mononuclear ZnII-containing metallo-beta-lactamase ImiS from *Aeromonas sobria*. *Biochemistry* **2006**, *45* (35), 10729-38.
19. Kovrigin, E. L.; Loria, J. P., Characterization of the transition state of functional enzyme dynamics. *J Am Chem Soc* **2006**, *128* (24), 7724-5.
20. Moran, G. R., Anaerobic methods for the transient-state study of flavoproteins: The use of specialized glassware to define the concentration of dioxygen. *Methods Enzymol* **2019**, *620*, 27-49.
21. Krezel, A.; Bal, W., A formula for correlating pKa values determined in D2O and H2O. *J Inorg Biochem* **2004**, *98* (1), 161-6.

APPENDIX

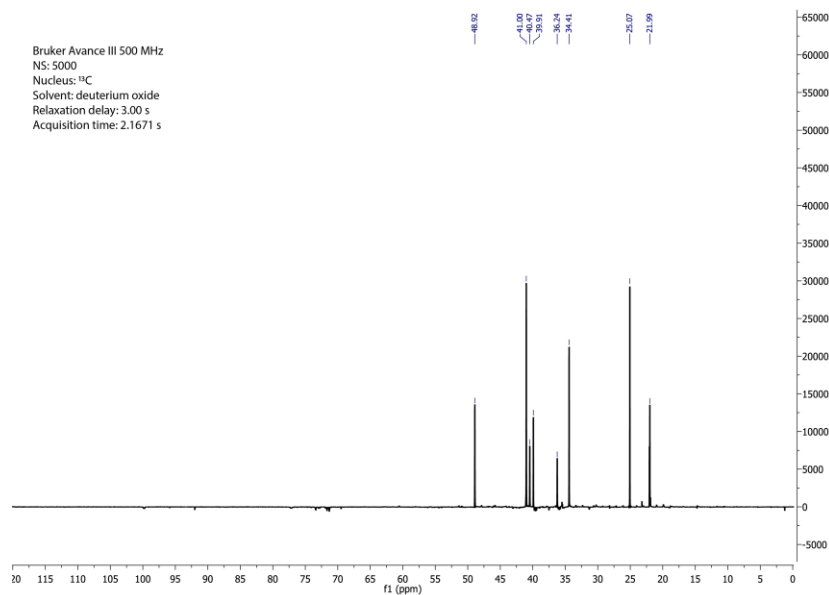
NMR spectra of enzymatically produced 2-ketoarginine

(A) ^1H NMR spectrum of 2KA in D_2O (B) ^{13}C NMR spectrum of 2KA in D_2O ; (C) HSQC-multiplicity edited spectrum of 2KA in D_2O

A

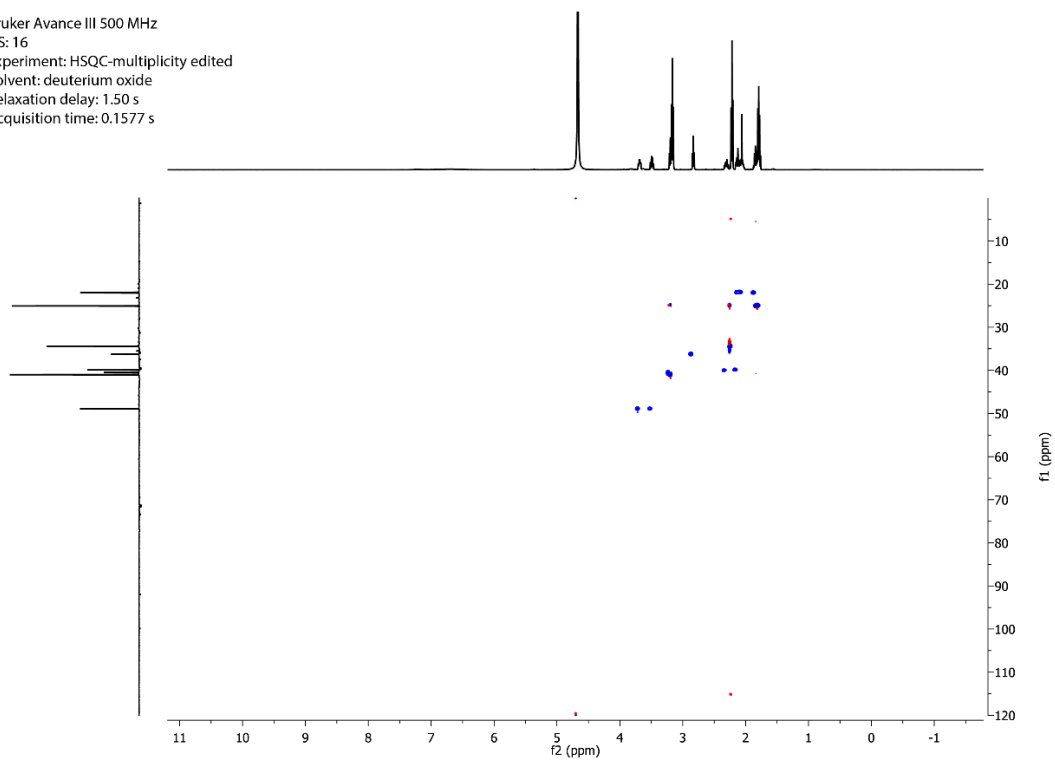


B



C

Bruker Avance III 500 MHz
NS: 16
Experiment: HSQC-multiplicity edited
Solvent: deuterium oxide
Relaxation delay: 1.50 s
Acquisition time: 0.1577 s



CURRICULUM VITAE

Nemanja Vuksanovic

EDUCATION

- Ph.D. Chemistry (Biochemistry) 2015-2020
University of Wisconsin-Milwaukee, Milwaukee, WI
Advisor: Nicholas R. Silvaggi
Thesis: *Structural and functional characterization of enzymes in the L-enduracididine biosynthetic pathway*
- M.S. Chemistry (Materials/Polymer Chemistry) 2013-2015
University of Wisconsin-Madison, Madison, WI
Advisor: Mahesh K. Mahanthappa
Investigated the universality of bicontinuous phase formation in polydisperse ABA triblock copolymers, in which the polydisperse B segment is a Li-ion transporting polymer.
- B.A. Chemistry (*Magna Cum Laude*) 2010-2013
Luther College, Decorah, IA
Advisor: Bradley M. Chamberlain
Honors Thesis: *Polymerization of D,L-Lactide by Novel Titanium (IV) and Tantalum (V) Amidoalkoxide Complexes*

RESEARCH

University of Wisconsin-Milwaukee, Department of Chemistry and Biochemistry

I. Structural and functional characterization of enzymes in the L-Enduracididine biosynthetic pathway. One publication. Three manuscripts in preparation. The non-proteinogenic amino acid L-enduracididine (L-End) is found in a number of cyclic peptide antibiotics, such as teixobactin, mannopeptimycin and enduracidin. The biosynthesis of L-End begins with L-arginine and involves the action of three enzymes, MppP, MppQ, and MppR, in the case of mannopeptimycin. The first enzyme in the pathway, MppP, is an unprecedented PLP-dependent L-Arg oxidase that catalyzes a 4-electron oxidation to give 4-hydroxy-2-ketoarginine. It also releases the partially-oxidized abortive product 2-ketoarginine. Using a variety of techniques, such as ¹H NMR, spin-trap EPR, stopped-flow based single turnover kinetic studies, quench-flow coupled with HILIC LC/MS-MS, I have addressed several unanswered mechanistic questions. By running the MppP reaction in deuterium oxide and observing hydrogen/deuterium exchange via ¹H NMR, I have identified position of the unsaturated carbon-carbon bond in the reaction intermediate. Using spin-trap EPR, I have confirmed that the reaction proceeds through a free radical mechanism. Several single turnover stopped-flow experiments measuring fluorescence and absorbance of reaction intermediates allowed me to globally fit this data in Kintek Explorer modelling software and confirm key steps in the hypothesized reaction mechanism. In order to directly quantify MppP reaction products instead of following molecular oxygen consumption using Clark electrode, I have developed a quench-flow method coupled with LC/MS-MS. Additionally, I have used this method to obtain steady state kinetic parameters for MppR, the enzyme responsible for conversion of 4-hydroxy-2-ketoarginine to 2-ketoenduracididine. I have also used this

method to obtain information about amino acid donor substrate specificity of MppQ, the aminotransferase which converts 2-ketoenduracididine to L-enduracididine.

II. Structural characterization of three NTF2-like proteins involved in polyketide biosynthesis. One publication. Proteins belonging to the NTF2-like superfamily are present in the biosynthetic pathways of numerous polyketide natural products, such as anthracyclins and benzoisochromanequinones. Some have been found to be bona fide polyketide cyclases, but many of them have roles that are currently unknown. I have used X-ray diffraction to solve structures of ActVI-ORFA, an NTF2-like protein in actinorhodin biosynthetic pathway, and its two homologues Caci_6494, a protein from an uncharacterized biosynthetic cluster in *Catenulispora acidiphila*, and Aln2 from *Streptomyces* sp. CM020, a protein in the biosynthetic pathway of alnumycin. This research was conducted in collaboration with Melancon Lab from University of New Mexico and Metsa-Ketela Lab from University of Turku (Finland), who synthesized the genes and provided me with S-DNPA, an intermediate from the actinorhodin pathway. I was able to obtain a crystal structure of Caci_6494 in complex with S-DNPA, which indicates a potential enzymatic function of these proteins due to the presence of a solvent-accessible cavity and the conservation of the His/Asp dyad that is characteristic of many polyketide cyclases.

III. Structural studies of SARS-CoV-2 Mac1 domain and screening for its inhibitors. Two publications. Previous studies involving viral macrodomains have shown evidence of these proteins playing an essential role in virulence. SARS-CoV-1 macrodomain can hydrolyze the bond between amino acid chains and ADP-ribose molecules, thus reversing protein ADP-ribosylation. In a recent work by Jean-Michel Claverie proposed of de-mono-ADP-ribosylation (de-MARylation) of STAT1 by the SARS-CoV-2 nsp3 as a putative cause for cytokine storm in COVID-19 patients, making nsp3 Mac1 important research target. I have solved apo structure of Mac1 at sub-atomic resolution (0.95 Å) which was used by collaborators to perform high-throughput molecular docking screening and identify potential inhibitors. Additionally, I have solved a structure of Mac1 in complex with cyclic AMP, which binds in a fundamentally different manner than AMP and ADP-ribose, thus providing insight into modes of binding of other potential inhibitors.

IV. Structural characterization of porcine pepsin in complex with HIV protease inhibitors in order to develop a novel treatment for patients with laryngopharyngeal reflux. One manuscript in preparation. The Johnston Lab at Medical College of Wisconsin has established that pepsin plays a role in cellular damage observed in patients with laryngopharyngeal reflux, by becoming re-activated once it enters acidic environment of cell lysosomes. Such damage can increase the risk of malignant neoplasm formation and exacerbate symptoms in this patient population. Due to such unmet need, the development of pepsin inhibitors is of crucial importance. I have solved structures of pepsin in complex with several different HIV protease inhibitors, and these structures could help provide insight into designing inhibitors with sub-micromolar affinity.

V. Engineering a highly specific *E. coli* glyoxylate reductase. One manuscript in preparation. I investigated *E. coli* glyoxylate reductase/hydroxypyruvate reductase (EcGhrA) as a coupling enzyme to monitor the transamination of 2-ketoarginine and glycine. The promiscuity of EcGhrA turned out to be problematic because, surprisingly, 2-ketoarginine is quite an efficient substrate for EcGhrA. Since the promiscuity of EcGhrA prevented its use as a coupling enzyme to monitor the aminotransferase activity of an MppQ, an enzyme in the L-Enduracididine biosynthetic pathway, I decided to engineer a more specific variant. X-ray crystal structures of EcGhrA were determined in the unliganded state, and with 2-ketoarginine bound. The electron density map of EcGhrA with 2-ketoarginine bound showed weak electron density for the 2-ketoarginine side chain, complicating the choice of active site residues to target for site-directed mutagenesis. The structure of the complex did suggest that the side chain of W45 could interact with the guanidinium group of 2-ketoarginine. I therefore generated the EcGhrA^{W45F} variant and tested it for activity with 2-ketoarginine, oxaloacetate, and alpha-ketoglutarate. The W45F variant exhibited a significant decrease in the specificity constant (k_{cat}/K_M) for 2-ketoarginine, oxaloacetate, and alpha-ketoglutarate, while the reaction with glyoxylate was not significantly impaired. This engineered EcGhrA^{W45F} variant could be generally useful as a coupling system for enzymes that produce glyoxylate, such as 4-hydroxy-2-oxoglutarate aldolase or isocitrate lyase.

PUBLICATIONS

Virdi, R. S.; Bavisotto, V.R.; Hopper C.N.; **Vuksanovic, N.**; Melkonian R.T.; Silvaggi N.R.; Frick D.N.; Discovery of Drug-like Ligands for the Mac1 Domain of SARS-CoV-2 Nsp3, *SLAS Discovery* **2020**, *Just accepted*

Citations: 0

Vuksanovic, N.; Zhu, X.; Serrano, D. A.; Siitonen, V.; Metsa-Ketela, M.; Melancon, C. E., 3rd; Silvaggi, N. R., Structural characterization of three noncanonical NTF2-like superfamily proteins: implications for polyketide biosynthesis. *Acta Crystallogr F Struct Biol Commun* **2020**, *76* (Pt 8), 372-383.

Citations: 0

Featured on the cover of the August 2020 issue

Frick, D. N.; Virdi, R. S.; **Vuksanovic, N.**; Dahal, N.; Silvaggi, N. R., Molecular Basis for ADP-Ribose Binding to the Mac1 Domain of SARS-CoV-2 nsp3. *Biochemistry* **2020**, *59* (28), 2608-2615.

Citations: 3

Third most accessed article for August 2020

Han, L.; **Vuksanovic, N.**; Oehm, S. A.; Fenske, T. G.; Schwabacher, A. W.; Silvaggi, N. R., Streptomyces wadayamensis MppP is a PLP-Dependent Oxidase, Not an Oxygenase. *Biochemistry* **2018**, *57* (23), 3252-3264.

Citations: 12

MANUSCRIPTS IN PREPARATION

Johnston, N.; Samuels, L.T.; Arnold, A.; Smith, B.; Goetz, J.C.; Ondrey, F.; Wiedmann, T.; Seabloom, D.; Wuertz, B.; Silvaggi, R.N.; **Vuksanovic, N.**; Miller, J.; Bock, J.; Blumin, H.J., Pepsin Inhibitors for the Treatment of Laryngopharyngeal Reflux (To be submitted to *Nature Medicine*)

Vuksanovic, N.; Patterson B.R.; Serrano D.A.; Silvaggi, N.R., Engineering a more specific *E. Coli* glyoxylate reductase/hydroxypyruvate reductase (To be submitted to *Biochemistry*)

Vuksanovic, N.; Serrano, D.A.; Schwabacher, A.W.; Silvaggi, N.R., Structural and Preliminary Biochemical Characterization of MppQ, a PLP-Dependent Aminotransferase from *Streptomyces hygroscopicus* (To be submitted to *Archives of Biochemistry and Biophysics*)

Vuksanovic, N.; Serrano, D.A.; Silvaggi N.R., Use of quench-flow module (qPod) coupled with LC/MS-MS to functionally characterize MppR, an enzyme in the L-Enduracididine biosynthetic pathway from *Streptomyces hygroscopicus* (To be submitted to *Analytical Biochemistry*)

Vuksanovic, N.; Han, L.; Serrano, D.A.; Melkonian, T.R.; Silvaggi, N.R., On the Mechanism of the L-Arginine Oxidase MppP from *Streptomyces Wadayamensis* (To be submitted to *ACS Biochemistry*)

CONFERENCE ABSTRACTS AND PROCEEDINGS

Nemanja Vuksanovic, Nicholas R. Silvaggi. "New Insights into the Mechanism of the L-Arginine Oxidase MppP from *Streptomyces wadayamensis*," *Midwest Enzyme Chemistry Conference*, Illinois Institute of Technology, Chicago, IL. October 26, 2019.

Dante A. Serrano, **Nemanja Vuksanovic**, Nicholas R. Silvaggi. "Nitric oxide trapping of carbon-centered radicals in an enzyme active site," *Midwest Enzyme Chemistry Conference*, Illinois Institute of Technology, Chicago, IL. October 26, 2019.

Nemanja Vuksanovic, Lanlan Han, Nicholas R. Silvaggi. "On the mechanism of the L-Arginine Oxidase MppP from *Streptomyces Wadayamensis*." *Enzyme Mechanisms Conference*, New Orleans, LA. January 6-9, 2019.

Nemanja Vuksanovic, Nicholas R. Silvaggi. "On the Mechanism of the L-Arginine Oxidase MppP from *Streptomyces wadayamensis*," *Midwest Enzyme Chemistry Conference*, Northwestern University, Chicago, IL. October 20, 2018.

Dante A. Serrano, **Nemanja Vuksanovic**, Nicholas R. Silvaggi. "Toward a Mass-Spectrometry-Based Arginine Oxidase Activity Assay," *Midwest Enzyme Chemistry Conference*, Northwestern University, Chicago, IL. October 20, 2018.

Nemanja Vuksanovic, Lanlan Han, and Nicholas R. Silvaggi. "On the Mechanism of the PLP-Dependent L-Arginine Oxidase MppP from *Streptomyces wadayamensis*." *Enzymes, Coenzymes and Metabolic Pathways Gordon Research Conference*, Waterville Valley Resort, Waterville Valley, NH. July 22-28, 2018.

Nemanja Vuksanovic, Brandon Patterson, Nicholas R. Silvaggi. "Engineering *E. coli* glyoxylate reductase with high substrate specificity," *UWM Chemistry Research Symposium*, University of Wisconsin-Milwaukee, Milwaukee, WI. May 22, 2018

Nemanja Vuksanovic, Xuechen Zhu, Charles E. Melançon III, Nicholas R. Silvaggi. "Deciphering the Function of NTF2-like Proteins Associated with Polyketide Biosynthesis in Actinomycetes," *ACS Milwaukee Section Meeting*, Milwaukee, WI. May 3, 2018.

Nemanja Vuksanovic, Xuechen Zhu, Charles E. Melançon III, Nicholas R. Silvaggi. "Deciphering the Function of NTF2-like Proteins Associated with Polyketide Biosynthesis in Actinomycetes," *Midwest Enzyme Chemistry Conference*, Loyola University, Chicago, IL. October 14, 2017..

Brandon Patterson, **Nemanja Vuksanovic**, Nicholas Silvaggi. "Engineering Glyoxylate Reductase's Active Site," *Midwest Enzyme Chemistry Conference*, Loyola University, Chicago, IL. October 14, 2017.

Anamarie Tomaich, William (Parker) May, **Nemanja Vuksanovic**, and Nicholas Silvaggi. "Assigning functions for two "hypothetical proteins" from *Pseudomonas* sp. RIT-PI-q," *Midwest Enzyme Chemistry Conference*, Loyola University, Chicago, IL. October 14, 2017.

Nemanja Vuksanovic, Xuechen Zhu, Charles E. Melançon III, Nicholas R. Silvaggi. "Deciphering the Function of NTF2-like Proteins Associated with Polyketide Biosynthesis in Actinomycetes," *44th UW System Chemistry Faculties Meeting*, University of Wisconsin-Milwaukee, Milwaukee, WI. September 29-30, 2017

Nemanja Vuksanovic, Xuechen Zhu, Charles E. Melançon III, Nicholas R. Silvaggi. "Deciphering the Function of NTF2-like Proteins Associated with Polyketide Biosynthesis in Actinomycetes," *UWM*

Chemistry Research Symposium, University of Wisconsin-Milwaukee, Milwaukee, WI. May 23, 2017

Nemanja Vuksanovic, Xuechen Zhu, Charles E. Melançon III, Nicholas R. Silvaggi. "Deciphering the Function of NTF2-like Proteins Associated with Polyketide Biosynthesis in Actinomycetes," *The FASEB Journal* **2017**, *31* (1_supplement), 766.8-766.8

Nemanja Vuksanovic, Xuechen Zhu, Charles E. Melançon III, Nicholas R. Silvaggi. "Deciphering the Function of NTF2-Like Proteins Associated with Polyketide Biosynthesis in Actinomycetes." *ASBMB Annual Meeting*, Chicago, IL. April 22-26, 2017

Nemanja Vuksanovic, Xuechen Zhu, Charles E. Melançon III, Nicholas R. Silvaggi. "Structural studies of type II polyketide cyclases from Actinobacteria," *Midwest Enzyme Chemistry Conference*, University of Illinois-Chicago, Chicago, IL. October 1, 2016

Bradley M. Chamberlain, **Nemanja Vuksanovic**, Logan Grado. "Titanium Complexes Bearing Optically Active Amidoalkoxides as Lactide Polymerization Catalysts," *Inaugural Conference on Sustainable Polymers* (American Chemical Society and the Royal Society of Chemistry), Safety Harbor, FL, 2013

Nemanja Vuksanovic, Logan Grado, Bradley M. Chamberlain, Adam R. Johnson. "New Corn-Based Plastics from Two Different Polymerization Technologies," *Luther College Research Symposium*, Decorah, IA. May, 2013.

Nemanja Vuksanovic, Logan Grado, Bradley M. Chamberlain, Adam R. Johnson. "Polymerization of D,L-lactide by titanium amidoalkoxide complexes," *National Conference On Undergraduate Research*, University of Wisconsin-La Crosse, La Crosse, WI. April 11-13, 2013

Chloe Gumpert, Nicole Woodson, Peter Douglas, Timothy Cutler, **Nemanja Vuksanovic**, Logan Grado, Bradley M. Chamberlain. "Substituted Glycolides Derived from Fatty Acids as Potential Monomers for the Production of Biodegradable Polymers" *National Conference On Undergraduate Research*, University of Wisconsin-La Crosse, La Crosse, WI. April 11-13, 2013

Nemanja Vuksanovic, Eric Eitheim, Bradley M. Chamberlain. "New Corn-Based Plastics from Two Different Polymerization Technologies" *Luther College Research Symposium*, Decorah, IA. May 2011.

PROTEIN DATA BANK (PDB) ENTRIES

6WEY: High resolution structure of SARS CoV-2 Macro X domain, 0.95 Å

7JME: Structure of the SARS-CoV-2 NSP3 Macro X domain in complex with cyclic AMP

6OVL: 2.1 Å structure of wild type Glyoxylate/Hydroxypyruvate reductase A from *Escherichia Coli* in complex with glyoxylate and NADP⁺

6P35: 2.5 Å structure of wild type Glyoxylate/Hydroxypyruvate reductase A from *Escherichia Coli* in complex with 2-keto arginine and NADP⁺

7JQH: 2.0 Å structure of wild type Glyoxylate/Hydroxypyruvate reductase A from *Escherichia Coli* in complex with NADP⁺ and alpha-ketoglutarate

7JQI: 2.4 Å structure of wild type Glyoxylate/Hydroxypyruvate reductase A from *Escherichia Coli* in complex with NADP⁺ and phosphate

7JQJ: 2.2 Å structure of W45F Glyoxylate/Hydroxypyruvate reductase A from *Escherichia Coli* in complex with NADP⁺

6OXN: 2.6 Å structure of W45F/H46S Glyoxylate/Hydroxypyruvate reductase A from *Escherichia Coli* in complex with NADP⁺ and glyoxylate

6P77: 2.5 Å structure of Caci_6494 from *Catenulispora Acidiphila*

6P7L: 1.8 Å structure of Aln2 from *Streptomyces sp.* CM020

5BKA: 2.1 Å structure of ActVI-ORFA from *Streptomyces Coelicolor*

6VW4: 2.35 Å structure of Caci_6494 from *Catenulispora Acidiphila* in complex with S-DNPA

6XCT: 2.0 Å structure of porcine pepsin in complex with amprenavir

6XCY: 2.0 Å structure of porcine pepsin in complex with ritonavir

6XD2: 1.9 Å structure of porcine pepsin in complex with darunavir

6XCZ: 1.9 Å structure of porcine pepsin in complex with saquinavir

AWARDS AND HONORS

Sosnovsky Dissertation Prize, 2020

Graduate Student Excellence Fellowship, 2019

UWM Sosnovsky Award for Graduate Research- 2nd Place Poster, 2018

UWM Graduate School Travel Grant 2019

UWM Graduate Council Travel Award 2017

Chancellor's Award 2015-2020

Phi Beta Kappa Society 2013

Pi Mu Epsilon (National Mathematics Honor Society) 2013

American Chemical Society Undergraduate Award in Inorganic Chemistry 2012

John G. And Mildred Breiland Endowed Scholarship (Excellence in Chemistry) 2012

Luther College Dean's List 2010-2013

Luther College Preus Presidential Scholarship 2010-2013

WORKSHOPS

CCP4/APS International School in Macromolecular Crystallography, Argonne National Laboratory, Lemont, IL, June 19-26, 2016

TEACHING

University of Wisconsin-Milwaukee, Department of Chemistry and Biochemistry
CHEM 603, Introduction to Biochemistry Laboratory (F2016, F2017, S2020)
CHEM 100, Chemical Science (F2017)
CHEM 501, Introduction to Biochemistry (F2016, F2017)
CHEM 102, General Chemistry (F2015, S2016)

University of Wisconsin-Madison, Department of Chemistry and Biochemistry
CHEM 103, General Chemistry I (F2013, F2014, Summer 2015)
CHEM 104, General Chemistry II (S2014)

Luther College, Department of Chemistry/Mathematics
Organic Chemistry Lab Assistant (2011-2013)
Student Academic Support Center Tutor (2012-2013)
Department of Mathematics Grader (2011-2013)

UNDERGRADUATE RESEARCH MENTORING

Brandon R. Patterson (2017-2018)
2nd place poster UWM Chemistry Undergraduate Symposium 2017
Senior Excellence in Research Award 2018

Parker W. May (2017)
1st place poster UWM Chemistry Undergraduate Symposium 2017

Anamarie Tomaich (2017)
1st place poster UWM Chemistry Undergraduate Symposium 2017

Dante A. Serrano (2018-2019)
3rd place poster UWM Chemistry Undergraduate Symposium 2019

Alex El Fakhoury (2020)

OUTREACH AND SERVICE

University of Wisconsin-Milwaukee Department of Chemistry
Silvaggi Lab Safety Officer 2016-2020

University of Wisconsin-Madison Department of Chemistry
Travel Grant Coordinator 2014-2015
International student representative on Graduate Student-Faculty Liaison Committee 2014-2015
First year representative on Graduate Student-Faculty Liaison Committee 2013-2014

Luther College

Clinton Global Initiative University Conference, Saint Louis, MO, 2013

Presented project "Stop Rural Child Slavery" (Honored Project)

Dell Social Innovation Challenge, 2013

Member of Luther College Chemistry Club 2012-2013

Member of Entrepreneurship Club 2010